JOURNAL OF CAVE AND KARST STUDIES

June 2019
Volume 81, Number 2
ISSN 1090-6924
A Publication of the National Speleological Society

DEDICATED TO THE ADVANCEMENT OF SCIENCE, EDUCATION, EXPLORATION, AND CONSERVATION

Published By
The National Speleological Society

http://caves.org/pub/journal

Office
6001 Pulaski Pike NW
Huntsville, AL 35810 USA
Tel:256-852-1300
nss@caves.org

Editor-in-Chief
Malcolm S. Field
National Center of Environmental
Assessment (8623P)
Office of Research and Development
U.S. Environmental Protection Agency
1200 Pennsylvania Avenue NW
Washington, DC 20460-0001
703-347-8601 Voice 703-347-8692 Fax
field.malcolm@epa.gov

Production Editor
Scott A. Engel
Knoxville, TN
225-281-3914
saecaver@gmail.com

Journal Copy Editor
Linda Starr
Albuquerque, NM

The *Journal of Cave and Karst Studies* , ISSN 1090-6924, CPM Number #40065056, is a multi-disciplinary, refereed journal published four times a year by the National Speleological Society. The *Journal* is available by open access on its website, or check the website for current print subscription rates. Back issues are available from the NSS office.

POSTMASTER: send address changes to the National Speleological Society Office listed above.

The Journal of Cave and Karst Studies is covered by the following ISI Thomson Services Science Citation Index Expanded, ISI Alerting Services, and Current Contents/Physical, Chemical, and Earth Sciences.

Front cover: A newly developed sinking stream. See Frisbee et al. in this issue.

M. D. Frisbee, et al. Processes leading to the re-activation of a sinkhole in buried karst and the subsequent drying of waterfalls in a small catchment located in northern Indiana, USA. *Journal of Cave and Karst Studies*, v. 81, no. 2, p. 69-83. DOI:10.4311/2017ES0116

PROCESSES LEADING TO THE RE-ACTIVATION OF A SINKHOLE IN BURIED KARST AND THE SUBSEQUENT DRYING OF WATERFALLS IN A SMALL CATCHMENT LOCATED IN NORTHERN INDIANA, USA

Marty D. Frisbee[1,C], Zachary P. Meyers[1], Jordyn B. Miller[1], Carolyn L. Gleason[1], Noah S. Stewart-Maddox[1,2], Erik B. Larson[3], Darryl E. Granger[1], Siddharth Saksena[4], Sayan Dey[4], and Emily E. Frisbee[5]

Abstract

A sinking stream pirated water from a series of waterfalls in a small catchment underlain by buried karst in northern Indiana after a sinkhole was scoured and enlarged over the course of 2016. The catchment has historical significance to Indiana, and the current landowners wish to restore flow to the waterfalls. We address the following questions: 1) where does the water go once it enters the sinking stream, 2) what transport processes are active in the carbonate rocks, and 3) what processes led to the re-activation of a buried sinkhole? Breakthrough curves (BTCs) of salt-slug tracer tests show that 24.6 % of the chloride mass was recovered at a conduit spring (Spring 1), located 150 m from the sinking stream, and 26.6 % of chloride mass was recovered at two diffuse springs (Springs 2 and 3), located 315 m from the sinking stream. Despite the difference in distances from the sinking stream, the salt-slug appeared in all springs in approximately two hours. The BTC for Spring 1 was single-peaked, consistent with advection through a single conduit, while the BTCs of Springs 2 and 3 were double-peaked and consistent with advection along bifurcated flowpaths. Spring 2 exhibited a long tail consistent with anastomosing flowpaths and/or presence of pooling along the flowpaths. The sinking stream and other inactive sinkholes are upstream of a dam built in the 1960s. Ponding conditions likely increased the hydraulic head over the buried karst and began dislodging sediment from open pores/conduits in the karst. Record rainfall and widespread flooding during the summer of 2015 scoured the pores leading to the enlargement and reactivation of the sinking stream by the fall of 2016.

Introduction

Hydrogeological processes in karst have been relatively well-studied in carbonate rocks of unglaciated southern Indiana (Murdock and Powell, 1967; Bassett, 1974; Bayless et al., 1994; Duwelius et al., 1996; Lee and Krothe, 2001; Zhou et al., 2002; Florea et al., 2018). However, these processes remain poorly quantified in glaciated northern Indiana. While much of Indiana is underlain by sequences of limestone and dolostone (Gray, 2000; Bedrock Geology of Indiana), it is more common to find carbonate rocks outcropping at the land-surface of southern Indiana in areas that were never glaciated. In comparison, carbonate rocks are typically buried under 30 to 120 m of glacial till in northern Indiana, and these rocks are only exposed at the land-surface, where erosion has uncovered them or streams have incised them (Casey, 1997; Gray, 2000; Hasenmueller and Packman). Bugliosi (1997), Casey (1997), and Eberts and George (1997) mentioned the presence of paleokarst (buried karst) in their studies of the hydrogeological and hydrogeochemical properties of the regional, carbonate aquifer that extends through northern Indiana, Ohio, and Illinois; they did not discuss the potential re-activation of buried karst features. Ultimately, our knowledge of groundwater/surface-water interactions that are facilitated by karst flowpaths and conduits in northern Indiana, Ohio, and Illinois is limited (Sasowsky et al., 2003; Torres and Bair, 2012).

Likewise, our hydrogeochemical understanding of the aquifers' susceptibility to contamination is limited. Groundwater can flow quickly and over long distances through carbonate rock aquifers; for example, groundwater traveled 9.5 km in just 25 hours in carbonate rocks in the Lost River karst basin located in Orange County, southern Indiana (Murdock and Powell, 1967). If groundwater velocities of this same magnitude are present in northern Indiana, where row-crop agriculture is widespread (Randall and Mulla, 2001; Pyron and Neumann, 2008), then it has important implications for the transport of nutrients into the carbonate aquifers and subsequent impacts to freshwater ecosystems (Karr et al., 1985). Sinkholes provide a direct pathway for contaminants to enter a carbonate aquifer (Hallberg and Hoyer, 1982; Wiersma et al., 1986; Field, 1992; Panno et al., 1996, 2001; Herczeg et al., 1997; Florea and Wicks, 2001; Dussart-Baptista et al., 2003; Panno and Kelly, 2004; Lindsey et al., 2010). Consequently, karst aquifers in agricultural landscapes

[1] Department of Earth, Atmospheric, and Planetary Sciences, Purdue University, 550 Stadium Mall Drive, West Lafayette, IN 47907
[2] Idaho Water Resources Research Institute, 322 East Front Street, Suite 242, Boise, ID 83702
[3] Department of Natural Sciences, Shawnee State University, 940 Second St, Portsmouth, OH 45662
[4] Department of Civil Engineering, Purdue University, 550 Stadium Mall Drive, West Lafayette, IN 47907
[5] Wood PLC, 115 W Abeyta Street, Suite A, Socorro, NM 87801
[C] Corresponding Author: mdfrisbee@purdue.edu

are particularly susceptible to pathogens such as fecal coliform (Ryan and Meiman, 1996; Reed et al., 2011) and nutrients such as nitrate (Panno and Kelly, 2004; Pronk et al., 2006; Long et al., 2008; Lindsey et al., 2010; Florea, 2019).

Sinkholes and sinking streams are common in southern Indiana (Bassett and Ruhe, 1974; Sinkhole Areas and Sinking-Stream Basins, 1997; Powell, 2002; Florea et al., 2018). In comparison, buried karst (Bosák et al., 1989; Zötl, 1989) is present in northern Indiana, where the open pores and conduits in the surface of the pre-existing carbonate rocks were covered and filled with glacial sediment during the Last Glacial Maximum. Buried karst features, plugged with low-permeability glacial till, may act as a barrier to downward vertical flow (Veress, 2016). However, there is no guarantee that these features will remain plugged (Armstrong and Osborne, 2003); Ford (1995) presents several scenarios through which descending water and ascending water can exhume and re-activate karst conduits. Once the sediment is removed, the conduit re-activates and impacts the hydrological behavior of the landscape around it. Thus, it is critical that we quantify how these buried karst features are re-activated and, once re-activated, how they impact the transport of water and contaminants from the land surface to the carbonate aquifer.

Here, we reconstruct and quantify the processes leading to the activation of a sinking stream in buried karst and the subsequent drying of waterfalls in a small, tributary catchment to the Wabash River (Figs. 1 and 2). This stream flows through a scenic, limestone canyon containing a series of four waterfalls (Fig. 2). The catchment, known locally as Fitch's Glen, has historical significance in Indiana, and the current landowners were interested in determining why the waterfalls dried up during 2016. A noticeable decrease in streamflow, in the catchment, was observed after the summer of 2015. This seemed strange since widespread flooding occurred in northern Indiana, following record rainfall in June

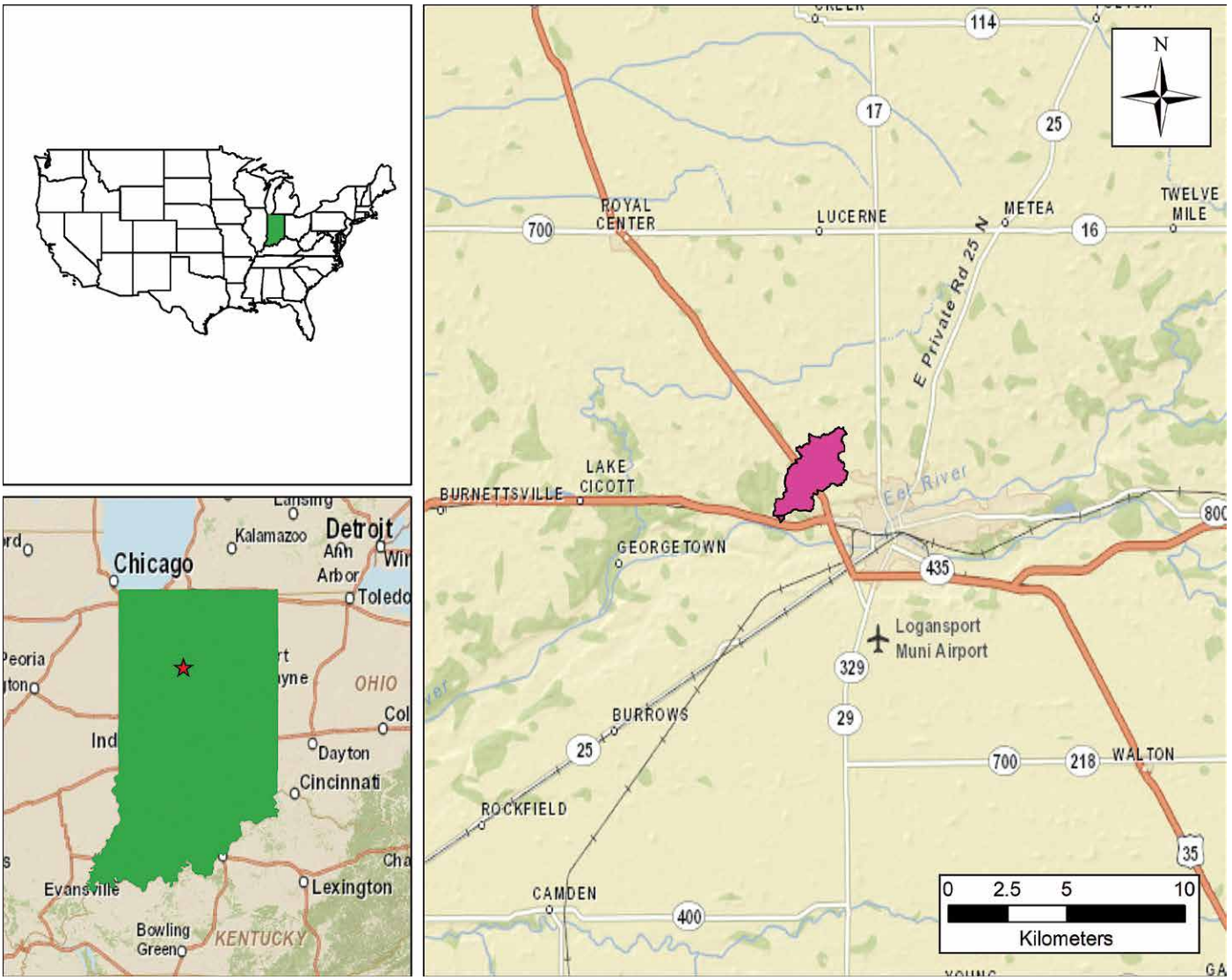

Figure 1. The national basemap is shown in upper left, the state basemap is shown in lower left, and the regional basemap is shown in the larger image on the right. The location of the Fitch's Glen catchment is shown by the magenta-colored polygon outlining the catchment boundary.

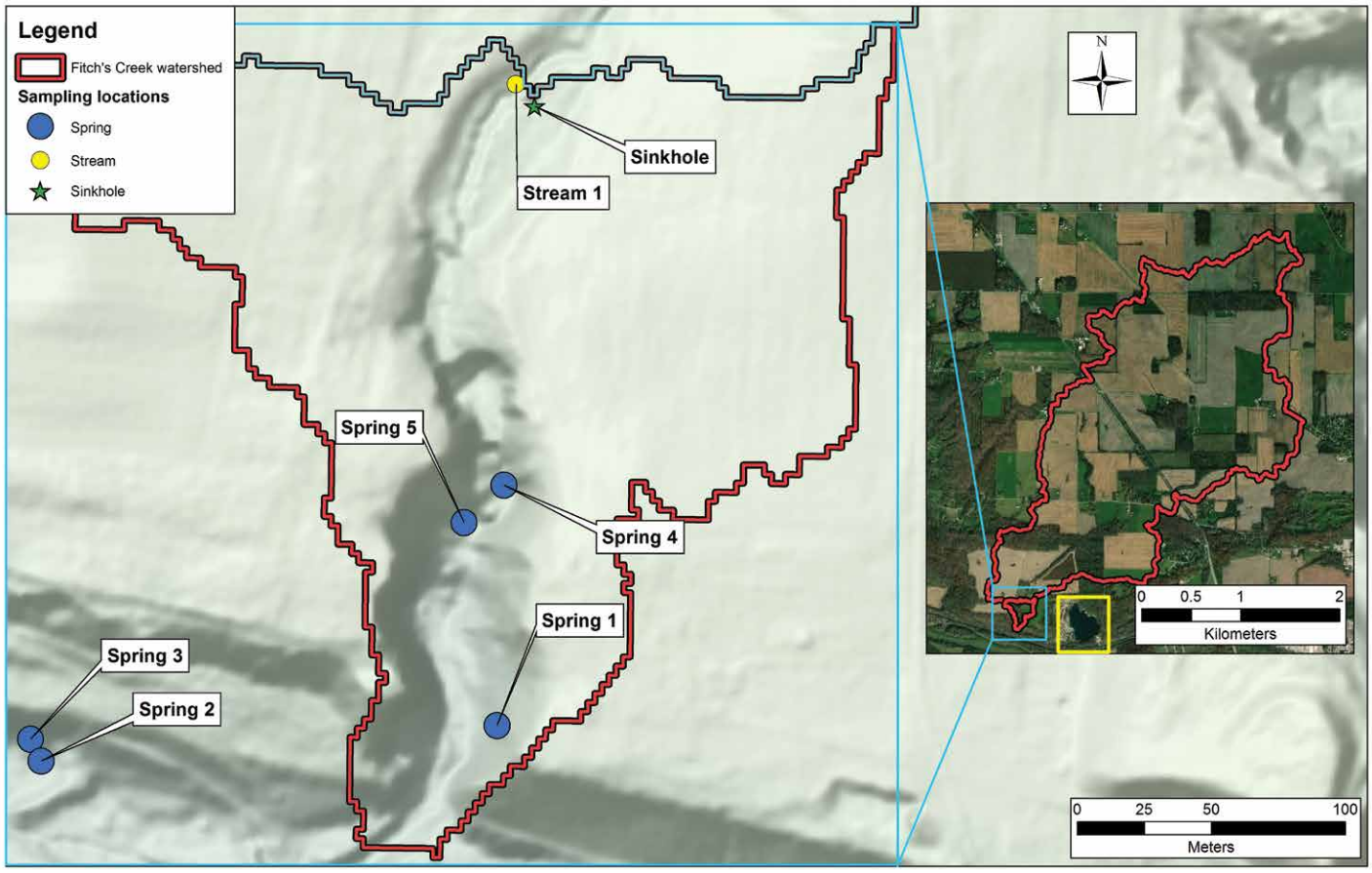

Figure 2. The image on the left is a LIDAR map (1 m resolution) showing locations of the sampling sites and sinking stream; the image on the right shows the boundary of the larger catchment, in red, and surrounding agricultural fields, which drain to this catchment. Please note: the quarry and lake that are mentioned in this article are outlined by the yellow box located to the left of the scale bar in the inset image.

and July of 2015 (Fig. 3). By the spring of 2016, the landowners noticed that a small sinkhole, upstream of the waterfalls, was diverting a small portion of streamflow. In early fall 2016 the sinkhole had developed into a large, sinking stream, and it had captured the entire stream, drying up the downstream waterfalls in the process.

We address these questions: 1) how did the sinking stream become re-activated in the buried karst; 2) where does the streamflow go once it enters the sinking stream; and 3) what transport processes are active in the carbonate rocks at Fitch's Glen? To address these questions, we used a combination of dye- and salt-tracing techniques, major element geochemistry of streams and springs, stable isotopes, and transport models to determine flow and transport parameters in the carbonate bedrock. Using this data, we traced recharge from the sinking stream to down-gradient springs, interpreted the breakthrough curves (BTCs), and addressed the implications of sinkhole development on nutrient loading into groundwater and other surface-water systems with particular reference to northern Indiana.

Materials and Methods

Historical Setting

The Fitch's Glen catchment is located 5.6 km west of Logansport, Indiana (16T 548674 mE, 4511822 mN; Fig. 1). Historically, the catchment has been considered the most picturesque place in Cass County (Powell, 1913) due to the deep, limestone canyon and series of small, 1.2 to 3.1 m, beautiful waterfalls on the property, especially since waterfalls are a rare feature on the till plains of northern Indiana. The property also has historical significance because it was the former home of Graham Fitch, a senator in Indiana from 1857–1861 and a brigade commander in the Union Army during the American Civil War. In addition, the site contains remnants of the old Wabash and Erie Canal constructed in the early 1800s. Fitch's Glen served as a trading post due to its proximity to the Wabash Canal and nearby grain warehouses, and the stream was used in the mid-1800s to supply hydropower to industrial mills (Powell, 1913). In the 1960s, a dam was built approximately 60 m downstream from the current sinking stream. The dam was later breached by private landowners, allowing the stream to freely flow through the catchment.

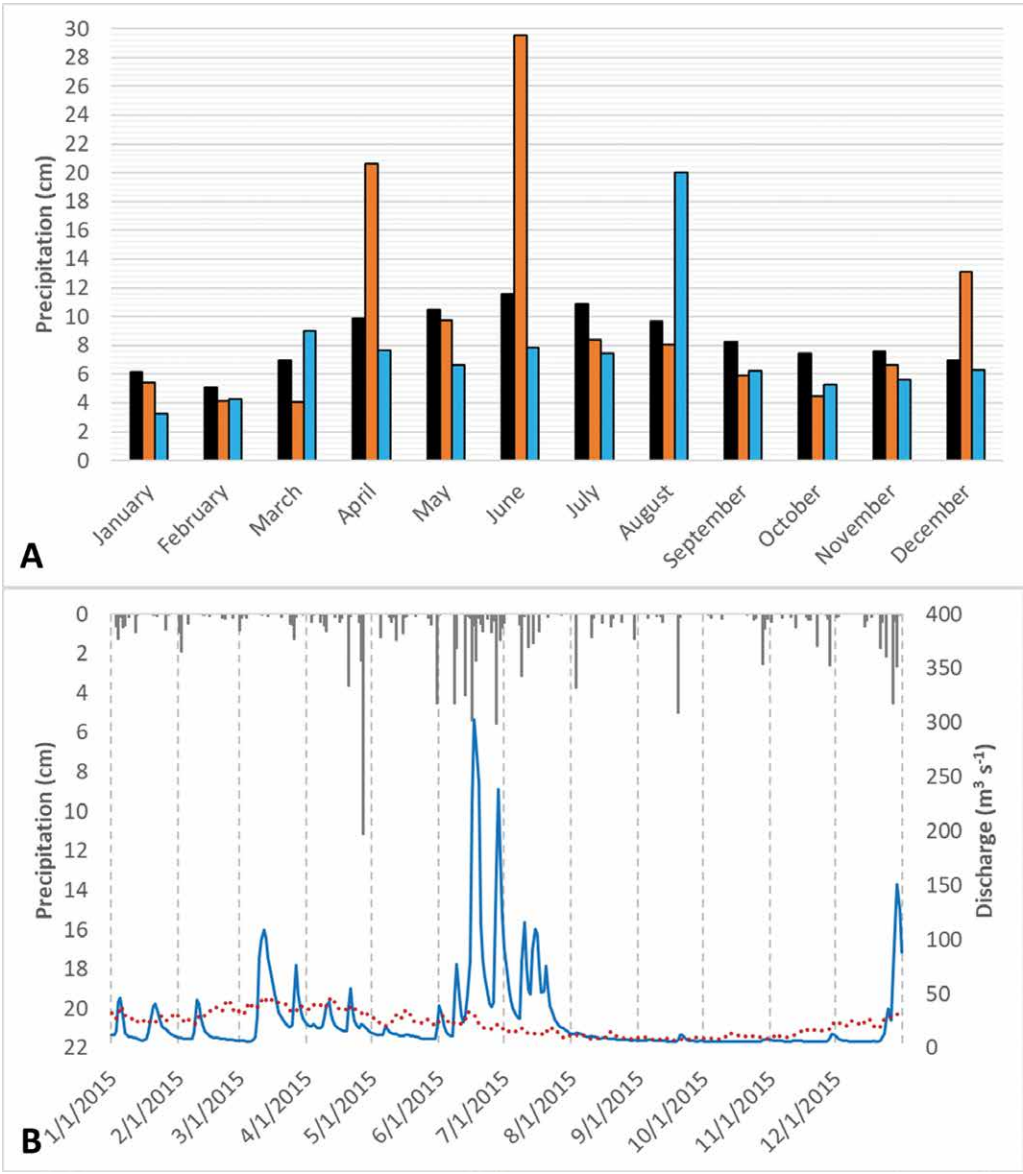

Figure 3. A) Plot showing monthly precipitation. Black bars represent the monthly precipitation averaged over the last 70 years (1947 to 2016), orange bars show monthly precipitation in 2015, and blue bars show monthly precipitation in 2016; and B) Combined hyetograph for Logansport, Ind., of a meteorological station located 3.1 km east of the Fitch's Glen catchment, and hydrograph for Eel River, a river located 13.6 km to the east of the catchment. The average daily discharge (measured from 1944 to 2016) is shown by the dotted red line, and the daily discharge for 2015 is shown by the solid blue line. The data was sourced from USGS Site 03328500; https://waterdata.usgs.gov/in/nwis/inventory/?site_no=03328500. The hyetograph shows daily precipitation in 2015, and the data was sourced from NOAA Site LOGANSPORT CICOTT ST., IN US (https://www.ncdc.noaa.gov/cdo-web/datasets/GHCND/stations/GHCND:USC00125117/detail).

Geological Setting

Fitch's Glen is developed in the Silurian Wabash Formation, which is composed of a variety of limestone to dolostone facies (Pinsak and Shaver, 1964). It is widespread regionally and outcrops in the lower 0.05 km^2 of the catchment. (Information on the Wabash Formation: Niagaran and Cayugan Series, Silurian System can be found at https://igs.indiana.edu/compendium/comp8qlg.cfm). At the surface, the rocks are massive, fine-grained, light gray, heavily weathered and vertically fractured (Fig. 4A). Vertical shafts (Fig. 4B) and conduits (Figs. 4A, B) are present in the canyon walls. Shafts cut through the fine-grained, weathered rock facies, and appear to have routed flow to the large conduits along a silty friable, tan-colored facies (Figs. 4A, B). A thick, nodular facies is present beneath the silty facies and overlies a planar-bedded facies; the contact between the nodular and planar-bedded facies is exposed near the outlet of the canyon. Planar-bedded, fine-grained limestone is present near the middle and lower waterfalls and springs (Fig. 4C); the waterfalls likely formed from knickpoints occurring in this unit. Large boulders, coated with thick, tufa deposits and extensive tufa accumulation on the waterfalls, are present in the lower reaches of the catchment.

Outwash and loamy till can be found on top of the bedrock, deposited by the Huron-Erie lobe during the Wisconsinan glaciation (Pinsak and Shaver, 1964). Glacial sediment also filled at least some of the conduits in the Wabash Formation, leading to the formation of buried karst. Locally, the stream, at the point of capture, flows across recent lake deposits that accumulated after construction of a small dam in the 1960s. Beneath the lake sediment is a thin, discontinuous layer of clay-rich sediment that appears to be glacial till.

Climate and Hydrogeological Setting

The average low and high January (winter) temperatures near Fitch's Glen are −8.8 °C and 0.3 °C, respectively, and average low and high July (summer) temperatures are 17.2 °C and 28.7 °C (NOAA Climate Data Online). Logansport receives an average of 101 cm of precipitation per year, and 40 cm of that occurs as snow from late October to late March

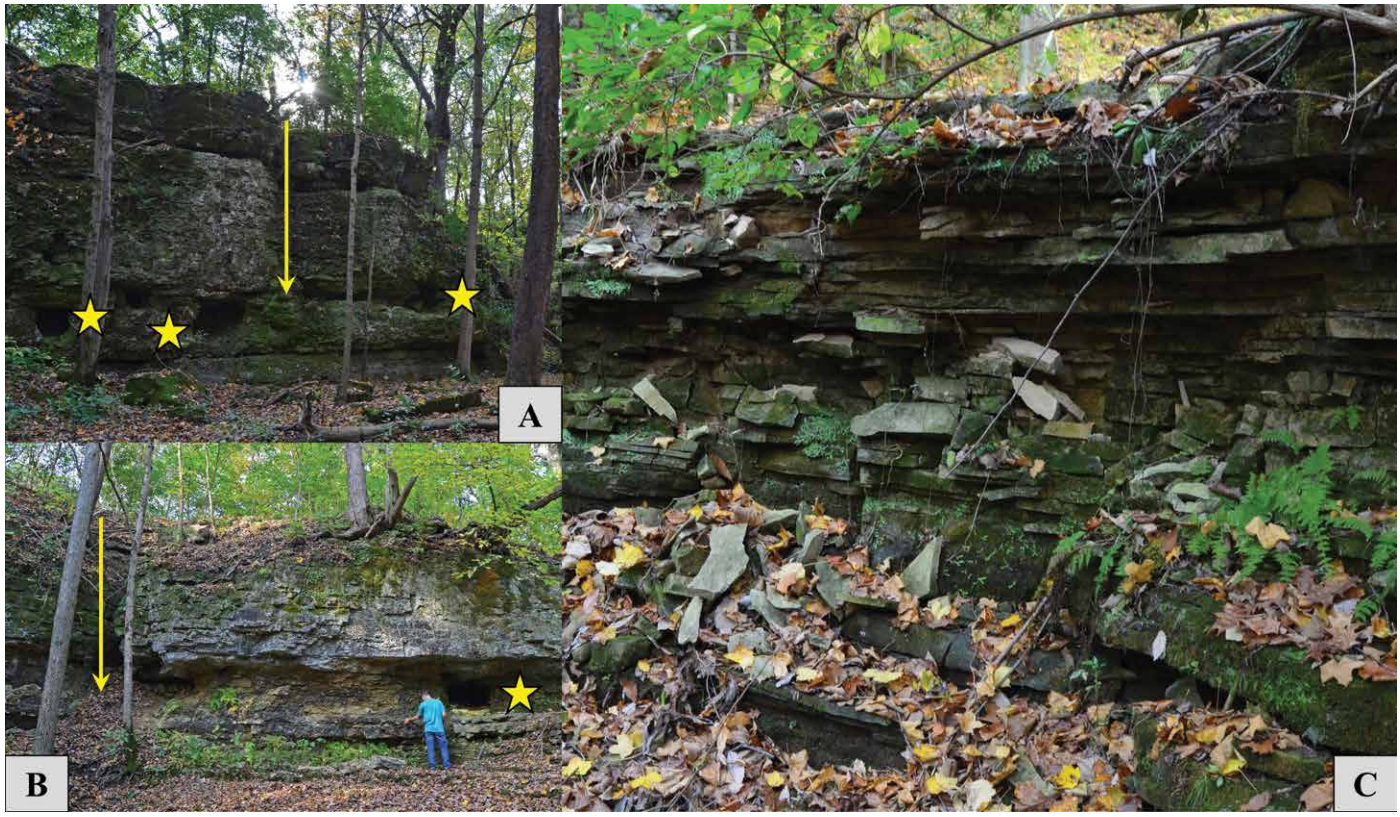

Figure 4. A) Photo showing the surficial massive, nodular limestone. The large conduit on the far left has a diameter of approximately 0.91 m; B) Photo showing the silty, friable layer. The student co-author, wearing a blue shirt in the background, is 1.85 m tall for reference; and C) Photo showing the fine-grained, planar-bedded limestone. The outcrop shown in this photo forms a waterfall, which is approximately 1.52 m. Stars show locations of large conduits and arrows show inferred shafts.

(Fig. 3A). Usually, Logansport receives 33 cm of rainfall from May through July. However, northern Indiana received 49 cm of rainfall during this period in 2015, which resulted in regionally widespread flooding. The Fitch's Glen catchment is ungauged. Yet, meteorological data for Logansport, Ind. (5 km from the study site) and discharge data for the Eel River, located 5.3 km from the catchment, illustrate the magnitude of the flooding event in 2015 (Fig. 3B).

The larger catchment has a total drainage of 6.2 km^2 (620 ha). A spring-fed stream drains the larger catchment and has incised a narrow canyon with steep walls with over 30 m of local relief in the lower 0.05 km^2 (5 ha) of the catchment known as Fitch's Glen. Waterfalls are located in the glen (Fig. 2). The stream passes through low-relief agricultural fields before reaching the canyon and ultimately drains into the Wabash River. Google Earth imagery shows that: 1) the stream capture may have been present as early as 1998 (Fig. 5A); 2) stream capture was occurring by 2005 (Fig. 5B); and 3) the captured stream channel was almost as large as the main channel by 2012 (Fig. 5C). Readers are encouraged to view the Google Earth imagery at location 16T 548685 mE, 4512067 mN. However, the landowners state that the stream was not completely captured by the sinking stream before early 2015, since the waterfalls were functioning at that time.

Chronology of Site Visits

The first trip to the site was made on March 25, 2016 to investigate the sinkhole (Fig. 6), identify potential discharge locations downgradient of the sinkhole, and propose future tracing experiments to quantify discharge locations and transport parameters. Five possible discharge points in the catchment were identified, including one conduit spring with a discrete emergence (Spring 1), two springs with diffuse emergences (Springs 2 and 3), and two springs discharging directly to the streambed (Springs 4 and 5; Fig. 7). Spring 1 emerges from a 1 m high by 1 m wide conduit in the planar-bedded limestone facies of the canyon wall, 150 m downstream from the sinking stream (Spring 1; Figs. 2, 7A). Water from this spring flows into the main stream channel providing almost all of the perennial flow to the lower reaches of the catchment. Springs 2 and 3 are located to the west of the mouth of the glen and provide flow to a small tributary that drains into the main stream. Approximately 500 m upstream of Spring 1, Springs 4 and 5 are located between a set of waterfalls. These two springs emerge in the streambed and discharge sufficient water to create localized mounding conditions in the stream.

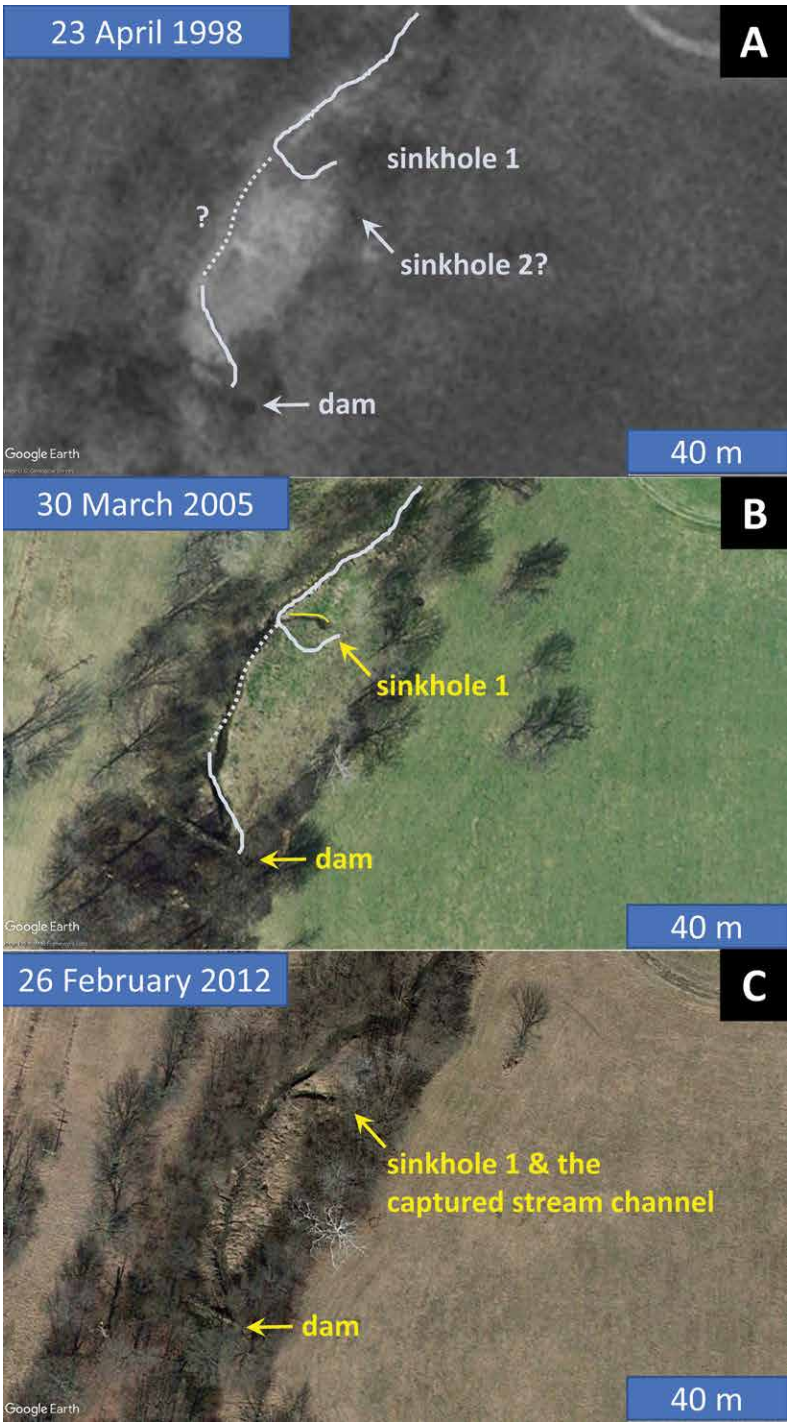

Figure 5. Google Earth imagery showing: A) the location of two possible sinkholes in 1998 (note that the main stream channel does not appear to be present or continuous to the dam(Source: Map data: Google Imagery © 2018, DigitalGlobe, Image U.S. Geological Survey); B) the location of the sinkhole and initiation of stream capture by 2005, indicated by the yellow line (note that the main stream channel is now present and continuous to the dam (Source: Map data: Google Imagery © 2018, DigitalGlobe, Image IndianaMap Framework Data); and C) presence of ongoing stream capture in 2012 (Source: Map data: Google Imagery © 2018, DigitalGlobe, Images IndianaMap Framework Data). The blue bar represents 40 m of distance. Images are oriented such that north is located at the top of each image.

The second trip to the site was made on October 29, 2016 to conduct a dye-tracing experiment for visual confirmation of the connection between the sinkhole and proposed discharge sites identified in the first trip. By October 2016, the sinkhole had greatly enlarged, and the entire stream was being diverted into the sinking stream (Fig. 6). The stream channel between the sinking stream and Spring 1 was completely dry, and the waterfalls were dewatered. Spring 1, therefore, supplied all of the water for streamflow downstream of the waterfalls until its confluence with a small tributary fed by Springs 2 and 3 (Figs. 2, 7B, and 7C). Springs 4 and 5, located between two waterfalls, were also dry. The dye-trace was successful; dye was observed at Springs 1, 2, and 3. However, the salt-trace was not successful due to equipment failure. Therefore, the salt-tracing results from the second trip are not reported.

The third trip was made on November 11, 2016. During this visit, a combined salt- and dye-tracing experiment was conducted on the sinking stream, water samples were collected from the stream and springs, and discharge was measured at each spring and in the stream, upstream of the sinking stream. The dye-trace and salt-trace were successful. During this trip, the researchers also measured the physical dimensions of the swallow and the sediment thickness overlying the carbonate rock near the hole. The opening of the sinking stream is roughly triangular, with an area of 1.9 m^2 and is 2 m deep, relative to the land-surface (Fig. 6B). There is approximately 1.2 m of sediment deposited on top of the carbonate rocks near the sinkhole. A thin 8- to 10 cm layer of clay is present at the bottom of the sediment and on top of the carbonate rocks.

Salt- and Dye-Tracing Methods

We used salt- and dye-tracing methods to directly quantify flow (Greene, 1997) and transport parameters of the conduits and fractures (Benischke et al., 2007) in the catchment. Solinst Model 3001 LTC Junior LTC leveloggers were placed at Springs 1, 2 and 3. The background SpC of the stream uphill of the swallow was measured to be 746 mS cm^{-1}. Approximately 4.32 kg of salt was measured in a large, graduated cylinder and then dissolved in a 19 L bucket filled with stream water, creating a salt-slug with a SpC of 255,940 mS cm^{-1}. Approximately 300 mL of Bright Dyes Fluorescent Industrial Red liquid dye was added to the salt-slug to provide a visible indicator of salt-slug breakthrough at observed discharge points (the technical data sheet for this dye can be found at: Bright Dyes Technical Data Bulletin. Team members were stationed at Springs 1, 2 and 3 because dye breakthrough was observed at these springs during the second visit. Team mem-

Figure 6. A) Photo showing the channel that was created as the sinking stream formed and diverted all of the stream. The enlargement of the sinkhole and ultimate development of the sinking stream, following the flooding event of 2015, significantly changed the stream gradient and geomorphology of the stream channel. The angle of this capture is much less than 90°; and B) photo showing the new channel created by the sinking stream.

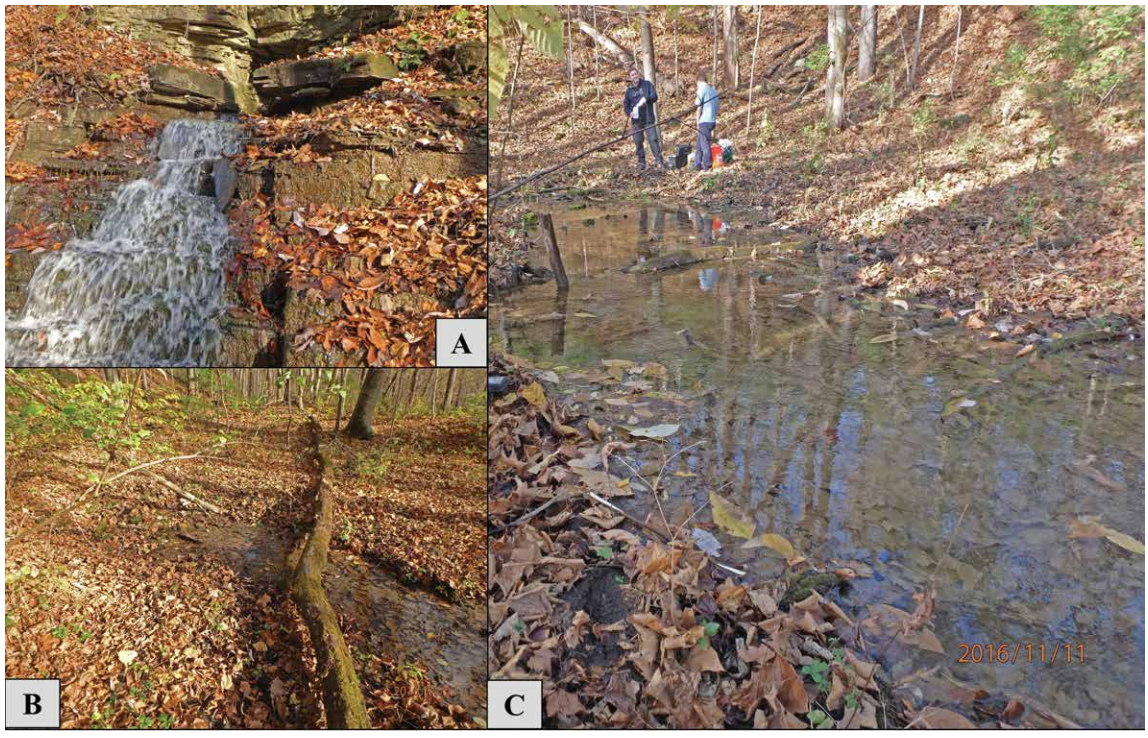

Figure 7. A) Spring 1, the emergence of this spring is approximately 75 cm wide; B) Spring 2, the spring-run is approximately 61 cm wide, immediately below the emergence; and C) Spring 3, the author, wearing a black jacket in the background, is 1.85 m tall for reference.

bers were also stationed along the lower reaches of the stream channel to watch for dye breakthrough directly into the streambed. The salt-slug was poured into the sinkhole at 17:05 EST. The leveloggers were set to record SpC at ten-second intervals and left in the springs overnight. Leveloggers were retrieved on 12 November 2016 at 11:36 EST (Spring 1), 11:45 EST (Spring 2), and 11:47 EST (Spring 3). BTCs were created for each of the spring locations.

Stream and Spring Discharge Measurement

During the third visit on November 11, 2016, a water mass-balance was created for the glen to assess water partitioning in the carbonate aquifer. We were specifically interested in determining how much of the total spring discharge was derived from the allogenic recharge at the sinking stream. In the case where all the spring discharge is derived from the allogenic recharge, the water mass-balance for the glen is given by: $Q_{Str1} - Q_{Spr1} - Q_{trib} = 0$; where Q_{Str1} is the discharge measured at Stream 1 (this is the water entering the sinking stream), Q_{Spr1} is the discharge measured at Spring 1, and Q_{trib} is the combined discharge measured at Springs 2 and 3 ($Q_{Spr2} + Q_{Spr3}$). Salt-dilution techniques were used to measure the discharge of each individual spring in its spring-run and in the stream uphill of the sinking stream using separate salt-slugs. The discharge of the stream entering the sinking stream (Q_{Str1}) was measured before the stream entered the sinking stream (Stream 1, Fig. 2). A Solinst Model 3001 LTC Junior LTC levelogger was placed downstream at a distance equal to 10× the width of the stream from where the salt-slug was going to be dumped. The salt-slug was then dumped and the SpC was recorded.

Once the slug breakthrough was complete at each site, the data were downloaded from the sonde and discharge was calculated based on the relationship between salt (Cl^-) content and SpC (Moore, 2005; Payn et al., 2009). In our case, $Cl^-_{mass} = 0.0006 \times SpC$; where Cl^-_{mass} is the concentration of chloride in g L^{-1}. A salt-slug was dumped into each individual spring-run, and a Solinst levelogger was placed downstream at a distance approximately equal to 10× the width of the spring-run where the slug was dumped. The salt-breakthrough was recorded in the same fashion as described above. We quantified the uncertainty in the salt-dilution discharge technique to range from ± 5 to ± 10 % by comparing salt-dilution discharge with independently gauged discharge at stations located outside the catchment. This range is consistent with the uncertainty of ± 5 % reported in Day (1976).

Geochemical and Stable Isotope Analyses

Water samples were collected for geochemical (major element) and stable isotope analyses during the third visit prior to dumping the salt-slug. Two 250 mL water samples were collected from each of the sites, and were filtered in the field using a peristaltic pump and Geotech 0.45 mm canister type filters. All water samples were stored in a refrigerator until they were analyzed by the Analytical Chemistry Laboratory of the New Mexico Bureau of Geology and Mineral Resources. Stable isotopes of water (^2H and ^{18}O) were analyzed by the Purdue Stable Isotope Lab using an LGR Triple Isotope Liquid Water Analyzer. The isotopic ratios, δ^2H and $\delta^{18}O$, were calculated relative to VSMOW (Vienna Standard Mean Ocean Water). A YSI Professional Plus multiparameter sonde was used to measure field chemistry including pH, temperature (°C), dissolved oxygen (DO; in percent and mg L^{-1}), and oxidation-reduction potential (ORP; mV). Total dissolved solids (TDS; mg L^{-1}) was calculated by the sonde using $TDS = 0.65 \times SpC$.

Determination of Karst Hydrogeological Parameters

QTRACER2 (Florea and Wicks, 2001; Field, 2002), an Environmental Protection Agency (EPA) software, was used to estimate the hydrogeological parameters of the karst network by entering the data from the salt-breakthrough curves. The following parameters were calculated for each spring using QTRACER2 and the measured BTC data: time to leading edge (t_{le}), time to peak (t_{pk}), peak concentration (C_{pk}), percent salt-mass recovery, mean transit time (*MTT*), Peclet number (*Pe*), and cross-sectional area of flow (*A*). Please refer to Field (2002) for detailed explanations on how these parameters are calculated in QTRACER2. We created BTCs and calculated percent salt-mass recovery for each spring using Excel. The percent salt-mass recovery can be calculated from

$$M = Q \int_0^\infty C(t)\, dt \quad (1)$$

where: M = mass of chloride recovered (g), Q is spring discharge (L s^{-1} and assumed to be constant through the duration of the salt-tracer test), and $C(t)$ is the chloride concentration as a function of time (Jones, 2012). The integral was evaluated over the time when the slug was dumped ($t = 0$) to the time the levelogger was retrieved ($t = t_{final}$). We compared the QTRACER2 calculations for t_{le} and t_{pk} to field observations and hand calculations, respectively.

Results

Salt- and Dye-Tracing Tests

BTCs were successfully captured at each spring site (Fig. 8). The timing of the initial breakthrough was approximately the same for all three springs despite significantly different radial distances between the sinking stream and the outflow at the springs (Table 1). The salt-slug emerged after 2.4 hours at both Spring 2 and Spring 3, and after 2.7 hours at Spring 1. There are subtle differences in the BTCs for each spring. Spring 1 has a single-peaked BTC with a fast rise and fast recession on the salt-pulse and relatively short tail (Figure 8A, B). Springs 2 and 3 both have double-peaked (bi-modal) recovery curves, with the first peak occurring after 2.4 hours and the second peak occurring after 3.1 hours. The BTC of Spring 2 has a substantially longer tail than Spring 1 or Spring 3 (Fig. 8A). Total chloride recovery was 51.2 %, calculated using QTRACER2, and the majority of the chloride mass was recovered at Spring 1 and Spring 3 (Table 1). Our hand calculations show that 49.9 % of the chloride mass was recovered at the three springs; a difference of 1.3 %.

Discharge and Water Mass-Balance

Since the main channel of the stream was dry between the sinking stream and Spring 1, surface flow in the channel in the lower reaches of the catchment is due almost exclusively to water discharged from Spring 1. The only other source of water to the stream is the small, western tributary, which is sourced from Springs 2 and 3 (Fig. 2). The measured discharge at Stream 1, Q_{Str1}, is 10.9 L s^{-1}, the measured discharge at Spring 1, Q_{Spr1}, is 4.3 L s^{-1}, and the combined discharge at Springs 2 and 3, Q_{trib}, is 7.0 L s^{-1}. Thus, the combined discharge of the springs is 0.4 L s^{-1} greater than the discharge of the stream entering the sinking stream, possibly indicating that the sinking stream is not the only source of water emerging from the springs. This is consistent with the landowners' observations that the springs were flowing before the sinking stream formed. However, given the uncertainty in our discharge measurements, it is difficult to determine how much

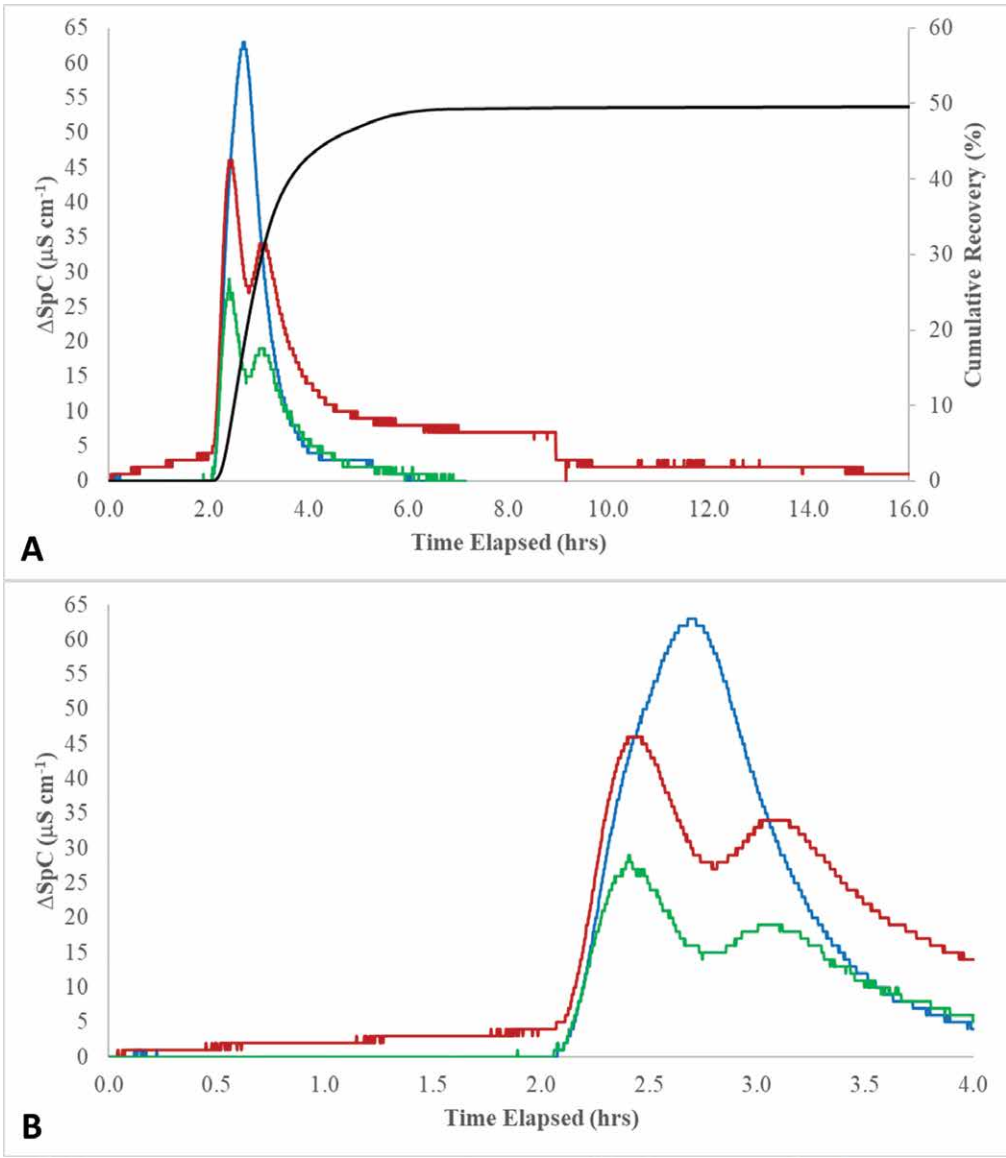

Figure 8. A) Breakthrough curve for Spring 1 (blue line), Spring 2 (red line), Spring 3 (green line), and cumulative recovery (black line); and B) close-up of breakthrough showing early breakthrough at Spring 2.

actual groundwater emerged from the springs before the sinking stream developed.

Geochemical and Stable Isotopic Results

The field chemistry (Table 2) and the geochemistry (Table 3) of the water entering the sinking stream is similar to the water discharging from the springs. The DO content of Stream 1 and Spring 1 are similar (Table 2) and consistent with surface water, not groundwater. Thus, Spring 1 discharges a large proportion of water that is either in equilibrium with the atmosphere or the oxygen has not been thoroughly used in geochemical reactions (namely redox reactions) or in the decomposition of organic matter in the aquifer. However, the lower DO content of Springs 2 and 3 (Table 2) indicates that these springs discharge a larger proportion of groundwater not sourced from allogenic recharge. The stable isotopic compositions of Stream 1 and all springs are relatively similar (Table 3), plot on the local meteoric water line (LMWL) given by $\delta^2H = 7.8(\delta^{18}O) + 9.3$ (Bowen et al., 2007), and do not show evidence of evaporation.

QTRACER2 Results

The data for the second salt-slug test conducted during the third site visit was analyzed using QTRACER2 (Table 1). The time to leading edge (t_{le}) was shorter for Spring 3 than for Spring 1. This is consistent with the observed dye breakthrough on the first salt-slug test. The mean transit time was shorter for Spring 1 (3.0 hours) than Spring 3 (3.2

Table 1. Summary of the salt-slug test and QTRACER2 analyses.

Site	Distance[a], m	t_{le}[b], h	t_{pk}[c], h	C_{pk}[d], µS cm^{-1}	*MTT*[e], h	*A*[f], m^2	*Pe*[g]	*M*[h], g	Recover[i], %
Spring 1	150	2.1	2.7	586	3.0	0.30	319	542	24.6
Spring 2	315	2.1	2.4	580	3.6	0.21	293	81	3.7
Spring 3	318	1.9	2.4	526	3.2	0.26	366	504	22.9

[a] Straight-line distance measured from the swallow hole to the spring.
[b] t_{le} is the time to the leading edge of the salt-slug pulse equivalent to the arrival time.
[c] t_{pk} is the time to the peak of the salt-slug peak.
[d] C_{pk} is the peak conductivity of the salt-slug pulse.
[e] *MTT* is the mean transit time for the salt-slug.
[f] *A* is the cross-sectional area for flow.
[g] *Pe* is the Peclet number.
[h] *M* is the amount of chloride recovered.
[i] Recover is the percent of total chloride recovered

Table 2. Field chemistry data.

Site	pH	T, °C	SpC, µs cm^{-1}	TDS, mg L^{-1}	DO, %	DO, mg L^{-1}
Stream 1	8.2	11.3	746	481	100	11.1
Spring 1	8.0	11.1	731	475	90	9.9
Spring 2	7.8	11.4	732	474	63	6.9
Spring 3	7.7	11.4	701	465	47	5.0

Note: T = temperature, SpC = specific conductivity at 25 °C, TDS = total dissolved solids, and DO = dissolved oxygen.

Table 3. Geochemical and stable isotopic data.

Site	Ca^{2+}, mg L^{-1}	Na^{+}, mg L^{-1}	K^{+}, mg L^{-1}	Sr^{2+}, mg L^{-1}	Cl^{-}, mg L^{-1}	NO_3^{-}, mg L^{-1}	HCO_3^{-}, mg L^{-1}	δ^2H, ‰	$\delta^{18}O$, ‰
Stream 1	96	14	2.3	0.21	27	11.0	377	−49.1	−7.29
Spring 1	100	13	2.1	0.22	26	11.0	389	−49.0	−7.34
Spring 2	101	13	2.1	0.22	23	11.0	389	−49.2	−7.18
Spring 3	97	11	1.9	0.24	18	9.3	389	−48.5	−7.35

hours) and Spring 2 (3.6 hours) suggesting that Spring 1 is controlled by purely advective flow along highly-connected flowpaths or perhaps one large conduit to the spring. The double-peaked (bi-modal) BTC and longer tail in the BTCs for Spring 2 and Spring 3 suggest that bifurcation of flowpaths or anastomosing flowpaths occur to these springs (Smart and Ford, 1982; Goldscheider et al., 2008; Field and Leij, 2012). The longer tail of the Spring 2 BTC may also be explained by the presence of pooling along the flowpaths, which has been shown to retard flow (Hauns et al., 2001).

Peclet numbers are dimensionless numbers representing the ratio of the advective transport rate to the diffusive transport rate. A *Pe* less than 1 indicates a diffusion-dominated flow system while, in comparison, a *Pe* greater than 1 indicates an advection-dominated flow system. All three springs had *Pe* greater than 290 indicating the karst aquifer is strongly advection dominated. This is relatively common in karst aquifers (Field and Nash, 1997; Covington and Perne, 2015; Luhmann et al., 2015). Based on these data, the calculated cross-sectional area for flow of Spring 1 (0.30 m^2) was larger than the cross-sectional area for Spring 2 and Spring 3, 0.21 m^2 and 0.26 m^2, respectively (Table 1). Total chloride-mass recovery was 51.2 %. Springs 1 and 3 accounted for the majority of chloride-mass recovery (24.6 and 22.9 %, respectively). Only 3.7 % of the chloride mass was recovered at Spring 2.

Discussion

The shape of the BTC for Spring 1 (single peak with rapid rise and rapid recession in chloride breakthrough) is indicative of advective flow with little bifurcation and/or flow through the trunk conduit of a conduit-dominated system. The high DO content (90 %), and high *Pe* (319) for Spring 1 indicate that this spring is well-connected to the sinking stream. However, since this spring was active before the sinking stream formed, the high DO suggests that the spring must discharge a large proportion of water that is either flowing quickly through the karst network, or, is in equilibrium with the atmosphere. One possibility is that the spring is hydraulically connected to a lake in a limestone quarry located east of the property (see Fig. 2B). Field observations and regional geologic maps (Wayne et al., 1966) indicate that there is a slight westerly dip to the rocks. The surface-elevation of the emergence for Spring 1 (182 m.a.s.l.) is approximately equal to the surface-elevation of the lake in the quarry (178 to 183 m.a.s.l.), thus we cannot rule out the possibility that Spring 1 is also connected to the lake. We could not sample the lake for stable isotopic analyses since it is located on private property; however, we expect the stable isotopic ratios of the lake water to show some evaporation effects, and that this evaporated signal would be present in Spring 1. Published evaporation rates for lakes in northern Indiana indicate that the evaporation rate can reach 78.7 cm y^{-1} (Perrey and Corbett, 1956) and the surface area of the quarry lake is large (~77,500 m^2). Combined with the published evaporation rates, we would expect to see a mixture of allogenic recharge and evaporated lake water discharging at Spring 1. We do not see evidence for evaporation in the water samples collected at Spring 1, although, we cannot rule out this possibility until we have samples from the lake. A second possibility is that Spring 1 is connected to another sinking stream in the area. Because there are no streams in the immediate vicinity of the spring (or in closer proximity than the lake), this explanation seems less likely than the hydraulic connection to the lake. A third possibility is that streamflow is lost to the bed upstream of the sinking stream. This could explain the presence of Spring 1 before the stream piracy event. In any case, it appears that at least 24 % to 25 % of the recharge from the sinking stream must discharge at Spring 1, based on chloride-mass recovery. These data suggest a short, direct connection between the sinking stream and Spring 1, as indicated by the greater calculated cross-sectional area for Spring 1.

The shape of the BTC for Springs 2 and 3 are both double-peaked (bi-modal; Fig. 8B) indicating bifurcation in the flowpaths or anastomosing flowpaths to the springs (Smart, 1988; Goldscheider et al., 2008). The BTC of Spring 2

showed a much longer tail than either of the other springs (Fig. 8). Long tails in flowpath distributions are common indicators of greater storage and/or slower flowpaths (Frisbee et al., 2013), retention of chloride mass along conduits or sediment in conduits of the aquifer (Drummond et al., 2012), and/or retardation of flow due to the presence of pooling (Hauns et al., 2001). We infer that the long tail in the BTC of Spring 2 indicates that some of the chloride mass was dispersed along slower flowpaths, located deeper in the karst aquifer. Recall that the emergence for Spring 1 is located approximately four meters above the modern stream elevation, whereas the emergences for Springs 2 and 3 are located nearer to the outlet and at an elevation that is only slightly higher than the stream elevation. The flowpaths must travel beneath the streambed or else the streambed springs would discharge water to the stream. Instead, since Springs 4 and 5 are now dry, this seems to indicate that the flowpaths connecting the sinking stream to Springs 2 and 3 must flow deep within the planar-bedded, fine-grained limestone. The flow then bifurcates vertically and laterally along the fractured planar beds. The streambed springs (Springs 4 and 5), in comparison, must be driven by short exchanges of water along interconnected, karst conduits, localized to the streambed, reminiscent of hyporheic zone flow in perennial sediment-bedded streams (Boulton et al., 1998; Wilson and Henry, 2013).

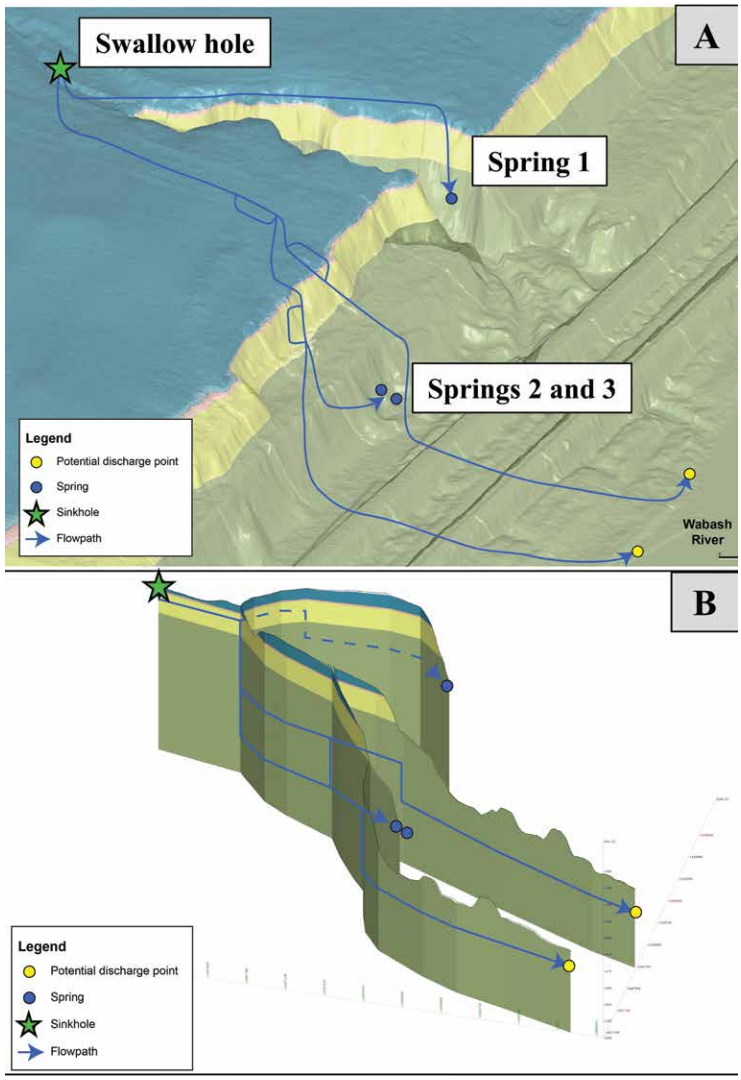

Figure 9. Conceptual flow model built using Leapfrog Hydro. A) Map-view illustrating possible lateral changes in flowpath lengths and tortuosities. Please note that the blue flowpaths do not follow or flow along the land-surface; they are shown relative to the land-surface. The loops in the flowpaths represent the lateral bifurcation of subsurface flowpaths. B) Cross-section view showing vertical changes in flowpath lengths and tortuosities. The upper teal-colored unit is the massive, fine-grained, fractured to nodular limestone layer shown in Figure 4B, the thin, pink layer is the silty facies of the limestone, also shown in Figure 4B. The yellow layer is the massive, nodular limestone, and the olive drab layer is the planar-bedded limestone layer shown in Figure 4C.

The conceptual flow model (Fig. 9) was developed based on the field observation, BTCs, and QTRACER2 results. The arrival times are a little faster at Springs 2 and 3 despite much longer lateral distances from the sinking stream to these springs (315 m and 317 m, respectively) as compared to the distance to Spring 1 (150 m). We infer that once the water enters the sinking stream, it flows along one conduit down to the top of a planar-bedded rock layer. At this point, the flowpaths must diverge, some of the water (~25 %, based on chloride-mass recovery) flows toward Spring 1 along either one, large conduit or a group of highly-interconnected conduits, creating the single-peaked BTC (Fig. 8). The remainder (~75 %, based on chloride-mass recovery) of the water must flow toward Springs 2 and 3. However, Springs 2 and 3 accounted for 3.7 % and 22.9 %, respectively, of the chloride-mass recovery, indicating that 48.8 % of the chloride mass did not discharge through the three monitored springs. We infer that the double-peaked BTC is created by bifurcation of flowpaths and/or anastomosing flowpaths in the planar-bedded facies, and these flowpaths converge prior to reaching Springs 2 and 3 (Fig. 9).

Approximately 51.2 % of the chloride mass was recovered [Cl^- mass recovered = Cl^- (Spring 1) + Cl^- (Spring 2) + Cl^- (Spring 3)]. It is rare to recover 100 % of a tracer since tracer mass may be retained or sorbed onto sediments in the aquifer or in longer flowpaths, or it may discharge at unmonitored discharge sites (Benischke et al., 2007). In Fitch's Glen, we propose three likely possibilities for the remaining chloride mass: 1) chloride mass was retained along deeper karst flowpaths; 2) chloride mass was discharged to other springs that were not found in the field; or 3) chloride mass was discharged directly to the Wabash River. The first explanation is supported by the very long tail observed in the BTC of Spring 2 (Fig. 8) and the third explanation is plausible given the relatively fast arrival times at Springs 2 and 3, and their close proximity to the Wabash River (~175 m from Springs 2 and 3 to the Wabash River; Fig. 2). We searched for other springs near Springs 2 and 3, but

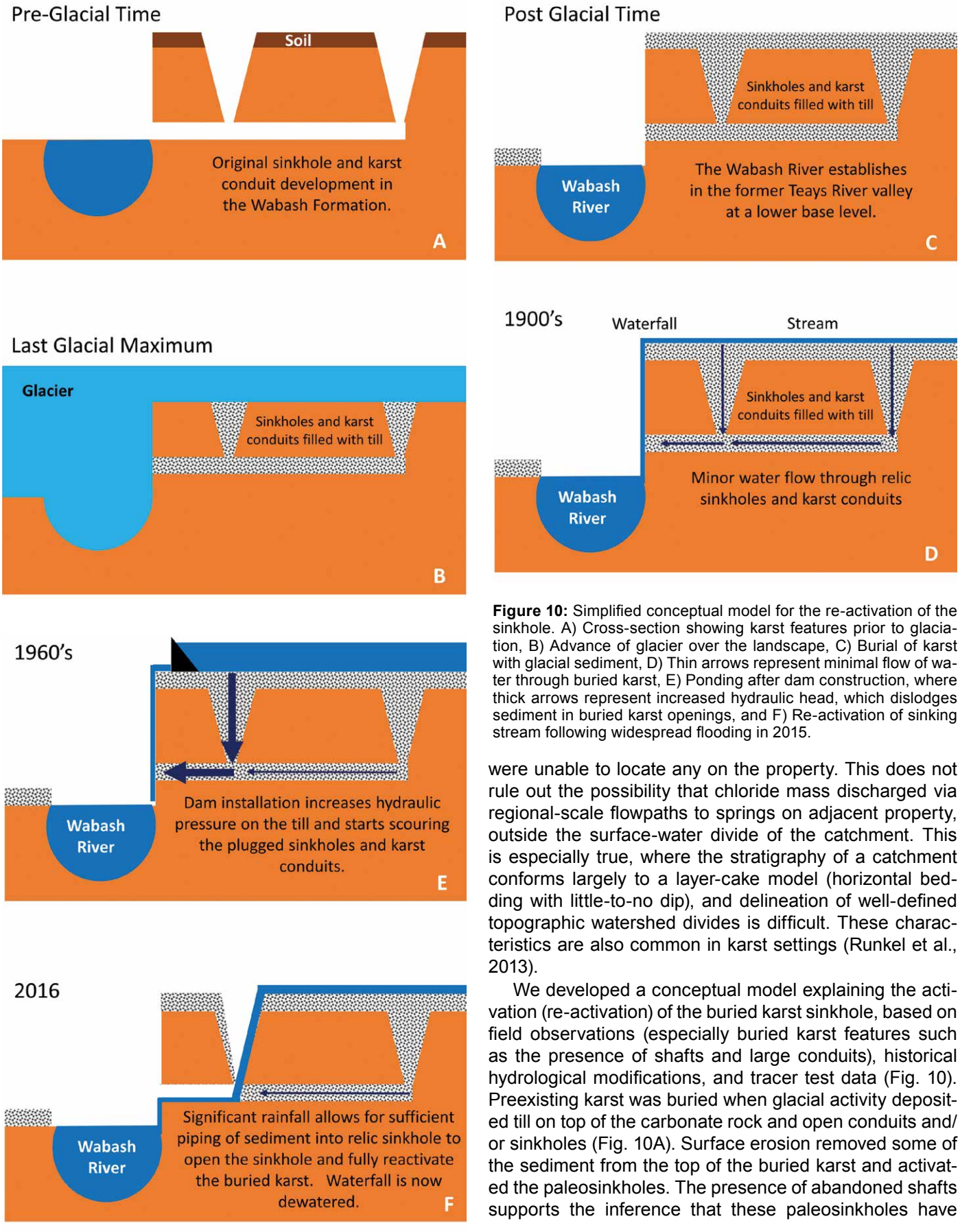

Figure 10: Simplified conceptual model for the re-activation of the sinkhole. A) Cross-section showing karst features prior to glaciation, B) Advance of glacier over the landscape, C) Burial of karst with glacial sediment, D) Thin arrows represent minimal flow of water through buried karst, E) Ponding after dam construction, where thick arrows represent increased hydraulic head, which dislodges sediment in buried karst openings, and F) Re-activation of sinking stream following widespread flooding in 2015.

were unable to locate any on the property. This does not rule out the possibility that chloride mass discharged via regional-scale flowpaths to springs on adjacent property, outside the surface-water divide of the catchment. This is especially true, where the stratigraphy of a catchment conforms largely to a layer-cake model (horizontal bedding with little-to-no dip), and delineation of well-defined topographic watershed divides is difficult. These characteristics are also common in karst settings (Runkel et al., 2013).

We developed a conceptual model explaining the activation (re-activation) of the buried karst sinkhole, based on field observations (especially buried karst features such as the presence of shafts and large conduits), historical hydrological modifications, and tracer test data (Fig. 10). Preexisting karst was buried when glacial activity deposited till on top of the carbonate rock and open conduits and/or sinkholes (Fig. 10A). Surface erosion removed some of the sediment from the top of the buried karst and activated the paleosinkholes. The presence of abandoned shafts supports the inference that these paleosinkholes have

been activated sporadically in the past. The dam was built in the 1960s, and ponding upstream of the dam increased the hydraulic head on the buried karst, which likely provided sufficient stress to begin washing some of the sediment out of the till-filled karst conduits in the carbonate rock (Fig. 10E), which has been documented elsewhere (e.g., Milanović, 2005; Upchurch et al., 2013; Veress, 2016). The extremely rainy summer of 2015 caused persistent flooding that flushed sediment from the buried karst conduit and formed the sinking stream, which eventually swallowed the stream. (Fig. 10F).

Conclusion

We addressed three primary questions in this study: 1) how did the sinkhole/sinking stream become re-activated in the buried karst, 2) where did the streamflow (allogenic recharge) go once it entered the sinking stream, and 3) what transport processes are active in the carbonate rocks at Fitch's Glen? The second and third questions are easier to answer because the data clearly show a hydrological connection between the sinking stream and three springs, while breakthrough curves and QTRACER2 results show strong evidence for advection-dominated flow in the karst with bifurcation occurring along deep flowpaths. Approximately 51 % of the chloride mass was recovered during the second salt-slug test leaving 49 % unaccounted for in the test. Based on the shapes of the BTC, average flow velocities, and close proximity to the Wabash River, we infer that some of the chloride mass and water from the sinking stream must discharge directly to the Wabash River, other springs, and/or some may be retained along slow and/or deep flowpaths in the carbonate aquifer. Regarding the first question, it is clear that land-use changes have played a role in the current hydrogeological behavior of this system. The area upstream of the old dam has numerous buried sinkholes, which may one day become reactivated and form sinking streams. We infer that the combination of land-use change (ponding following the installation of the dam), presence of buried karst, and an extremely rainy year with widespread flooding worked together to re-activate the karst sinking stream present today.

Google Earth imagery (Fig. 5) shows that sinkholes have been present in the landscape since at least 1998, and field reconnaissance indicates that there are numerous inactive sinkholes (i.e., plugged conduits) near the existing active sinkhole today. In addition, the presence of the vertical shafts and large conduits further down the valley indicate that there have been active sinking streams with connectivity to large springs in the past. In fact, the location of these suggests that these sinkholes and their associated springs may have contributed to the development of this small, limestone canyon in a landscape that is otherwise extremely flat. It is beyond the scope of this article to describe potential remediation techniques in great detail (examples can be found in Zhou and Beck, 2008); however the presence of the numerous inactive sinkholes near the modern sinking stream suggests that remediation techniques may only provide a temporary fix to the problem.

Acknowledgements

We would like to thank the landowners, Kevin Coryea and Dee Dee Neumeyer, for their help and generosity. Also, we thank Laura Alejandra Beltrán Daza, Benjamin Sadler, and Catherine Wilsbacher for field assistance. Research expenses were covered by start-up funding from Purdue University. We thank Benjamin Schwartz (Associate Editor), Malcolm Field (Editor-in-Chief), and three anonymous reviewers for their constructive feedback on this article. We thank Lee J. Florea for providing a review and helpful discussions on the article.

References

Armstrong, R., and Osborne, L., 2003, Paleokarst: Cessation and rebirth?, Speleogenesis and Evolution of Karst Aquifers: The Virtual Scientific Journal, v. 1, no. 2, p. 1–10.

Bassett, J.L., 1974, Hydrology and geochemistry of karst terrain, Upper Lost River Drainage Basin, Indiana, [M.A. Thesis]: Bloomington, Ind., Indiana Univeristy, 102 p.

Bassett, J.L. and Ruhe, R.V., 1974, Geomorphology, hydrology, and soils in karst, southern Indiana, Field Conference, April 24−25: Bloomington, Indiana, Indiana Water Resources Research Center, Indiana University, 54 p.

Bayless, E.R., Taylor, C.J., and Hopkins, M.S., 1994, Directions of ground-awter flow and locations of ground-water divides in the Lost River Watershed near Orleans, Indiana: U.S. Geological Survey, Water-Resources Investigations Report 94-4195, 25 p.

Bedrock Geology of Indiana, Indiana Geological and Water Survey, Indiana University, https://igs.indiana.edu/Bedrock/, [last accessed on June 28, 2018].

Benischke, R., Goldscheider, N., and Smart, C., 2007, Tracer techniques, *in* Goldscheider, N. and Drew, D., Methods in Karst Hydrogeology, p. 147–170.

Bosák, P., Ford, D.C., and Glazek, J., 1989, Terminology, *in* Bosák, P., Ford, D.C., Glazek, J., and Horáček, eds., Paleokarst: A Systematic and Regional Review, Elsevier and Academia, Amsterdam and Praha, 726 p.

Boulton, A.J., Findlay, S., Marmonier, P., Stanley, E.H., and Vallett, H.M., 1998, The functional significance of the hyporheic zone in streams and rivers: Annu. Rev. Ecol. Syst., v. 29, p. 59–81. https://doi.org/10.1146/annurev.ecolsys.29.1.59.

Bowen, G. J., Ehleringer, J.R., Chesson, L.A., Stange, E., and Cerling, T.E., 2007, Stable isotope ratios of tap water in the contiguous United States: Water Resources Research, v. 43, p. W03419. https://doi.org/10.1029/2006WR005186.

Bright Dyes Technical Data Bulletin, https://brightdyes.com/wp-content/uploads/2018/02/TDS-106000.pdf; [last accessed on June 28, 2018].

Buglosi, E.F., 1997, The Midwestern Basins and Arches Regional Aquifer System in parts of Indiana, Ohio, Michigan, and Illinois – Summary, U.S. Geological Survey, Professional Paper 1423-A, 60 p.

Casey. G.D., 1997, Hydrogeologic framework of the Midwestern Basins and Arches Region in parts of Indiana, Ohio, Michigan, and Illinois, U.S. Geological Survey, Professional Paper 1423-B, 54 p.

Covington, M.D. and Perne, M., 2015, Consider a cylindrical cave: A physicist's view of cave and karst science: Acta Carsologica, v. 44, no. 3, p. 363–380.

David Dian Zhang, Yingjun Zhang, An Zhu, and Xing Cheng, 2001, Physical mechanisms of River Waterfall Tufa (Travertine) Formation: Journal of Sedimentary Research, v. 71, p. 205–216. https://doi.org/10.1306/061600710205.

Day, T.J., 1976, On the precision of salt dilution gauging: Journal of Hydrology, v. 31, 293–306. https://doi.org/10.1016/0022-1694(76)90130-X.

Drummond, J.D., Covino, T.P., Aubeneau, A.F., D. Leong, Patil, S., Schumer, R., and Packman, A.I., 2012, Effects of solute breakthrough curve tail truncation on residence time estimates: A synthesis of solute tracer injection studies: Journal of Geophysical Research, v. 117, p. G00N08, https://doi/org/10.1029/2012JG002019.

Dussart-Baptista, L., Massei, N., Dupont, J.P., and Jouenne, T., 2003, Transfer of bacteria-contaminated particles in a karst aquifer: Evolution of contaminated materials from a sinkhole to a spring: Journal of Hydrology, v. 284, p. 285–295, https://doi.org/10.1016/j.jhydrol.2003.08.007.

Duwelius, J.A., Bassett, J.L., and Keith, J.H., 1996, Application of fluorescent dye tracing techniques for delineating sinkhole drainage routes, Highway 37 improvement project, Lawrence County, Indiana: International Journal of Rock Mechanics and Mining Sciences and Geomechanics Abstracts, v. 2.

Eberts, S.M. and George, L.L., 1997, Regional ground-water flow and geochemistry in the Midwestern Basins and Arches Aquifer System in parts of Indiana, Ohio, Michigan, and Illinois, U.S. Geological Survey, Professional Paper 1423-C, 116 p.

Field, M.S., 1992, Karst hydrology and chemical contamination: Journal of Environmental Systems, v. 22, p. 26. https://doi.org/10.2190/X7MV-C93E-66GK-BFH7.

Field, M.S., and Nash, S.G., 1997, Risk assessment methodology for karst aquifers: (1) estimating karst conduit-flow parameters: Environmental Monitoring and Assessment, v. 47, p. 1–21. https://doi.org/10.1023/A:1005753919403.

Field, M.S., 2002, The QTRACER2 program for Tracer-Breakthrough Curve Analysis for tracer tests in karstic aquifers and other hydrologic systems, U.S. EPA, EPA/600/R-02/001, 194 p.

Field, M.S. and Leij, F.J., 2012, Solute transport in solution conduits exhibiting multi-peaked breakthrough curves: Journal of Hydrology, v. 440–441, p. 26–35. https://doi.org/10.1016/j.jhydrol.2012.03.018.

Florea, L.J. and Wicks, C.M., 2001, Solute transport through laboratory-scale karstic aquifers: Journal of Cave and Karst Studies, v. 63, no. 2, p. 59–66.

Florea, L.J., Hasenmueller, N.R., Branam, T.D., Frushour, S.S., and Powell, R.L., 2018, Karst geology and hydrogeology of the Mitchell Plateau of south-central Indiana, *in* Florea, L.J., ed., Indianapolis Field Guide, Geological Society of America Field Guide 51, p. 1–18. https://doi.org/10.1130/2018.0051(XX).

Florea, L.J., 2019, Evaluation of karst aquifer water quality associated with agricultural land use *in* Younos, T., Schreiber, M., and Ficco, K.K., eds., Kasrt Water Environment: Advances in Research, Management and Polcy, p. 157-190. https://doi.org/10.1007/978-3-319-77368-1.

Ford, D.C., 1995, Paleokarst as a target for modern karstification: Carbonates and Evaporites, v. 10, n. 2, p. 138–147. https://doi.org/10.1007/BF03175399.

Frisbee, M.D., Wilson, J.L., Gomez-Velez, J.D., Phillips, F.M., and Campbell, A.R., 2013, Are we missing the tail (and the tale) of residence time distributions in watersheds?, Geophysical Research Letters, v. 40, p. 4633–4637. https://doi.org/10.1002/grl.50895.

Goldscheider, N., Meiman, J., Pronk, M., and Smart, C., 2008, Tracer tests in karst hydrogeology and speleology: International Journal of Speleology, v. 37, p. 27–40. https://doi.org/10.5038/1827-806X.37.1.3.

Gray, H. H., 2000, Physiographic divisions of Indiana, Indiana Geological Survey Special Report 61, 15 p.

Greene, E.A., 1997, Tracing recharge from sinking streams over spatial dimensions of kilometers in a karst aquifer: Ground Water, v. 35, p. 898–904. https://doi.org/10.1111/j.1745-6584.1997.tb00159.x.

Hallberg, G.R., and Hoyer, B.E., 1982, Sinkholes, hydrogeology, and groundwater quality in northeast Iowa: Iowa Department of Natural Resources, Geological Survey Bureau, Open File Report 82–83, 120 p.

Hasenmueller, N.R., and Packman, D.M., Karst Features in Indiana, Indiana Geological and Water Survey, https://igs.indiana.edu/bedrock/karst.cfm, [last accessed on June 28, 2018].

Hauns, M., Jeannin, P.-Y., and Atteia, O., 2001, Dispersion, retardation and scale effect in tracer breakthrough curves in karst conduits: Journal of Hydrology, v. 241, p. 177–193. https://doi.org/10.1016/S0022-1694(00)00366-8.

Herczeg, A.L., Leaney, F.W.J., Stadter, M.F., Allan, G.L., and Fifield, L.K., 1997, Chemical and isotopic indicators of point-source recharge to a karst aquifer, South-Australia: Journal of Hydrology, v. 192, p. 271–299. https://doi.org/ 10.1016/S0022-1694(96)03100-9.

Jones, W.K., 2012, Water tracing in karst aquifers, *in* White, W.B. and Culver, D.C., eds., Encyclopedia of Caves, 2nd Edition, Academic Press, 966 p. https://doi.org/10.1016/B978-0-12-383832-2.00128-6.

Karr, J.R., Toth, L.A., and Dudley, D.R., 1985, Fish communities of midwestern rivers: A history of degradation: BioScience, v. 35, p. 90–95. https://doi.org/10.2307/1309845.

Lee, E.S., and Krothe, N.C., 2001, A four-component mixing model for water in a karst terrain in south-central Indiana, USA. Using solute concentration and stable isotopes as tracers: Chemical Geology, v. 179, p. 129–143. https://doi.org/ 10.1016/S0009-2541(01)00319-9.

Lindsey, B.D., Katz, B.G., Berndt, M.P., Ardis, A.F., and Skach, K.A., 2010, Relations between sinkhole density and anthropogenic contaminants in selected carbonate aquifers in the eastern United States: Environ. Earth Sci., v. 60, p. 1073–1090. https://doi.org/10.1007/s12665-009-0252-9.

Long, A.J., Sawyer, J.F., Putnam, L.D., 2008, Environmental tracers as indicators of karst conduits in groundwater in South Dakota, USA; Hydrogoelogy Journal, v. 16, p. 263−280. https://doi.org/10.1007/s10040-007-0232-7.

Luhmann, A.J., Covington, M.D., Myre, J.M., Perne, M., Jones, S.W., Alexander Jr., E.C., and Saar, M.O., 2015, Thermal damping and retardation in karst conduits: Hydrology and Earth System Sciences, v. 19, p. 137−157. https://doi.org/10.5194/hess-19-137-20015.

Milanović, P.T., 2000, Geological engineering in karst. Zebra, Belgrade, 347 p.

Moore, R.D., 2005, Introduction to salt dilution gauging for streamflow measurement Part III: Slug injection using salt in solution: Streamline Watershed Management Bulletin, v. 8, no. 2, p. 1–6.

Murdock, S.H., and Powell, R.L., 1967, Subterranean drainage routes of Lost River, Orange County, Indiana, *in* Proceedings, Indiana Academy of Science, v. 77, p. 250–255.

NOAA Climate Data Online, https://www.ncdc.noaa.gov/cdo-web/, [last accessed on June 28, 2018].

Panno, S. V., Hackley, K.C., Huehwa H. Hwang, and Kelly, W.R., 2001, Determination of the sources of nitrate contamination in karst springs using isotopic and chemical indicators: Chemical Geology, v. 179, p. 113–128. https://doi.org/10.1016/S0009-2541(01)00318-7.

Panno, S. V., and Kelly, W.R., 2004, Nitrate and herbicide loading in two groundwater basins of Illinois' sinkhole plain: Journal of Hydrology, v. 290, p. 229–242. https://doiorg/10.1016/j.jhydrol.2003.12.017.

Panno, S.V., Krapac, I.G., Weibel, C.P., and Bade, J.D., 1996, Groundwater Contamination in Karst Terrain of Southwestern Illinois: Champaign, Illinois, Illinois State Geological Survey v. 151, p. 43.

Payn, R.A., Gooseff, M.N., McGlynn, B.L., Bencala, K.E., and Wondzell, S.M., 2009, Channel water balance and exchange with subsurface flow along a mountain headwater stream in Montana, United States: Water Resources Research, v. 44, p. W11427. https://doi.org/10.1029/2008WR007644.

Perrey, J.I. and Corbett, D.M., 1956, Hydrology of Indiana Lakes, U.S. Geological Survey, Water Supply Paper 1363, 360 p.

Pinsak, A.P., and Shaver, R.H., 1964, The Silurian formations of northern Indiana, Indiana Geological Survey Bulletin, v. 32, 87 p.

Powell, J.Z., 1913, History of Cass County Indiana: From its Earliest Settlement to the Present Time; with Biographical Sketches and Reference to Biographies Previously Compiled, Lewis Publishing Company, v. 1, p. 715.

Powell, R.L., 2002, Distribution of sinkholes, sinking-stream basins, and cave openings in southeastern Indiana: Bloomington, Indiana, Indiana Geological Survey.

Pronk, M., Goldscheider, N., and Zopfi, J., 2006, Dynamics and interaction of organic carbon, turdbidity, and bacteria in a karst aquifer system: Hydrogeology Journal, v. 14, p. 473–484. https://doi.org/10.1007/s10040-005-0454-5.

Pyron, M. and Neumann, K., 2008, Hydrologic alterations in the Wabash River Watershed, USA; River Research and Applications, v. 24, p. 1175−1184. https://doi:10.1002/rra.1155.

Randall, G.W., and Mulla, D.J., 2001, Nitrate nitrogen in nurface waters as influenced by climatic conditions and agricultural practices: Journal of Environmental Quality, v. 30, p. 337–344. https://doi.org/ 0.2134/jeq2001.302337x.

Reed, T.M., Fryar, A.E., Brion, G.M., and Ward, J.W., 2011, Differences in pathogen indicators between proximal urban and rural karst springs, Central Kentucky, USA: Environmental Earth Sciences, v. 64, p. 47–55. https://doi.org/10.1007/s12665-010-0816-8.

Runkel, A.C., Steenberg J.R., Tipping R.G., Retzler A.J., 2013, Physical hydrogeology of the groundwater-surface water system of southeastern Minnesota and geologic controls on nitrate transport and stream baseflow concentrations: Minnesota Geological Survey report delivered to the Minnesota Pollution Control Agency, Contract number B50858 (PRJ07522).

Ryan, M., and Meiman, J., 1996, An examination of short-term variations in water quality at a karst spring in Kentucky: Ground Water, v. 34, no. 1, p. 23–30. https://doi.org/10.1111/j.1745-6584.1996.tb01861.x.

Sasowsky, I.D., Dinsmore, M.A., Salvati, R., Bixby, R., Raymond, H., and Mazzeo, P., 2003, Subtle but significant karst on the glaciated Bellevue-Castalia karst plain, Ohio, USA, *in* Ninth Multidisciplinary Conference on Sinkholes and the Engineering and Envionmental Impacts of Karst, Huntville, Alabama, p. 95–109. https://doi.org/10.1061/40698(2003)8.

Sinkhole Areas and Sinking-Stream Basins (1997), Indiana Geological and Water Survey, Indiana University, http://maps.indiana.edu/previewMaps/Hydrology/Karst_Sinkhole_Areas.html, [last accessed on June 28, 2018].

Smart, C.C. and Ford, D.C., 1982, Quantitative dye tracing in a glacierized alpine karst: Beit. Geol. Schweiz. Hydrol., v. 28, no. 1, p. 191–200.

Smart, C.C., 1988, Artificial tracer techniques for the determination of the structure of conduit aquifers: Ground Water, v. 26, p. 445–453. https://doi.org/10.1111/j.1745-6584.1988.tb00411.x.

Torres, M.C. and Bair, E.S., 2012, Paleokarst in central and northwest Ohio: The Newburg Zone as a system of Silurian flank margin caves: Geological Society of America Abstracts with Programs, v. 44, no. 5, p. 3.

Upchurch, S.B., Dobecki, T.L., Scott, T.M., Meiggs, S.H., Fratesi, S.E., and Alfieri, M.C., 2013, Development of sinkholes in a thickly covered karst terrane, *in* Land, L., Doctor, D.H., and Stephenson, J.B., eds., Sinkholes and the Engineering and Environmental Impacts of Karst: Proceedings of the Thirteenth Multidisciplinary Conference, May 6−10, Carlsbad, New Mexico: NCKRI Symposium 2. Carlsbad (NM), National Cave and Karst Research Institute, 497 p.

Veress, M., 2016, Covered Karsts: Dordrecht, Springer, 536 p.

Wabash Formation: Niagaran and Cayugan Series, Silurian System; Indiana Geological and Water Survey, Indiana University, https://igs.indiana.edu/compendium/comp8qlg.cfm [last accessed on June 28, 2018.

Wanfang Zhou, Beck, B.F., Pettit, A.J., and Stephenson, B.J., 2002, A groundwater tracing investigation as an aid of locating groundwater monitoring stations on the Mitchell Plain of southern Indiana: Environmental Geology, v. 41, p. 842–851. https://doi.org/10.1007/s00254-001-0464-0.

Wanfang Zhou, and Beck, B.F., 2008, Management and mitigation of sinkholes on karst lands: An overview of practical applications: Environmental Geology, v. 55, no. 4, p. 837−851. https://doi.org/10.1007/s00254-007-1035-9.

Wayne, W.J., Johnson, G.H., and Keller, S.J., (1966), Geologic map of the 1 degree × 2 degree Danville quadrangle, Indiana and Illinois, showing bedrock and unconsolidated deposits [Part A –bedrock units only: Regional Geologic Map No. 2, Indiana Geological Survey, Bloomington, Indiana.

Wiersma, J.H., Stieglitz, R.D., Cecil, D.L., and Metzler, G.M., 1986, Characterization of the shallow groundwater system in an area with thin soils and sinkholes: Environ. Geol. Water Sci., v. 8, no. 1/2, p. 99−104. https://doi.org/10.1007/BF02525563.

Wilson, J.L. and Henry, K., 2013, Karst conduit sinuosity as a driver of karst hyporheic exchange, Abstract # EP12A-07, American Geophysical Union, Fall Meeting.

Zötl, J., 1989, Paleokarst as an important hydrogeological factor, in Bosák, P., Ford, D.C., Glazek, J., and Horáček, eds., Paleokarst: A Systematic and Regional Review, , Elsevier and Academia, Amsterdam and Praha, 726 p.

Majid Dashti Barmaki, Mohsen Rezaei, Ezzat Raeisi, and Javad Ashjari. Comparison of surface and interior karst development in Zagros Karst Aquifers, Southwest Iran. *Journal of Cave and Karst Studies*, v. 81, no. 2, p. 84-97. DOI:10.4311/2017ES0120

COMPARISON OF SURFACE AND INTERIOR KARST DEVELOPMENT IN ZAGROS KARST AQUIFERS, SOUTHWEST IRAN

Majid Dashti Barmaki[1], Mohsen Rezaei[2, C], Ezzat Raeisi[3], and Javad Ashjari[4]

Abstract

Aggressive recharge water is capable of widening the surface and interior openings of karstic layers that leads to the easy flowing of water in this type of aquifers. The object of this study is to understand if surface karstification is the same as the interior karst development of an aquifer. Surface karstification was analyzed using Geographic Information System and remote sensing techniques, while interior karstification was studied with spring hydrograph analysis. The study area includes seven carbonate aquifers in the Zagros Region of Iran. The surface karstification of these aquifers is controlled by different factors including the thickness of carbonate formations, distance from faults, fracture density, precipitation, temperature, vegetation index, slope, and relief. The most important factors are precipitation and presence and density of faults and fractures; while the least significant factor is the vegetation cover. The spring hydrograph analysis shows that there are different ways of estimating the relative karst development, but each parameter that impacts the specific character of the karst aquifer might be independent of others. Furthermore, comparing the relative surface and interior karst development demonstrates that the possible relationship between them is unpredictable. Consequently, we define a specific and unique numeric method to assess the interior karst development that permits a meaningful concept and comparison among different aquifers throughout the world.

Introduction

The progression of the dissolution and development of karst in carbonate formations usually results in increased complexity in the structure and hydrogeologic properties of the karstic aquifer. The degree of karst development in these aquifers is influenced by various factors. Lithology, carbonate rocks thickness, tectonic setting (e.g., fractures and faults), relief, temperature, type and amount of precipitation, and partial pressure of CO_2 are the most important factors determining the degree of karst development (White, 1988). Moreover, the vegetation type and intensity, and the thickness of the soil layer also play a meaningful role in karstification (Barany Kevei, 2007).

Carbonate pure lithology is more suitable for karst development, as the presence of impurities such as marl and silica minerals may impede the dissolution progress. The thickness of soluble rock layers and the stratigraphic position of them among the non-soluble layers control the extent of karst development. In the case of thin soluble rocks sandwiched between non-soluble layers, it is less likely that karstification occurs (Seif and Ebrahimi, 2014). Furthermore, the impermeable and non-soluble thin layers of rocks as interfering layers in the carbonate layers impede the water movement into the deeper parts, and hence, the dissolution only occurs in the top carbonate sequences (Lowe, 1992; Shabab-Brojeni, 2011).

Faults and fractures represent the effects of the tectonic setting. Most fractures are caused by the tectonic forces, weathering, and mechanical breakdown. Relief and local base level are the main geomorphologic factors that control the regional groundwater flow in karstic aquifers. They define boundary conditions and control the recharge and discharge locations of the aquifer (White, 1988; Palmer, 2000). The location of local base level is inherited from historical and regional tectonic processes. Temperature and precipitation, which determine the availability of water, are certainly the principal variables controlling total denudation of the rocks by dissolution (Ford and Williams, 2007). The climate variability in regional and global scale results in the various spatial distribution of precipitation, temperature, and evapotranspiration, and consequently, significant changes in vegetation cover (Ekmekci and Tezcan, 2011). The type and density of vegetation cover of karst terrains are variable. Due to the activity of soil microbes, the vegetation cover usually improves the water aggressiveness by increasing the P_{CO2}. Furthermore, the presence of vegetation regulates dissolution over a vast area. The slope controls water recharge into the subsurface. The residence time of surface runoff in gentle dips is considerably more than in steep dips, so the rate of infiltration in the gentle dips can be more than the steep dips.

These parameters must be active together to increase the karstification and enhancement of one of them imposes positive feedback to the others, though their weighted effects on dissolution vary.

[1] Faculty of Earth Sciences, Kharazmi University of Tehran, Iran
[2] Department of Earth Sciences, Shiraz University, Shiraz, Iran.
[3] Department of Earth Sciences, College of Science, Shiraz University, Shiraz, Iran
[4] Abanrood Tadbir Engineering Company, Tehran, Iran
[C] Corresponding author: mohsen-rezaei@shirazu.ac.ir

The Zagros Mountains Ranges are crucial sources of surface water and groundwater of Iran, which outcrop more than 100,000 km^2 of carbonate formations (Raeisi, 2002). The groundwater of carbonate aquifers emerge at springs, discharge to the adjacent alluvial aquifer, or pour into traversing rivers (Ashjari and Raeisi, 2006). The Asmari Formation, with lithology of limestone and dolomite, is the most important groundwater and oil reservoir in this region. Aquifers formed in the Asmari Formation have different hydraulic behavior.

A lot of research has been developed to understand the hydrogeologic characteristics of Zagros Karst aquifers, including from Dashti et al. (2015), Ashjari (2007), Raeisi and Stevanovic (2010), Karimi et al. (2005 and 2016), Chitsazan et al. (2015), and Kalantri et al. (2010). The main object of this research is to investigate the causes of the diversity in surface and interior karstification. Furthermore, springs responses to external stresses are investigated. The combined methods of GIS and spring hydrograph analyses in seven selected karstic springs are used to achieve these goals.

Study Area

The Zagros Mountains extend from the south of Turkey and north and northeast of Iraq to the south of Iran. The carbonate formations including limestone, dolomite, and dolomitic-limestone, form the high mountains and mainly expose as sequential anticlines and synclines (Alavi, 2004). Foldings cause superimposing of some of these carbonate formations, mostly near to the main thrust fault, with very steep dips of the layers. Gentler dips and broader spacing among the folds peak by distancing from the frequency of faults allow for the deposition of recent sediments as alluvium. The selected anticlines lie in the central segment of the Zagros in Iran (Fig 1). The rivers traverse these folds from the limbs or the plunges. In this research, five anticlines including Anar, Dashtak, Pabdeh, Rig, and Delisib have been studied. The locations of these anticlines are presented in Figure 1.

The fold axes of selected anticlines trend from the northwest to the southeast parallel to the main Zagros thrust fault. The lithology and the exposed formations of these anticlines are summarized in Table 1 in chronologic order from the youngest to oldest according to Stöcklin (1968 and 1974). Surface geology and cross sections of these five anticlines are shown in Figures 2 to 5.

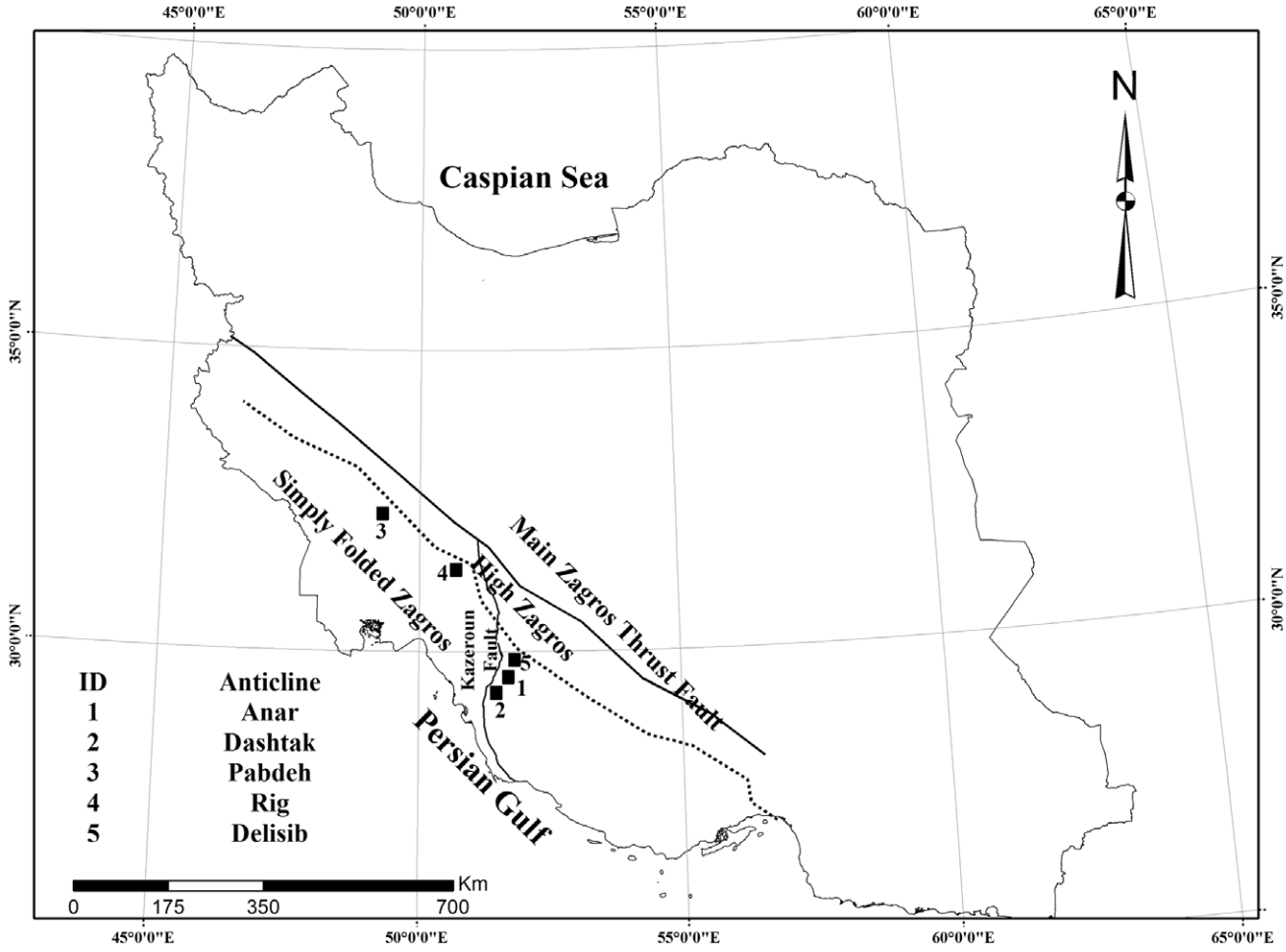

Figure 1. The study areas include location of Anar, Dashtak, Pabdeh, Rig, and Delisib anticlines.

Table 1. The lithologic characteristics of the exposed formations at anticlines (Aghanabati, 2004; Alavi, 2004).

Anticlines	Formation name	Abbreviation	Age	Lithology	Thickness
Anar	Gachsaran	Gs	Miocene	salt, anhydrite, colorful marls	>1000
	Asmari-Jahrum	As-Ja	Paleocene –Miocene	limestone, anhydrite, and dolomite	300
	Pabdeh-Gurpi	Pd-Gu	upper Cretaceous- Eocene	marl, Shale, mudstone, and layers of limestone with thin clay	650
Dashtak	Bakhtiari	Bk	Pleistocene	conglomerate	<200
	Gachsaran	Gs	Miocene	salt, anhydrite, colorful marls	>1000
	Asmari-Jahrum	As-Ja	Paleocene –Miocene	limestone, anhydrite, and dolomite	350
	Pabdeh-Gurpi	Pd-Gu	upper Cretaceous- Eocene	marl, Shale, mudstone, and layers of limestone with thin clay	650
	Ilam-Sarvak	Il-Sv	upper Cretaceous	limestone	450
Pabdeh	Aghajari	Aj	upper Neogene	sandstone	150
	Mishan	Mn	lower Neogene	shale, limestone, and layers of dolomite	100
	Asmari	As	Oligocene–Miocene	limestone, anhydrite	300
	Pabdeh	Pd	Paleocene –Eocene	marl, Shale, and layers of limestone with thin clay	400
Rig	Bakhtiari	Bk	Pleistocene	conglomerate	100
	Gachsaran	Gs	Miocene	salt, anhydrite, colorful marls	300
	Asmari	As	Oligocene–Miocene	limestone, anhydrite, and dolomite	364
	Pabdeh	Pd	Paleocene -Eocene	marl, Shale, and layers of limestone with thin clay	700
Delisib	Bakhtiari	Bk	Pleistocene	conglomerate	100
	Razak	Rz	Miocene	shale and layers of limestone	200
	Asmari-Jahrum	As-Ja	Paleocene –Miocene	limestone, anhydrite, and dolomite	480
	Pabdeh-Gurpi	Pd-Gu	upper Cretaceous- Eocene	marl, Shale, mudstone, and layers of limestone with thin clay	650
	Bakhtiari	Bk	Pleistocene	conglomerate	100

Asmari and Sarvak are the most important karst formations and constitute the largest karst aquifers and reservoirs with many spring discharges. In our research, information has been collected from seven important karst springs including Bavan (Sp_1), Sarabroud (Sp_2), Sasan (Sp_4), Bibitalkhun (Sp_7), Atashgah (Sp_{11}), Kharandaz (Sp_{19}), and Abshar (Sp_{21}). The characteristics of these springs are presented in Table 2, and their locations are depicted in Figures 2 to 5. The resurgences of these springs and the main part of each catchment area are located in the Asmari Formation.

Bavan (Sp_1) and Sarabroud (Sp_2) springs are two important springs of the Anar anticline (Fig 2). The core of this anticline is formed by the Sarvak Formation, which lies under the impermeable layers of the Pabdeh-Gurpi Formations. The Asmari-Jahrum Formations cover the latter formation in the Zagros, but it has been eroded by the active tectonics in the middle sections of the anticline and near to the peak. As a result, the Asmari-Jahrum formations are disconnected into two distinct parts; north and south limbs. Spring Sp_1 emerges from the northern sector of the Asmari Formation while the Sp_2 discharges the southern sector. Several faults, mainly in the perpendicular or oblique direction to the fold axis, cross the anticline. The solution features of dry valleys, karren, grike, rain pits, solution pans, and polje are observed. Dasht-e-Arzhan polje is formed at the southeast end of the anticline as a result of interactions of two normal faults and consequently the formation of a wide depression (Jamali et al., 2015). The Fahlian River is parallel to anticline elongation and turns in response to the plunge of the anticline from the northwest plunge and continues its flow to the south of the region.

Sasan Spring (Sp_4) (Fig. 2) is the most important spring for the Dashtak anticline. There are several other small springs adjacent to Sasan Spring. The anticline is composed of Asmari-Jahrum Formations. Since the Shapor River traverses and erodes the anticline near to the northwest plunge, the Pabdeh-Gurpi, as the bedrock of the aquifer, is

Table 2. Physicochemical parameters of springs.

Anticline	Spring ID	Spring Name	Discharge (L/S)	T (°C)	EC (µS/cm)	pH	Ca^{2+} (meq/L)	Mg^{2+} (meq/L)	Na^{+} (meq/L)	K^{+} (meq/L)	HCO_3^{-} (meq/L)	CO_3^{2-} (meq/L)	Cl^{-} (meq/L)	SO_4^{2-} (meq/L)
Anar[a]	Sp_1	Bavan	59.5	21	450	8.1	2.95	1.35	0.14	0.02	4.1	0	0.35	0.08
	Sp_2	Sarab roud	979	17	290	7.5	2.3	1.5	0.39	0.05	3.35	0	0.4	0.29
	Sp_3	Chenar	60	22	280	8.2	2.3	1.45	0.38	0.02	3.3	0	0.3	0.2
Dashtak[b]	Sp_4	Sasan	1912.8	21	646	6.93	4	2	0.86	0.04	3.5	0	1.1	2.26
	Sp_5	Sarabshir	1345	19	499	7.06	2.5	2.4	0.07	0.02	4	0	0.75	0.22
	Sp_6	Pirsabz	5	21	897	6.99	4.5	4.5	0.86	0.04	3.5	0	1.2	5.18
	Sp_4	Sasan	1912.8	21	646	6.93	4	2	0.86	0.04	3.5	0	1.1	2.26
Pabdeh[c]	Sp_7	Bibitalkhun	1256	23.3	1264	7.5	4.42	3.03	4.82	0.03	3.88	0	5.63	2.58
	Sp_8	Gariveh	7	25.2	507	7.7	2.56	2.53	0.47	0.03	3.54	0	0.8	1.05
	Sp_9	Talug	5	22.2	1252	7	4.51	2.35	4.69	0.05	3.9	0	5.7	1.7
Rig[d]	Sp_{10}	Shoosh	77.1	14	313	8	1.8	1.4	0.03	0.01	2.8	0.2	0.1	0.1
	Sp_{11}	Atashgah	963	12	354	8	1. 9	1.3	0.1	0.01	2.9	0.2	0.1	0.11
	Sp_{12}	Chamanbid	5	12	273	7.8	2.39	0.6	0.08	0.01	2.6	0	0.2	0.1
	Sp_{13}	Parvaz	975	11	375	7.6	2.7	0.64	0.2	0.01	3	0	0.2	0.06
	Sp_{14}	Dorak	37	13	309	8	1.4	1.5	0.1	0.01	2.5	0.2	0.1	0.2
	Sp_{15}	Varkaab	129	12	310	7.8	1.7	1.3	0.05	0.01	2.7	0.2	0.1	0.06
	Sp_{16}	Faaj	43.5	14.7	350	7.9	1.5	2	0.1	0.01	3.1	0.1	0.1	0.3
	Sp_{17}	Delli	70	13	280	7.9	1.7	1.1	0.03	0.01	2.6	0.1	0.1	0.04
	Sp_{18}	Einakak	284	11.8	315	7.5	1.8	1.4	0.03	0.01	3	0	0.1	0.1
Delisib[a]	Sp_{19}	Kharandaz	600	11	400	7.6	3.3	1.4	0.62	0.03	3.6	0	0.9	0.55
	Sp_{20}	Tangtubadi	800	23.2	310	8.3	2.4	1.2	0.23	0.03	3	0.1	0.6	0.4
	Sp_{21}	Abshar	40	14	331	7.7	2.9	0.5	0.08	0.01	2.8	0	0.3	0.5
	Sp_{22}	Gerdukangak	280	13.8	290	8.3	1.6	1.2	0.23	0.01	2.7	0.1	0.4	0
	Sp_{23}	Abnahr	30	15	300	8	1.7	1.1	0.21	0.01	2.3	0.2	0.7	0

[a] Water samples measured (July 2016).
[b] Data from FRWA (2012).
[c] Data from KWPA (2012).
[d] Data from CBRWA (2012).

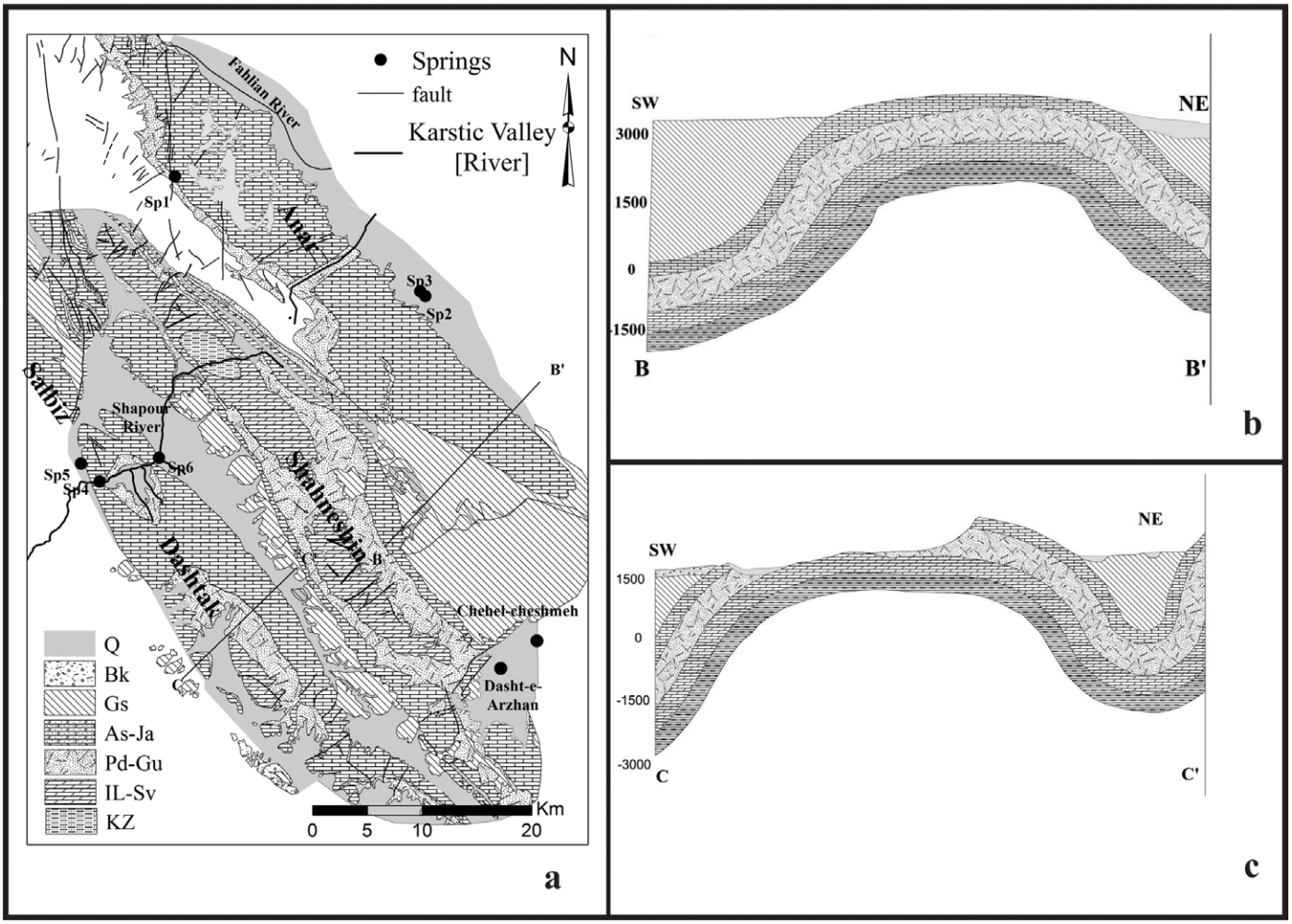

Figure 2. A) Geologic map of Anar and Dashtak anticlines, B) Cross section of Anar anticline, C) Cross section of Dashtak anticline.

exposed. The impermeable layer of the Gachsaran Formation lies on top of the Asmari-Jahrum and may be outcropped clearly or hidden by a thin layer of alluvium. The regional fault of Qatar–Kazerun passes from the northwest plunge and continues to the south in the Kazerun plain. The branches of this fault are crushed severely in the west part of the anticline, which leads to the formation of several small compartments of the carbonate aquifers. The main karst features are caves, especially prominent is the cave of Shapour (Raeisi and Kowsar, 1997).

The Pabdeh anticline, Bibitalkhun Spring (Sp_7) emerges from the Asmari-Jahrum Formations of the southern limb of the anticline (Fig 3). The geologic settings of the layers are fairly similar to the Anar anticline. The Asmari-Jahrum Formations are separated into two parts in the limbs with the Pabdeh Formation exposed in the core. Moreover, the Gachsaran Formation overlays the Asmari-Jahrum in the base of the anticline. A thrust fault passes from the southern limb in the same direction of the fold that causes the high depression of the southern plain. Dolines are observed along a strike-slip fault near the southern plunge. The Talug River passes through the anticline and cuts into the carbonate formation.

Atashgah Spring (Sp_{11}) appears on the southern limb of the Rig anticline (Fig 4). The Pabdeh Formation outcrops in the core and disconnects the Asmari-Jahrum Formations of the limbs. The impervious formation of Gachsaran is adjacent to the northern limb while the alluvium is deposited beside the southern limb. Since the anticline lies very close to the main thrust fault of the Zagros, the rocks are intensively fractured and faulted. Neither doline nor polje are observed. The Khersan River passes near to the southern plunge and then turns to the northwest, parallel to the anticline elongation. Few springs emerge from the southern limb and discharge water to the river.

The Delisib anticline is the source of the Kharandaz and Abshar Springs (Sp_{19} and Sp_{21}) (Fig 5). The core of the anticline is a thick layer of the Pabdeh-Gurpi. The Razak Formation lies on top of the carbonate rocks of Asmari-Jahrum Formations. This Formation is hidden under thin alluvium at some areas. The solution features of dry valleys, karren, grike, rain pits, solution pans, and polje are observed.

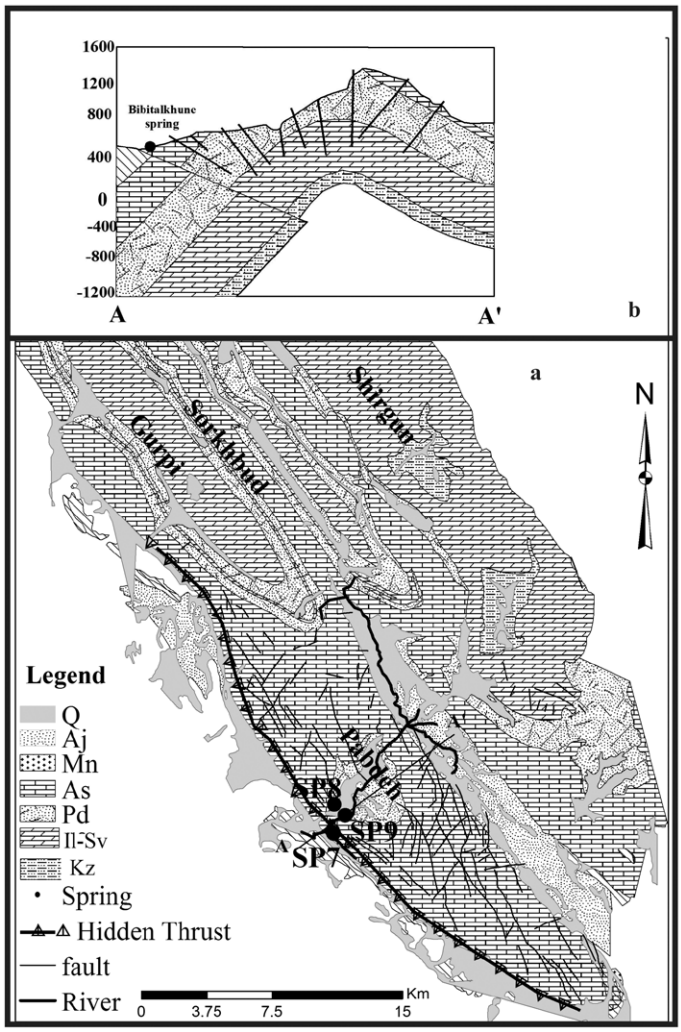

Figure 3. A) Geologic map of Pabdeh anticlines, B) Cross section of Pabdeh anticline.

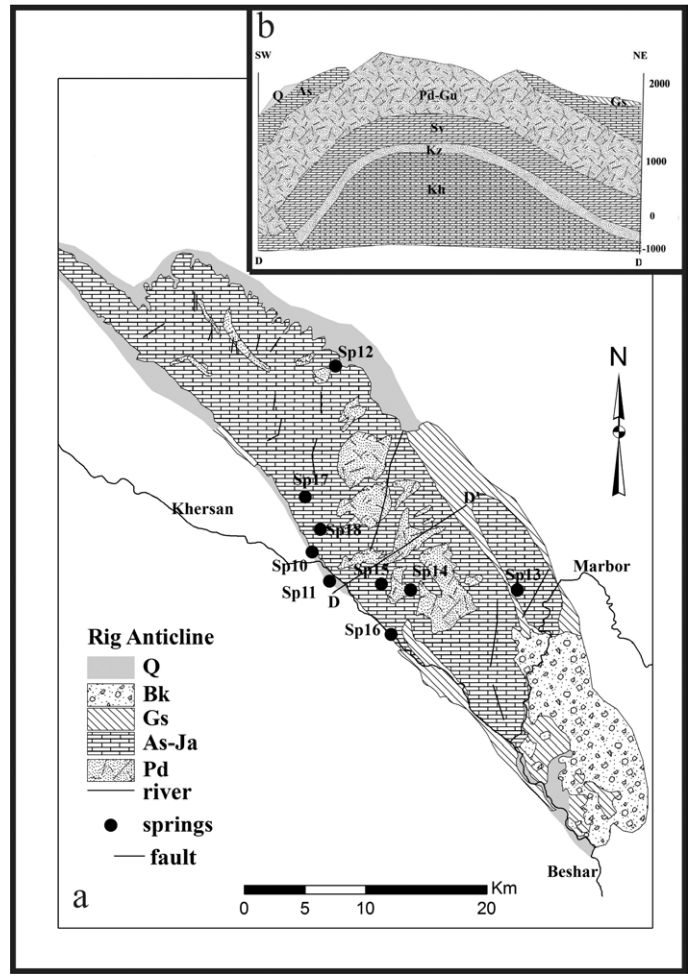

Figure 4. A) Geologic map of Rig anticlines, B) Cross section of Rig anticline.

Material and Methods

The geologic maps of the study areas were prepared based on geologic maps of 1/100,000 and 1/250,000 from the Iranian Oil Operating Company of Iran. Physicochemical parameters of springs (Table 2), and rainfall data were collected from the Fars Regional Water Authority (FRWA, 2012), the Chaharmahal and Bakhtiari Water Authority (CBRWA, 2012), and the Khuzestan Water and Power Authority (KWPA, 2012). The field study and water sampling of groundwater resources were conducted if there were not enough data from previous studies.

In our study, GIS and remote sensing techniques were used to evaluate surface karstification. Thickness of carbonate formations (Th), tectonic setting (distance from faults (FB) and fracture density (FD)), climate (precipitation (P) and temperature (T)), vegetation index (V), slope (S), and relief (R) were applied as interpretation elements to extract the thematic layers.

The karstic layers are carbonate formations of Sarvak and Asmari Formations that give the highest karst potential scores. The stratigraphic thickness of these rocks had an important effect on karst development. Precipitation, determining the availability of water for chemical reactions, and temperature, determining the speed of chemical reaction, are essential factors in dissolution. The impact of changes in the elevation can be checked as climate factors; the value and type of precipitation, as well as values of temperature. For this reason, the elevation was not mentioned as an independent factor. Accordingly, the correlation charts of (precipitation—altitude) and (temperature—altitude) were plotted. By using extrapolating from the different stations, a linear equation was fitted to the available data. Vegetation is found to have an important role in karst development through absorption of calcium and magnesium by roots and production of

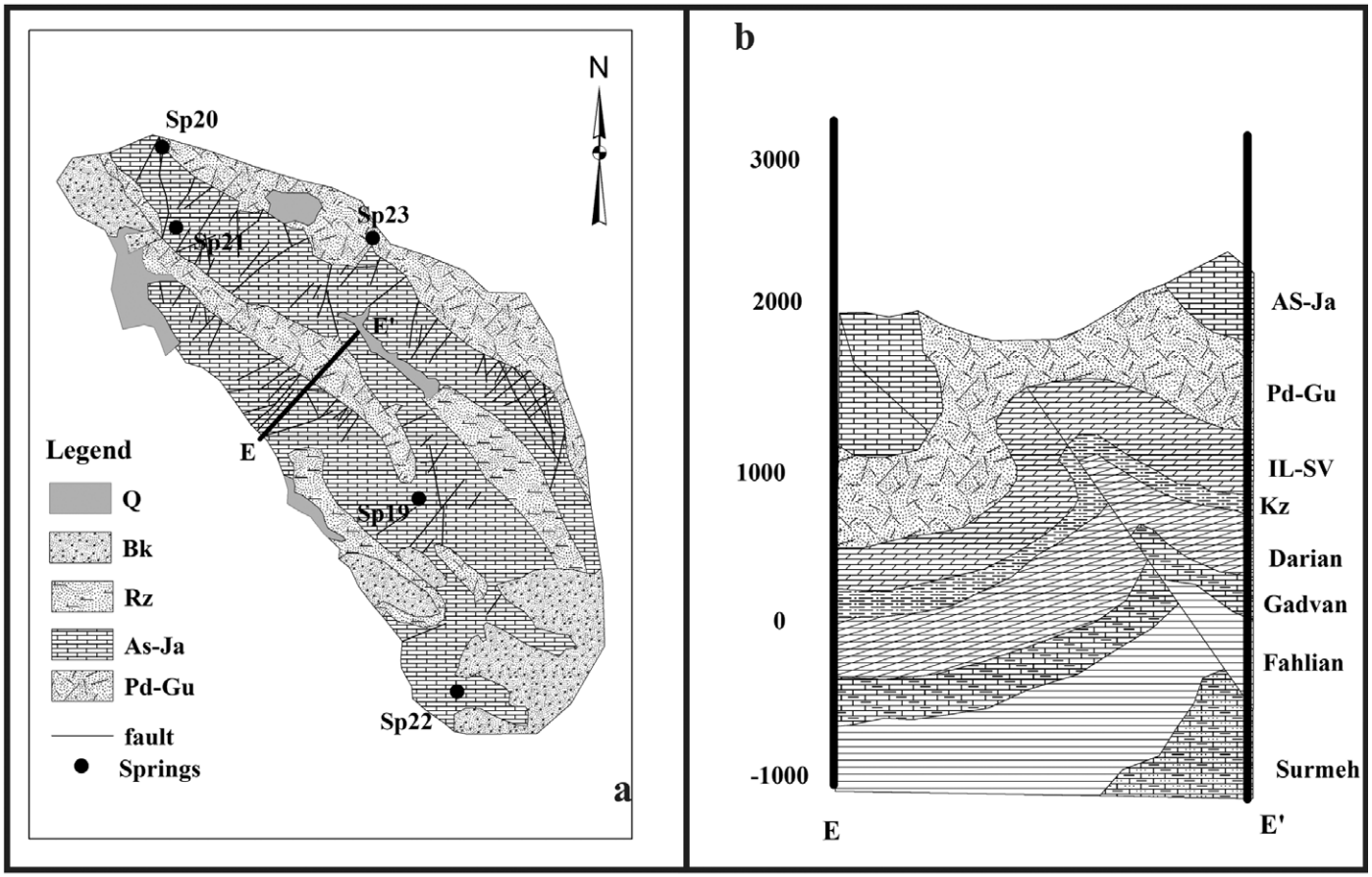

Figure 5. A) Geologic map of Delisib anticlines, B) Cross section of Delisib anticline.

carbon dioxide (Ford and Williams, 2007). Soil Adjusted Vegetation Index (SAVI) was used in areas with low vegetative cover (i.e., $<$ 40 %) (Huete, 1988; Panda et al., 2010). The SAVI was used for detection of natural vegetation cover change in this study because of its acceptable accuracy and ability to detect the vegetation at study areas. The slope map, calculated based on percentage, was derived from a digital elevation model (DEM). Relief is the last factor affecting karst development. This parameter is the controlling factor of flow direction at carbonate anticlines. As mentioned previously, the link between aquifer discharge locations and major flow direction indicates the local base level at study areas. First, the water flow direction at each of the anticlines should be defined. The local base level of karst areas was the lowest point to which water can flow, such as karst valley rivers or springs. Therefore, the local base level should be defined to obtain the relief factor at each anticline based on assigned local base levels.

Each factor was provided as a separate layer in GIS to determine karst development at study areas. GDEM of Iran (DEM, Iran SRTM - Shuttle Radar Topography Mission Dem data available at 3 arc second, ca. 90 m), geologic maps (1/100,000, 1/250,000), Landsat ETM$^+$ 8 images, as well as hydrologic and groundwater data of study areas were used. GIS (ArcGIS 10) and remote sensing (PCI Geomatica) software packages were applied in data management and processing. All data were converted to digital format. Then, different layers were created and integrated in GIS. These steps, then followed by analysis and interpretation of the results. To determine which factors affect karst development and to what degree, experts were consulted to provide judgments on the importance of criteria (Table 3). Weighting of the maps was performed by using an Analytical Hierarchical Process (AHP). AHP, as a multi-objective and multi-criteria decision-making approach, was developed by Saaty (1980). It was based on a pair-wise criteria comparison that has been extensively studied and refined. This approach enables the user to achieve a scale of preference drawn from a set of alternatives. Maps were combined applying the weighted index overlay in GIS that is a technique for applying a common measurement scale of values to diverse and dissimilar inputs to create an integrated analysis.

The recharge of the study areas is mainly in the form of direct precipitation, rarely as snow, and in some cases, as seepage from rivers traversing the anticlines. The average precipitation over anticline sub-basin surfaces was estimated by using the precipitation—altitude relation and the DEM. Since it is the basis for all hydrologic analysis, the next

Table 3. Factors affecting the karst development, and the assigned weights and ranks for aquifers.

Factor	Range	R[a]	W[b]
Thickness of Carbonate Formations, Th (m)	< 300	1	0.14
	>300 and <350	2	0.14
	>350 and <400	3	0.14
	>400 and <450	5	0.14
	> 450	8	0.14
Precipitation, P (mm/y)	<500	1	0.13
	500 − 600	2	0.13
	600 − 700	3	0.13
	700 − 800	5	0.13
	800 − 900	7	0.13
	>900	9	0.13
Distance from Faults, FB (m)	<100	9	0.23
	100 − 200	8	0.23
	200 − 350	7	0.23
	350 − 500	6	0.23
	500 − 650	5	0.23
	650 − 800	4	0.23
	800 − 1000	3	0.23
	>1000	1	0.23
Fracture Density, FD (%)	<25	2	0.19
	25 − 50	5	0.19
	50 − 75	7	0.19
	>75	9	0.19
Temperature, T (°C)	<10	8	0.05
	10 − 15	6	0.05
	15 − 20	4	0.05
	>20	2	0.05
Soil Adjusted Vegetation Index, SAVI (%)	No Vegetation	0	0.09
	Low Vegetation	2	0.09
	Medium Vegetation	5	0.09
	High Vegetation	8	0.09
Slope, S (%)	<20	9	0.05
	20 − 40	7	0.05
	40 − 60	5	0.05
	60 − 80	3	0.05
	>80	1	0.05
Relief, R (m)	<150	1	0.12
	150 − 450	3	0.12
	450 − 750	5	0.12
	750 − 1100	6	0.12
	1100 − 1450	7	0.12
	1450 − 1700	8	0.12
	>1700	9	0.12

[a] Ranks of each factor (expert judgment).
[b] Weight of the factors (AHP method).

step was the springs' catchment area delineation (Bonacci, 1987). The catchment area of each spring is calculated by the simple water-balance equation CA = Q/PI (Bonacci et al., 2006; Pezeshkpour, 1991; Karimi et al., 2001) where CA is the catchment area of the spring (km^2), Q is the total annual volume of water discharging from the spring ($Mm^3 y^{-1}$)], P is the annual precipitation (mm y^{-1}) and I (mm) is the recharge coefficient. Determination of recharge coefficient is very difficult. It depends on many factors such as the presence or absence of sinkholes and dolines, joints and fractures, the thickness and granulation of soil cover, the slope of beds and topography, amount, type, time and space distribution of precipitation, temperature, and vegetation cover. The borderlines of the catchment areas were determined by using the proposed steps by Ashjari and Raeisi (2006).

Results

Remote sensing (RS) and GIS

Remote-sensing and GIS techniques were used to obtain the qualitative map of karstification in the study areas. The surface karstification index values were extracted by using

$$KD = (W\sum R_K)_{Th} + (W\sum R_K)_{FB} + (W\sum R_K)_{FD} + (W\sum R_K)_P + (W\sum R_K)_T + (W\sum R_K)_{SAVI} + (W\sum R_K)_S + (W\sum R_K)_R \quad (1)$$

Where KD was karstification value, W was the weighting value of each factor, and R_K assigned ranks to ranges of factors, including the thickness of carbonate formations Th, distance from faults FB, fracture density FD, precipitation P, temperature T, vegetation index SAVI, slope S, and relief R. Each aquifer, from the karstification aspect, was classified into three classes from low, medium, and high. The index-weighting factors were done by using a combination of expert knowledge and database hierarchical analysis.

Karst development is carried out in seven karst aquifers (A1−A7) (Fig 6). In Figure 6, the positions of aquifers on the anticlines are also shown. A_1, A_2, A_3, A_4, A_5, A_6, and A_7 aquifers are the catchment areas of Sp_1, Sp_2, Sp_4, Sp_7, Sp_{11}, Sp_{19}, and Sp_{21} springs, respectively. The final results of the estimated surface karstification index are presented in Table 4 and Figure 6. The aquifers A_1 and A_2 have the lowest rates of karstification whereas the aquifers A_6 and A_7 show high rates of karstification. Other aquifers are distributed between these two groups.

The values of effective factors on karst development at the aquifers are presented in Table 5. The orders and effects of the factors on the karstification are dissimilar among the aquifers.

The highest value belongs to precipitation. Unless the aquifer rocks are crushed by a fault or the aquifer is located in lower elevation (i.e. less than 1500 meters). The catchment area of A_3 and A_4 are located at lower elevations relative to the others. Consequently, they receive the lowest precipitation. A_7 and A_4 are crushed by faults, which mainly control the karst development of the area. The thickness of aquifers is one of the lowest ranking factors in the condition that the catchment area is limited merely to the Asmari-Jahrum Formations. For instance, the catchment area of A_3 and A_4 extend to the Sarvak Formation, which is thicker than Asmari-Jahrum.

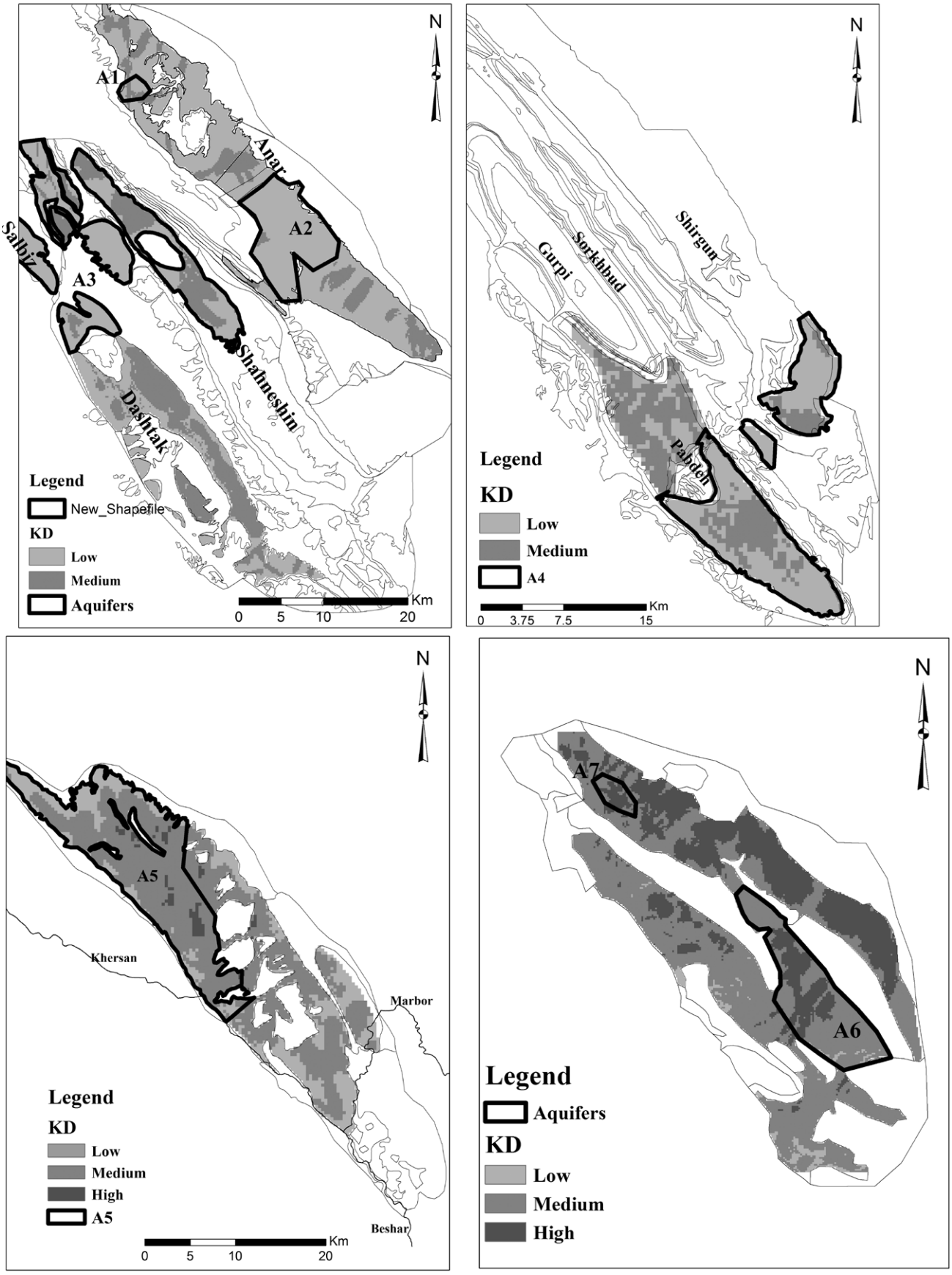

Figure 6. Karst Development at aquifers: A) A_1, A_2, and A_3 aquifers; B) A_4 aquifer; C) A_5 aquifer; D) A_6 and A_7 aquifers.

Table 4. Descriptive classification and statistical parameters of karst development (KD) in the study areas.

Parameters	Statistical Description	A_1	A_2	A_3	A_4	A_5	A_6	A_7
Percent area of karst development, KD	Low	75	84	68.5	69.8	57.49	2	0
	Medium	25	16	31.5	30.2	40.11	68	49
	High	0	0	0	0	2.4	30	51
Statistical parameters of karst development, KD	Min	2.01	2.31	1.84	1.72	1.63	3.79	5.14
	Max	2.54	5.46	5.96	5.46	7.34	7.18	6.48
	Average	3.76	3.88	3.9	3.6	4.49	5.48	5.99

Table 5. Values of the effective factors on karst development at aquifers.

ID	Thickness of Carbonate Formations, Th[a] (m)	Precipitation, P[b] (mm/y)	Distance from Faults, FB[b] (m)	Fracture Density, FD[b] (%)	Temperature, T[b] (°C)	Soil Adjusted Vegetation Index, SAVI[b] (%)	Slope, S[b] (%)	Relief, R[b] (m)
A_1	28	86	76.51	59.32	28	7.34	42.9	12
A_2	28	98.73	40.33	70.92	32.5	2.1	42.2	19.7
A_3	75.78	41.95	69.1	64.4	21.64	18.1	36	27.9
A_4	51.9	35.28	132.94	58.2	14.25	0.02	39	20.75
A_5	28	805.31	48.87	87.6	36.1	18	38	53.1
A_6	112	117	100.1	47	35.1	18	38.9	68
A_7	112	117	177.3	73.2	30	18.3	30.1	43.3

[a] Values based on equation: [(% Area × Rank)] × Weight
[b] Values based on equation: [∑ (% Area × Rank)] × Weight

The SAVI, slope, and temperature are among the lowest ranking factors. As expected, due to the dominance of the bare carbonate rocks in the Zagros region, the SAVI has received the lowest credit in all cases. The slope controls the recharge rate of the area, but the Asmari-Jahrum Formations are characterized by fractured aquifers. Therefore, the recharge role of the slope is weak. The precipitation and temperature are regarded as climatologic factors, but their effects on the karstification are dissimilar because the temperature variation rates are very low relative to the precipitation.

Relief and local base level, plays an unclear role in the karstification. If the aquifer is located near to the High Zagros Zone, the role of relief is important. Anticlines of this zone are pushed intensively together, and elevation variations are vast. The aquifers of the Simply Folded Zone are characterized by the broad amplitude of folding and a lower rate of elevation variations.

The results show that the karstification values of the aquifers of the same anticline are not equal or follow the same order. For instance, the A_6 and A_7 are located in the Delisib anticline, but the precipitation is more important in the A_6 than A_7. In fact, several faults cross the A_7 impact the precipitation priority, whereas the main faults are absent in the A_6.

Springs Hydrograph Analyses

Shokri et al. (2016) suspected to the equality of the surface karstification and internal karstification and suggested that they might be completely independent. Therefore, to understand the aquifer karstification value, the spring hydrographs are used to extract the karstification value based on the recession coefficients, the ratio of the quick flows to base flows, the ratio of dynamic storages to the catchment areas, and drying time of springs.

Hydrograph recession curve analysis is a technique commonly used to determine flow characteristics and karst development (Bonacci, 1993; Brodie and Hostetler, 2009; Kresic and Bonacci, 2010). The Maillet method (Maillet, 1905) for defining a hydrograph recession curve and determine spring flow characteristics is used, so hydrographs for springs were prepared.

Based on Kullman (2000), Malík (2007), and Malík and Vojtková (2012), a description of the recession of springs indicates that catchment areas of all springs are aquifers with irregularly developed fissure networks, with a majority of open macro-fissures, and with the possible presence of karst conduits of limited extent. In extreme cases, short-term turbulent flow might occur in this type of rock environment. Table 6 gives recession curve data, calculations related to dynamic storage, and drying time of springs.

Table 6. Recession curve data, calculations related to dynamic storage and drying time of springs.

Spring	Recession Coefficient (d^{-1})			Time (d)			Discharge Ratio	Dynamic Storage (Mm^3)			V_0/CA	Drying Time of Springs
	α_1	α_2	α_3	t_1	t_2	t_3	(Q/B)	V_0	V*	V	(Mm^3/km^2)	(d)
Sp_1	0.047	0.008	···	20	15	···	1.5	2.43	0.68	1.75	0.32	770
Sp_2	0.0062	0.0058	···	91	93	···	2.4	22.06	7.34	14.72	0.24	1200
Sp_4	0.02	0.009	0.002	31	33	78	1	97	61.57	35.43	0.4	3445
Sp_7	0.02	0.005	···	36	20	···	0.2	43.79	25.92	17.87	0.33	1400
Sp_{11}	0.011	0.0025	···	45	60	···	0.35	40	28.5	11.5	0.46	2800
Sp_{19}	0.01	0.003	···	96	70	···	0.25	35.48	16.58	18.9	1.31	2300
Sp_{21}	0.007	0.017	···	106	31	···	1.5	5.02	0.46	4.56	2.79	400

Calculation of Recession Curve of Springs

$\alpha_1 = \frac{\log Q_0 - \log Q_1}{0.4343_{(t_0 - t_1)}}$; $\alpha_2 = \frac{\log Q_1 - \log Q_2}{0.4343_{(t_2 - t_1)}}$; $\alpha_3 = \frac{\log Q_2 - \log Q_3}{0.4343_{(t_3 - t_2)}}$

Q_0 is spring discharge rate at the start time of recession curve. Q1, Q2, and Q3 are spring discharge rate at the change of slope in recession curve.

Q/B: Quick flow/Base flow

V_0: Dynamic Volume, $V_0 = [(Q_{01}/\alpha_1) + (Q_{02}/\alpha_2) + (Q_{03}/\alpha_3)] \times (86400)$

V*: The remaining volume at the end of microregim, $V^* = (Q^*/\alpha_3) \times 86400$

V: Volume drained during the recession time, $V = V_0 - V^*$

CA: Catchment areas of springs; Area of aquifers

The first discharge recession coefficients of the springs are more than the second recession coefficients ($\alpha_1 > \alpha_2$) except the spring of Sp_{21} in the catchment area of A_7 where α_1 is less than α_2 due to recharge from snow melting that perturbs the recessional processes. The values of α_1 vary from 0.0062 in Sp_2 to 0.047 in Sp_1 while the minimum and maximum values of the α_2 are 0.0025 in Sp_{11} and 0.017 in Sp_1. The ratio of recession coefficients (α_1:α_2) changes from 0.4 in Sp_{21} to 5.9 in Sp_1. The results show that the springs of the same anticlines may have highly different values of the recession parameters. For examples, Sp_{19} and Sp_{21} are emerging from the Delisib anticline, but the values of α_1, α_2, and α_1:α_2 for Sp_{19} are 0.01, 0.003, and 3.33 and values for Sp_{21} are 0.007, 0.017, and 0.41. The high value of α_1 can be representative of high internal karst development. The order of cases from high to low development is Sp_1, Sp_4, Sp_7, Sp_{11}, Sp_{19}, Sp_{21}, and Sp_2. If the value of α_2 is regarded as representative of karstification, the order of the springs will change from Sp_{21}, Sp_4, Sp_1, Sp_2, Sp_7, Sp_{19}, and Sp_{11}. The values of α_1: α_2 are considered in reverse order. The lowest value shows the highest development. In this condition, the springs' orders are Sp_{21}, Sp_2, Sp_4, Sp_{19}, Sp_7, Sp_{11}, Sp_1. Therefore, the obtained results are non-unique in the recession coefficient analysis.

The next criterion considered as representative of the karstification of aquifers is the ratio of quick flow to base flow. Karst systems contain quick flow and slow flow components. These components are reflected in the springs' hydrographs. The highly developed aquifer has a very well-developed conduit system that stores and transfers the groundwater to the springs. Thus, the higher volume of quick flow/base flow can be considered as a fair criterion to karstification. So, the orders of springs from a high value of quick flow/base flow to a low value are Sp_2, Sp_1, Sp_{21}, Sp_4, Sp_{11}, Sp_{19}, and Sp_7. The first three cases show the volume of the quick flow is more than base flow, whereas the other cases illustrate that the volume of the base flow is more than the volume of the quick flow.

The ratio of the dynamic volume of an aquifer to the catchment area is another criterion. The higher value of the ratio might be a representative of higher karst development. Regarding this criterion, the order of springs from the high value to the low value is Sp_{21}, Sp_{19}, Sp_{11}, Sp_4, Sp_7, Sp_1, and Sp_2.

The last parameter which we address is the drying time of the spring. The well-developed conduit system of springs permits the groundwater flow from the farthest spot to the spring. Therefore the spring lasts for a long time in a drought climate. The order of springs from long lasting (3445 days) to short lasting (400 days) are Sp_4, Sp_{11}, Sp_{19}, Sp_7, Sp_2, Sp_1, and Sp_{21}.

The springs of Sp_1 and Sp_2 are emerging from the Anar anticline and the springs of Sp_{19} and Sp_{21} are discharging the Delisib anticline. Although springs are located in the same anticline and in the same climate region, their obtained karstification orders are dissimilar. Therefore, it is impossible to compare results about one aquifer in one anticline to another aquifer in the same anticline.

Discussion comparing surface and internal karstification

Seven aquifers from five anticlines are located in different regions where their geologic structure and climatic characters are dissimilar in spite of their similarity of main lithology. Considering the priority of the aquifers in terms of karst development by different methods, they show absolutely non-unique orders that make it vexing to discriminate a highly karstified aquifer from other aquifers. For instance, the Sp_{21} shows the highest karstification order by using the GIS and

remote sensing approach while the other methods assign it at least 4th except the α_2. The similarity of the order of the α_2 and the GIS is not seen in other aquifers.

To find a probable relationship among these methods, linear and non-linear correlations of the absolute values of them were evaluated. The results show that in all methods, except between the obtained karstification values of the GIS-RS and dynamic volumes of the aquifers, there is no possible relationship among them. In fact, each method is referring to the specific character of a karstic aquifer. For instance, the α_1 is mainly controlled by the conduit system development of an aquifer, which transfers the recharge water from the surface and epikarst to the spring. The α_2 depends upon the matrix-medium interconnection of the aquifer and their exchange rates to the conduits delivering to the springs. The ratio of the α_1:α_2 shows the general proportion of the conduit system to the matrix. The drying time of an aquifer is related to the geometry of the aquifer and storativity of the matrix.

The GIS-RS method mainly regarded the surface parameters of an aquifer and climatic parameters that may enhance the karstification which may not apply for the interior part of it. The ratio of the dynamic volume to the catchment area of the aquifer is related to the surface infiltration rate and precipitation. These parameters are inherently similar to the parameters of the GIS-RS method that cause the high correlation between them (Fig 7).

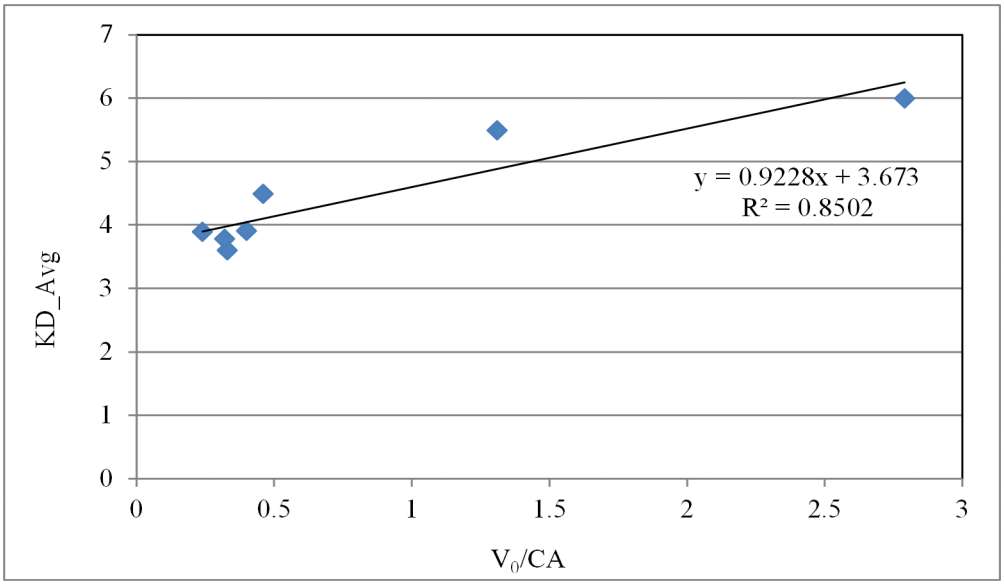

Figure 7. The relationship between the ratio of dynamic volume to catchment area versus KDavg.

Conclusion

The main question of this research was to determine if the surface and interior characteristics of karst aquifers were related in terms of karstification. GIS and remote-sensing methods aimed to assess the surface karst development in the study aquifers. The various methods include the α_1 value of the discharge recession coefficient, α_1: α_2 ratio, the ratio of the quick flows to base flows, the ratio of dynamic storages to the catchment areas, and drying time of springs, were used to assess the interior characteristics of karst aquifers. The comparison of GIS and remote-sensing studies with other methods for evaluating interior karst development indicated that these two processes are completely independent. Moreover, it is observed that the karstification values of the aquifers of the same anticline are not equal or follow the same order, suggesting that each method refers to the specific character of a karstic aquifer. The α_1 and α_2 values are mainly controlled by the conduit system and matrix of an aquifer, respectively. Thus, the ratio of the α_1:α_2 shows the general proportion of conduit system and matrix. The ratio of the quick flow to base flow is a reasonable criterion for karstification so that the higher volume of this ratio indicates higher karstification. The drying time of an aquifer is related to the geometry of the aquifer and storage capacity of the matrix. The most similarity between GIS-RS methods and other methods is its relation to the ratio of dynamic storages to the catchment areas. In fact, the ratio of the dynamic volume to the catchment area of the aquifer is related to the surface infiltration rate and precipitation.

In addition, mapping the degree of karst development in aquifers, based on some effective factors such as thicknesses of soluble rock and tectonic setting, precipitation, vegetation density, temperature, relief, and slope revealed that the orders and effects of these factors on the karstification are not uniform among the aquifers. It should be noted that the GIS-RS method is a comprehensive approach to assess surface karst development on a regional scale. The ability to alter weights on local scales is the main advantage of the GIS-RS method.

References

Aghanabati, A., 2006, Geology of Iran: Tehran, Ministry of Industry and Mines, Geological Survey of Iran, (In Persian) 587 p.

Alavi, M., 2004, Regional stratigraphy of the Zagros Folds-Thrust Belt of Iran and its proforeland evolution: American Journal of Science, v. 304, p. 1–20. https://doi.org/10.2475/ajs.304.1.1.

Ashjari, J., 2007, Classification of Zagros karstic aquifers based on general direction of groundwater flow and physico-chemical properties: [Ph.D. Dissertation]: Shiraz, Iran, University of Shiraz, Iran.

Ashjari, J., Raeisi, E., 2006, Influences of anticlinal structure on regional flow, Zagros, Iran: Journal of Cave and Karst Studies, v. 68, n. 3, p. 118−129.

Barany Kevei, I., 2007, Rules of climate, soils and vegetation development of karstsystem. – Time in Karst, Postojna, Slovenia: Short Scientific Papers. p. 1-4.

Bonacci, O., 1987, Karst Hydrology. Springer Verlag, Berlin, Germany. https://doi.org/10.1007/978-3-642-83165-2.

Bonacci, O., 1993, Karst springs hydrographs as indicators of karst aquifers: Hydrological Sciences Journal, v. 38 no. 1-2, p. 51-62. https://doi.org/10.1080/02626669309492639.

Bonacci, O., Jukic, D., and Ljubenkov, I., 2006, Definition of catchment area in karst: case of the rivers Krčić and Krka, Croatia: Hydrological Sciences Journal, v, 51, no. 4, p. 682-699, https://doi.org/10.1623/hysj.51.4.682.

Brodie, R.S., and Hostetler, S., 2009, A review of techniques for analyzing baseflow from stream hydrographs, Where Waters Meet, Auckland, New Zealand, New Zealand Hydrological Society (NZHS)..

CBRWA, 2012, Ministry of energy. Iranian water resource management: Chaharmahal and Bakhtiari Water Authority, http://www.cbrw.ir.

Chitsazan, M., Karimi Vardanjani, H., Karimi, H., an Charchi, A., 2015, A comparison between karst development in two main zones of Iran: case study—Keyno anticline (Zagros Range) and Shotori anticline (Central Iran): Arabian Journal of Geosciences, v.8, no. 12, p. 10833–10844. https://doi.org/10.1007/s12517-015-1961-x.

Dashti Barmaki, M., Rezaei, M., Ashjari, J., 2016, Recognition of karst hydrology and water resources interaction in Kazerun karstic zones, South of Iran: Arabian Journal of Geosciences. v. 9, no. 54, https://doi.org/10.1007/s12517-015-2092-0.

Ekmekci, M., and Tezcan, L., 2011, Management of karst aquifers under climate change: Implications for sustainable use: Baba, A., et al. (eds.), Climate Change and its Effects on Water Resources, NATO Science for Peace and Security Series C: Environmental Security 3.

Ford, D., and Williams, P., 2007, Karst Hydrogeology and Geomorphology: Chichester, U.K., John Wiley and Sons, Ltd, 562 p. https://doi.org/10.1002/9781118684986.

FRWA, 2012, Ministry of energy. Iranian water resource management: Fars Regional Water Authority, www.frrw.ir/

Huete, A.R., 1988, A soil adjusted vegetation index (SAVI): Remote Sensing of the Environment, v. 25, p. 295−309. https://doi.org/10.1016/0034-4257(88)90106-X.

Jamali, M., Moghimi, E., and Jafarpour, Z., 2015, Geomorphology of karst features of Shiraz City and Arjan Plain and development limitations: International Journal of Environmental, Chemical, Ecological, Geological and Geophysical Engineering, v. 9, no. 1, p. 25−31.

Kalantari, N., Keshavarzi, M.R., Hamidzadeh, F., and Sahebdel, M., 2010, Characteristics of heterogeneous Shimbar Karstic Systems in Southwest Iran: Advances in Research in Karst Media, Part of the Environmental Earth Sciences book series (EESCI), p. 69−74. https://doi.org/10.1007/978-3-642-12486-0_11.

Karami, G.H., Bagheri, B., and Rahimi, F., 2016, Determining the groundwater potential recharge zone and karst springs catchment area: Saldoran region, western Iran: Hydrogeology Journal, v. 24, no. 8, p. 1981–1992. https://doi.org/10.1007/s10040-016-1458-z,

Karimi, H., Raeisi, E., and Bakalowicz, M., 2005, Characterizing the main karst aquifers of the Alvand basin, northwest of Zagros, Iran, by a hydrogeochemical approach: Hydrogeology Journal, v. 13, no. 5–6, p. 787–799. https://doi.org/10.1007/s10040-004-0350-4.

Karimi, H.; Raeisi, E. and Zare, M., 2001, Determination of catchment area of aquifer bearing Tangab dam site using water balance method, *in* Proceedings of the Second National Conference on Engineering Geology and the Environment, Tehran, 16-18 Oct. 2001, v.2, p. 773−755.

Kresic, N., and Bonacci, O., 2010, Spring discharge hydrograph, *in* Kresic, N. and Stevanovich, Z., eds., Groundwater Hydrology of Springs: Engineering, Theory, Management, and Sustainability: Burlington, Mass., Butterworth-Heineman, p. 129–163.

Kullman, E., 2000, Nové metodické prístupy k riešeniu ochrany a ochranných pásiem zdrojov podzemných vôd v horninových prostrediach s krasovo-puklinovou priepustnost'ou (New methods in groundwater protection and delineation of protection zones in fissure-karst rock environment; in Slovak). Podzemná voda, no. 6/2, p. 31–41.

KWPA, 2012, Ministry of energy. Iranian water resource management: Khuzestan Water and Power Authority, http://www.kwpa.ir.

Lowe, D.J, 1992, The origin of limestone caverns: an inception horizon hypothesis, [Ph.D. Dissertation]: Manchester, U.K., Manchester Metropolitan University, 511 p.

Shokri, M., Ashjari, J., and Karami G., 2016, Surface and subsurface karstification of aquifers in arid regions: the case study of Cheshme-Ali Spring, NE Iran: Journal of Cave and Karst Studies, v. 78, no. 1, p. 25–35. https://doi.org/10.4311/2014ES0020.

Maillet, E., 1905, Essais d'hydraulique souterraine et fluviale. Hermann, Paris.

Malík, P., 2007, Assessment of regional karstification degree and groundwater sensitivity to pollution using hydrograph analysis in the Velka Fatra Mts., Slovakia: Water resources and environmental problems in karst: Environmental Geology, v. 51, p. 707–711. https://doi.org/10.1007/s00254-006-0384-0.

Malík, P., and Vojtková, S., 2012, Use of recession-curve analysis for estimation of karstification degree and its application in assessing overflow/underflow conditions in closely-spaced karstic springs: Environmental Earth Science, v. 65, p. 2245–2257. https://doi.org/10.1007/s12665-012-1596-0.

Palmer, A.N., 2000, Hydrogeologic control of cave patterns: Speleogenesis: Evolution of Karst Aquifers, p. 77−90.

Panda, S.S., Ames, D.P., and Panigrahi, S., 2010, Application of vegetation indices for agricultural crop yield prediction using neural network techniques: Remote Sensing, v. 2, p. 673−696. https://doi.org/10.3390/rs2030673.

Pezeshkpour, P., 1991, Hydrogeological and hydrochemical evaluation of Kuh-e Gar and Barm-Firooz springs [M.S. Thesis]: Shiraz, Shiraz University, 282 p.

Raeisi, E., 2002, Carbonate karst caves in Iran Evolution of karst: From prekarst to Cessation, Ljubljana-Postojna, p. 339−344.

Raeisi, E., and Kowsar, N., 1997, Development of Shahpour Cave, southern Iran: Cave and Karst Science, v. 24, no. 1, p. 27–34.

Raeisi, E., and Stevanovic, Z., 2010, Case Study: Springs of the Zagros mountain range (Iran and Iraq), *in* Kresic, N. and Stevanovic, Z., eds., Groundwater Hydrology of Springs, Elsevier, p. 498–515.

Saaty, T. L., 1980, The Analytic Hierarchy Process: New York, McGraw-Hill.

Seif, A. and Ebrahimi, B., 2014, Using GIS to evaluate degree of karstification according to some important factors in carbonate rocks in Iran: Carbonates Evaporites. v. 29, p. 107–126. https://doi.org/10.1007/s13146-014-0189-2.

Shabab Boroujeni, B., 2011, Determination of effective factors on permeability in karstic dams in west of Zagros [M.Sc. Thesis]: Tehran, Iran, Tehran University.

M. Shokri., Ashjari, J., and Karami, G., 2016, Surface and subsurface karstification of aquifers in arid regions: the case study of Cheshme-Ali Spring, NE Iran: Journal of Cave and Karst Studies, v. 78, no. 1, p. 25–35. DOI: 10.4311/2014ES0020.

Stöcklin, J., 1968, Structural history and tectonics map of Iran: a review: American Association of Petroleum Geologists Bulletin, v. 52, no. 7, p. 1229–1258.

Stöcklin, J., 1974, Possible ancient continental margins in Iran, *in* Burk, C.A. and Drake, C.L. eds., The Geology of Continental Margins: New York, Springer-Verlag, p. 873−887. https://doi.org/10.1007/978-3-662-01141-6_64.

White, W.B., 1988, Geomorphology and Hydrology of Karst Terrains: New York, Oxford University Press, 464 p.

S. Riechelmann, S. F. M. Breitenbach, A. Schröder-Ritzrau, A. Mangini, and A. Immenhauser. Ventilation and cave air PCO_2 in the Bunker-Emst Cave System (NW Germany): implications for speleothem proxy data. *Journal of Cave and Karst Studies*, v. 81, no. 2, p. 98-112. DOI:10.4311/2018ES0110

VENTILATION AND CAVE AIR *P*CO_2 IN THE BUNKER-EMST CAVE SYSTEM (NW GERMANY): IMPLICATIONS FOR SPELEOTHEM PROXY DATA

Sylvia Riechelmann[1,C], Sebastian F.M. Breitenbach[1], Andrea Schröder-Ritzrau[2], Augusto Mangini[2], and Adrian Immenhauser[1]

Abstract

Cave air pCO_2 (carbon dioxide partial pressure) is, along with drip rate, one of the most important factors controlling speleothem carbonate precipitation. As a consequence, pCO_2 has an indirect but important control on speleothem proxy data (e.g., elemental concentrations, isotopic values). The CO_2 concentration of cave air depends on CO_2 source(s) and productivity, CO_2 transport through the epikarst and karst zone, and cave air ventilation. To assess ventilation patterns in the Bunker-Emst Cave (BEC) System, we monitored the pCO_2 value approximately 100 m from the lower entrance (Bunker Cave) at bi-hourly resolution between April 2012 and February 2014. The two entrances of the BEC system were artificially opened between 1860–1863 (Emst Cave) and 1926 (Bunker Cave). Near-atmospheric minimum pCO_2 dynamics of 408 ppmv are measured in winter, and up to 811 ppmv are recorded in summer. Outside air contributes the highest proportion to cave air CO_2, while soil, and possibly also ground air, provide a far smaller proportion throughout the whole year. Cave air pCO_2 correlates positively with the temperature difference between surface and cave air during summer and negatively in winter, with no clear pattern for spring and autumn. Dynamic ventilation is driven by temperature and resulting density differences between cave and surface air. In summer, warm atmospheric air is entrained through the upper cave entrance where it cools. With increasing density, the cooled air flows toward the lower entrance. In winter, this pattern is reversed, due to cold, atmospheric air entering the cave via the lower entrance, while relatively warm cave air rises and exits the cave via the upper entrance. The situation is further modulated by preferential south-southwestern winds that point directly on both cave entrances. Thus, cave ventilation is frequently disturbed, especially during periods with higher wind speed. Modern ventilation of the BEC system—induced by artificially openings—is not a direct analogue for pre-1860 ventilation conditions. The artificial change of ventilation resulted in a strong increase of $\delta^{13}C_{speleothem}$ values. Prior to the cave opening in 1860, Holocene $\delta^{13}C_{speleothem}$ values were significantly lower, probably related to limited ventilation due to the lack of significant connections between the surface and cave. Reduced ventilation led to significantly higher pCO_2 values, minimal CO_2 degassing from drip water and low kinetic isotope fractionation. Both modern and fossil speleothem precipitation rates are driven by water supply and carbonate saturation, and not by cave air pCO_2. Today, pCO_2 variability is too small to affect carbonate precipitation rates and the same is likely true for pCO_2 variability prior to artificial opening of the cave. Thus, fossil speleothems from BEC System are likely more sensitive to temperature and infiltration dynamics. The Bunker-Emst Cave System, therefore, represents different ventilation patterns and their influence on speleothem proxy data in an exemplary manner, and it may serve as a template for other cave systems.

Introduction

Over the last two decades, paleoclimate reconstructions based on speleothems increased significantly in number and hind-casting value (Henderson, 2006). Precise ^{230}Th/U dating and single or multi-proxy geochemical approaches allow for detailed paleoclimate reconstructions (Fairchild and Baker, 2012). A wide range of processes in the soil, epikarst (the uppermost zone of the karst in contact with the soil; Bakalowicz, 2012; Fairchild and Baker, 2012), and karst zone, as well as fractionation dynamics, can alter proxy data. To gain a better and quantitative understanding of the processes involved, sophisticated monitoring programs have been established (Spötl et al., 2005; Mattey et al., 2008, 2010, 2016; Riechelmann et al., 2011, 2017; van Rampelbergh et al., 2014; Breitenbach et al., 2015; Ridley et al., 2015; Czuppon et al., 2018). In this context, a large variety of parameters have been recorded, including surface, soil, and cave air temperature, air pressure, ^{222}Rn, pCO_2 (carbon dioxide partial pressure) and humidity, as well as the geochemical composition of rain, soil, and dripwater. Data obtained from such monitoring programs were placed in context with recent carbonate precipitates or speleothems (Miorandi et al., 2010; Tremaine et al., 2011; Riechelmann et al., 2013, 2014; Rossi and Lozano, 2016).

pCO_2 values of cave air are generally elevated relative to the outside air (Spötl et al., 2005; Baldini et al., 2006; Riechelmann et al., 2011; Breecker et al., 2012; Mattey et al., 2016). CO_2 plays an essential role in speleothem carbonate precipitation (besides the degree of carbonate supersaturation of the dripwater and water supply), as well as on the

[1]Ruhr-University Bochum, Institute of Geology, Mineralogy and Geophysics, Universitätsstraße 150, D-44801 Bochum, Germany
[2]Ruprecht-Karls-University Heidelberg, Institute of Environmental Physics, Im Neuenheimer Feld 229, D-69120 Heidelberg, Germany
[C]Corresponding author: Sylvia.Riechelmann@rub.de

fractionation and incorporation of isotopic and elemental signatures in speleothems (Dreybrodt, 1988, 2008; Baldini et al., 2006; Banner et al., 2007; Lechleitner et al., 2016; Pu et al., 2016). Thus, recording cave air pCO_2 is critical for those interested in assessing speleothem precipitation behavior and proxy dynamics.

Generally applied concepts imply that rainwater infiltrating the soil zone absorbs plant- and microbial-derived CO_2 and constitutes a main source for CO_2 in caves. Carbonic acid is produced in the soil and subsoil, dissociates to hydrogen carbonate, and is transported into the cave via fissures in the host rock. Low cave air pCO_2 values, relative to the pCO_2 of the dripwater, facilitate CO_2 degassing, with higher CO_2 gradients, leading to higher precipitation rates of calcium carbonate polymorphs (Bögli, 1978; Hammerschmidt et al., 1995; Fairchild and Baker, 2012). A long-underestimated CO_2 source is ground air, which exists in gaseous form in the karst vadose zone and is transported into the cave system via fissures, fractures, and pore-space of the rock. More recent studies revealed that ground air is most likely the main source of cave air CO_2 rather than soil air (Mattey et al., 2010, 2016; Baldini et al., 2018). CO_2 ground air is produced by microbial oxidation of organic matter in infiltrating water, as revealed by radiocarbon measurements, hinting on CO_2 derived from the decay of old carbon and elevated $\delta^{13}C_{CO2}$ values (e.g., Atkinson, 1977; Wood, 1985; Noronha et al., 2015; Mattey et al., 2016). Cave lakes or stream water, biological productivity in the cave, and hydrothermal CO_2 can act as additional CO_2 sources for cave air CO_2 (James, 1977; Baldini, 2010; Fairchild and Baker, 2012).

Cave air pCO_2 depends on the CO_2 productivity of its source, and cave ventilation processes (Fairchild and Baker, 2012; Breitenbach et al., 2015; Lechleitner et al., 2016). Cave ventilation also influences speleothem isotope composition and growth dynamics, hence also trace element incorporation into carbonate. Ventilation can be classified into different types by physical mechanisms: cave breathing, with air pressure differences driving air exchange, wind-induced air flow, chimney circulation driven by air density differences (temperature; at least two cave entrances), convection, either forced or free, due to differences in air density, and water-induced air flow (Fairchild and Baker, 2012). These processes can act from hourly to multi-annual timescales (Fairchild and Baker, 2012). Microclimate monitoring in caves is rarely conducted at excessively high resolution (Tremaine et al., 2011; Breitenbach et al., 2015; Ridley et al., 2015), and, due to logistical limitations, sampling at weekly to monthly intervals still prevails (Spötl et al., 2005; Banner et al., 2007; Riechelmann et al., 2011).

Here, we present results from a two-year-long and bi-hourly resolved monitoring of cave air pCO_2, and air temperature in the Bunker-Emst Cave System. Physico-chemical data from modern carbonate precipitates on watch glasses, and speleothem data complement the monitoring dataset. The results are compared with meteorological data to identify the ventilation processes and their physical drivers, document changes in cave air pCO_2 at different timescales, and determine the impact of CO_2 dynamics on speleothem precipitation and geochemical proxies in the Bunker-Emst Cave System.

Cave Setting and Monitoring Protocol

The Bunker-Emst Cave (BEC) System is located in the Rhenish Slate Mountains in the NW part of the Sauerland, Germany between the towns of Iserlohn and Letmathe (Fig. 1). This system has two south-oriented entrances. The entrance of Bunker Cave is the lower one of the 3.5 km long BEC System and is located at 184 meters above sea level (m a.s.l.) at 51°22'N and 07°40'E (Fig. 2A). The Emst Cave entrance is located 197 m a.s.l. (Fig. 2A), thus is 13 m higher and was opened from 1860 to 1863, during railway constructions, while Bunker Cave was opened in 1926 during road construction (Grebe, 1993; Hammerschmidt et al., 1995).

Automatic logging of cave pCO_2 and cave air temperature was conducted from April 2012 to February 2014 with the monitoring device CORA, equipped with a non-dispersive infrared (NDIR) sensor (Luetscher and Ziegler, 2012). The long-term precision of pCO_2 measurements is $\pm$ 1.6 %, with $\pm$ 3 % accuracy. A bi-hourly measuring interval was chosen to allow detection of diurnal variability. CORA was installed in the Photographer's Chamber (forming part of Chamber 2; Fig. 2), located at a distance of ca. 100 m from the Bunker Cave (lower) Entrance. Gaps in the record are due to technical problems during the monitoring period.

Two drip-site monitoring setups with watch glasses were placed in Chamber 1 (TS 1 / U I) and Chamber 2 (TS 8 / U IV; Fig. 2). Drip rate and dripwater saturation indices with regard to calcite, as well as carbonate precipitation rates on the watch glasses, and $\delta^{13}C$ and $\delta^{18}O$ of precipitated carbonates were measured or calculated. Additionally, soil air was sampled using fixed soil gas lances. Soil air was analyzed for its CO_2 concentration and $\delta^{13}C_{CO2}$ value. Details on measurement protocols and analyses can be found in Riechelmann et al. (2011, 2013, 2014, 2017).

Instrumental climate data of the meteorological station Hemer (51°23'N, 07°45'E, 200 m a.s.l.; www.meteogroup.com; Fig. 1), located ~7 km northeast of BEC system, are used at hourly resolution (temperature (°C), wind direction (°) and wind velocity (km h^{-1})). Calculated standard deviations of mean values of all above mentioned parameters are given as 1σ.

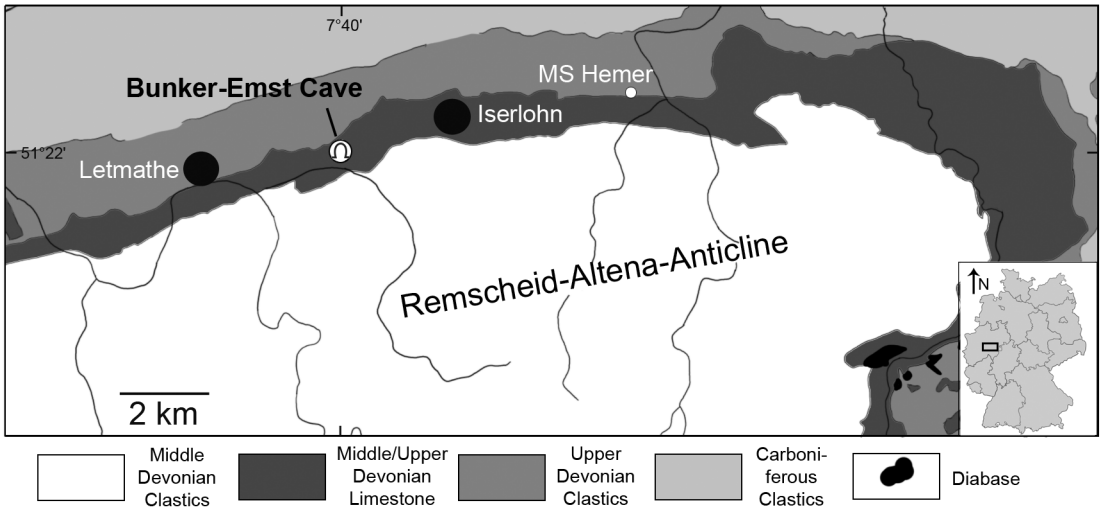

Figure 1. Geological map with the location of Bunker-Emst Cave System and the meteorological station (MS) Hemer.

Results

Cave Air pCO_2 Concentration

Bunker-Emst Cave pCO_2 values measured with the CORA logger show a long-term mean of 519 ± 84 ppmv; n = 5248). Seasonal variations display lower pCO_2 values in winter (DJF; mean: 490 ± 29 ppmv, n = 890) and spring (MAM; mean: 454 ± 19 ppmv, n = 1588), and higher values in summer (JJA; mean: 589 ± 89 ppmv, n = 1760) and autumn (SON; mean 527 ± 74 ppmv, n = 1009) months (Fig. 3A). Minimum pCO_2 values for all seasons range from 408 to 436 ppmv, whereas maximum values are highest in summer (811 ppmv) and autumn (716 ppmv), and lowest in winter (558 ppmv) and spring (598 ppmv). Consequently, the maximal seasonal amplitude of pCO_2 values is higher in summer (375 ppmv) and autumn (300 ppmv) than in winter (137 ppmv) and spring (190 ppmv) months.

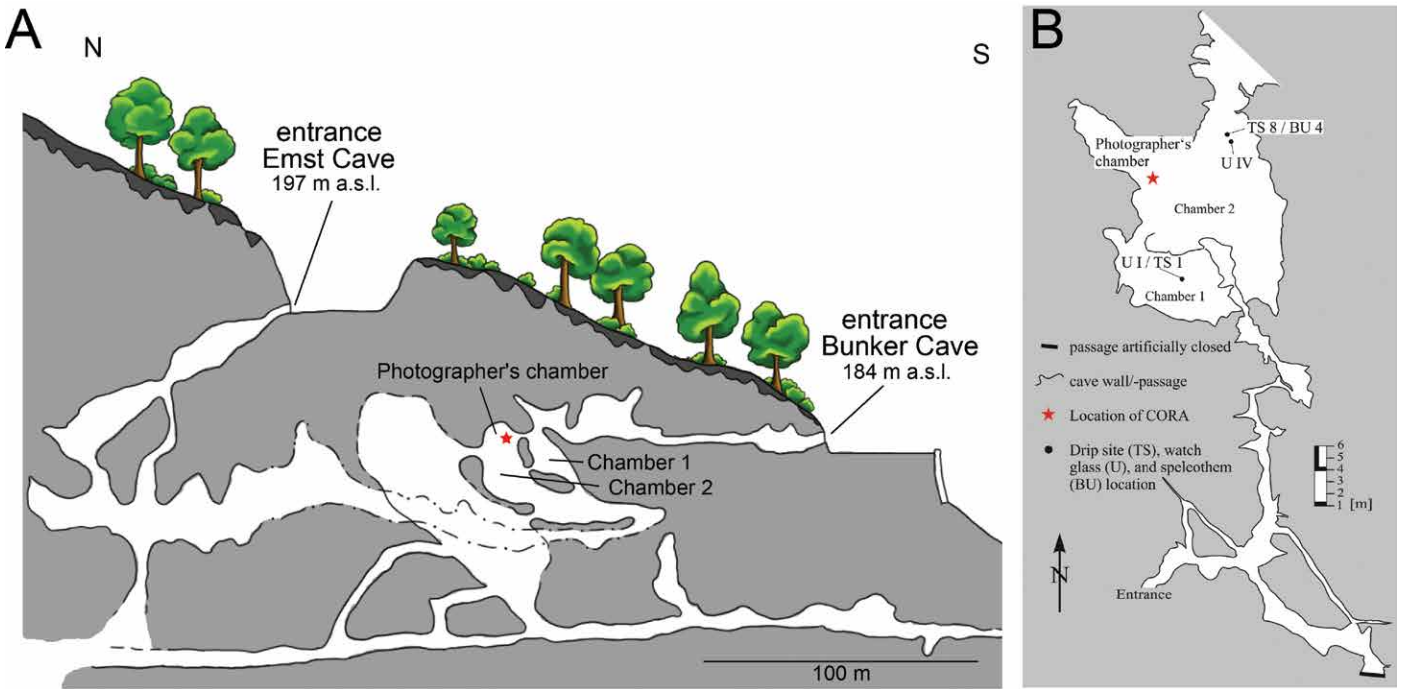

Figure 2. **(A)** Vertical profile indicating the Photographer's Chamber with the location of the CO_2 logger CORA, and the chambers 1 and 2 of previous monitoring (Riechelmann et al., 2011). **(B)** Map of BEC System with the locations of the CO_2 logger CORA in the Photographer's Chamber and of the drip and watch glass sites TS 1 / U I (Chamber 1) and TS 8 / U IV and speleothem BU 4 in Chamber 2.

Monthly pCO_2 values vary irregularly from 10 to 160 ppmv over several days up to a few weeks (Fig. 4). Significant pCO_2 variations are observed at a diurnal scale, although these patterns are detectable only for a range of a few days, up to a week (Fig. 4). The most obvious examples for strong, diurnal variations were recorded in March and July 2013. In March 2013 pCO_2 values increased from midnight toward morning, then decreased until the next evening, before they increased again during the next night (Fig. 5A). The opposite behavior is observed in July 2013 (Fig. 5B). A pattern similar to the one observed in March 2013 occurs mostly during the winter months, whereas during summer months, a pattern similar to that in July 2013 is observed. During spring and autumn months, both the winter and the summer patterns can be ob-

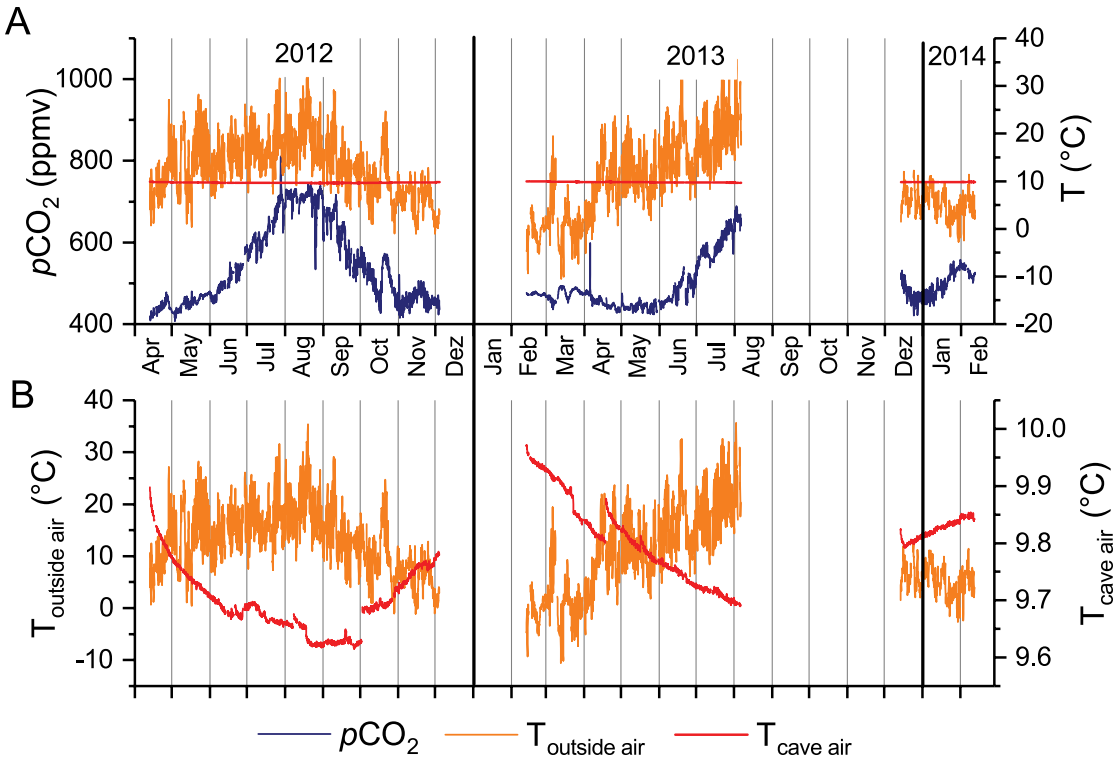

Figure 3. **(A)** Outside air temperature and cave air pCO_2 and temperature at BEC (April 2012 to February 2014). **(B)** Outside air and cave air temperature. Note the anti-correlation between both curves.

served, respectively. Diurnal pCO_2 amplitudes reach 10 ppmv to 50 ppmv. Besides the variations described above, significant decreasing pCO_2 values with amplitudes of up to 150 ppmv can be observed within a few hours. Such decreasing events were particularly pronounced in August 25, 2012 (150 ppmv) and August 26, 2012 (100 ppmv) (Fig. 6) and July 30−31, 2013 (50 ppmv) (Fig. 4).

Surface and Cave Air Temperatures

The climate of NW Germany is temperate, with no distinct dry season and warm

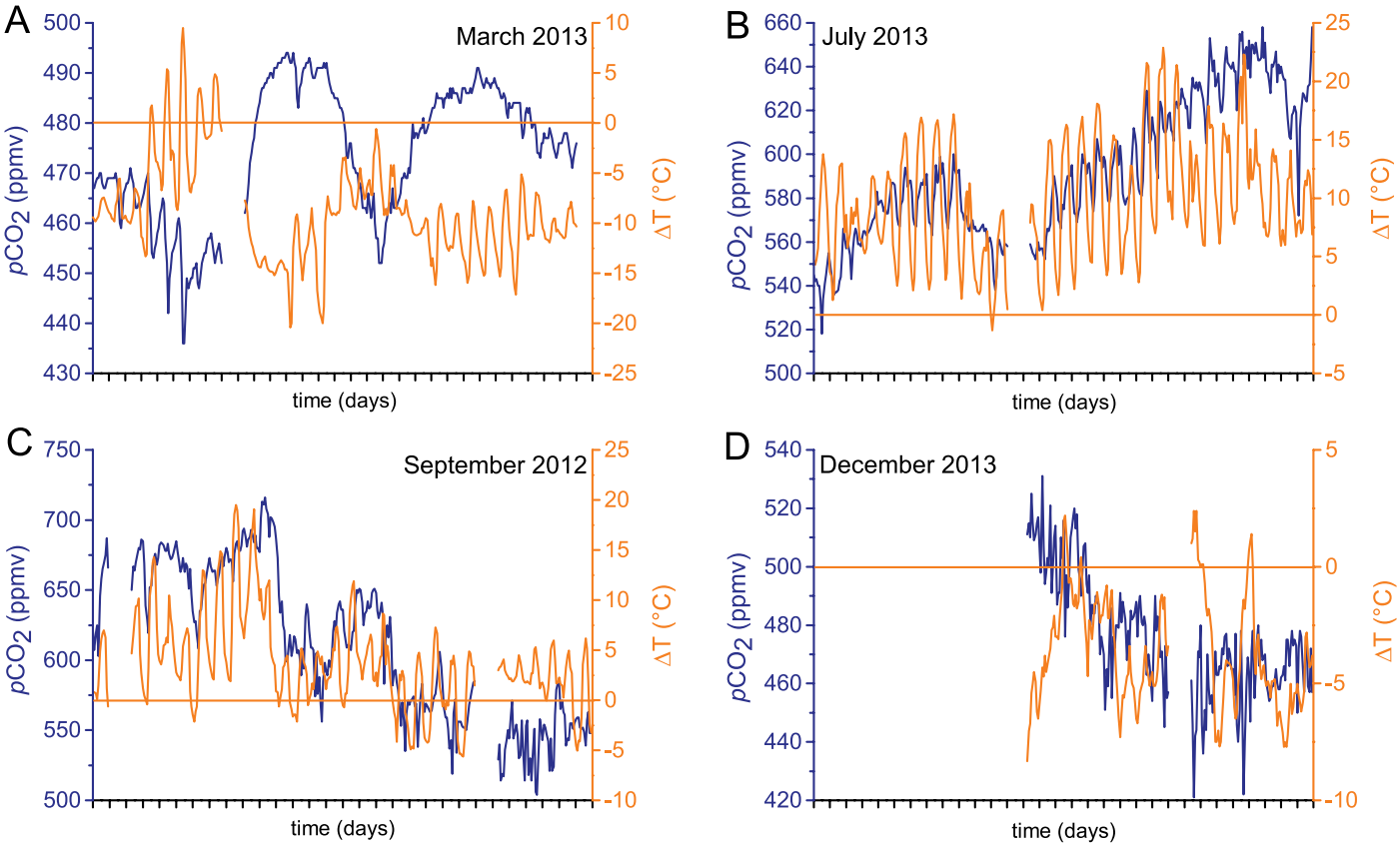

Figure 4. Variations of pCO_2 and ΔT in **(A)** spring (March 2013), **(B)** summer (July 2013), **(C)** autumn (September 2012) and **(D)** winter (December 2013). Note positive ΔT values (cave air colder than outside air) in summer and mostly negative ones (cave air warmer than outside air) in winter, while in spring and autumn both positive and negative ΔT values occur.

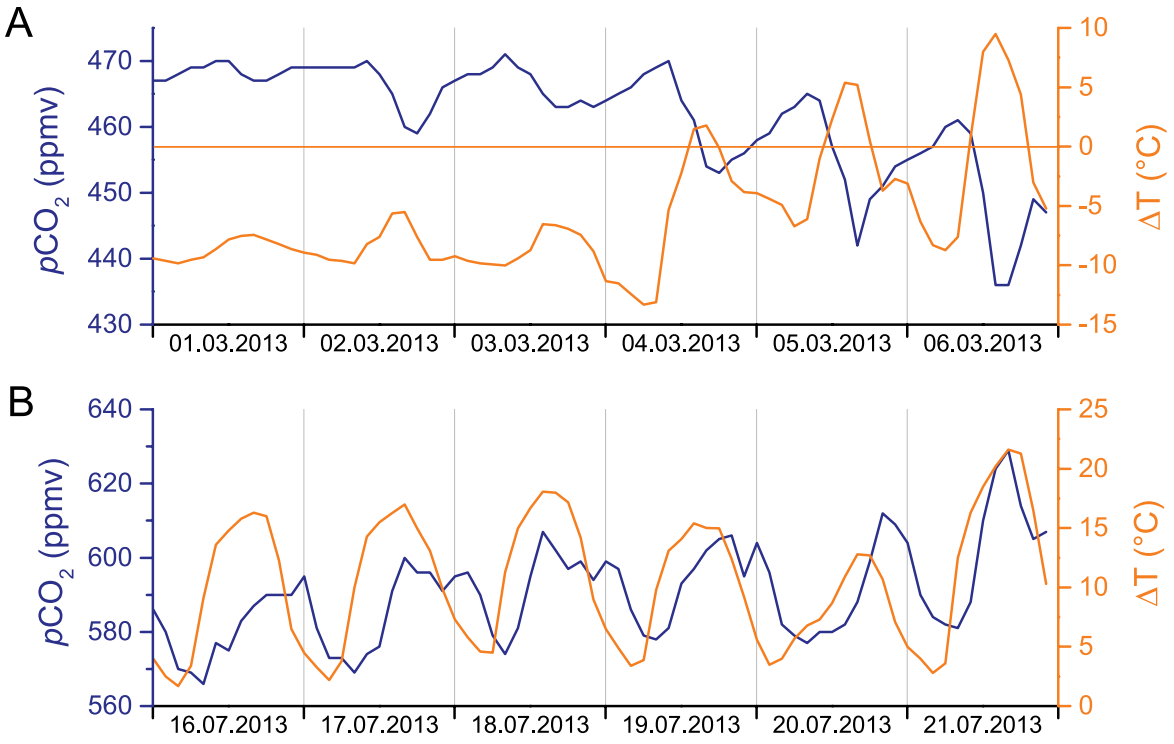

Figure 5. Variations of pCO_2 and ΔT at diurnal scale in **(A)** March 2013 and **(B)** July 2013. Note the anti-correlation between pCO_2 and ΔT in March and the correlation in July with a small time lag.

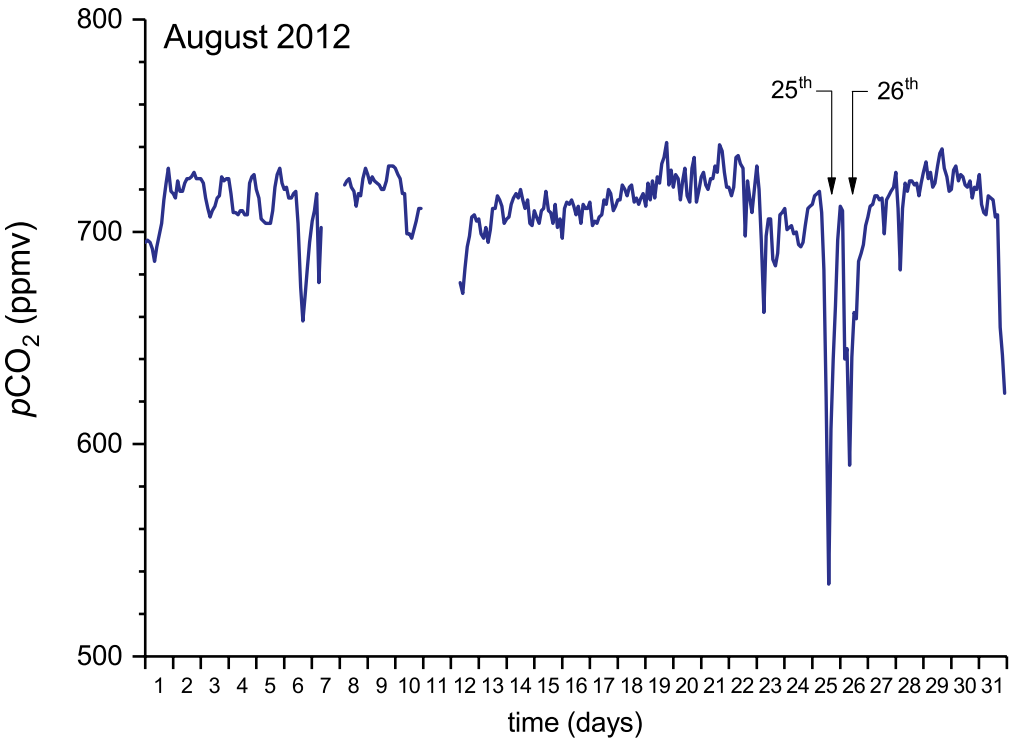

Figure 6. Variations of pCO_2 in August 2012. Note the strong decreases in pCO_2 during the August 25−26, 2012 period.

summers. Mean air temperature of the warmest month is below 22 °C, and more than four months have temperatures > 10 °C (Cfb climate in the Köppen classification, Peel et al., 2007). Over the monitoring period, outside air temperature ranges from −11.0 °C (March 2013) to 35.7 °C (August 2013), with a mean of 10.0 ± 7.4 °C (n = 16,771; Fig. 3). Seasonal variations display lower temperatures in winter (DJF; mean: 3.4 ± 4.1 °C, n = 4320) and higher temperatures in summer (JJA; mean: 17.4 ± 5.2 °C, n = 4416). Spring (MAM; mean: 8.9 ± 6.9 °C, n = 3672) and autumn (SON; mean: 10.0 ± 5.3 °C, n = 4363) months display temperatures close to the yearly mean.

Cave air temperature ($T_{cave\ air}$) is rather constant compared to outside air temperature ($T_{outside\ air}$) with a mean of 9.8 ± 0.1 °C (n = 5248) (Fig. 3A). The difference between maximum (10.0 °C; February 2013) and minimum $T_{cave\ air}$ (9.6 °C; August and September 2012) recorded values of 0.4 °C (Fig. 3B). Lowest $T_{cave\ air}$ values are observed in summer and autumn, while the highest values occur in winter and spring (Fig. 3B). The difference between $T_{outside\ air}$ and $T_{cave\ air}$ is:

$$\Delta T = T_{outside\ air} - T_{cave\ air} \quad (1)$$

Negative ΔT values indicate warmer conditions in the cave, compared to surface conditions, and *vice versa*. Positive ΔT values are mainly observed in summer, while ΔT is usually found to be negative in winter (Fig. 4). In spring and

autumn, Δ*T* switches between positive and negative values over weeks and even within a day (Figs. 4 and 5). Diurnal Δ*T* changes are also observed for all seasons, with decreasing values at night and increasing ones during daytime (Figs. 4 and 5). Although this pattern is mostly well pronounced (e.g., July 2013, Fig. 4), irregular patterns may occur. An example of an irregular pattern was recorded in December 2013 (Fig. 4).

Wind Directions and Velocity

Winds above the cave are characterized by preferential southerly to westerly directions (Fig. 7B-C). The mean wind direction from April 2012 to February 2014 is 193° ± 83° (i.e., SSW; n = 16,769). Mean wind directions vary between southerly directions in winter and spring, and SSW directions in summer and autumn. Only during February and March 2013, the wind blew mainly from northern to eastern directions (Fig. 7A). The mean wind velocity was 9.2 ± 5.1 km h^{-1} (n = 16,769), with a maximum of 35.2 km h^{-1} (December 2013). Wind velocities are lower during summer (JJA; mean 7.7 ± 4.0 km h^{-1}, n = 4416) and higher in winter (DJF; mean: 11.4 ± 6.0 km h^{-1}, n = 4320; Fig. 7). Spring and autumn months display intermediate, mean wind speeds (MAM: 9.2 ± 4.8 km h^{-1}, n = 3672; SON: 8.4 ± 4.8 km h^{-1}, n = 4361; Fig. 7).

Dripwater and Carbonate Precipitates

Drip sites TS 1 / U I and TS 8 / U IV have been monitored (from 2006 to 2013) to evaluate carbonate precipitation rate dynamics. Here, data from 2012 to 2013, i.e., the same time interval as the pCO_2 monitoring, is presented. Drip rates, SI_{Cc} and carbonate precipitation rates are higher for site TS 1 / U I compared to site TS 8 / U IV (Fig. 8). At both watch glass sites, precipitation rates are higher during winter and spring and lower during summer and autumn (Fig. 8). At TS 1, water supply (drip rate) is highest in spring, whereas drip rates are rather constant at site TS 8. At site TS 1, the SI_{Cc} displays an increasing trend over the monitoring period, while at site TS 8 SI_{Cc} shows highest values in spring and summer (Fig. 8). Carbonates precipitated at site TS 1 / U I display lower $\delta^{18}O$ and $\delta^{13}C$ values in contrast to precipitates at site TS 8 / U IV (Fig. 9A). Generally, $\delta^{18}O$ and $\delta^{13}C$ values of carbonate precipitates on watch glasses are higher in winter and spring, but the variability of data is relatively small (Fig. 9A).

Interpretation and Discussion

Heat Transport Mechanism

The Bunker-Emst Cave air temperature is close to the mean annual outside air temperature and the seasonal cave air temperature pattern is close to a sinusoidal curve (Fig. 3). This implies that heat conduction is the main factor influencing cave air temperature. Thereby, the outside air temperature is recorded by the soil and transmitted to the host rock (e.g., Pollack and Huang, 2000; Smerdon et al., 2006). The transport mechanism of heat conduction through the host rock depends on its thermal

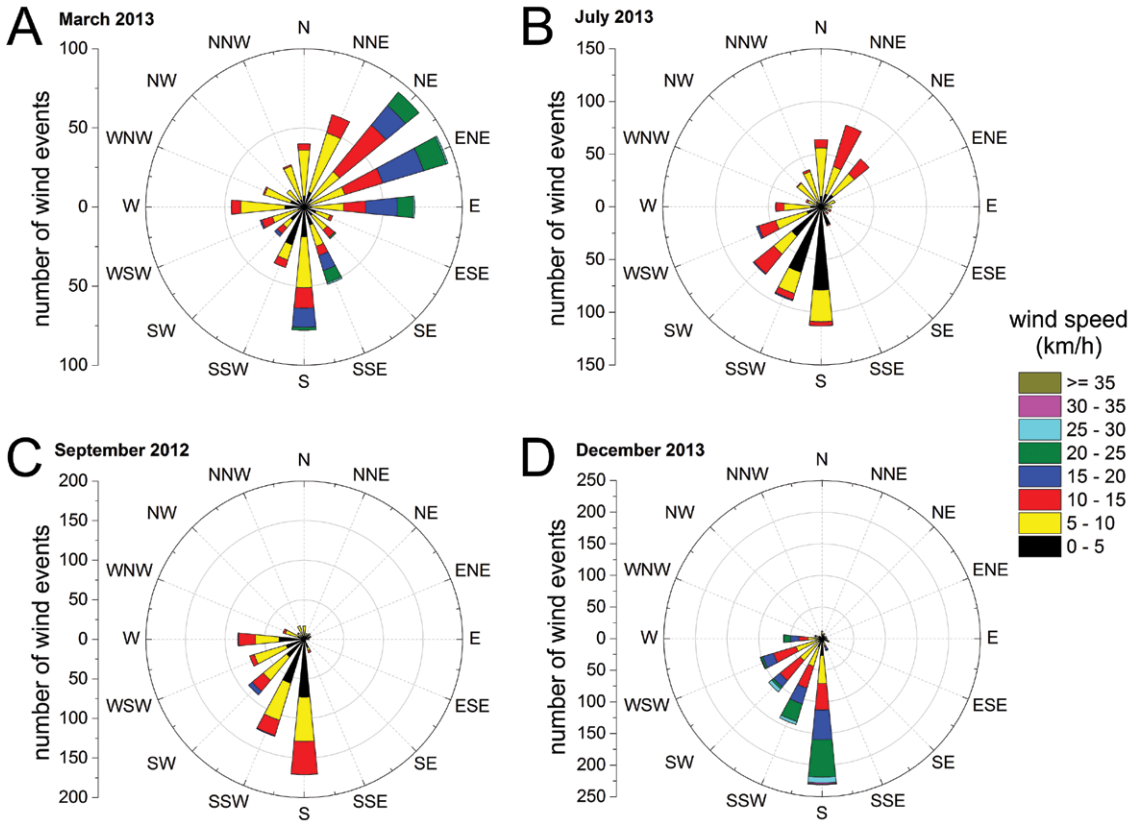

Figure 7. Wind directions, number of wind events and respective wind speed in **(A)** spring (March 2013), **(B)** summer (July 2013), **(C)** autumn (September 2012) and **(D)** winter (December 2013). Higher wind speeds occur mostly in winter months and occasionally in spring and autumn. Southern to western directions are the preferred wind directions.

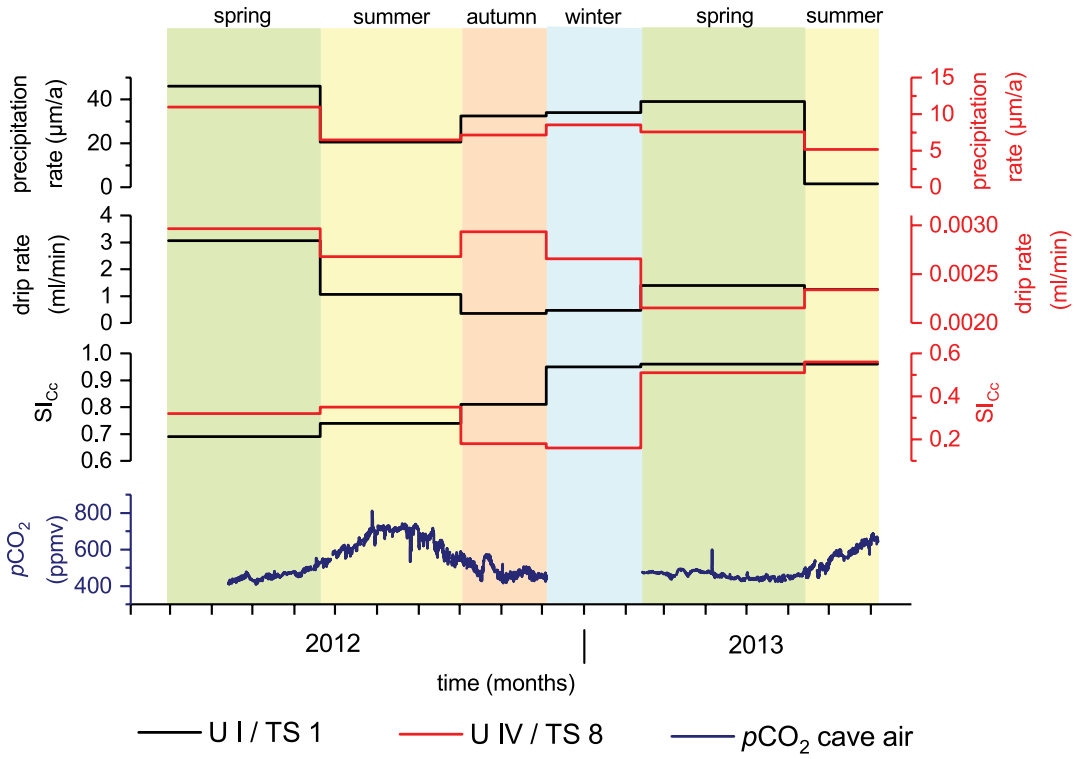

Figure 8. Carbonate precipitation, drip rate and saturation index of calcite of recent watch- glass precipitates (U I and U IV) and their respective drip waters (sites TS 1 and TS 8) as well as cave air pCO_2.

diffusivity, resulting in a time lag between outside air and cave air temperature. Inverse temperature curves of outside and cave air (Fig. 3B) suggest a time lag of approximately six months. Nevertheless, such short time lags are only observed for very shallow portions of the cave (< 5 m in depth; Domínguez-Villar, 2012), whereas the rock overburden of the photographer's chamber, the main study site documented in this paper, is on the order of 15 to 30 m (Grebe, 1993). Under these conditions, a time lag of several years is expected. Heat advection induced by ventilation adds additional noise to the cave air temperature record, resulting in an asymmetrical curve (Domínguez-Villars, 2012). In BEC, this is best observed between June to September 2012 (Fig. 3B). The total contribution of heat advection is, however, small due to the relatively small entrances. Therefore, the authors conclude that $T_{cave\ air}$ is mainly influenced by heat transferred by conduction, and on a smaller scale by heat advection due to ventilation.

Cave Air CO_2 Sources

Compared to other caves worldwide, the BEC System displays relatively low cave air pCO_2 values (Spötl et al., 2005; Baldini et al., 2006; Banner et al., 2007; Cowan et al., 2013; Pla et al., 2016; Pu et al., 2016). Previous CO_2 mea-

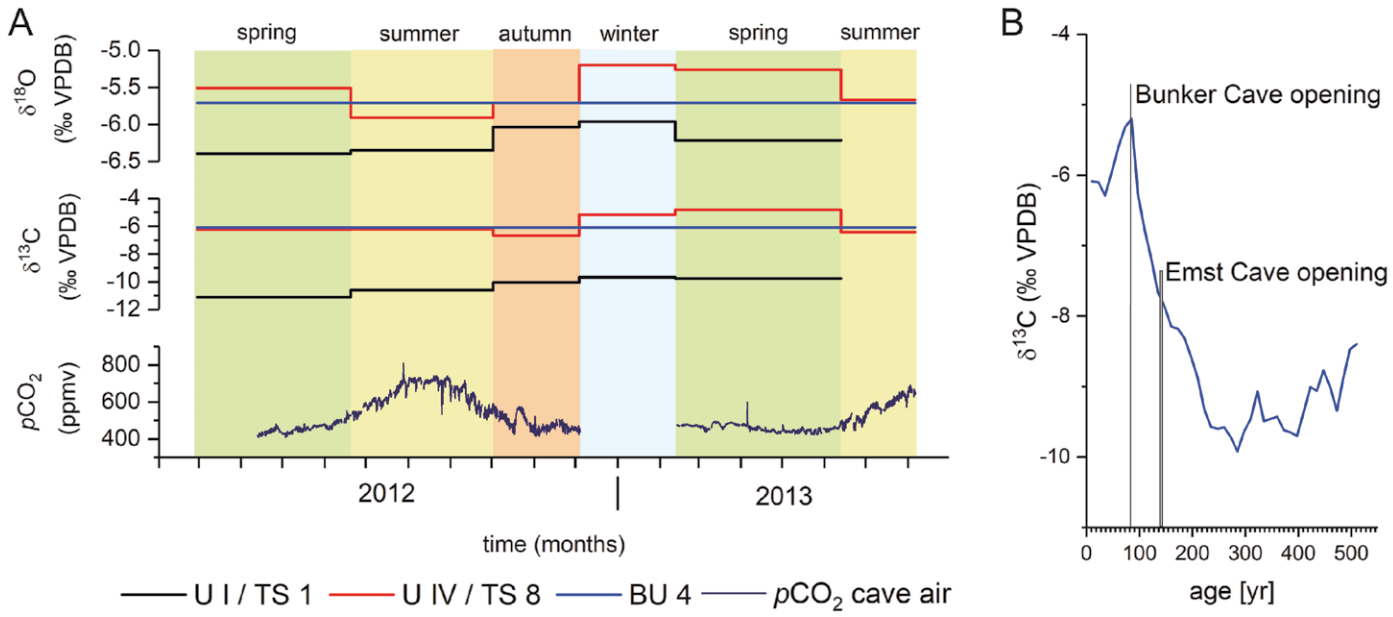

Figure 9. **(A)** Oxygen and carbon isotope values of modern watch-glass precipitates (U I and U IV) and of the most recent part of speleothem BU 4, as well as cave air pCO_2. Note that oxygen and carbon isotopic composition of BU 4 corresponds to that of watch glass U IV. **(B)** Carbon isotope signatures of the last 500 years of speleothem BU 4. The opening of both cave entrances is marked. Data are from Fohlmeister et al. (2012).

surements in Chamber 1, Chamber 2, and the Photographer's Chamber in Bunker Cave (Fig. 2) revealed CO_2 concentrations between 580 to 1200 ppmv (Riechelmann et al., 2011). These are higher than those measured in the current study. This discrepancy is assumed to be a methodological artifact, since Riechelmann et al. (2011) measured with a hand-held device during the monthly monitoring tours, and contamination of cave air with human breath could not be fully excluded in the narrow cave chambers. Consequently, we assume the CO_2 data of the current study to be more representative of the CO_2 variability in the BEC System than the previous measurements. pCO_2 values in winter and spring (minimum 408 ppmv) in BEC System are only slightly higher than outside air values, while summer and autumn in-cave pCO_2 values are slightly elevated (up to 811 ppmv; Fig. 3A). Hence, the relatively low pCO_2 values observed throughout the year in the BEC System suggest a continuous exchange between cave and outside air (~398 ppmv (2012−2014); air monitoring station *Schauinsland*, Germany; German Federal Environmental Agency, 2018). Nevertheless, an independent source introducing CO_2 to the cave air is required to explain the higher summer and autumn pCO_2 values. There is no evidence for CO_2 degassing from cave lakes or streams and hydrothermal CO_2 in the BEC System (Riechelmann et al., 2011). CO_2 produced by microbial activity, however, in the cave was not assessed, so this might represent a possible, but poorly quantified, source of CO_2. The most likely sources of CO_2 in the BEC System and its seasonal variability, however, are increased soil zone activity in summer, driven by higher temperatures and soil humidity (e.g., Tremaine et al., 2011; Ek and Godissart, 2014), or seasonal, varying ground air produced by microbial activity in the vadose karst zone being introduced into the cave system (Mattey et al., 2010, 2016; Baldini et al., 2018).

Previous work, taking measurements of the $\delta^{13}C_{CO2}$ of soil air above BEC System, suggested a mean value of −22 ‰ (Riechelmann et al., 2011). This relatively high value might be due to a methodological offset. The portable soil gas probe, used by Riechelmann et al. (2011) for sampling, might have contaminated the sample with surface air (with a mean value of ~ −8 ‰). Sampling with a fixed soil gas lance gave $\delta^{13}C_{CO2}$ values of up to −28 ‰ for soil air, suggesting C3 plants as a source for soil air CO_2. The $\delta^{13}C$ values of C3 plant respiration varies between −22 ‰ to −35 ‰ with a mean value of −27 ‰ (e.g., Bender, 1971; O'Leary, 1988; Madhavan et al., 1991; Glaser, 2005). Soil zone CO_2 is delivered to the cave system via dripwater, and additionally through open cracks and fissures in the host rock (Baldini et al., 2006). Ground air is another alternative source for cave air pCO_2. Being mainly produced in the vadose zone of karst aquifers, gaseous ground air CO_2 is transported via fissures, fractures, and pore-space of the rock (e.g., Atkinson, 1977). Modelled and measured $\delta^{13}C_{CO2}$ rates of gaseous ground air (in boreholes) suggest values between −24 ‰ and −18 ‰ (Benavente et al., 2010; Mattey et al., 2016). In the BEC system, cave air pCO_2 $\delta^{13}C$ values vary between −14 ‰ and −17 ‰. On the basis of the $\delta^{13}C_{CO2}$ values, it cannot be established which is the lower endmember source (ground air or soil air CO_2). In previous work, Riechelmann et al. (2011) suggested that Bunker Cave air represents an admixture between soil air and outside air. Baldini et al. (2018), in contrast, suggested ground air as an additional source for cave air in several cave sites worldwide (including Bunker Cave). Because ground air CO_2 concentrations are often very high, and range between 12,000 to 70,000 ppmv (occasionally even higher than soil air CO_2 concentrations; e.g., Atkinson, 1977; Benavente et al., 2010; Hendry and Wassenaar, 2005; Baldini et al., 2018), the contribution of ground air to cave air pCO_2 is expected to be small, in view of the low cave air CO_2 concentrations. Soil air CO_2 concentrations reach up to 11,000 ppmv above the BEC System (Riechelmann et al., 2011); thus, the contribution of soil air to cave air can also be expected to be small.

Mattey et al. (2016), reported large seasonal CO_2 variations in boreholes. Exceptions included only the deepest portions of these boreholes, where no difference between summer and winter month values was found. Consequently, seasonal variation of cave air pCO_2 can be explained by seasonal variations in soil air or ground air. Because ground air is so much more enriched in CO_2 compared to soil air, and cave air displays such low concentrations, we argue that the fraction of soil air contributing to cave air is higher than the fraction of ground air. Although, both have to be low compared to the fraction of outside air. By applying a simple mass balance, the fractions of outside air and soil air (ground air) can be estimated. The following equation is used here:

$$F_{\text{outside air}} \times CO_{2\,\text{outside air}} + F_{\text{soil air}} \times CO_{2\,\text{soil air}} = 1 \times CO_{2\,\text{cave air}} \quad (2)$$

where

$$F_{\text{soil air}} = 1 - F_{\text{outside air}} \quad (3)$$

$$F_{\text{outside air}} = \frac{(CO_{2\,\text{cave air}} - CO_{2\,\text{soil air}})}{(CO_{2\,\text{outside air}} - CO_{2\,\text{soil air}})} \quad (4)$$

where $F_{\text{outside air}}$ is the fraction of the outside air, $F_{\text{soil air}}$ is the fraction of soil air, and CO_2 refers to the CO_2 concentrations of each air type. Calculations were made for winter (DJF) and summer (JJA), using the mean CO_2 cave air values of these months as described above. The CO_2 concentration of outside air is assumed to be 398 ppmv (2012–2014; air

monitoring station Schauinsland, Germany; German Federal Environmental Agency, 2018), whereas soil air CO_2 concentration is 1170 ppmv in winter and 6600 ppmv in summer. This results in a mixing of 88 % outside air and 12 % soil air (or ground air) in winter and 97 % outside air and 3% soil air (or ground air) in summer. When inserting the minimum pCO_2 value in winter (408 ppmv) and the maximum pCO_2 value in summer (811 ppmv) in the above equations, a fraction of 99 % outside air in winter and 93 % outside air in summer results. We conclude that the main contribution to cave air is outside air, while soil and ground air represent a far smaller proportion. Hence, the ventilation in BEC System is generally well developed.

Ventilation Systematics in Bunker-Emst Cave System

Due to its two entrances, the BEC System exhibits a dynamic ventilation *sensu* Geiger (1961), and with the entrances being on different levels (13 m vertical difference), chimney circulation is suggested as the possible ventilation mechanism. This is supported by the observed airflow directions in the narrow passage connecting the Bunker Cave Entrance with Chamber 1 (Fig. 2), as measured during the monitoring tours. During summer months, the preferential direction was an outflow through the lower entrance, whereas during winter months, we observed inflow of air through the lower entrance. Particularly during very cold days (−10 °C to 0 °C), ascending warm, humid air could be detected at the upper Emst Cave Entrance. Since the logging device is close to the lower entrance and on a similar altitude with it, the ventilation concept applies only for passages and chambers near the two entrances, where cave and outside air interact and coalesce (Tremaine et al., 2011; McDonough et al., 2016). We would like to emphasize that the pCO_2 levels and ventilation systematics of deeper parts of the BEC System remain poorly constrained at present, since no monitoring of these portions of the cave has been performed. We assume, however, that the deeper parts of the cave have higher CO_2 concentrations because of significantly reduced ventilation in these passages. In contrast, increasing amounts of ground air are observed in other cave systems (Baldini et al., 2006, 2018; Mattey et al., 2016).

Chimney circulation is driven by air density gradients between outside and cave air. These, in turn, are governed by air temperature differences (Fairchild and Baker, 2012). Another possible driving factor is a pressure difference induced by the altitude gradient of the cave entrances. This scenario, however, seems unlikely because the altitude difference is too small, and pressure differences above the cave (on level with Emst Cave Entrance) relative to such taken inside the cave revealed no difference. As outlined above, positive ΔT values imply warm outside air and cold cave air, which is the usual pattern during summer months. Conversely, during winter, the cave is warmer than the land surface and ΔT values are negative (Fig. 3). Monthly (and diurnal) ΔT values and cave air pCO_2 are mostly positively correlated in summer, and negatively in winter, whereas autumn and spring months show both positive and negative correlations (Table 1). We conclude that pCO_2 variations are driven by temperature (density) differences.

Generally, two different ventilation regimes can be discerned: a summer (positive ΔT values and positive correlation) and a winter (negative ΔT values and negative correlation) pattern. During summer (Fig. 4 and Table 1), warm surface air enters the upper entrance. The air cools down while passing through the cave, and hence, its density increases, resulting in outflowing colder air through the lower entrance (Fig. 10A). During winter months, this pattern is reversed; cold and dense surface air enters through the lower entrance. After warming in the cave, this air mass ascends toward the upper entrance, where it leaves the cave (Fig. 10B). In spring and autumn, ventilation switches back and forth, depending on ΔT, at monthly to daily timescales. During these transitional periods, surface temperatures can be warmer than cave air temperatures during day, but colder during the night. Furthermore, ventilation can stagnate if ΔT values are close or equal to zero, reflected in lacking correlation between pCO_2 and ΔT (Table 1). However, increasingly negative or positive ΔT values result in higher variations of pCO_2 due to intensified ventilation. Similar ventilation patterns were also observed in other cave systems (e.g., De Freitas et al., 1982; Spötl et al., 2005; Tremaine et al., 2011; Gregorič et al., 2014).

Changes in ΔT are due to outside air temperature being influenced by insolation, cloudiness, wind speed, and occurrences of warm or cold fronts (Lauer and Bendix, 2006). Consequently, ΔT and pCO_2 do not only display clear diurnal signals, such as in March and July 2013, but also irregular patterns, depending on surface weather conditions (Figs. 4 and 5). Both March and July 2013, displayed stable and rather extreme weather conditions over longer time periods, leading to well-defined diurnal patterns driven solely by insolation. During March 2013, extremely cold, arctic air reached NW Germany, leading to preferential wind from northern to eastern directions and generally too cold temperatures for March (Fig. 7A; DWD, 2013a), whereas in July, a stable, high-pressure cell developed resulting in warm temperatures (DWD, 2013b).

Diurnal pCO_2 variations in winter and summer are governed by more complex processes. Surface temperature usually increases with insolation during the day, and thus, ΔT increases too, while at night, the surface cools and ΔT decreases (Figs. 4 and 5). During winter months, however, we observe that daily pCO_2 anti-correlates with ΔT. A possible explanation is suction of CO_2 from ground air or soil air into the cave through host rock fissures, or from deeper cave parts during the night hours when ventilation is intensified (Fig. 5A). This is because both soil and deeper cave air

Table 1. Correlation values between monthly pCO_2 and ΔT.

CO_2 vs. ΔT	*r*	*p*	*n*
Apr 12	**0.32**	**3.60×10^{-6}**	**198**
May 12	**0.30**	**4.46×10^{-9}**	**355**
Jun 12	**0.54**	**0**	**313**
Jul 12	**0.24**	**4.36×10^{-6}**	**356**
Aug 12	**0.16**	**0.002**	**347**
Sep 12	**0.52**	**0**	**328**
Oct 12	**0.54**	**0**	**337**
Nov 12	0.00	0.93	344
Dec 12	−0.03	0.83	42
Feb 13	−0.06	0.47	174
Mar 13	**−0.80**	**0**	**345**
Apr 13	**−0.44**	**0**	**338**
May 13	**0.35**	**9.66×10^{-12}**	**351**
Jun 13	**0.19**	**4.17×10^{-4}**	**340**
Jul 13	**0.43**	**0**	**356**
Aug 13	**0.60**	**4.47×10^{-6}**	**49**
Dec 13	−0.06	0.42	197
Jan 14	**−0.70**	**0**	**356**
Feb 14	−0.17	0.06	122

Note: Negative correlations occurred most often in winter and positive correlations occurred most often in summer, while spring and autumn show both, positive and negative correlations. Significant correlations are printed bold.

are enriched in CO_2. Although in winter, soil air is less concentrated in CO_2 due to lower plant activity. When Δ*T* returns to less negative values (near zero) during the day, ventilation diminishes, and this suction effect is weaker or absent. Thus, pCO_2 decreases due to higher inflow of outside air from the lower entrance. In summer, daily pCO_2 and Δ*T* values correlate positively. Due to more positive Δ*T* values during the day, ventilation is increased. A suction of soil air or ground air CO_2 through fissures in the host rock, or from deeper cave portions, leads to increased pCO_2 values. During summer months, air enters through the upper entrance and flows out through the lower entrance. Hence, it seems possible that ground air from deeper parts of the cave system is sucked into the main airflow path between the two entrances, leading to a higher fraction of ground air contributing to cave air. During night hours, ventilation intensity decreases (Δ*T* values are less positive) and, consequently, pCO_2 decreases, too. The CO_2 variability of outside air at BEC System was not recorded in the context of this study. However, it can be assumed that outside air CO_2 variability, although small (Keeling et al., 2005), influences pCO_2 cave air variability at diurnal and seasonal scale.

Obviously, pCO_2 slightly lags variations in Δ*T* (Fig. 5). This is best explained by the intensity and rapidity of adjustment of the ventilation, and the distance the air needs to pass from the entrance to reach the data logger. We computed running correlations for the periods with the most pronounced diurnal variations (March 2013 and July 2013; Fig. 5) to determine the lag between change of outside temperature (air density) and response of pCO_2 levels in the cave. The running correlations suggest a lag of two hours for March 2013, and six hours for July 2013. Since the CO_2 logger is at a distance of only 100 m to the lower entrance, the shorter transfer time in March 2013 is easily explained. Surface air entering the lower entrance in winter reached the logger three times faster compared to summer months, when the air enters through the upper entrance and has to overcome a distance of ~300 m to reach the logger. This results, in both cases, in an especially low air flow velocity of 0.014 m s^{-1}. Due to this, air entering the cave through the lower or upper entrance is near-equilibrated with rock temperature when it reaches the logger. This is documented by the low, cave air temperature variability due to heat advection (Fig. 3B). Air flow velocity, however, is expected to vary throughout the year.

Most variations of cave air pCO_2 can be explained by temperature-driven air density differences. An additional factor, however, influences the ventilation pattern and is responsible for strong CO_2 decreases of up to 150 ppm within a few hours (Figs. 4 and 6). This secondary ventilation pattern for the BEC System is wind-induced flow. Wind-induced flow is facilitated by the orientation of both cave entrances toward the south, and thus, toward the main wind sector (Figs. 4, 6 and 7). Particularly, during periods of higher wind speed, and especially during winter months, the normal chimney circulation is disturbed; surface air is blown into the cave, lowering the CO_2 level. The period of August 25–26, 2012 was particularly well suited to exemplify this wind-induced disturbance. August 25, 2012 wind speed varied between 13 to 19 km h^{-1}, with directions between 190° and 240° (SSW). This resulted in a reduction of cave air pCO_2 by ca. 150 ppm (Fig. 6). During the first part of the night, wind speed was below 8 km h^{-1} and no disturbance could be detected in the cave. In the early hours of August 26, 2012, however, wind picked up again with speeds of 11 to 17 km h^{-1} from directions of 190° to 230°, again accompanied by a lowering of cave air pCO_2 by around 100 ppm (Fig. 6). After the wind direction changed westward and outside air was no longer pushed into the cave, the background ventilation reactivated.

In summary, the ventilation of the BEC System qualifies as dynamic in nature, with changes on seasonal to diurnal timescales. Chimney circulation is driven by air density differences forced by differential cave and outside air temperatures. This pattern is frequently overprinted by wind-induced air flow into the cave entrances. All of these factors make the Bunker-Emst Cave System an outstanding case example to highlight the forcing and interaction of multiple ventilation patterns.

Implications for Speleothem Proxy Data

The high resolution pCO_2 monitoring was accompanied by placement of watch glasses (U I, U IV) under two drip sites (TS 1, TS 8). This was performed to assess carbonate precipitation dynamics in direct relation to ventilation

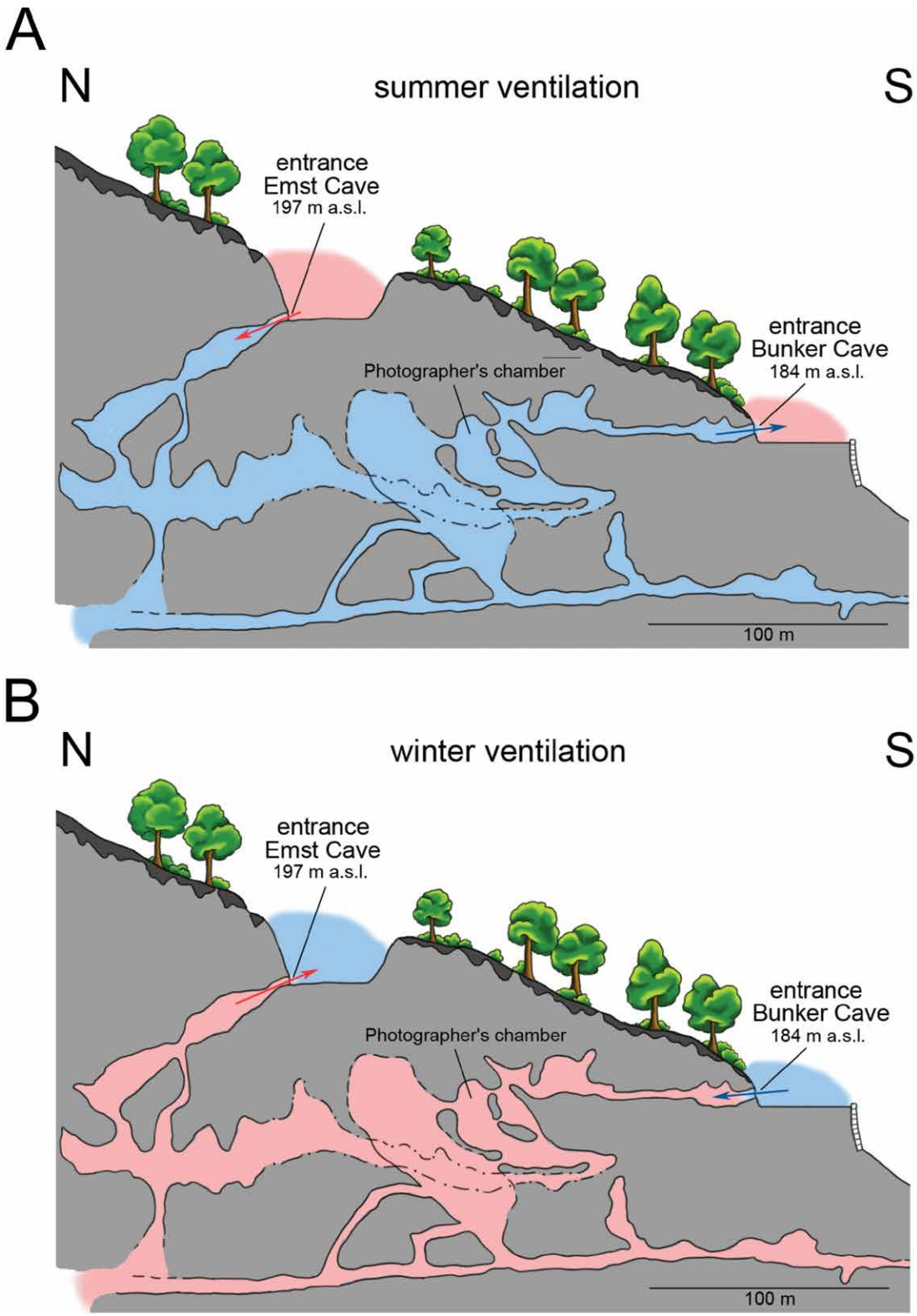

Figure 10. Schematic of winter and summer ventilation systematics. In summer, cave air is colder (blue) than outside air (red), and warm, less-dense outside air enters the upper entrance, to cool and descend, and exit through the lower entrance. During winter, outside air is colder (blue) than cave air (red). Thus, colder, denser, outside air flows through the lower entrance into the cave, warms up, ascends and flows out through the upper entrance.

patterns. Carbonate precipitation on glasses U I and U IV was slightly higher during winter and spring, and lower during summer and autumn (Fig. 8). This correlates with lower pCO_2 during winter and spring and higher pCO_2 levels in summer, a feature that is in agreement with the general observation of lower calcite precipitation rates at higher pCO_2 in summer. During winter months, this pattern is reversed (e.g., Baldini et al., 2008; Cowen et al., 2013; Pu et al., 2016). However, in the BEC System, air pCO_2 levels remain rather low in summer (maximum of 811 ppmv), and the difference between summer and winter pCO_2 is only about 400 ppmv. The drip rate at site TS 1 / U I (seasonal drip characteristic) correlates well with the precipitation rate of the carbonate on the watch glass (both highest in spring), while $SI_{calcite}$ of dripwater from TS 1 is relatively high, with a constant increase over the discussed period. Thus, the supply of ions to form carbonate is sufficient throughout the whole year. In the case of site TS 8 / U IV, water supply (seepage flow characteristic, Riechelmann et al., 2017) and saturation index are relatively constant, which explains the especially stable precipitation rates at this site (Fig. 8). The very significant differences in calcite saturation and drip rate between both drip sites explains the equally significant differences in

carbonate precipitation rates (Fig. 8). Carbon and oxygen isotope signatures of carbonate precipitates on both watch glasses depend on drip rate variability as previously shown (Riechelmann et al., 2013), but also seem to partly correspond with pCO_2 variability (Fig. 9A). Drip rate differences between both drip sites (Fig. 8) are reflected in isotopic equilibrium in the case of site TS 1 / U I and isotopic disequilibrium at site TS 8 / UIV. Consequently, $\delta^{13}C$ and $\delta^{18}O$ are significantly higher in precipitates from site TS 8 / U IV (Fig. 9A; Riechelmann et al., 2013). Apparently, the modern range in seasonal pCO_2 (~400 ppmv) is too low to cause an observable change in calcite precipitation rates or isotopic composition on seasonal or annual timescales. Water supply (drip rate) and saturation ($SI_{calcite}$), rather, govern carbonate precipitation and isotopic fractionation of the recent watch glass precipitates (e.g., Dreybrodt, 1988, 2008; Fairchild and Baker, 2012). To apply these observations to speleothem proxy data, the carbon (−6.09 ‰) and oxygen (−5.71 ‰) isotope values of the most recent part of speleothem BU 4 (located beneath drip site TS 8; Fig. 2) were compared with those of the precipitates on the corresponding watch glass U IV (mean $\delta^{13}C$: -5.92 ± 0.72 ‰; mean $\delta^{18}O$: -5.54 ± 0.26 ‰; Fig. 9A). Because these values are similarly within error, watch glass carbonate precipitates and speleothem carbonate are directly comparable. We conclude that the subdued modern pCO_2 variability in the BEC System has little, if any, influence on speleothem precipitation rate or isotopic composition. Consequently, speleothem proxy records at this site are probably not significantly controlled by CO_2 variations, but are rather more sensitive to temperature and rainfall shifts.

The artificial opening of both entrances in 1860–1863 and 1926, respectively, changed the ventilation dynamics of the BEC System, and the modern ventilation system is not analogous to the pre-1860-time interval. The opening of an entrance (naturally or artificially) to a cave without a natural entrance leads to immediate ventilation to adjust gradients between surface and cave, and likely to a rapid drop in cave air pCO_2. This results in higher speleothem precipitation rates and an increase in $\delta^{13}C$ values (Baldini et al., 2006). In analogy, stalagmite BU 4 displays a strong increase of ~2 ‰ in $\delta^{13}C$ over the last 150 years (Fig. 9B), which fits well with the opening of the first entrance in 1860–1863 (Emst Cave; Fohlmeister et al. 2012). Carbon isotope values in subsamples of speleothem calcite prior to this event are consistently lower (mean: -8.85 ± 0.85; Fohlmeister et al., 2012). This suggests that during the Holocene, no large, natural entrance existed to facilitate ventilation. We suggest that without major entrances to the cave system during the Holocene, ventilation was minimal and pCO_2 values were significantly higher and relatively stable. Precipitation rates found for BEC system stalagmites, which record decadal rather than annual or seasonal scale climate conditions, are mostly low, but comparable to carbonate precipitation rates of recent watch glass precipitates (Fohlmeister et al., 2012). Therefore, the precipitation rate of speleothem calcite is apparently unaffected by the opening of the cave entrances. Winterly water supply and higher saturation indices of calcite are, without much doubt, the two factors regulating past speleothem growth in the BEC System and not pCO_2. This fact would lead to a climate signal biased toward the winter season as observed today. Although pCO_2 variations, driven by the pre- and post-1860 ventilation patterns, have no influence on speleothem growth and isotopic composition, the artificial opening of the Bunker-Emst Cave System represents a particularly instructive example of the influence of changes in ventilation dynamics on speleothem proxy data.

Conclusions

The present-day ventilation patterns in the Bunker-Emst Cave System are mostly driven by air density (temperature) differences between cave and outside air. The resulting chimney circulation drives pCO_2 variability in the cave. Ventilation direction changes seasonally. During winter, air flow from the lower to the upper entrance takes place, while in summer, the opposite air movement prevails. In spring and autumn, ventilation switches between these two patterns. Wind pressure, driving outside air into the southward-facing cave entrances, affects and overrides the density-driven chimney circulation. Sources of cave air CO_2 include mostly outside air and, to smaller fractions, soil air and possibly even ground air. Under present-day conditions, the low variability of pCO_2 in the BEC System does not affect speleothem precipitation rate, or the isotopic composition of carbonate precipitates, as documented by recent watch glass precipitates. Rather, speleothems are more sensitive to shifts in temperature and rainfall. The opening of the two artificial entrances in 1860–1863 and 1926, respectively, most likely led, to a shift in the ventilation patterns of the Bunker-Emst Cave System, with changes from seasonal to diurnal scale, relative to its pre-1860 state. This change in ventilation dynamics had a significant impact on speleothem carbon isotopes, which show a strong increase in their values. We suggest that during the Holocene, no comparably large access routes to the cave existed, and that prior to the opening of artificial entrances, cave air circulation was strongly reduced. Speleothem calcite precipitated prior to cave entrance opening suggests that pCO_2 levels were significantly higher than today. The Bunker-Emst Cave System represents an exceptional natural laboratory that enables us to study recent ventilation patterns, as well as the transition from a natural to an anthropogenically-altered system and related shifts in speleothem isotope proxy data. Lessons learned here have wider significance for studies dealing with cave ventilation in general.

Acknowledgements

This work received funding by the German Science Foundation (DFG) Research Group 668 (DAPHNE). We would like to thank the Speleogroup Letmathe for their support in monitoring Bunker Cave, and the student assistants F. T. Meyer and M. Lyhs are thanked for their help during the monitoring tours. We thank J. Schug (Meteogroup) for providing the data of the meteorological station Hemer. We thank editor M. Field and D. Tremaine, D. Mattey and one anonymous reviewer for their constructive and detailed comments on our manuscript.

References

Atkinson, T.C., 1977, Carbon dioxide in the atmosphere of the unsaturated zone: an important control of groundwater hardness in limestones: Journal of Hydrology, v. 35, p. 111–123. https://doi.org/10.1016/0022-1694(77)90080-4.

Bakalowicz, M., 2012, Epikarst. *in* Culver, D.C., eds., Encyclopedia of Caves (Second Edition): Academic Press, p. 284–288.

Baldini, J.U.L., 2010, Cave atmosphere controls on stalagmite growth rate and paleoclimate Records, *in* Pedley, H. M., and Rogerson, M., eds., Tufas and speleothems: Unravelling the microbial and physical controls: Geological Society London, Special Publications 336, p. 283–294.

Baldini, J.U.L., Bertram, R.A., and Ridley, H.E., 2018, Ground air: A first approximation of the Earth's second largest reservoir of carbon dioxide gas: Science of the Total Environment, v. 616-617, p. 1007–1013. https://doi.org/10.1016/j.scitotenv.2017.10.218.

Baldini, J.U.L., Baldini, L.M., McDermott, F., and Clipson, N., 2006, Carbon dioxide sources, sinks, and spatial variability in shallow temperate zone caves: Evidence from Ballynamintra Cave, Ireland: Journal of Cave and Karst Studies, v. 68, no. 1, p. 4–11.

Baldini, J.U.L., McDermott, F., Hoffmann, D.L., Richards, D.A., and Clipson, N., 2008, Very high-frequency and seasonal cave atmosphere pCO_2 variability: Implications for stalagmite growth and oxygen isotope-based paleoclimate records: Earth and Planetary Science Letters, v. 272, p. 118–129. https://doi.org/10.1016/j.epsl.2008.04.031.

Banner, J.L., Guilfoyle, A., James, E.W., Stern, L.A., and Musgrove, M., 2007, Seasonal variations in modern speleothem calcite growth in central Texas, U.S.A.: Journal of Sedimentary Research, v. 77, p. 615–622. https://doi.org/10.2110/jsr.2007.065.

Benavente, J., Vadillo, I., Carrasco, F., Soler, A., Liñán, C., and Moral, F., 2010, Air carbon dioxide contents in the vadose zone of a Mediterranean karst: Vadose Zone Journal, v. 9, p. 126–136. https://doi.org/10.2136/vzj2009.0027.

Bender, M.M., 1971, Variations in the $^{13}C/^{12}C$ ratios of plants in relation to the pathway of photosynthetic carbon dioxide fixation: Phytochemistry, v. 10, p. 1239–1244. https://doi.org/10.1016/S0031-9422(00)84324-1.

Bögli, A., 1978, Karsthydrographie und physische Speläologie, Environmental Geology: Heidelberg, Springer, 292 p. https://doi.org/10.1007/978-3-662-08051-1.

Breecker, D.O., Payne, A.E., Quade, J., Banner, J.L., Ball, C.E., Meyer, K.W., and Cowan, B.D., 2012, The sources and sinks of CO_2 in caves under mixed woodland and grassland vegetation: Geochimica et Cosmochimica Acta, v. 96, p. 230–246. https://doi.org/10.1016/j.gca.2012.08.023.

Breitenbach, S.F.M., Lechleitner, F.A., Meyer, H., Diengdoh, G., Mattey, D., and Marwan, N., 2015, Cave ventilation and rainfall signals in dripwater in a monsoonal setting—a monitoring study from NE India: Chemical Geology, v. 402, p. 111–124. https://doi.org/10.1016/j.chemgeo.2015.03.011.

Cowan, B.D., Osborne, M.C., and Banner, J.L., 2013, Temporal variability of cave-air CO_2 in Central Texas: Journal of Cave and Karst Studies, v. 75, no. 1, p. 38–50. https://doi.org/10.4311/2011ES0246.

Czuppon, G., Demény, A., Leél-Össy, S., Óvari, M., Molnár, M., Stieber, J., Kiss, K., Kármán, K., Surányi, G., and Haszpra, L., 2018, Cave monitoring in the Béke and Baradla caves (Northeastern Hungary): implications for the conditions for the formation cave carbonates: International Journal of Speleology, v. 47, p. 13-28. https://doi.org/10.5038/1827-806X.47.1.2110,

De Freitas, C. R., Littlejohn, R. N., Clarkson, T. S., and Kristament, I.S., 1982, Cave climate: Assessment of airflow and ventilation: International Journal of Climatology, v. 2, p. 383–397. https://doi.org/10.1002/joc.3370020408.

Domínguez-Villars, D., 2012, Heat flux, *in* Fairchild, I.J., and Baker, A., eds., Speleothem science: From process to past environments: Chichester, Wiley-Blackwell, p. 137-145.

Dreybrodt, W., 1988, Processes in Karst Systems—Physics, Chemistry and Geology, Berlin, Springer, 288 p. https://doi.org/10.1007/978-3-642-83352-6.

Dreybrodt, W., 2008, Evolution of the isotopic composition of carbon and oxygen in a calcite precipitating H_2O-CO_2-$CaCO_3$ solution and the related isotopic composition of calcite in stalagmites: Geochimica et Cosmochimica Acta, v. 72, p. 4712–4724. https://doi.org/10.1016/j.gca.2008.07.022.

DWD (Deutscher Wetterdienst), 2013a, Pressemitteilung—Deutschlandwetter im März 2013, https://www.dwd.de/DE/presse/pressemitteilungen/DE/2013/20130328_DeutschlandwetterimMaerz.pdf?__blob=publicationFile&v=3 [accessed December 11, 2017].

DWD (Deutscher Wetterdienst), 2013b, Pressemitteilung—Deutschlandwetter im Juli 2013, https://www.dwd.de/DE/presse/pressemitteilungen/DE/2013/20130730_DeutschlandwetterimJuli.pdf?__blob=publicationFile&v=3 [accessed December 11, 2017].

Ek, C., and Godissart, J., 2014, Carbon dioxide in cave air and soil air in some karstic areas of Belgium. A prospective view: Geologica Belgica, v. 17, no. 1, p. 102–106.

Fairchild, I. J., and Baker, A., 2012, Speleothem science: From Process to Past Environments, Blackwell Quaternary Geoscience Series: Chichester, Wiley-Blackwell, 432 p. https://doi.org/10.1002/9781444361094.

Fohlmeister, J., Schröder-Ritzrau, A., Scholz, D., Spötl, C., Riechelmann, D.F.C., Mudelsee, M., Wackerbarth, A., Gerdes, A., Riechelmann, S., Immenhauser, A., Richter, D.K., and Mangini, A., 2012, Bunker Cave stalagmites: an archive for central European Holocene climate variability: Climate of the Past, v. 8, p. 1751–1764. https://doi.org/10.5194/cp-8-1751-2012.

Geiger, R., 1961, Das Klima der bodennahen Luftschicht, Braunschweig, Vieweg & Sohn, 640 p.

German Federal Environmental Agency, 2018, Luftmessnetz des Umweltbundesamts: www.umweltbundesamt.de/themen/luft/messenbeobachtenueberwachen/luftmessnetz-des-umweltbundesamtes [accessed July 31, 2018].

Glaser, B., 2005, Compound-specific stable-isotope ($\delta^{13}C$) analysis in soil science: Journal of Plant Nutrition and Soil Science, v. 168, p. 633–648. https://doi.org/10.1002/jpln.200521794

Grebe, W., 1993, Die Bunkerhöhle in Iserlohn-Letmathe (Sauerland): Mitt. Verb. dt. Höhlen- und Karstforsch., v. 39, no. 2, p. 22–23.

Gregorič, A., Vaupotič, J., and Šebela, S., 2014, The role of cave ventilation in governing cave air temperature and radon levels (Postojna Cave, Slovenia): International Journal of Climatology, v. 34, no. 5, p. 1488–1500. https://doi.org/10.1002/joc.3778.

Hammerschmidt, E., Niggemann, S., Grebe, W., Oelze, R., Brix, M. R., and Richter, D. K., 1995, Höhlen in Iserlohn: Schriften zur Karst- und Höhlenkunde in Westfalen, v. 1, p. 153.

Henderson, G. M., 2006, Caving in to new chronologies: Science, v. 313, p. 620–622.

Hendry, M. J., and Wassenaar, L.I., 2005, Origin and migration of dissolved organic carbon fractions in a clay-rich aquitard: ^{14}C and $\delta^{13}C$ evidence. Water Resources Research, v. 41, p. W02021.

James, J.M., 1977, Carbon dioxide in the cave atmosphere, *in* Transactions of the British Cave Research Association 4, p. 417–429

Keeling, C. D., Piper, S. C., Bacadtow, R.B., Wahlen, M., Whorf, T.P., Heimann, M., Meijer, H.A., 2005, Atmospheric CO_2 and $^{13}CO_2$ exchange with the terrestrial biosphere and oceans from 1978 to 2000: Observations and carbon cycle implications, *in* Baldwin, I.T., Caldwell, M.M., Heldmaier, G., Jackson, R.B., Lange, O.L., Mooney, H. A., Schulze, E.D., Sommer, U., Ehleringer, J.R., Denise Dearing, M., Cerling, T.E., eds., A History of Atmospheric CO_2 and Its Effect on Plants, Animals, and Ecosystems: Springer, p. 83–113.

Lauer, W., and Bendix, J., 2006, Klimatologie, Das Geographische Seminar: Braunschweig, Westermann, 352 p.

Lechleitner, F.A., Baldini, J.U.L., Breitenbach, S.F.M., Fohlmeister, J., McIntyre, C., Goswami, B., Jamieson, R.A., van der Voort, T.S., Prufer, K., Marwan, N., Culleton, B.J., Kennett, D.J., Asmerom, Y., Polyak, V., and Eglinton, T.I., 2016, Hydrological and climatological controls on radiocarbon concentrations in a tropical stalagmite: Geochimica et Cosmochimica Acta, v. 194, p. 233–252. https://doi.org/10.1016/j.gca.2016.08.039.

Luetscher, M., and Ziegler, F., 2012, CORA: a dedicated device for carbon dioxide monitoring in cave environments: International Journal of Speleology, v. 41, no. 2, p. 275–283. https://doi.org/10.5038/1827-806X.41.2.13.

Madhavan, S., Treichel, I., and O'Leary, M.H., 1991, Effects of relative humidity on carbon isotope fractionation in plants: Botanica Acta, v. 104, p. 292–294. https://doi.org/10.1111/j.1438-8677.1991.tb00232.x.

Mattey, D.P., Latin, J.P., and Ainsworth, M., 2008, Cave monitoring and calibration of a $\delta^{18}O$-climate transfer function for a Gibraltar speleothem: PAGES News, v. 16, p. 15–17. https://doi.org/10.22498/pages.16.3.15.

Mattey, D.P., Fairchild, I.J., Atkinson, T.C., Latin, J.-P., Ainsworth, M., and Durell, R., 2010, Seasonal microclimate control of calcite fabrics, stable isotopes and trace elements in modern speleothem from St. Michaels Cave, Gibraltar, *in* Pedley, H.M., and Rogerson, M., eds., Tufas and speleothems: Unravelling the microbial and physical controls: Geological Society, London, Special Publications 336, p. 323–344. https://doi.org/10.1144/SP336.17.

Mattey, D.P., Atkinson, T.C., Barker, J.A., Fisher, R., Latin, J.P., Durrell, R., and Ainsworth, M., 2016, Carbon dioxide, ground air and carbon cycling in Gibraltar karst: Geochimica et Cosmochimica Acta, v. 184, p. 88–113. https://doi.org/10.1016/j.gca.2016.01.041.

McDonough, L.K., Iverach, C.P., Beckmann, S., Manefield, M., Rau, G.C., Baker, A., and Kelly, B.F. J., 2016, Spatial variability of cave-air carbon dioxide and methane concentrations and isotopic compositions in a semi-arid karst environment: Environmental Earth Sciences, v. 75, p. 700. https://doi.org/10.1007/s12665-016-5497-5.

Miorandi, R., Borsato, A., Frisia, S., Fairchild, I.J., and Richter, D.K., 2010, Epikarst hydrology and implications for stalagmite capture of climate changes at Grotta di Ernesto (NE Italy): results from long-term monitoring: Hydrological Processes, v. 24, p. 3101–3114. https://doi.org/10.1002/hyp.7744.

Noronha, A.L., Johnson, K. R., Southon, J.R., Chaoyong Hu, Jiaoyang Ruan, McCabe-Glynn, S., Radiocarbon evidence for decomposition of aged organic matter in the vadose zone as the main source of speleothem carbon: Quaternary Science Reviews, v. 127, p. 37–47. https://doi.org/10.1016/j.quascirev.2015.05.021.

O'Leary, M.H., 1988, Carbon isotopes in photosynthesis: Fractionation techniques may reveal new aspects of carbon dynamics in plants: BioScience, v. 38, p. 328–336. https://doi.org/10.2307/1310735.

Peel, M.C., Finlayson, B.L., and McMahon, T.A., 2007, Updated world map of the Köppen-Geiger climate classification: Hydrology and Earth System Sciences, v. 11, p. 1633–1644. https://doi.org/10.5194/hess-11-1633-2007.

Pla, C., Cuezva, S., Garcia-Anton, E., Fernandez-Cortes, A., Cañaveras, J.C., Sanchez-Moral, S., and Benavente, D., 2016, Changes in the CO_2 dynamics in near-surface cavities under a future warming scenario: Factors and evidence from the field and experimental findings: Science of The Total Environment, v. 565, p. 1151–1164. https://doi.org/10.1016/j.scitotenv.2016.05.160.

Pollak, H.N., and Shaopeng Huang, 2000, Climate reconstruction from subsurface temperatures: Annual Review of Earth and Planetary Science, v. 28, p. 339–365. https://doi.org/10.1146/annurev.earth.28.1.339.

Junbing Pu, Aoyu Wang, Licheng Shen, Jianjan Yin, Daoxian Yuan, and Heping Zhao, 2016, Factors controlling the growth rate, carbon and oxygen isotope variation in modern calcite precipitation in a subtropical cave, Southwest China: Journal of Asian Earth Sciences, v. 119, p. 167–178. https://doi.org/10.1016/j.jseaes.2015.12.010.

Ridley, H.E., Baldini, J.U.L., Prufer, K.M., Walczak, I.W., and Breitenbach, S.F.M., 2015, High-resolution monitoring of Yok Balum Cave, Belize: An investigation of seasonal ventilation regimes and the atmospheric and drip-flow response to a local earthquake: Journal of Cave and Karst Studies, v. **77**, no.3, p. 183–199. https://doi.org/10.4311/2014ES0117.

Riechelmann, D.F.C., Schröder-Ritzrau, A., Scholz, D., Fohlmeister, J., Spötl, C., Richter, D.K., and Mangini, A., 2011, Monitoring Bunker Cave (NW Germany): A prerequisite to interpret geochemical proxy data of speleothems from this site: Journal of Hydrology, v. 409, no. 3-4, p. 682–695. https://doi.org/10.1016/j.jhydrol.2011.08.068.

Riechelmann, D.F.C., Deininger, M., Scholz, D., Riechelmann, S., Schröder-Ritzrau, A., Spötl, C., Richter, D.K., Mangini, A., and Immenhauser, A., 2013, Disequilibrium carbon and oxygen isotope fractionation in recent cave calcite: Comparison of cave precipitates and model data: Geochimica et Cosmochimica Acta, v. 103, p. 232–244. https://doi.org/10.1016/j.gca.2012.11.002.

Riechelmann, S., Schröder-Ritzrau, A., Spötl, C., Riechelmann, D.F.C., Richter, D.K., Mangini, A., Frank, N., Breitenbach, S.F.M., and Immenhauser, A., 2017, Sensitivity of Bunker Cave to climatic forcings highlighted through multi-annual monitoring of rain-, soil-, and dripwaters: Chemical Geology, v. 449, p. 194–205. https://doi.org/10.1016/j.gca.2012.11.002

Riechelmann, S., Schröder-Ritzrau, A., Wassenburg, J.A., Schreuer, J., Richter, D.K., Riechelmann, D.F.C., Terente, M., Constantin, S., Mangini, A., and Immenhauser, A., 2014, Physicochemical characteristics of drip waters: Influence on mineralogy and crystal morphology of recent cave carbonate precipitates: Geochimica et Cosmochimica Acta, v. 145, p. 13–29. https://doi.org/10.1016/j.gca.2014.09.019.

Rossi, C., and Lozano, R.P., 2016, Hydrochemical controls on aragonite versus calcite precipitation in cave dripwaters: Geochimica et Cosmochimica Acta, v. 192, p. 70–96. https://doi.org/10.1016/j.gca.2016.07.021.

Smerdon, J.E., Pollack, H.N., Cermak, V., Enz, J.W., Kresl, M., Safanda, J., and Wehmiller, J.F., 2006, Daily, seasonal and annual relationships between air and subsurface temperatures: Journal of Geophysical Research, v. 111, p. D07101 https://doi.org/10.1029/2004JD005578.

Spötl, C., Fairchild, I.J., and Tooth, A F., 2005, Cave air control on dripwater geochemistry, Obir Caves (Austria): Implications for speleothem deposition in dynamically ventilated caves: Geochimica et Cosmochimica Acta, v. 69, no. 10, p. 2451–2468. https://doi.org/10.1016/j.gca.2004.12.009.

Tremaine, D.M., Froelich, P.N., and Yang Wang, 2011, Speleothem calcite farmed *in situ*: Modern calibration of $\delta^{18}O$ and $\delta^{13}C$ paleoclimate proxies in a continuously-monitored natural cave system: Geochimica et Cosmochimica Acta, v. 75, p. 4929–4950. https://doi.org/10.1016/j.gca.2011.06.005.

Van Rampelbergh, M., Verheyden, S., Allan, M., Quinif, Y., Keppens, E., and Claeys, P., 2014, Monitoring of a fast-growing speleothem site from the Han-sur-Lesse cave, Belgium, indicates equilibrium deposition of the seasonal $\delta^{18}O$ and $\delta^{13}C$ signals in the calcite: Climate of the Past, v. 10, p. 1871–1885. https://doi.org/10.5194/cp-10-1871-2014.

Wood, W.W., 1985, Origin of caves and other solution openings in the unsaturated (vadose) zone of carbonate rocks: A model for CO_2 generation: Geology, v. 13, p. 822–824. https://doi.org/10.1130/0091-7613(1985)13%3C822:OOCAOS%3E2.0.CO;2.

Patricia Fragoso-Servón, Alberto Pereira-Corona, and Francisco Bautista. The karst and its neighbors: Digital map of geomorphic environments in Quintana Roo, Mexico. *Journal of Cave and Karst Studies*, v. 81, no. 2, p. 113-122. DOI:10.4311/2018ES0112

THE KARST AND ITS NEIGHBORS: DIGITAL MAP OF GEOMORPHIC ENVIRONMENTS IN QUINTANA ROO, MEXICO

Patricia Fragoso-Servón[1], Alberto Pereira-Corona[1], and Francisco Bautista[2, C]

Abstract

The Yucatan peninsula is a large, carbonate platform with several geomorphic environments, the largest of which is the karst. The other geomorphic environments have not drawn much scholarly attention. The objective of this work is to spatially identify the geomorphic environments found in Quintana Roo, Mexico. These environments were characterized and defined through their geomorphic and environmental conditions, such as climate and vegetation. The soil types associated with them using cluster statistical analysis, principal components and classification analysis, processed through a GIS system. Seven geomorphic environments were defined for Quintana Roo based on their geomorphological characteristics and types of coverage: littoral, paludal, pseudopaludal, tecto-karstic, karstic, gypsum karst and mixed karst, with 12 subtypes. The karstic and tecto-karstic geomorphic environments occupy the largest surface. The digital map (1:50,000) of geomorphic environments that resulted from this investigation has an accuracy level of more than 80%, which makes it an important tool for developing plans and strategies for the use and management of land in Quintana Roo.

Introduction

The Yucatan Peninsula is a large, calcareous plateau that is often considered a plain because of its low elevation compared to other parts of Mexico, such as the western, eastern and southern sierras. The official maps distinguish only three sub-provinces corresponding to geomorphic environments: Carso Yucateco; Carso and Lomeríos de Campeche; and the lower coast of Quintana Roo (INEGI, 2000a). It is usually believed that the Yucatan Peninsula is mostly environmentally homogeneous in terms of rock type and relief; however, there are large-scale morphometric differences involving karst depressions (Fragoso-Servón et al., 2014a), as well as small karst depressions and altitude variations (Lugo et al., 1992; Bautista et al., 2011).

In the study of the environment, and particularly of relief, the classification system proposed by Zinck (2012), which has been applied and validated in various parts of the world, constitutes an especially useful methodological tool for the identification of geomorphic environments.

The geomorphoedaphic environment (GE) is a category (suborder) of the Zinck (2012) system for the study of relief at a scale of 1:500,000. It is a biophysical medium formed and controlled by certain internal and/or external geodynamic processes (Zinck, 2012).

Characterizing a GE helps to understand and explain spatial distribution of soil-scapes and the pedogenetic processes that take place in it; this, in turn, allows a better understanding of its soil resources and helps evaluate their potential and limitations of use (Bautista et al., 2007; Zinck, 2012; Zinck et al., 2016). However, there is often not enough geographic information to make large-scale maps of geomorphic environments.

These limitations can be overcome through digital soil maps using multivariate techniques, data mining, and geographic information systems, which allow both to handle and infer geographic information, particularly of soils, in unsampled sites (Hartemink and Minasny, 2014; Minasny and McBratney, 2016).

The state of Quintana Roo, Mexico, is part of the karst plateau; it has 12 types of vegetation (Ek, 2011), six climatic subtypes (INEGI, 2008) and 14 soil groups (Fragoso et al., 2017). However, only three geomorphic environments have been reported. This work aimed to identify the diversity of geomorphoedaphic environments that exist in the state of Quintana Roo, Mexico, some of them consisting of karst with neighbors of other types.

Study Area

The state of Quintana Roo, Mexico, is located in the eastern part of the Yucatan Peninsula between 17° 40' and 21° 36' N and between 86° 44' and 89° 24' W. The Peninsula is a karst formation, composed mainly of calcite, dolomite and gypsum, that emerged at the end of the Tertiary or during the early Quaternary (López-Ramos, 1981; Bautista et al., 2011); the oldest geologic formations are located in the south and the most recent to the north and east.

Karst depressions, such as sinkholes, uvalas and poljes, abound in the state (Fragoso-Servón et al., 2014a). The center and north of the state are sub-horizontal and hilly plains, while the southern part is dominated by rolling hills (Fragoso-Servón et al., 2014a).

[1]Universidad de Quintana Roo. Boulevard Bahía s/n colonia del Bosque, Chetumal, Quintana Roo, México. C.P. 77019.
[2]Centro de Investigaciones en Geografía Ambiental (CIGA), Universidad Nacional Autónoma de México (UNAM). Antigua Carretera a Pátzcuaro No. 8701, Col. Ex-Hacienda de San José de la Huerta. C.P. 58190. Morelia Michoacán México.
[C]Corresponding Author: leptosol@ciga.unam.mx

The climate in Quintana Roo is humid warm (Am(f)) with rain year-round, and warm sub-humid with rain in summer (Aw), with five variants: rainy with rain in winter $Aw_2(x')$, moderately rainy Aw_1, moderately rainy with rain in winter $Aw_1(x')$, the least amount of rain in the summer Aw_0, the least amount of rain in the summer and with rain in winter $Aw_0(x')$ (INEGI, 2008). According to WRB (2014), 14 principal soil groups (WRB) or soil orders (soil taxonomy) have been identified; of these, Leptosols (Entisols), Gleysols (Inceptisols), Phaeozems (Mollisols), Vertisols (Vertisols) and Luvisols (Ultisols) occupy the largest area (Fragoso-Servón et al., 2017). The vegetation is very diverse, including medium forests, low forests, palm groves, mangroves, tular or vegetation of swamps, and lakes (plants 1 m to 3 m high, with narrow leaves and without foliar organs; the representative genera are *Typha, Scirpus, Cyperus, Phragmites* and *Cladium*) and popal (herbs in freshwater marshes rooted in the ground that emerge from the floodwater) (Ek, 2011).

Materials and Methods

Making the map of the geomorphic environments involved three stages (Fig. 1). The first stage consisted in making a morphometric description of the relief and the forms of coverage, based on 1:50,000 topographic information from INEGI, with the support of a Geographic information System (GIS) using the ArcGIS software.

Positive forms of the relief were identified using the vertical dissection coefficient (Priego et al., 2010; Fragoso-Servón et al., 2014b). Thirteen geomorphic units were identified, from sub-horizontal plains to strongly dissected mountains. The information about the negative forms of relief, their characteristics and distribution were taken from Fragoso-Servón et al. (2014a).

Geomorphometric units derived from the previous analyses were classified using geological information from the study Geological-Petrographic Prospection of the Yucatan Peninsula (PEMEX, 1967) and López-Ramos (1981); the information about faults and fractures was obtained from INEGI (2000b).

Then, geomorphometric units identified were classified within the GIS according to their environmental attributes, using climate information from INEGI (2008), vegetation information from INEGI (2009) and CONAFOR-SEMARNAT (2011), and soil information from Fragoso-Servón et al. (2017).

The second stage consisted of three successive analyses: a cluster analysis to reduce the volume of information represented by the polygons of the initial data matrix, a principal components analysis to determine which factors have the greatest weight in determining the existing environments, and a classification decision tree analysis to determine the uncertainty of the obtained results.

Cluster analysis was performed with the unweighted average linkage method using the Goodman-Kruskal Gamma coefficient

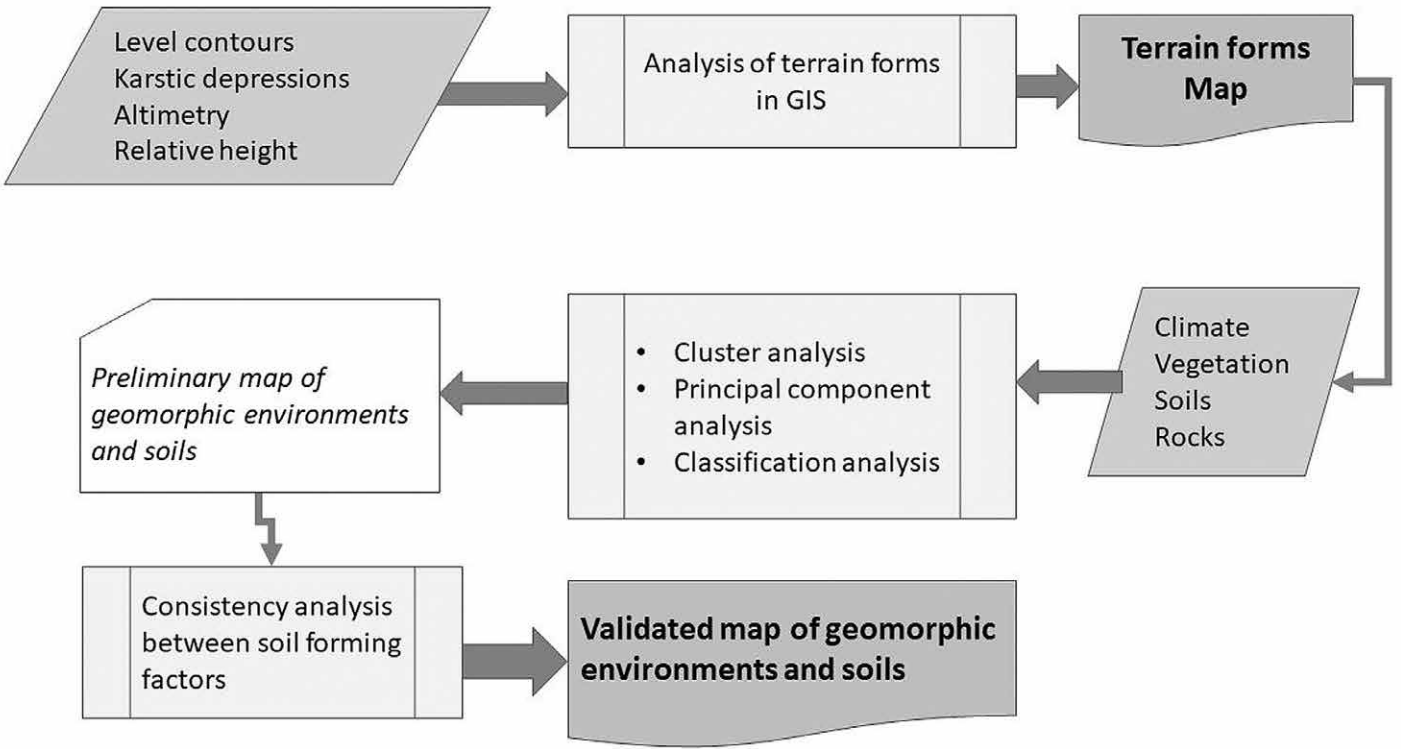

Figure 1. Methodological diagram.

$$D = 1 - \left(\frac{N_s - N_d}{N_s + N_d}\right), \quad (1)$$

where: D is the distance between pairs of objects, N_s is the number of objects with matching attributes and sequences, and N_d is the number of objects with different attributes and sequences.

This estimator is known as one of maximum similarity that is useful to handle large volumes of hierarchical data that have matches in order and value (Nelson, 1986). This analysis was validated using the Pseudo-F test, the Pseudo-T test, and Dunn's test (Halkidi et al., 2002; Havens et al., 2008; Omran et al., 2007) to verify the resulting cluster.

The Pseudo-F test yields a probability value for each node based on the probability of all the nodes that form the cluster

$$F = \left(\frac{U_1 / d_1}{U_2 / d_2}\right), \quad (2)$$

where U_1 and U_2 follow a chi-square distribution with d_1 and d_2 degrees of freedom, and U_1 and U_2 are statistically independent. The Pseudo-T test compares the mean distances and the intra and intergroup variances to estimate the dispersion of the nodes

$$T = \frac{\bar{X}_1 / \bar{X}_2}{s_{\bar{X}_1} / s_{\bar{X}_2}}, \quad (3)$$

where $\bar{X}_1 - \bar{X}_2$ is the mean intragroup and intergroup distances and $S_{\bar{X}_1} - S_{\bar{X}_2}$ is the difference in variances according to the size of the clusters. Dunn's Consistency or Distortion test is used to validate the cluster (Halkidi et al., 2002; Havens et al., 2008; Omran et al., 2007)

$$D = \frac{d_{\min}}{d_{\max}}, \quad (4)$$

where $d_{\min}$ is the minimum intercluster distance and $d_{\max}$ = maximum intracluster distance.

The resulting classes or clusters were subjected to principal component analysis to identify the sources of data set variability and the relative importance of each of them (Jongman et al., 1995).

Additionally, the result of the principal components analysis was subjected to a classification decision tree analysis, using the software WEKA to estimate the uncertainty of the classification (Bouckaert et al., 2009; Hall et al., 2009). Three different algorithms were used in four runs, and the results were compared to determine the consistency of the classification: a) Classification by decision tables with simple and exhaustive search (Kohavi, 1995; Mukerjee, 2012); b) Classification by exceptions to the initial rule (RIDOR or RIpple-Down-Rules) (Gaines and Compton, 1995); c) Classification by partition rules (Frank and Witten, 1998).

In the third stage, a preliminary map of the geomorphic environments was obtained; it was simplified by merging adjacent polygons with the same characteristics into each of the five resulting categories (structural, depositional, erosional, dissolutional, residual or mixed).

For each of these simplified units, we verified that the relationships between geomorphology, soils, vegetation, and climate were congruent with the field data and with the existing bibliographic references. This was done to validate the map of the geomorphic environments of Quintana Roo.

Results

As a result of the cluster analysis, it was possible to reduce the 16,456 polygons to 869 clusters of units that had identical attributes. The subsequent merger of clusters with minor differences reduced the total to 188 clusters with different geomorphometric conditions. The results of the statistical tests used on the clustering output gave to the estimated morphometric structure of clustering tree an uncertainty of less than 5 %.

Adding soil information to polygons of those 188 clusters allowed the identification of 123 clusters with complete soil information, which represent more than 99.5 % of the surface of the state.

The main components analysis allowed the identification of the groups of variables that are the source of the system's variability; they can be grouped into: relief conditions (vertical dissection, karsticity and faults), type and distribution of soils and rainfall, and temperature and flood regime. Relief conditions, constituted by the vertical dissection, shape, distribution and flood regime of the karst depressions and faults, explained approximately 51 % of the variation in the geographical distribution of soils. These relief conditions, together with the resulting soil distribution and the climatic conditions of precipitation and temperature, explain approximately 65 % of the observable environmental variability.

Certainty of these results was calculated using the confusion matrix from the classification analysis. Simply put, this matrix shows how many polygons were correctly classified and how many were not. It yielded a result that was consistent with the determination of the variance explained by the principal components analysis; for the three algorithms considered, the percentage of polygons correctly classified was above 83 %, which indicates that the environments

were correctly identified using this procedure (Table 1). The results indicate that the identification of the environments, based on the selected variables, has an uncertainty between 14 % and 16 % associated with inaccuracies in the data (Table 1).

Based on the variables analyzed and the definition of morphogenetic environments (Zinck, 2012), seven geomorphic environments were identified for Quintana Roo (Table 2), two of them were depositional (paludal and pseudopaludal), one was erosional (litoral), one was structural (tecto-karst), two were dissolutional (karst and gypsum karst) and one was mixed.

Littoral Environment

This geomorphic environment is the most recent; it formed at the end of the Tertiary (Pliocene) or during the early Quaternary (López-Ramos, 1981); it is located in the coastal area, at the transition between the mainland (karst) and the sea, and it is, therefore, influenced by both environments (Fig. 2).

There are two types of littoral environments: erosive-accumulative littoral and erosive littoral (Table 2). The first is located in the northern coastal areas, where sandy and rocky beaches alternate at short distances. Southern Quintana Roo is the locale of the second type. Both occupy 1.24 % and 1.06 % of the state's surface, respectively (Table 3).

In the northern part of the state, where the littoral environment is erosive-accumulative, the most common soils are Arenosol/Gleysol/Histosol; on these soils grow coastal scrub vegetation, low deciduous forest and halophytic plants. In some places it is possible to find soil associations such as Regosol/Gleysol/Histosol and Regosol/Arenosol, on which xerophytic plants grow. It is also possible to find Leptosols in rocky coastal areas.

In the south, the coastal environment is mainly accumulative and the soils that developed are Gleysol/Histosol/Regosol/Arenosol and the mangrove vegetation occupies the largest area.

A conjunction of factors determine the presence of the littoral environment. For example, the Chetumal Bay, despite being a coastal area, has different characteristics than the rest of the coast. Its innermost part has low salinity (between 7 ppm and 10 ppm), since it is the mouth of the Hondo River and the Bacalar Lagoon system; it is more similar to a river bank or a lagoon than to a coastline. From the ecological point of view, it shows an estuarine behavior; for that reason, the areas bordering the bay present paludal and pseudopaludal environments. The characteristics of a littoral environment appear only at the mouth of the bay, where salinity increases, and the conditions are similar to those of the seafront.

In the southern coastal zone, the influence of the Caribbean marine current creates cumulative environments, while the northern zone shows an alternation between erosive and cumulative environments, depending on the profile of the coast (geological history). The characteristics of the soils in the coastal area of Quintana Roo are linked to the dynamics of the marine currents and the transport of sediments. This causes Gleysols and Histosols to be more frequent in the cumulative environments of the south, in the area corresponding to Bahías de Ascensión and Espíritu Santo, while Regosols and Arenosols are more frequent in the central zone (Costa Maya); the northern zone, where the geomorfoedaphological environment is erosive-accumulative, favors the presence of different mixtures of Arenosols, Gleysols and Histosols. In these conditions, the vegetation is influenced by two factors: the amount of subsurface (fresh water) and underground water (saline water) and the depth at which it is found. Mangrove areas dominate in the south and coastal scrub in the north, where it alternates with low forest formations.

Paludal Environment

Toward the west coast, in the sub-horizontal plains, the proximity of the water table, the abundant rainfall and the frequency of the salt wedge penetration have favored the presence of a paludal environment, where flood conditions have produced soils such as Gleysols and Solonchaks, with the characteristic vegetation of mangrove, popal and tular.

The paludal environment is found in areas of sub-horizontal plains that are close to the coast, where the water is permanently or semi-permanently stagnated due to the almost complete absence of slope, the abundant rainfall,

Table 1. Quality of the classification of polygons in the map of geomorphic environments.

Method	No. of Polygons Examined	No. of Rules	Polygons Correctly Classified, %	Polygons Incorrectly Classified, %
Decision table corresponding to a simple search	16353	1119	83.26	16.74
Decision table corresponding to an exhaustive search	15353	1119	83.26	16.74
Exceptions (Ripple-Down-Rules)	16456	357007	84.19	15.81
Partition rules (PART)	16456	389	85.69	14.31

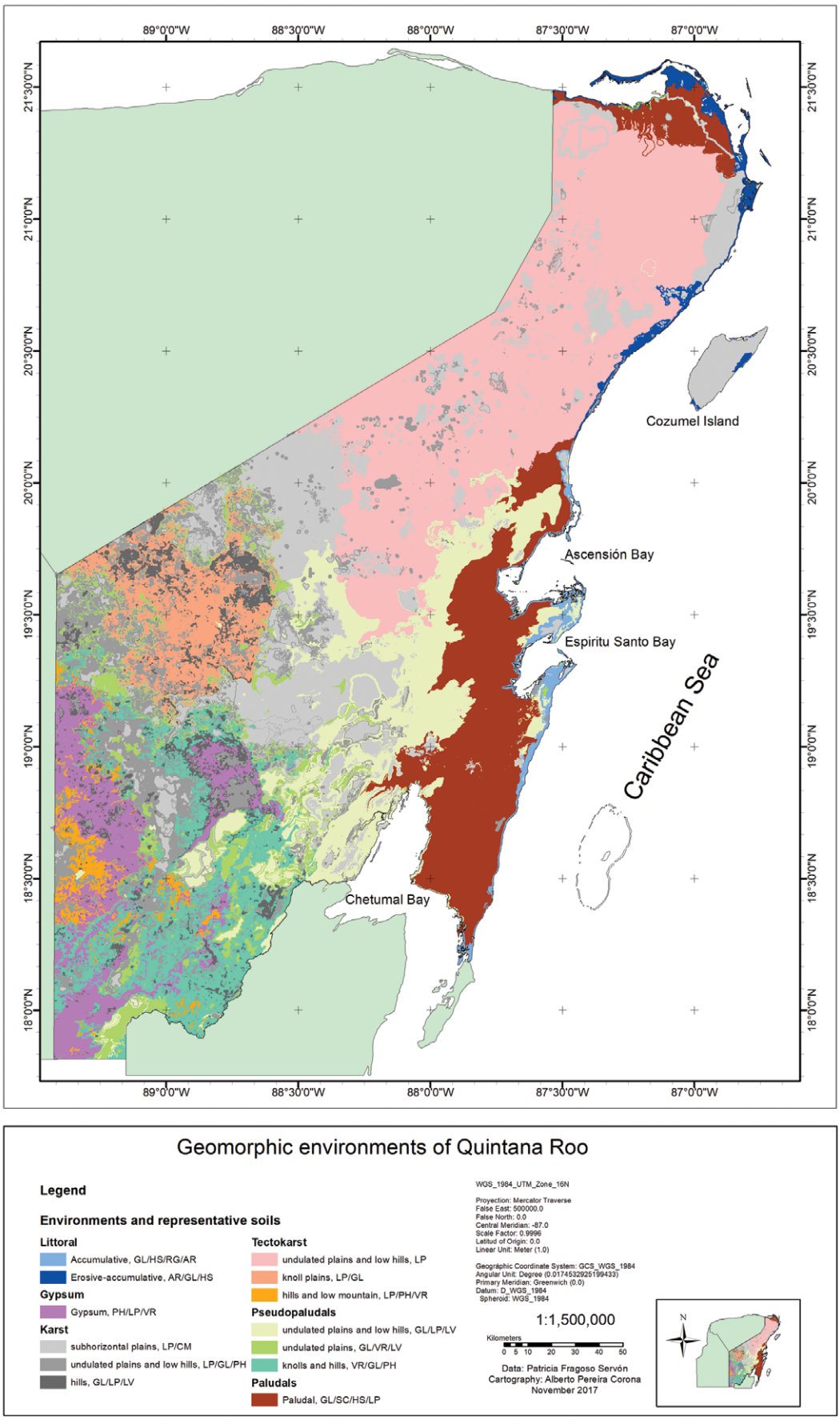

Figure 2. Map of the geomorphic environments of the state of Quintana Roo.

the frequent penetration of the salt wedge in coastal areas, the upwelling of underground water or the rise and fall of the water table, all of which can produce periods of flooding (Bonacci, et al., 2006; Hughes, et al., 2011; Pereira, et al., 2016) (Fig. 2).

This environment occupies 11.28 % of the state; it is found over the Pliocene formation in two zones, one involving a large area parallel to the coast, where rainfall is abundant (Aw_2), and another smaller area in the north with a drier climate (Aw_0), but with the presence of subsurface water flows. The soils that occur in this environment are Gleysol, Solonchak, Histosol and Leptosol; the vegetation that grows on them is mainly mangrove and tular-popal, with low forest in high relief formations (on hills and knolls).

Pseudopaludal Environment

As the vertical dissection of the relief increases, a transition zone between paludal environments and karstic and tecto-karstic environments emerges; this zone corresponds to pseudopaludal environments, where a large amount of water accumulates during the rainy season and stays there most of the year. In some areas, the water infiltrates quickly (Luvisols), while in other areas, it accumulates (Gleysols and Vertisols), resulting in a permanent flooding.

Medium forests and even high forests can develop in this environment with deeper soils. It is the area with the largest sur-

Table 2. Geomorphic environments in the state of Quintana Roo, Mexico.

Geomorphoedaphic Environments	Subtypes	Soils	Vegetation
Littoral	erosive-accumulative	AR/GL/HS	Scrub
	accumulative	GL/HS/RG/AR	Mangrove
Paludal	accumulative	GL/SC/HS/LP	Mangrove, tular, popal, low semi-evergreen forest
Pseudopaludal	undulated plains and low hills	GL/LP/LV	Low and medium semi-evergreen forests
	undulating plains	GL/VR/LV	Low and medium semi-evergreen forests, agriculture, cultivated pasture
	hill-billies and hills	VR/GL/PH	Medium semi-evergreen forest, agriculture, cultivated pasture
Tectokarst	Undulated plains and low hills	LP	Medium semi-deciduous and semi-evergreen forests
	Hill-billie plains	LP/GL	Medium semi-evergreen forest and cultivated pastures
	hills and low mountain	LP/PH/VR	Low and medium semi-evergreen forests, cultivated pastures
Karst	subhorizontal plains	LP/CM	Low deciduous forest, medium semi-evergreen forest, agriculture
	undulating and hilly plains	LP/GL/PH	Low semi-deciduous forest, medium semi-deciduous forest, agriculture
	Hills	LP/LV/GL	Low semi-evergreen forest, medium semi-evergreen and semi-deciduous forests, cultivated pastures
Gypsum karst	No Subtypes	PH/LP/VR	High and medium semi-evergreen forest
Mixed	Data depend on place and observability at scales of 1:50,000		

face dedicated to agriculture in the state and also the one with the greatest heterogeneity of soils. The pseudopaludal environment occupies 21.89 % of the state surface. It shows three main types of geoforms: sub-horizontal rolling plains that are slightly dissected, rolling plains, and areas of knolls and mountains.

The first type, which has lower vertical dissection and higher precipitation (Aw^1x'), can be found next to the paludal environment, on the formations of the Miocene, Oligocene and Pliocene (Bacalar, Estero Franco and Carrillo Puerto). The low slope favors hydromorphic conditions and the development of soils such as Gleysol/Leptosol/Luvisol, with low and medium semi-evergreen forests.

The second type of geoforms, to the west, in the oldest formations of the late Mesozoic, upper Cretaceous (Peten Limestone), over rolling plains, the accumulation of materials has allowed the development of deeper soils. The most common are an association between Gleysols, Vertisols and Luvisols, with medium and low semi-evergreen forests, in addition to agricultural areas and cultivated grassland.

The third type of geoform can be found on the plains with hills and knolls slightly dissected, located in the south of the state; the representative soils are Vertisols, Gleysols and Phaeozems. The most important agricultural activity of the state is carried out on this area (Fig. 2).

Tecto-Karstic Environment

This environment appears where two simultaneous characteristics occur: a medium or high density of faults and a high density of karst depressions (sinkholes, uvalas and poljes). Depending on the vertical dissection, the geology and soils, three subtypes of tecto-karstic environment can be identified: sub-horizontal and undulating plains, plains with hills and knolls, and mountains.

The tecto-karstic environment found in sub-horizontal plains occupies the largest area (29.76 %); it is located in the northernmost part of the state of Quintana Roo, over recent geological formations (Pliocene and Quaternary); the dom-

Table 3. Surface occupied by different geomorphic environments.

Geomorphic Environments	Surface Area, km²	Surface Area, %
Erosive-accumulative littoral	627.63	1.24
Accumulative littoral	534.33	1.06
Paludal	5708.04	11.28
Pseudopaludal, undulating plains and low hills	5424.13	10.72
Pseudopaludal, undulating plains	2201.61	4.35
Pseudopaludal, knolls and hills	3448.34	6.82
Tectokarst, undulating plains and low hills	11948.51	23.62
Tectokarst, knoll plains	2323.02	4.59
Tectorkarst, hills and low mountains	784.25	1.55
Karst of subhorizontal plains	7684.82	15.19
Karst, undulating plains and low hilly	5464.91	10.80
Karst, hills	1653.00	3.27
Gypsum	2753.51	5.44
Reefs	37.61	0.07
Total	50593.71	100.00

inant vegetation is medium sub-evergreen forest growing on Leptosols. However, there are also areas with presence of Leptosols/Luvisols (negative tecto-karst like sinkholes, uvalas, caves and underground rivers) (Fig. 2). A second zone with tecto-karstic environment is found on the hilly plains of the central-western part of the state over the Eocene formation (Chichen Itza); this zone is dominated by Leptosols and Gleysols, which are used for man-induced grasslands. The third zone occupies the smallest area and is located over the oldest formations of Quintana Roo (Icaiché), on knolls and mountains located in the western region of the state (dissolution formations associated to faults and fractures or positive tecto-karst), where deeper soils have developed in the lower parts. The dominant soils are Leptosols, Phaeozems and Vertisols, with medium semi-evergreen forest.

Karstic Environment

This environment is produced by the dissolution processes of limestone, involving rainfall, halo-phreatic mixing of groundwater and vegetation, which produce negative exokarstic (sinkhole, uvalas and poljes) (Fig. 2) and endokarstic (caves and caverns) relief formations. This environment occupies 29.26 % of the surface of the state of Quintana Roo, similar to the tectokarstic environment.

The karstic environment has three subtypes: in the sub-horizontal plains to the north of Quintana Roo; in the undulated and hilly plains of the central part; and in the knolls located to the west. The sub-horizontal plains of the karstic environment to the north of the state occupy small areas scattered among tecto-karstic zones. The karstic zones to the south and the central part of the state occupy large areas, where the relief starts to get higher. Representative soils are Leptosols and Cambisols, with low and medium semi-evergreen forests.

Karsticity decreases toward the west, as well as the size of the areas occupied by this environment. The undulating and hilly plains have deeper soils, the most common of which are Leptosols, Gleysols and Phaeozems, with low and medium semi-deciduous forests. Leptosols, Luvisols and Gleysols can be found among knoll areas with both medium semi-evergreen and semi-deciduous forests, as well as in some places with low semi-evergreen forest.

Gypsum Karstic Environment

This environment occurs in the oldest geological formations of the state of Quintana Roo (Upper Cretaceous and Paleocene), in the extreme west, which is the highest area, containing gypsum bedrock, where mountains, knolls and undulating plains are formed (Fig. 2). It has Leptosols on the slopes and Vertisols in the valleys, where materials accumulate under the influence of a strong karstification process. The dominant soil association is Phaeozem/Leptosol/Vertisol, with high and medium semi-evergreen forests.

Mixed Environment

This environment can be identified in some areas of the state when working at a scale of 1:50,000 or more detail. These are small areas that contain several geomorphoedaphic environments. In the north of the state, for example, these areas contain coastal, paludal, pseudopaludal and karstic environments.

Discussion

Geomorphic Environments

Quintana Roo has a great diversity of environments; however, maps of the Yucatan Peninsula with a scale of 1:500,000 do not show this (INEGI, 2000a; Bautista et al., 2011). A physiographic approach with which these maps were made, based on the types of rock and relief, distinguish only three physiographic subprovinces in the state of Quintana Roo (INEGI, 2000a). Using the traditional geopedological approach, Bautista et al. (2011) identified six geomorphic environments (coastal, fluvio-paludal, tecto-karstic and three karst subtypes). On the other hand, using a combined geomorphological and digital approach, seven environments and 12 subtypes were identified.

The geomorphic environments reported in this study were identified based on the dominant soil-forming processes in each of them, and their combinations within a defined hierarchical model. This hybrid approach, based on a hierarchical classification system, allows creation of accurate definitions of the environment types, and even allows assessment of each definition's accuracy (Zinck, 2012; Hall et al., 2009).

At the scale used in this study, the variable "vegetation" does not allow determination of the soil distribution; only some extremely particular types of vegetation, such as mangrove, can identify a soil group. Nevertheless, it is not a determining factor (Peris et al., 1994; Leyva et al., 2009). Additionally, vegetation serves to confirm the congruence between relief and soils, as in the case of plains with karst depressions, Gleysols and low semi-evergreen forest, or Arenosols and xerophilous scrub (Leirana-Alcocer et al., 2004), or Solonchack and halophilic scrub (Leirana-Alcocer et al., 2004).

The karst terrain gives the geomorphic environments reported in this study certain characteristics, such as, the presence of calcium carbonate, the presence of Leptosols, soils with pH values ranging from neutral to basic, and abundance of calcium ions. Arenosols and Regosols had particles with abundant calcium carbonate, which make these soils very different to Arenosols and Regosols from other parts of the country.

One of the greatest advantages of the method used in this study is its replicability. Being based on a hierarchical system, its categories are well defined, excluding subjective assessments. New information technologies, that can manage and analyze large volumes of information in a short time, make it possible to use this method in other areas and at different scales, in a relatively straightforward manner (Gessler et al., 1995; MacMillan et al., 2005; Hartemink et al., 2013).

The statistical analysis used in this study (cluster analysis, principal components analysis and classification analysis) indicated that, of the variables considered, vertical dissection, karstic formations, climate and geology have the greatest weight in the distribution of geomorphic environments.

Soils

According to Hall and Olson (1991; in Bautista et al., 2007), the variability of soils is both systematic and random. Systematic variability is predictable and associated with relief (edaphic landscapes), while random variability occurs when one of the soil-forming factors exerts its influence with greater intensity (Bautista et al., 2011; Mulder et al., 2011; Hu, 2013; Lagacherie et al., 2013).

Systematic variability, for example, can be observed in the presence of Arenosols in the littoral environment, originating and depicting an identifiable pattern. An example of random variability is the presence of Leptosols across the entire study area in markedly different geoforms and climatic conditions and no identifiable distribution pattern.

The characterization of the landscape formations allows both to understand the existing relationships between geoforms and soils and to identify the degree of development of landscape. For instance, the presence of Leptosols is more frequent in the lower part of the system of slightly inclined and incised hilly plains. Whereas in the south, where hills are found in greater density and with greater inclination, Leptosols are less frequent and the presence of richer and deeper soils, such as Phaeozems and Luvisols, increases. This could indicate that the wideness of the intermontane valleys is related to these soil formations in a similar way that the extension of catenae in the state of Yucatan is related to the soils associated with them, as reported by Bautista et al. (2004, 2015), by Berg and Oliveira (2000a, 2000b) in Brazil, by Fonseca (2010) in Portugal, Hennemann and Nagelhout (2004) in Kenya, by Lo Curzio (2009) in Italy and Möller et al. (2008) in Germany.

Time as a soil-forming factor is spatially expressed; thus, the oldest karst zones are in the south and west of the state of Quintana Roo, while the more recent zones are located on the coast (north and center) not considering Quaternary deposits as rocks. In the same way, the most frequent and predominant soil groups in the most recent (or with the shortest exposure time) karst area, are the less developed ones (those with AC horizons), while the more developed soils (those with ABC horizons) are in the center and south of the state, as reported by Bautista et al., (2011).

The relief irregularities produced by the karstification process, when the depressions were formed, explains the presence of different soils within small areas located in other parts of the Yucatan Peninsula, as reported by Bautista et al. (2003, 2004, 2015 , Kueny and Day (2002), Day (2010) and Aguilar et al. (2016).

Conclusions

This new hybrid, methodological proposal, which includes the classical approach to the study of geomorphic environments and reliefs and a method based on digital soil maps, has made it possible to: a) increase the identification of seven geomorphic environments and 12 variants, while also representing the interaction of its components and dynamics; b) identify the environmental factors that explain spatial variability; c) infer soil information in unsampled geomorphic environments; d) validate the generated map by calculating that the uncertainty of geomorphic environmental representation, for which there is no soil information, is 16%.

Acknowledgments

The authors would like to thank the General Directorate for Academic Personnel Affairs (DGAPA) of the National Autonomous University of Mexico (UNAM) for their financial support to the PAPIIT project, IN209218, and the UQROO-FOMIX-2012 Project for granting permission to use the computing equipment for statistical analysis.

References

Aguilar, Y., Bautista, F., Mendoza, M., Frausto, O., and Ihl, T., 2016, Density of karst depressions in Yucatan State, Mexico: Journal of Cave and Karst Studies, v.78, no. 2, p. 51–60. http://doi.org/10.4311/2015ES0124

Bautista, F., Jiménez, J., Navarro, J., Manu, A., Lozano, R., 2003. Microrrelieve y color del suelo como propiedades de diagnóstico en Leptosoles cársticos. Terra Lat. v. 21, p. 1–11.

Bautista, F., Estrada, H., Jiménez, J., and González, A., 2004, Relación entre el relieve y unidades de suelo en zonas cársticas de Yucatán: Terra Latinoamericana, v. 22, p. 243–254.

Bautista, F., Batllori, S.E., Ortiz, P.M., Palacio, G., and Castillo, G.M., 2005, Integración del conocimiento actual sobre los paisajes geomorfológicos de la Península de Yucatán, *in* Caracterización y manejo de suelos en la Península de Yucatán: implicaciones agropecuarias, forestales y ambientales: UACAM-UADY, México, 33–58.

Bautista, F., Aguilar, Y., Rivas, H., and Paez, R., 2007, Los suelos del estado de Yucatán, *in* Importancia del binomio suelo-materia orgánica en el desarrollo sostenible: Agencia Española de Cooperación Internacional y el Centro de Edafología y Biología Aplicada del Segura de Murcia: España, p. 11–42.

Bautista, F., Palacio, G., Quintana, P., and Zinck, A., 2011, Spatial distribution and development of soils in tropical karst areas from the Peninsula of Yucatan, Mexico: Geomorphology, v. 135, p. 308–321. https://doi.org/10.1016/j.geomorph.2011.02.014.

Bautista, F., Frausto, O., Ihl, T., and Aguilar, Y., 2015, Actualización del mapa de suelos del Estado de Yucatán México: Enfoque geomorfopedológico y WRB: Ecosistemas y recursos agropecuarios, v. 2, no. 6, p. 303–315.

Berg, M., and Oliveira, B., 2000a, Variability of apparently homogeneous soilscapes in São Paulo state, Brazil: I. Spatial analysis: Revista Brasileira de Ciência do Solo, v. 24, p. 377–391. https://doi.org/10.1590/S0100-06832000000200015.

Berg, M., and Oliveira, B. 2000b, Variability of apparently homogeneous soilscapes in São Paulo state, Brazil: II. Quality of soil maps: Revista Brasileira de Ciência do Solo v. 24, p. 393–407. https://doi.org/10.1590/S0100-06832000000200016.

Bonacci, O., Ljubenkov, I., Roje-Bonacci, T., 2006, Karst flash floods: an example from the Dinaric karst (Croatia): Natural Hazards and Earth System Science, 6, no. 2, 195–203. https://doi.org/10.5194/nhess-6-195-2006.

Bouckaert, R.R., Frank, E., Hall, M., Kirkby, R., Reutemann, P., Seewald, A., and Scuse, D., 2009, WEKA Manual for Version 3-6-1: University of Waikato, New Zealand.

CONAFOR-SEMARNAT, 2011, Inventario Forestal Nacional: Comisión Nacional Forestal, Secretaría de Medio Ambiente y Recursos Naturales, México.

Day, M., 2010, Human interaction with Caribbean karst landscapes: past, present and future: Acta Carsologica, v. 39, no. 1, p. 137–146. https://doi.org/10.3986/ac.v39i1.119.

Ek, A., 2011, Vegetación in: Riqueza Biológica de Quintana Roo. Un Análisis Para Su Conservación: El Colegio de la Frontera Sur (ECOSUR), Comisión Nacional para el Conocimiento y Uso de la Biodiversidad (CONABIO), Gobierno del Estado de Quintana Roo y Programa de Pequeñas Donaciones (PPD), México.

Fragoso-Servón, P., Bautista, F., Frausto, O., and Pereira, A., (2014a), Caracterización de las depresiones kársticas (forma, tamaño y densidad) a escala 1:50,000 y sus tipos de inundación en el Estado de Quintana Roo, México: Revista Mexicana de Ciencias Geológicas, v. 31. no. 1, p. 127–137.

Fragoso-Servón P., Pereira A., Frausto O., Bautista F. (2014b) Relación Entre La Geodiversidad De Quintana Roo Y Su Biodiversidad. Quivera 16:97–125.

Fragoso-Servón, P., Pereira, A., Bautista, F., and Zapata, G., 2017, Digital soil map of Quintana Roo, México: Journal of Maps, v. 13, no. 2, p. 449–456. https://doi.org/10.1080/17445647.2017.1328317.

Fonseca, I. L., 2010, Modelaccão de formas de relevo para aplicaccão à cartografia de solos. Presented at the V Congresso Nacional de Geomorfologia, Porto, Portugal.

Frank, E., and Witten, I., 1998, Generating Accurate Rule Sets Without Global Optimization: Morgan Kaufmann, p. 144–151.

Gaines, B.R., and Compton, P., 1995, Induction of Ripple-Down Rules Applied to Modeling Large Databases: Engineering Research Council of Canada.

Gessler, P., Moore, I., McKenzie, N., and Ryan, P., 1995, Soil-landscape modelling and spatial prediction of soil attributes: International Journal of Geographical Information Systems, v. 9, p. 421–432. https://doi.org/10.1080/02693799508902047.

Halkidi, M., Batistakis, Y., and Vazirgiannis, M., 2002, Clustering validity checking methods: part II. ACM: Sigmod Record, v. 31, p. 19–27. https://doi.org/10.1145/601858.601862.

Hall, M., Frank, E., Holmes, G., Pfahringer, B., Reutemann, P., and Witten, I., 2009, The WEKA data mining software: An update: SIGKDD Explorations, no. 11, p. 10–18. https://doi.org/10.1145/1656274.1656278.

Hartemink, A., and Minasny, B., 2014, Toward digital soil morphometrics: Geoderma, v. 230, p. 305−317. https://doi.org/10.1016/j.geoderma.2014.03.008.

Hartemink, A., Krasilnikov, P., and Bockheim, J., 2013, Soil maps of the world: Geoderma, v. 207, p. 256–267. https://doi.org/10.1016/j.geoderma.2013.05.003.

Havens, T., Bezdek, J., Keller, J., and Popescu, M., 2008, Dunn's cluster validity index as a contrast measure of VAT images, *in* Pattern Recognition, 19th International Conference on IEEE, p. 1–4.

Hennemann, G., and Nagelhout, A., 2004, Searching for effective, low-cost methods to detect and assess wind erosion damage: the promise of small-format aerial photography (SFAP). Wind Erosion and Dust Dynamics: Observations, Simulations and Modelling: ESW Publications, p. 123–127.

Hughes, A. G., Vounaki, T., Peach, D. W., Ireson, A. M., Jackson, C. R., Butler, A. P., Bloomfield, J. P., Finch, J., Wheater, H. S., 2011, Flood risk from groundwater: examples from a Chalk catchment in southern England: Journal of Flood Risk Management, v. 4, no. 3, 143–155. https://doi.org/10.1111/j.1753-318X.2011.01095.x.

INEGI, 2000a, Diccionario de datos fisiográficos 1:1,000,000: Instituto Nacional de Estadística Geografía e Informática, México.

INEGI, 2000b, Cartas Geológicas 1:250,000: Instituto Nacional de Estadística Geografía e Informática, México.

INEGI, 2008, Carta de Climas para la República Mexicana 1:1,000,000: Instituto Nacional de Estadística Geografía e Informática, México.

INEGI, 2009, Carta de uso de suelo y vegetación serie V 1:250,000: Instituto Nacional de Estadística Geografía e Informática. México.

IUSS Working Group WRB, 2014, World reference base for soil resources 2014. Rome: FAO.

Jongman, R., Ter Braak, C., and Van Tongeren, O. F., 1995, Data analysis in community and landscape ecology: Cambridge University Press. https://doi.org/10.1017/CBO9780511525575.

Kueny, J., Day, M., 2002, Designation of protected karstlands in Central America: a regional assessment: Journal of Cave and Karst Studies, v. 64, p. 165–174.

Kohavi, R., 1995, The power of decision tables, *in* Proceedings of the European Conference on Machine Learning: Springer Verlag, p. 174–189. https://doi.org/10.1007/3-540-59286-5_57.

Lagacherie, P., Sneep, A., Gomez, C., Bacha, S., Coulouma, G., Hamrouni, M., and Mekki, I., 2013, Combining Vis–NIR hyperspectral imagery and legacy measured soil profiles to map subsurface soil properties in a Mediterranean area (Cap-Bon, Tunisia): Geoderma, v. 209, p. 168–176. https://doi.org/10.1016/j.geoderma.2013.06.005.

Leirana-Alcocer J., and Bautista, F., 2014, Patrones de asociación entre la cobertura vegetal y la calidad del suelo en el matorral costero de la reserva de Ría Lagartos, Yucatán: Ciencia UAT, v. 82, p. 44–53. https://doi.org/10.29059/cienciauat.v8i2.297.

Leyva, J., Rocha, O., Mata, R., and Gutiérrez, M., 2009, Cronología de la regeneración del bosque tropical seco en Santa Rosa, Guanacaste, Costa Rica: II. La vegetación en relación con el suelo: Revista de Biología Tropical, v. 57, no. 3, p. 817–836.

Lo Curzio, S., 2009, Identification of soil erosion land surfaces by Landsat data analysis and processing: Italian Journal of Remote Sensing, v. 41, no. 1, p. 25–36. https://doi.org/10.5721/ItJRS20094113.

López-Ramos, E., 1981, Paleogeografía y tectónica del Mesozoico de México: Revista Mexicana de Ciencias Geológicas, v. 5, p. 158–177.

Lugo-Hubp, J., Aceves-Quesada, J.F., and Espinasa-Pereña, R., 1992, Rasgos geomorfológicos mayores de la Península de Yucatán: Revista Universidad Autónoma de México Instituto de Geología, v. 10, no. 2, p. 143–150.

MacMillan, R., Pettapiece, W., and Brierley, J., 2005, An expert system for capturing and applying soil survey tacit knowledge to automatically link soils to landform position in soil-landform models: Canadian Journal of Soil Science, v. 85, no. 1, p. 103–112. https://doi.org/10.4141/S04-029.

Minasny, B., and McBratney, A., 2016, Digital soil mapping: A brief history and some lessons: Geoderma, v. 264, p. 301–311. https://doi.org/10.1016/j.geoderma.2015.07.017.

Möller, M., Volk, M., Friedrich, K., and Lymburner, L., 2008, Placing soil-genesis and transport processes into a landscape context: A multiscale terrain-analysis approach: Journal of Plant Nutrition and Soil Science, v. 171, p. 419–430. https://doi.org/10.1002/jpln.200625039.

Mulder, V., de Bruin, S., Schaepman, M., and Mayr, T., 2011, The use of remote sensing in soil and terrain mapping–A review: Geoderma, v. 162, p. 1–19. https://doi.org/10.1016/j.geoderma.2010.12.018.

Mukerjee, P., 2012, Classification & Association Rule Generation: Vinod Gupta School of Management, India.

Nelson, T.O., 1986, BASIC programs for computation of the Goodman-Kruskal gamma coefficient: Bulletin of the Psychonomic. Society, v. 24, p. 281–283. doi:10.3758/BF03330141

Omran, M., Engelbrecht, A., and Salman, A., 2007, An overview of clustering methods: Intelligent Data Analysis, v. 11, p. 583–605. https://doi.org/10.3233/IDA-2007-11602.

Pemex., 1967, Prospección geológico petrográfica de la Península de Yucatán: Petróleos Mexicanos, México.

Pereira, C.A., Fragoso, S.P., Frausto, M.O, 2016, Suelos, agua, inundaciones y cambio climático en zonas de karst: el caso de Quintana Roo, México. GEOS 36: 275–290.

Peris, J., Sanchis, E., and Roig, C., 1994, Relación suelo/vegetación en la plana cuaternaria del Golfo de Valencia: Cuadernos de Geografía, v. 56, p. 155–162.

Priego, Á., Bocco, G., Mendoza, M.E., Garrido, A., 2010, Propuesta para la generación semiautomatizada de unidades de paisajes: Planeación Territorial, SEMARNAT/INE/CIGA-UNAM, México, D.F. 108 pp. ISBN 978-968-817-923-9.

Xue Yu Hu, 2013, Application of Visible/Near-Infrared Spectra in Modeling of Soil Total Phosphorus: Pedosphere, v. 23, p. 417–421. https://doi.org/10.1016/S1002-0160(13)60034-X.

Zinck, A., 2012, Geopedología: Elementos de geomorfología para estudios de suelos y de riesgos naturales, ITC, Enschede, Netherlands.

Zinck, J. A., Metternicht, G., Bocco, G., and Del Valle, H. F., 2016, Geopedology. An integration of geomorphology and pedology for soil and landscape studies. Springer International Publishing Switzerland. doi: 10.1007/978-3-319-19159-1.

Yunxia Li, Shengrui Zhang, Xiaokang Liu, Yongli Gao, and Zhiguo Rao. Variations of the stable isotopic composition of precipitation and cave drip water at zhenzhu cave, north China: a two-year monitoring study *Journal of Cave and Karst Studies*, v. 81, no. 2, p. 123-135. DOI:10.4311/2018ES0128

VARIATIONS OF THE STABLE ISOTOPIC COMPOSITION OF PRECIPITATION AND CAVE DRIP WATER AT ZHENZHU CAVE, NORTH CHINA: A TWO-YEAR MONITORING STUDY

Yunxia Li[1, 2, 3], Shengrui Zhang[4], Xiaokang Liu[1, 5], Yongli Gao[2], and Zhiguo Rao[3, C]

Abstract

We investigated potential factors influencing variations in isotopic composition of external precipitation and internal drip water at Zhenzhu Cave, Hebei Province, north China. Two meteoric precipitation sites and three cave drip sites were monitored monthly during April 2012–April 2014. The results of meteoric precipitation present: on monthly timescale, $\delta^{18}O_p$ and δD_p showed a significant seasonal double peak characterized by depleted isotopic values in both dry and wet seasons (but a significant seasonal variation in *d*-excess). There is a weakly negative correlation with monthly mean precipitation amount but no significant correlation with surface air temperature. Based on GNIP data, there are no significant correlations on an interannual scale between annual weighted mean $\delta^{18}O_p$ (and δD_p) and annual precipitation or annual mean temperature. This implies the variation of $\delta^{18}O_p$ (and δD_p) in the area cannot be interpreted solely as reflecting an "amount effect" or "temperature effect" on either seasonal or interannual scale, and may be affected by moisture sources. There isn't any significant change in $\delta^{18}O_d$ and δD_d values of cave drip water during monitoring period, demonstrating that cave drip water comprise a mixture of precipitation integrated over a long period rather than seasonal timescale. There were significant seasonal changes in cave air CO_2 concentration, with higher concentrations in summer and lower concentrations in winter that is well correlated with environmental variables such as surface temperature and precipitation, which may help improve the interpretation of stable carbon isotope records from speleothems ($\delta^{13}C_s$) in relation to cave air CO_2.

Introduction

Owing to the availability of various environmental proxies and precise chronology, speleothems are widely recognized as one of the most important archives of information for high-resolution paleoclimatic studies (Fairchild et al., 2006; Fairchild and Baker, 2012). In particular, the oxygen isotope and carbon isotope ratios of speleothems ($\delta^{18}O_s$, $\delta^{13}C_s$) have been widely used to reconstruct past climatic variability (Wang et al., 2001, 2008; Cosford et al., 2009; Cheng et al., 2009). $\delta^{18}O_s$ is often considered to inherit the $\delta^{18}O$ signal of atmospheric precipitation ($\delta^{18}O_p$) (Cheng et al., 2005; Luo and Wang, 2008), and thus, climatic factors effecting changes in $\delta^{18}O_p$ are usually regarded as drivers of variations in $\delta^{18}O_s$ (Wang et al., 2001; Dayem et al., 2010; Cheng et al., 2012; Tan, 2009, 2014). However, $\delta^{18}O_p$ is a function of air temperature, rainfall amount, moisture source, and other complex factors (Craig, 1961; Rozanski et al., 1982). Consequently, it is often difficult to separate the effects of these variables for the climatic interpretation of $\delta^{18}O_p$ records, although research has indicated that changes in $\delta^{18}O_p$ are mainly controlled by rainfall amount in low latitude regions and by temperature in high latitude regions (Dansgaard, 1964). Furthermore, $\delta^{18}O_s$ is not controlled solely by changes in $\delta^{18}O_p$. Cave conditions such as host rock lithology, ventilation, CO_2 concentration, and the in-cave process of calcite precipitation could also influence variations in $\delta^{18}O_s$ (Feng et al., 2012, 2014; Genty et al., 2014; Duan et al., 2016). Consequently, the interpretation of $\delta^{18}O_s$ is ambiguous, especially in the case of $\delta^{18}O_s$ records from the Asian monsoon region which are often interpreted as a proxy of local rainfall amount or monsoon intensity (Clemens et al., 2010; Pausata et al., 2011; Tan, 2009, 2014; Liu et al., 2015; Rao et al., 2015, 2016).

From the foregoing, it is evident that cave monitoring can help improve our understanding of the relationship between $\delta^{18}O_p$ and $\delta^{18}O_s$ (Luo and Wang, 2008; Ruan and Hu, 2010; Li et al., 2011; Genty et al., 2014; Duan et al., 2016). In the past decade, cave monitoring research has yielded valuable information (Luo and Wang, 2008; Ruan and Hu, 2010; Li et al., 2011; Genty et al., 2014; Duan et al., 2016), but monitoring results may be difficult to interpret and vary among different caves. Moreover, in some cases even results for different sites within the same cave are inconsistent (Duan et al., 2016). Therefore, more cave monitoring studies of longer duration are needed to clarify the significance of the $\delta^{18}O$ record of speleothems.

[1] Key Laboratory of Western China's Environmental Systems (Ministry of Education), College of Earth and Environmental Sciences, Lanzhou University, Lanzhou 730000, China
[2] Center for Water Research, Department of Geological Sciences, University of Texas at San Antonio, San Antonio, TX 78249, USA
[3] College of Resources and Environmental Sciences, Hunan Normal University, Changsha 410081, China
[4] College of Resources and Environment, Hebei Key Laboratory of Environmental Change and Ecological Construction, Hebei Normal University, Shijiazhuang 050024, China
[5] School of Soil and Water Conservation, Beijing Forestry University, Beijing 100083, China
[C] Corresponding Author: raozhg@hunnu.edu.cn.

The present study seeks to provide a reference for reconstructing past environmental changes in the Zhenzhu Cave region in north China and to better understand the cave environment. For this purpose, we conducted a two-year (April 2012–April 2014) on-site monitoring study of precipitation and drip water with a monthly sampling interval.

Study area and sampling sites

Zhenzhu ('Pearl' in English) Cave (38°15′ N, 113°42′ E, 990 m) is in the Tiangui Mountains in Pingshan County, Hebei Province, north China (Fig. 1). The current climate in the study area is dominantly monsoonal, characterized by two distinct seasons: a cool and dry winter from November to February and a hot and rainy summer from June to September. According to the meteorological data covering 1981-2010 from the nearest weather station (Pingshan city, National Meteorological Information Center, http://data.cma.cn/data/weatherBk.html), the mean annual temperature (MAT) is ~13 °C, and the mean annual precipitation (MAP) is ~539 mm, with ~80 % of the annual precipitation occurring in summer (June to September). However, because Zhenzhu Cave is located in the high elevation mountainous area, the MAT in this cave area is ~2-3 °C lower than that in Pingshan city, but the MAP in this cave area is ~110 mm more than that in Pingshan city, with a final MAT of 8-11 °C and MAP of 649-690 mm (Chen, 2010). The bedrock of Zhenzhu Cave is upper Cambrian-lower Ordovician dolomite, lime-dolomite, and dolomitic limestone. The cave was formed along a NNW-SSE oriented fault zone. The thickness of the bedrock overlying the cave is very thin (~10 m). At present, the natural vegetation above the cave is well-developed (Wang et al., 2011). According to the results of monitoring covering April 2012–April 2014, the thermohydrograph (hourly average output) showed that the relative humidity inside Zhenzhu Cave maintains 99%~100% during almost the whole monitoring period. The average temperature inside the cave is 9 °C, with a standard deviation of 1 °C, consistent with annual air temperature in this area.

Two precipitation monitoring stations (W1 and W2) were established for this study. W1 was located on the rooftop of a water house at a scenic location near Zhenzhu Cave and W2 was located on the rooftop of the administration building near site W1. The linear distance between W1 and W2 is 600 m (Fig. 1B). Three drip monitoring sites (D1, D2, D3) were chosen from different localities along cave passages, with increasing distance from the cave entrance to the innermost part of the cave (Fig. 1C). Cave conditions, including cave air CO_2 concentration (CO_2 meter), cave air temperature (T_{in}) and inside cave relative humidity (RH) (Thermohydrograph), were also monitored (Fig. 1C).

Methods And Data

Two precipitation-monitoring stations and three drip sites were visited every month from April 2012–April 2014 and corresponding water samples were collected. Drip water samples were collected in 100 mL high-density polyethylene (HDPE) bottles and stored at ~4 °C until processing. Storage and processing of precipitation samples were the same as those for drip water. All samples were filtered using a 0.45 μm glass fiber membrane filter and stable isotopic composition of oxygen and hydrogen were measured using a liquid water isotope analyzer (Los Gatos Research, DLT-100) in the Key Laboratory of Western China's Environmental Systems (Ministry of Education), College of Earth and Environmental Sciences, Lanzhou University. Results are expressed relative to V-SMOW (Vienna Standard Mean Ocean

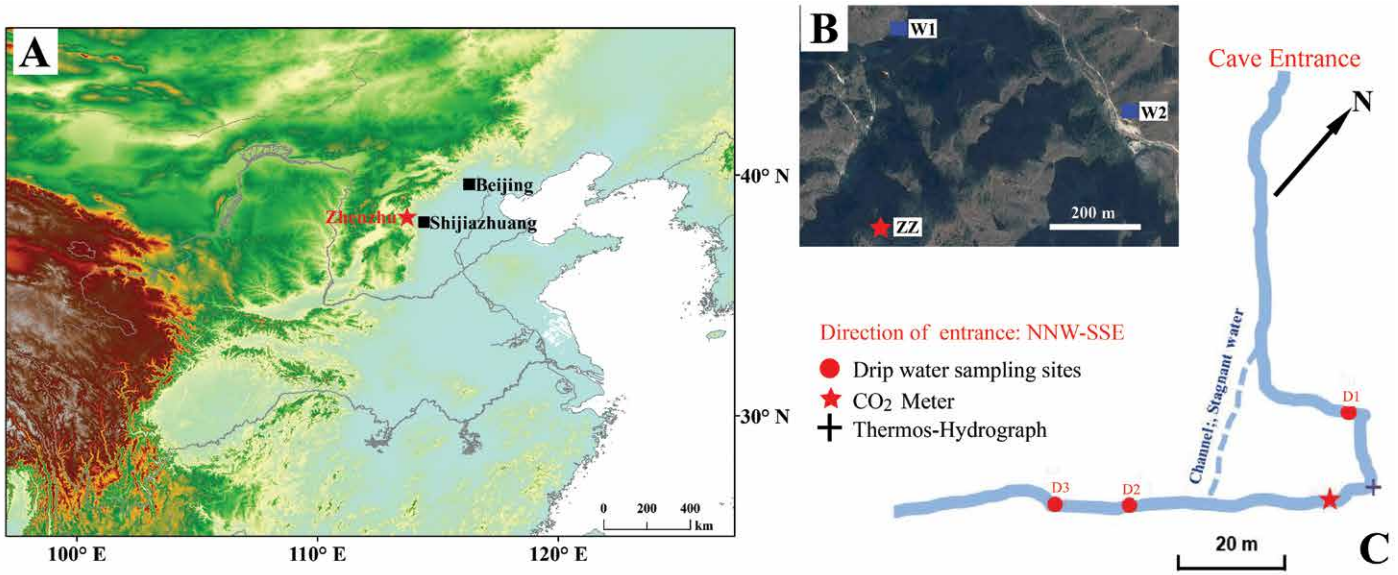

Figure 1. (A) Location of Zhenzhu Cave (red star) in Pingshan County, Hebei Province, China. The locations of Beijing and Shijiazhuang are also shown; (B) Location of rainfall sampling sites (blue rectangles, W1: 38.2643°N, 113.7149°E; W2: 38.2621°N, 113.7231°E), (Google Maps Image); (C) Plan view of the passages of Zhenzhu Cave, showing the locations of dripwater sampling sites (red circles), CO_2 meter (red star), and thermohydrograph (purple cross).

Water). Measurement errors of hydrogen isotope (δD) and oxygen isotope ($\delta^{18}O$) measurements were 0.3 ‰ and 0.1 ‰, respectively. Because meteorological data of a specific month in Pingshan city isn't available in the National Meteorological Information Center, meteorological data (monthly temperature and monthly precipitation) of Shijiazhuang (80 km away from Zhenzhu Cave) is downloaded from NOAA (https://gis.ncdc.noaa.gov/maps/ncei/summaries/monthly) to represent the local climate conditions.

Results and Discussion

Stable isotopic composition of precipitation

Seasonal variations

The hydrogen (δD_p) and oxygen ($\delta^{18}O_p$) isotopic compositions of precipitation samples from sites W1 and W2 during April 2012–April 2014 range from −84.4 ‰ to −16.9 ‰, and from −11.7 ‰ to −4.0 ‰, respectively. Because of the absence or limited amount of rainfall in some months, δD_p and $\delta^{18}O_p$ data for March 2013, December 2013, January 2014 and March 2014 are not available (Supplementary 1). In principle, precipitation isotopic values of sites W1 and W2 should be the same or similar. However, there are minor differences in the values in December 2012, January 2013, February 2013 and February 2014. Evidently, this difference occurred in months in which precipitation amount and temperature were very low, and thus water samples may have been affected by environmental factors such as evaporation and freezing. Minor variations in sampling and storage procedures during sample collection, as well as measurement errors, may also have been responsible for the differences. Nevertheless, precipitation isotopic values of the two sites were generally consistent during the monitoring period, suggesting that the data are valid.

Precipitation isotopic data was used to construct the local meteoric water line in the Zhenzhu Cave region (LMWL): $\delta D = 7.6\ \delta^{18}O + 9.0$ ($n = 41$, $R^2 = 0.94$) (Fig. 2A). The slope of the LMWL is close to but slightly smaller than that of the global meteoric water line (GMWL: $\delta D = 8\ \delta^{18}O + 10.0$, Craig, 1961) and the Chinese meteoric water line (CMWL: $\delta D = 7.9\delta^{18}O + 8.2$, Zheng et al., 1983), implying that isotopic composition of precipitation in the area was weakly affected by unbalanced secondary evaporation and other fractionation factors, such as considerable seasonal temperature variations and relatively low condensation temperature (Liu et al., 2014).

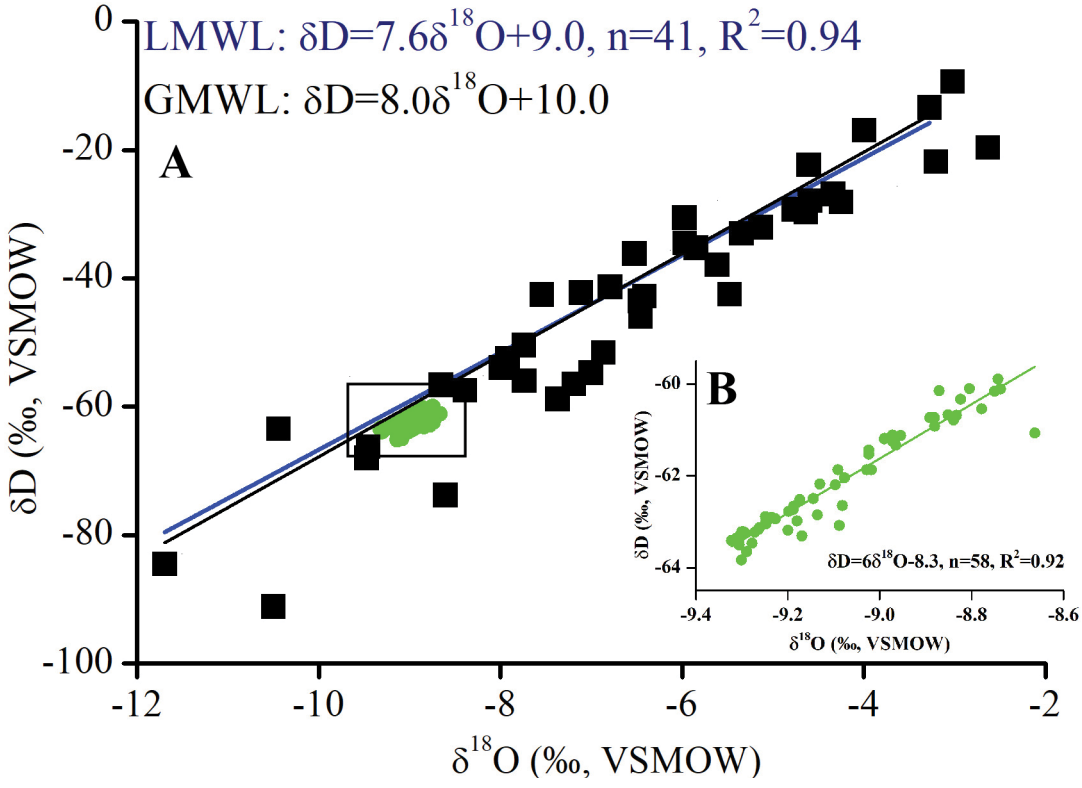

Figure 2. (A) Relationship between δD and $\delta^{18}O$ of drip water and local precipitation in Zhenzhu Cave. The Local meteoric water line (LMWL, blue line) is defined by all the precipitation data from two precipitation monitoring sites (W1 and W2). Within the analytical uncertainty, the Zhenzhu Cave drip-water samples fall on the Global meteoric water line (GMWL, black line) and below the LMWL; (B) Relationship between δD and $\delta^{18}O$ of drip water (grey box).

A seasonal double-peak is evident in the data. δD_p and $\delta^{18}O_p$ were lower in the summer/rainy seasons and cold/dry seasons (Fig. 3A and 3B). This result differs from isotopic compositions of precipitation in South China, which are lower only in the summer/rainy season, but are similar to those in northeast China (Liu et al., 2008, 2009, 2014). Correlation analysis of the monthly mean $\delta^{18}O_p$ (and δD_p) and precipitation amount or temperature revealed a relatively weak negative correlation between isotopic composition ($\delta^{18}O_p$ and δD_p) and monthly precipitation (MP) (W1: $\delta^{18}O_p = -0.014P - 6.0$,

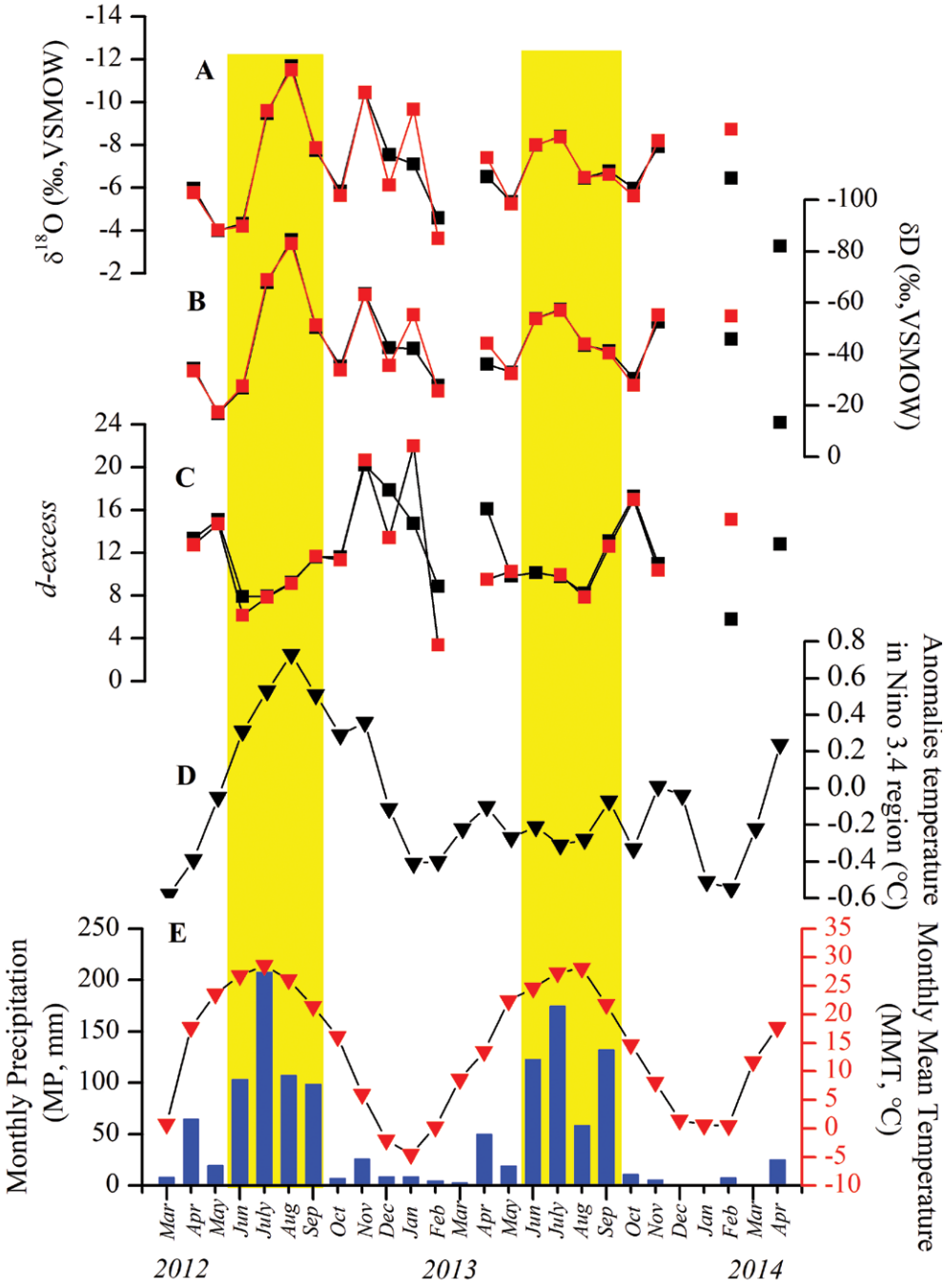

Figure 3. Time series of $\delta^{18}O$ (A), δD (B) and *d*-excess (C) from the W1 (black squares) and W2 (red squares) rainfall sampling sites in the Zhenzhu Cave area; (D) Temperature anomalies in the Niño 3.4 region (black triangles); (E) Variation of monthly precipitation (blue bars) and monthly mean temperature (red triangles) (the yellow bar represents the summer period).

n = 21, R^2 = 0.19; δD_p = −0.14P−34.4, n = 21, R^2 = 0.26; W2: $\delta^{18}O_p$ = −0.011P−6.5, n = 20, R^2 = 0.11; δD_p = −0.12P−37.9, n = 20, R^2 = 0.2) (Fig. 4). This demonstrates that $\delta^{18}O_p$ and δD_p in the Zhenzhu Cave area were either uninfluenced or only slightly influenced by the rainfall amount effect on a seasonal scale. There was no significant correlation between isotopic composition and monthly mean air temperature (W1: $\delta^{18}O_p$ = −0.011T−6.6, n = 21, R^2 = 0.003; δD_p = −0.22T−39.4, n = 21, R^2 = 0.019; W2: $\delta^{18}O_p$ = 0.010T−7.3, n = 20, R^2 = 0.003; δD_p = −0.16T−43.4, n = 20, R^2 = 0.006) (Fig. 4). Therefore, isotopic compositions of precipitation on a seasonal scale in the study area cannot be interpreted solely in terms of rainfall amount or temperature effect.

Changes in moisture source and vapor transport path have substantial effects on variations in isotopic compositions of precipitation (Welker, 2000; Liu et al., 2008, 2009, 2014). In studies of modern isotopic compositions of precipitation, deuterium excess (*d*-excess), defined as $d = \delta D - 8\delta^{18}O$, is an important parameter that may reflect climatic conditions in the moisture source area such as the distance from the source area to the precipitation location, and condensation and re-evaporation processes during vapor transport (Araguás-Araguás et al., 2000; Merlivat and Jouzel, 1979; Johnsen et al., 1989; Pfahl and Wernli, 2008; Pfahl and Sodemann, 2014).

We calculated *d*-excess during the monitoring period, using the monthly averaged $\delta^{18}O_p$ and δD_p data (Fig. 3C). Compared to the double-peak signal in the record of the isotopic composition of precipitation, a significant seasonal variation is evident, with higher values in winter and lower values in summer. For the Zhenzhu Cave area, which is very sensitive to changes in the summer and winter monsoon, the wind direction in summer is from the ocean towards the interior land, which is determined by the land-sea thermal gradient, or the local inland atmospheric circulation pattern. The temperature and relative humidity over the ocean result in a lower *d*-excess value than that of air masses originating from inland (Pfahl and Sodemann, 2014). By contrast, air masses transported by winter winds originate in high latitude regions, characterized by dry conditions and strong evaporation in the source area and by a long transport distance, resulting in a higher value of *d*-excess. In addition, based on NOAA/ARL HYSPLIT back trajectory modelling

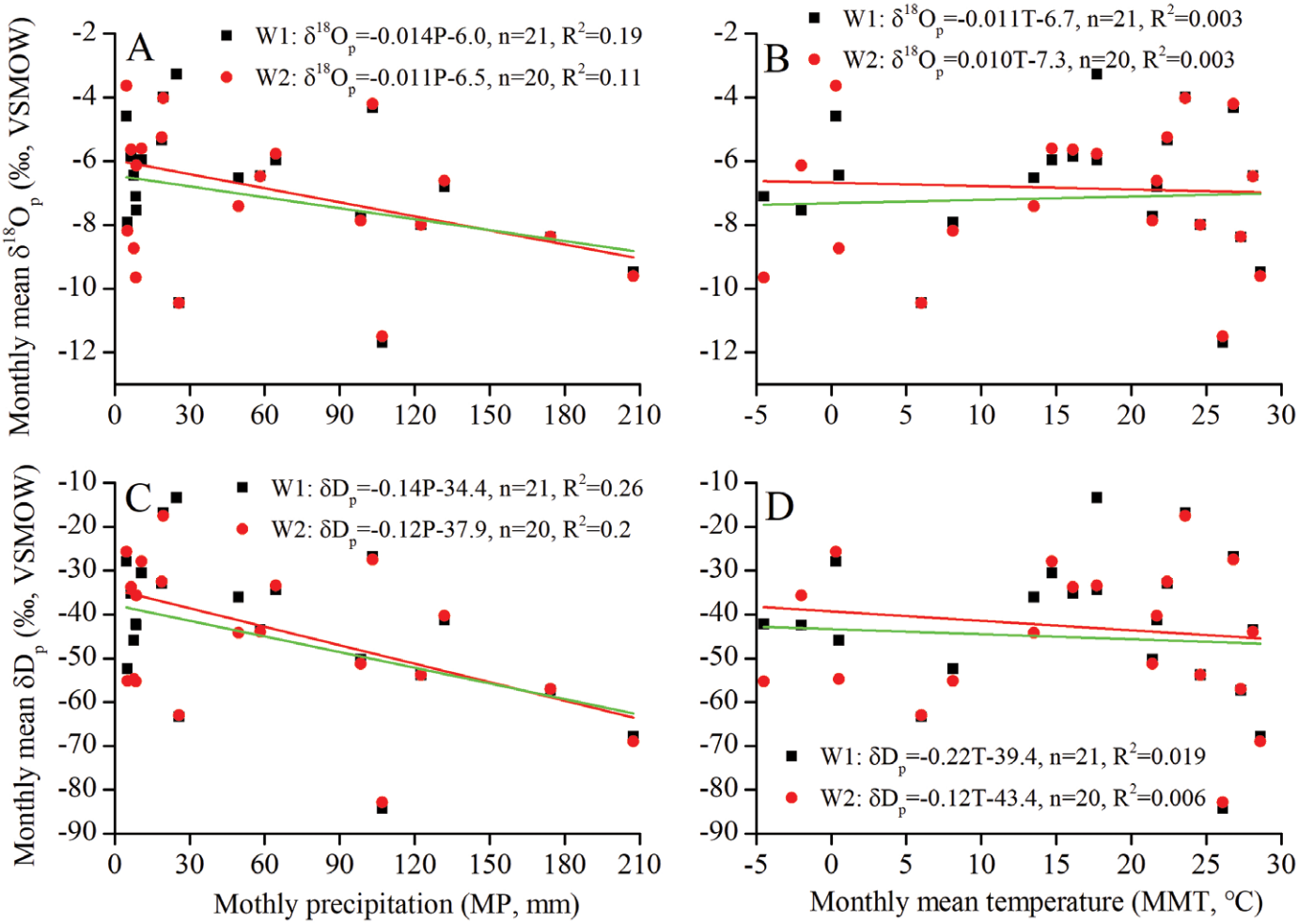

Figure 4. Relationship between monthly precipitation (MP, A) or monthly mean temperature (MMT, B) and monthly mean $\delta^{18}O_p$ for the Zhenzhu Cave area; C and D are the same as A and B, but for monthly mean δD_p.

(https://www.ready.noaa.gov/HYSPLIT_traj.php, Zhang et al., 2015), the air mass trajectory of a typical summer month (July 2013) and a typical winter month (January 2013) was determined weekly. Results demonstrated that the air mass trajectory in July 2013 was complex and mainly sourced from local inland circulation (Fig. 5). However, the air mass in January 2013 was mainly transported by northerly or westerly winds from high latitudes or by westerly winds far inland (Fig. 6), which is consistent with our *d*-excess data and results from previous research (Wang et al., 2003). On the other hand, this characteristic pattern of variation of *d*-excess is also in accord with the double-peak evident in the isotopic composition of precipitation mentioned above (Pfahl and Sodemann, 2014). Precipitation in the rainy season in the Zhenzhu Cave area is derived from local recycled vapor or oceanic sources, with lower values of precipitation isotopic compositions ($\delta^{18}O_p$ and δD_p) resulting from the rain-out effect. For the winter/dry season, precipitation is mainly sourced from remote inland air masses or polar air masses, with a long transport distance and evaporation, which finally result in lower isotopic values of precipitation.

Interannual variations

On an interannual scale, taking W1 for example, the amplitude of variation of $\delta^{18}O_p$, δD_p during April 2012 to February 2013 ($\delta^{18}O_p$: −11.7 ‰ to −4.0 ‰; δD_p: −84.4 ‰ to −16.9 ‰) was greater than that during the same period from 2013-2014 ($\delta^{18}O_p$: −8.4 ‰ to −5.4 ‰; δD_p: −57.4 ‰ to −30.5 ‰). In addition, the mean value of $\delta^{18}O_p$ (δD_p) weighted by monthly precipitation amount (MWP) for April 2012–February 2013 was −8.2 ‰ (−55.4 ‰), −8.6 ‰ (−60.0 ‰) for June 2012–September 2012 (warm/rainy season), and −8.4 ‰ (−50.5 ‰) for October 2012–February 2013 (cold/dry season). These values are lower than those for the same period in 2013–2014 (Table 1). On the other hand, meteorological data show that the total amount of precipitation during April 2012 to February 2013 (653.5 mm) was greater than that during April 2013–February 2014 (578.5 mm) (Table 1). Combining the corresponding MWP isotopic values for the aforementioned periods (Table 1), it suggests that the greater the rainfall amount, the more depleted the isotopic composition (i.e., the rainfall amount effect). This conclusion is tentative due to the relatively short monitoring period, however.

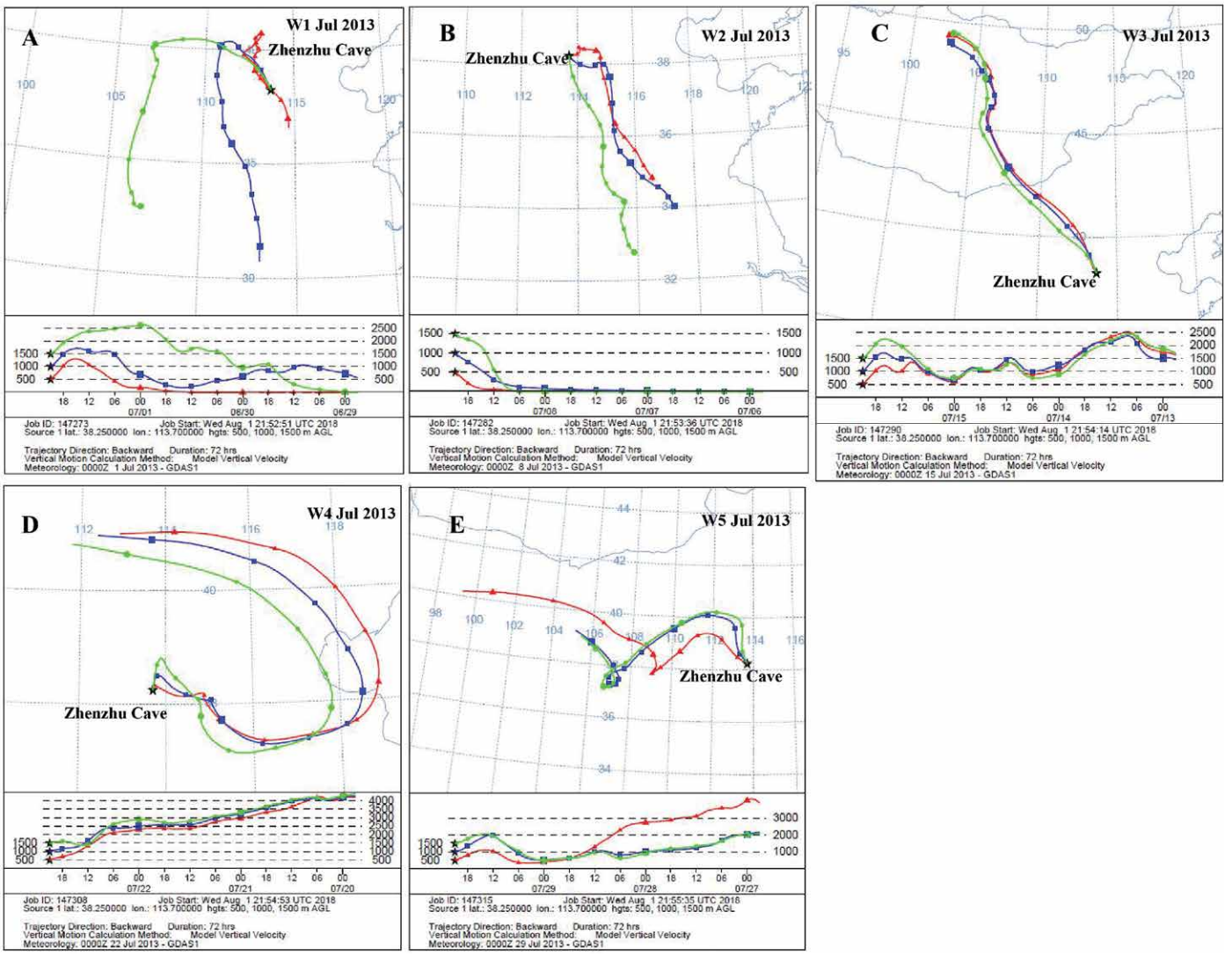

Figure 5. Weekly trajectory modeling of the air mass path in a typical summer month (July 2013) based on NOAA/ARL HYSPLIT.

To examine the relationships between $\delta^{18}O_p$ (and δD_p) and environmental variables (rainfall amount and temperature) on an interannual scale, due to the lack of monitoring data covering a longer interval, we referred to results of previous research (Li et al., 2015; Rao et al., 2016). Based on GNIP data from Shijiazhuang meteorological station, weighted mean annual $\delta^{18}O_p$ (and δD_p) spanning a 13-year interval was used to analyze the relationship between weighted mean annual $\delta^{18}O_p$ (and δD_p) and annual precipitation amount or annual mean temperature (Fig. 7). Results show that correlations between weighted mean annual $\delta^{18}O_p$ (and δD_p) and annual precipitation amount or annual mean temperature are weak (Fig. 7), and thus we cannot attribute the variation in $\delta^{18}O_p$ to a rainfall amount effect or temperature effect on interannual scales.

It has been suggested that the El Niño-Southern Oscillation (ENSO) cycle is the dominant control on the interannual variation in $\delta^{18}O_p$ in the monsoon regions of China, via its effect on the ratio of water vapor originating from distant oceanic sources (progressively depleted in $\delta^{18}O$) and local oceanic sources (relatively enriched in $\delta^{18}O$) at an observation site (Tan, 2014). Hence, we compared our precipitation isotopic values with an ENSO index, defined by the sea-surface temperature anomaly (SSTA) in the Niño 3.4 region (5°S – 5°N, 170°W – 120°W) in the tropical Pacific (NOAA, https://www.cpc.ncep.noaa.gov/data/indices/sstoi.indices). The results demonstrate that the pattern of variation of SSTA in the Niño 3.4 region is similar to that of the isotopic composition in precipitation, with the amplitude of variation in 2012-2013 greater than that during 2013–2014 (Fig. 3D), implying that the variation of the isotopic composition of precipitation during the monitoring period may be affected by the SSTA or by an atmosphere-ocean circulation anomaly, which can effect changes in moisture source or transport path, causing variations in the isotopic composition of precipitation. However, more research is needed to confirm this conclusion.

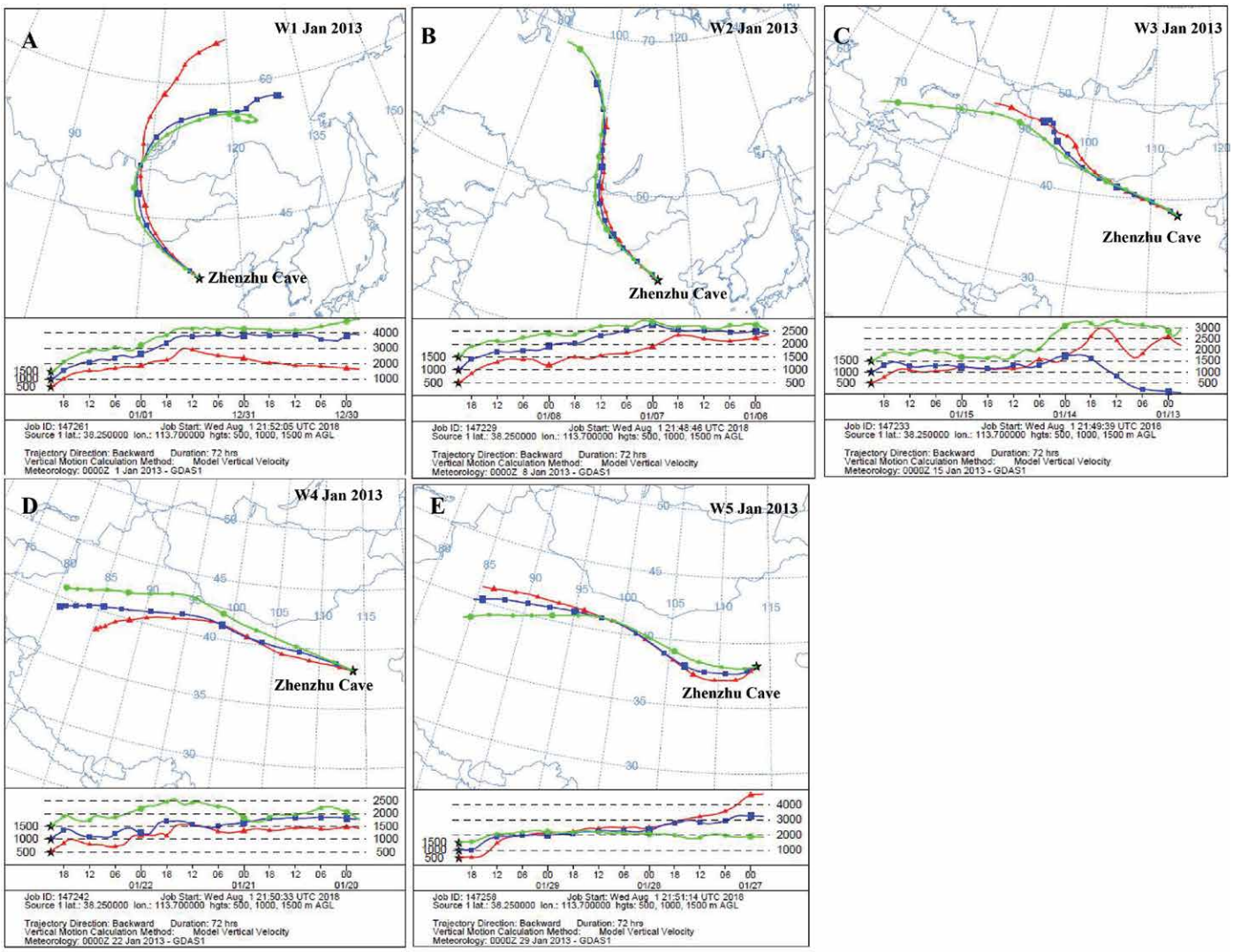

Figure 6. Weekly trajectory modeling of the air mass path in a typical winter month (January 2013) based on NOAA/ARL HYSPLIT.

Table 1. Summary of average temperature, total precipitation, mean $\delta^{18}O_p$ and δD_p, weighted by monthly precipitation amount (MWP), and average $\delta^{18}O_d$ and δD_d for specific periods for the Zhenzhu Cave area.

Projects for Statistics	April 2012–April 2014	April 2012–February 2013	June 2012–September 2012	October 2012–February 2013	April 2013–February 2014	June 2013–September 2013	October 2013–February 2014
Average temperature (°C)	14.4	14.55	25.7	3.2	14.8	25.4	5.1
Total precipitation (mm)	1260	653.5	515.9	53.8	578.5	486.9	23.3
MWP $\delta^{18}O_p$ (‰, VSMOW)	−7.7	−8.2	−8.6	−8.4	−7.3	−7.6	−6.9
MWP δD_p (‰, VSMOW)	−51.1	−55.4	−60.0	−50.5	−48.5	−50.3	−41.4
Average $\delta^{18}O_d$ (‰, VSMOW)	−9.1	−9.0	−9.0	−9.0	−9.1	−9.1	−9.1
Average δD_d (‰, VSMOW)	−62.1	−61.6	−61.5	−61.9	−62.4	−62.6	−61.3

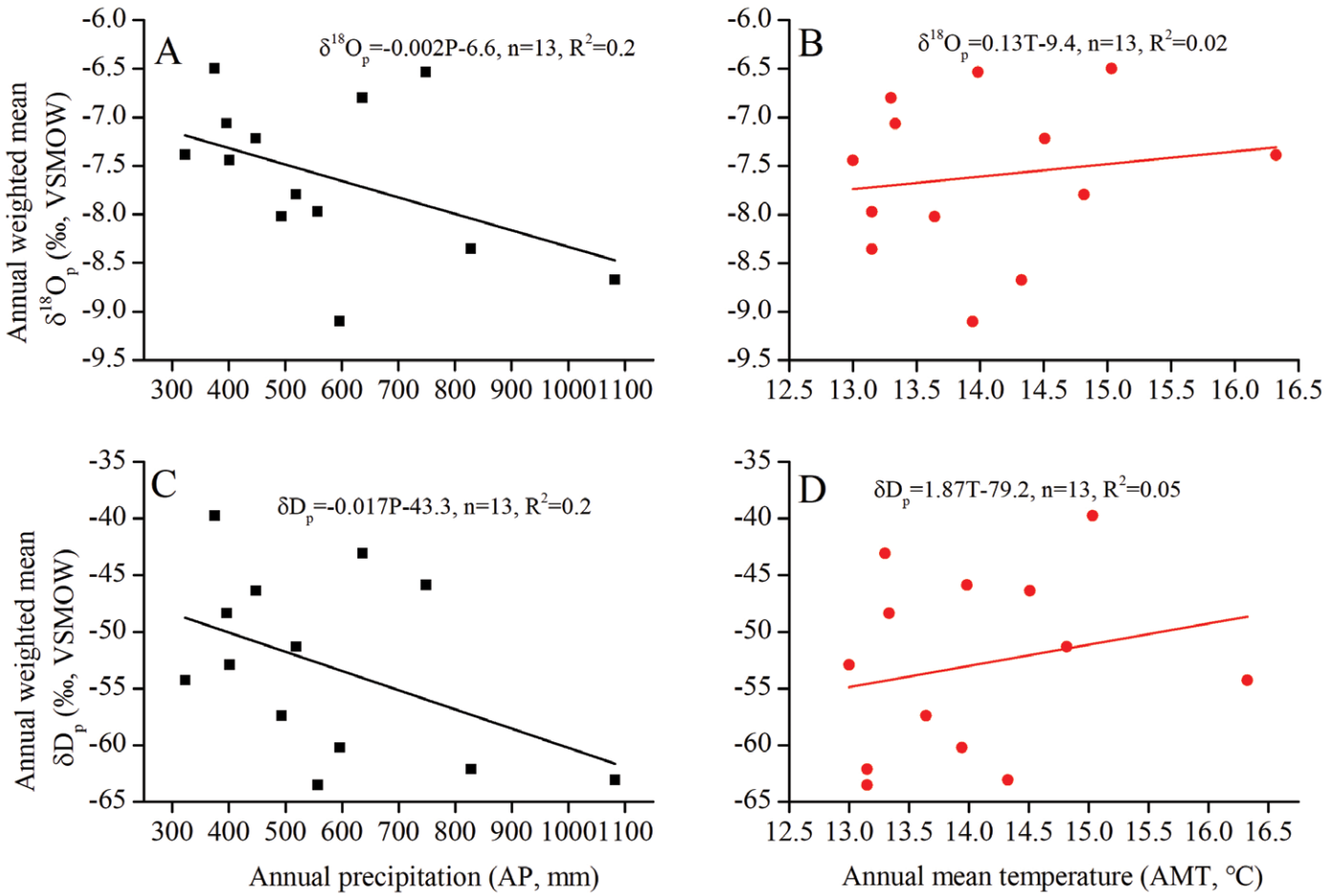

Figure 7. Relationships between annual weighted mean precipitation $\delta^{18}O$ and annual precipitation (A) or annual mean temperature (B) at Shijiazhuang.

In summary, the variation of the precipitation isotopic composition in the Zhenzhu Cave area during the monitoring period cannot be attributed solely to the rainfall amount effect or temperature effect, on either seasonal or interannual timescales.

Stable isotopic composition of drip water

Three drip monitoring sites (D1, D2 and D3) were sampled monthly. Drip rate were measured at the time of sample collection from April 2012–April 2014. All three sites had perennial drips, but the drip rates of all sites were very low (>30 minutes per drip).

The range of variation of the hydrogen (δD_d) and oxygen ($\delta^{18}O_d$) isotopic composition of drip water samples from the three sites was as follows. D1: δD_d: −62.9 ‰ to −60.1 ‰, and $\delta^{18}O_d$: −9.1 ‰ to −8.7 ‰; D2: δD_d: −63.7 ‰ to −60.1 ‰, and $\delta^{18}O_d$: −9.3 ‰ to −8.8 ‰; D3: δD_d: −63.8 ‰ to −59.9 ‰, and $\delta^{18}O_d$: −9.3 ‰ to −8.7 ‰. Isotopic compositions of drip water for some months are unavailable because of conditions such as limited drip water amount and evaporation during storage (Fig. 8, Supplementary 2).

Isotopic composition of the drip water samples generally plot close to or slightly below the LMWL (Fig. 2). In the meantime, the average value of $\delta^{18}O_d$ (δD_d) during the entire monitoring period is −9.1 ‰ (−62.1 ‰), which is close to or slightly more depleted than the $\delta^{18}O_p$ (δD_p) with values of −7.7 ‰ (−51.1 ‰) (Table 1), which indicates that in general $\delta^{18}O_d$ (δD_d) inherits the signal of the meteoric water above the caves (Luo and Wang, 2008; Pape et al., 2010; Genty et al., 2014). The drip water $\delta^{18}O_d$ (δD_d) plotting below the LMWL and the lower value of $\delta^{18}O_d$ (δD_d) may result from more depleted precipitation recharge of the drip water. Compared with the variation of the isotopic composition of precipitation (δD_p and $\delta^{18}O_p$), the $\delta^{18}O_d$ (δD_d) at the three sites had a low degree of variability (range of $\delta^{18}O_d < 1$ ‰), and a seasonal signal is absent (Fig. 8A), which is in accord with results in other cave sites (Genty et al., 2014; Duan et al., 2016). The pattern furthermore confirmed that the variation of $\delta^{18}O_d$ (δD_d) in drip water may be attributed to groundwater homogenization via the mixing of different timescales or multi-year timescales precipitation in the soil and epikarst zone above the cave (Williams and Fowler, 2002; Pape et al., 2010; Benton and Doctor, 2018; Eagle et al., 2015). The range

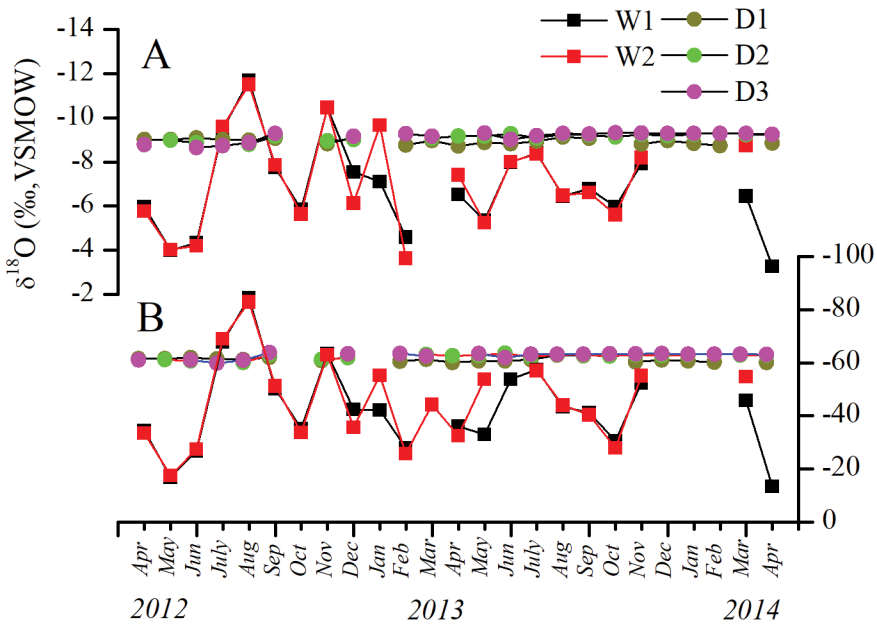

Figure 8. Time series of monthly water δ18O (A), δ D (B) for two precipitation and three drip sites in Zhenzhu Cave

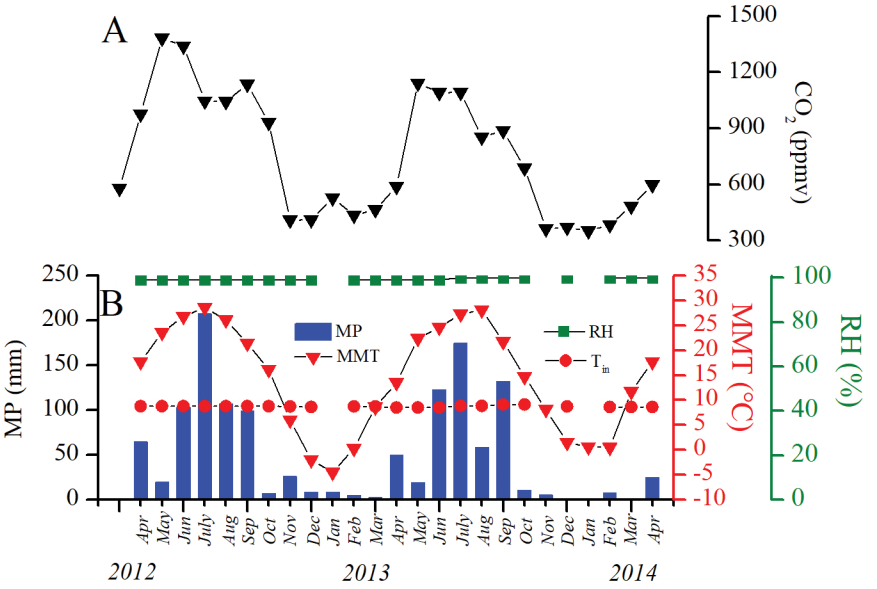

Figure 9. (A) Time series of cave air CO_2 concentration at Zhenzhu Cave; (B) variability of monthly precipitation (blue bars), monthly mean temperature (red triangles), and relative humidity (RH, green rectangle) inside the cave and cave air temperature (T_{in}, red dot).

of variation of the isotopic composition of the drip waters was small, implying that the resulting speleothem δ18O ($\delta^{18}O_s$) could not reflect seasonal-scale variations in the isotopic composition of precipitation in the Zhenzhu Cave region.

Cave air CO_2 concentration, cave air temperature and relative humidity

In contrast to δD_d and $\delta^{18}O_d$, cave air CO_2 concentration exhibits a clear seasonal pattern of variation, ranging between 352 to 1383 ppmv, with lower values in the winter/dry season and higher values in the summer/wet season (Fig. 9). The average temperature inside the cave is 9 °C, with a standard deviation of 1 °C, consistent with annual air temperature in this area (Fig. 9). The RH in Zhenzhu Cave is 99 % to 100 % during the entire monitoring period. These characteristics of cave air CO_2 concentration, T_{in}, and the RH in Zhenzhu Cave were also observed in other studies (Hu et al., 2007; Li et al., 2011; Pu et al., 2015).

The variability of cave air CO_2 concentration is mainly affected by CO_2 sources: including the overlying soil, bacterial oxidation of organic matter in the cave system, outside atmosphere CO_2, and deep gas diffusion or transport (Liñán et al. 2008; Pu et al., 2015). However, contributions of other factors (e.g., the concentration of the outside atmospheric CO_2 and deep gas diffusion or transport) were minor, compared to the ~1000 ppmv range observed in the CO_2 level of Zhenzhu Cave. Thus, we conclude that the variation of cave air CO_2 concentration in Zhenzhu Cave was dominated by variations in CO_2 generated in the overlying soil, which were controlled by vegetation conditions and biological activity. In addition, biological productivity of vegetation and soil above a cave are influenced by climatic variables such as precipitation and temperature.

As shown in Fig. 9, seasonal variations of cave air CO_2 concentration in Zhenzhu Cave are highly consistent with the surface monthly mean temperature (MMT) and monthly precipitation (MP). There is also a significant positive correlation between CO_2 concentration and MP or MMT (Fig. 10). During the warm/wet season, when vegetation and soil biological activity are flourishing, the biogenic production of CO_2 would increase. As the outside air temperature increases, cave ventilation effects resulting from the barometric pressure (or density) difference between the outside air and cave air begin to decrease and the soil CO_2 yield begins to increase. In addition, an increasing amount of CO_2 from the overlying soil enters the cave with dripwater (or seepage water) that passes through the zone, maintaining the cave air CO_2 concentration at a higher level because of the continuous supply from the soil (Buecher 1999; Fernandez-Cortes et al. 2009). In the dry/cold season, when biological activity and the outside air temperature are lower, the soil CO_2 yield would decrease. Colder and denser air with lower CO_2 concentration enters the cave via the entrance and karst fissures, diluting the cave air CO_2 and leading to lower cave air CO_2 concentration (Li et al., 2012; Liñán et al.

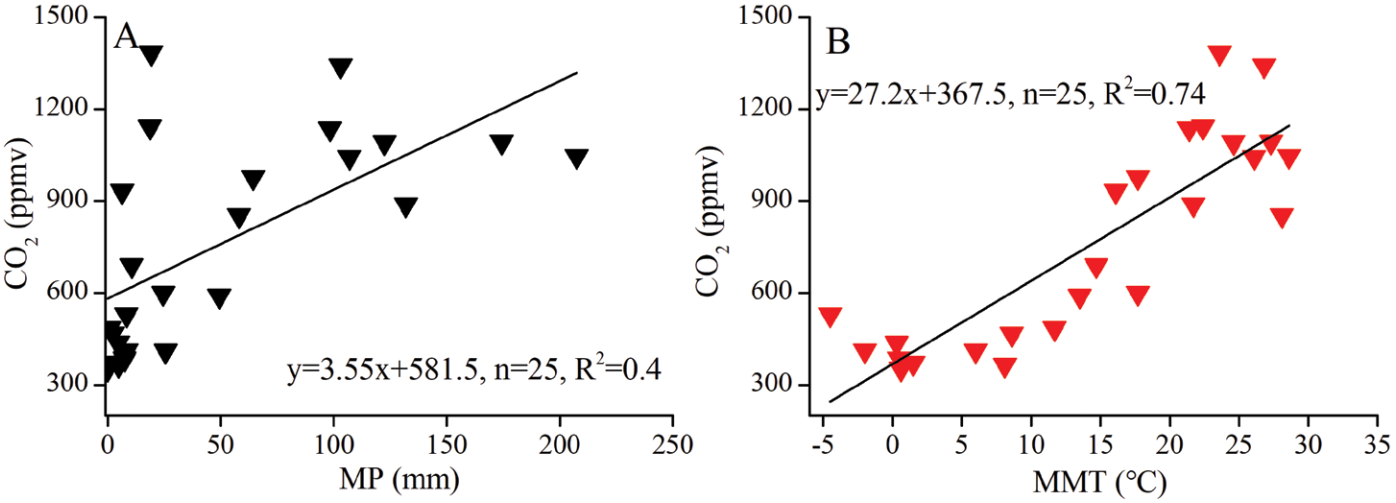

Figure 10. Linear regression between cave air CO_2 and MP (A) or MMT (B) for Zhenzhu Cave.

2008; 2015). However, statistical results including average temperature, total precipitation amount, and monthly mean CO_2 concentration during April–October of 2012 and 2013 (Table 2) show that the monthly mean CO_2 concentration during April–October of 2012 was greater than that during 2013, and was also the case for total precipitation, although the temperature was not significantly different between 2012 and 2013. The cave air CO_2 concentration may be more sensitive to precipitation variations. More sites for long-term monitoring are needed to verify these inferences.

In summary, climatic conditions (temperature and especially precipitation) outside the cave are likely responsible for

Table 2. Summary of average temperature, total precipitation, and monthly mean CO_2 concentration during April − October in 2012 and 2013 for the Zhenzhu Cave area.

Year	Average temperature (°C)	Total precipitation (mm)	Monthly mean CO_2 (ppmv)
2012	22.9	606.2	1122.6
2013	21.8	565.9	906.6

the seasonal changes in cave air CO_2 concentration, which may control cave ventilation and biological activity in the vegetation and soil overlying the cave.

Implications of results for paleoclimatic studies

Our findings have several implications for the use of stable isotope values of speleothems from Zhenzhu Cave for paleoclimatic reconstruction. First, in the study area, there is no significant correlation between the stable isotopic composition of precipitation and rainfall amount or air temperature, on either seasonal or interannual scales. Therefore, variations in precipitation isotopic composition cannot be interpreted as a proxy of local rainfall amount or air temperature on these timescales. Second, because the relatively constant isotopic composition of drip water is caused by the mixing of meteoric waters in the epikarst zone above Zhenzhu Cave, the isotopic composition of drip water should reflect the long-term weighted average composition of local precipitation above the cave. Therefore, paleoclimatic records based on the oxygen isotopic composition of speleothems growing from such drip sites should reflect multi-year variations in the climate of the Zhenzhu Cave area.

Cave air CO_2 is closely related to speleothem $\delta^{13}C$ ($\delta^{13}C_s$), which is demonstrated by the following: $\delta^{13}C_s$ is mainly influenced by the $\delta^{13}C$ of soil CO_2 and CO_2 degassing of the drip water, which are also the dominant factors controlling cave air CO_2 concentration. Conversely, cave air CO_2 concentration plays an important role in the degassing of CO_2 and carbonate reprecipitation, which in turn affect variations in $\delta^{13}C_s$ (Paulsen et al., 2003; Fairchild et al., 2006, 2009; Spötl et al., 2005). Thus, the study of cave air CO_2 complements and reinforces our interpretation of $\delta^{13}C_s$ records. The cave air CO_2 level in Zhenzhu Cave during April 2012–April 2014 exhibited distinct seasonal changes and were well-correlated with outside climate conditions especially precipitation. Climatic conditions outside the cave substantially influenced the variations of cave air CO_2 concentration. Furthermore, the history of vegetation changes and deforestation based on the $\delta^{13}C_s$ record covering the past millenium from Zhenzhu Cave has been successfully reconstructed (Yin et al., 2017). CO_2 results with seasonal variation may be useful for interpreting the significance of $\delta^{13}C_s$ on seasonal timescale.

Conclusions

The major conclusions of our two-year monitoring study of Zhenzhu Cave in north China are

1. In the study area there was no significant correlation between $\delta^{18}O_p$ and δD_p and precipitation and temperature on the seasonal and interannual scales. Variations in $\delta^{18}O_p$ (δD_p) cannot be interpreted solely by the temperature effect or amount effect. They could be influenced by other factors such as changes in moisture sources caused by changes in atmospheric circulation.
2. The narrow range of variation and absence of seasonality in the drip-water $\delta^{18}O_d$ (δD_d) values suggest that the drip water is derived from the mixing of different timescales or multi-year meteoric waters in the epikarstic zone. Thus, the $\delta^{18}O_s$ records of speleothems fed by this type of drip water should reflect multi-year variations in the isotopic composition of the local precipitation.
3. The CO_2 concentration of Zhenzhu Cave exhibited significant seasonal changes and was well-correlated with climate conditions especially precipitation, implying seasonal variations in CO_2 concentration likely impact the signatures of $\delta^{13}C_s$, and possibly providing a seasonal signal that does not appear in $\delta^{18}O_s$ data.

Acknowledgements

We appreciate the efforts of students from Hebei Normal University who joined us in field trips to the cave and provided assistance with sampling of precipitation and drip water. The work was supported by the Fundamental Research Funds for the Central Universities (lzujbky-2016-240, lzujbky-2018-it77), and the National Natural Science Foundation of China (Grant Nos. 41772373, 41428202, and 41372181).

References

Araguás-Araguás, L., Froehlich, K., and Rozanski, K., 2000, Deuterium and oxygen-18 isotope composition of precipitation and atmospheric moisture: Hydrological Processes, v. 14, no. 8, p. 1341−1355. https://doi.org/10.1002/1099-1085(20000615)14:8<1341::AID-HYP983>3.0.CO;2-Z.

Baker, A., Asrat, A., Fairchild, I. J., Leng, M. J., Wynn, P. M., Bryant, C., Genty, D., and Umer, M., 2007, Analysis of the climate signal contained within $\delta^{18}O$ and growth rate parameters in two Ethiopian stalagmites: Geochimica et Cosmochimica Acta, v. 71, no. 12, p. 2975−2988. https://doi.org/10.1016/j.gca.2007.03.029.

Banner, J. L., Guilfoyle, A., James, E. W., Stern, L. A., and Musgrove, M., 2007, Seasonal variations in modern speleothem calcite growth in central Texas, USA: Journal of Sedimentary Research, v. 77, no. 8, p. 615−622. https://doi.org/10.2110/jsr.2007.065.

Benton, J. R. and D. Doctor, 2018, Investigating Vadose Zone Hydrology in a karst terrain through hydrograph and chemical time series analysis of cave drips at Grand Caverns, Virginia: *In* NCKRI Symposium 7: Proceedings of the 15th Multidisciplinary Conference on Sinkholes and the Engineering and Environmental Impacts of Karst and the 3rd Appalachian Karst Symposium, p. 213−219.

Buecher, R. H., 1999, Microclimate study of Kitchener Caverns, Arizona: Journal of Cave and Karst Studies, v. 61, no. 2, p. 108–120.

Caballero, E., De Cisneros, C. J., and Reyes, E., 1996, A stable isotope study of cave seepage waters: Applied Geochemistry, v. 11, no. 4, p. 583−587. https://doi.org/10.1016/0883-2927(96)00026-1.

Chen, Z., 2010, The formation and evolution of Karst in Tianguishan area, Hebei Province: Master thesis, Hebei Normal University, Shijiazhuang, p. 15−16 (in Chinese with English abstract).

Cheng, H., Edwards, R. L., Broecker, W. S., Denton, G. H., Kong, X., Wang, Y., Zhang, R., and Wang, X., 2009, Ice Age Terminations: Science, v. 326, no. 5950, p. 248−252. https://doi.org/10.1126/science.1177840.

Cheng, H., Edwards, R. L., Wang, X. F., Wang, Y. J., Kong, X. G., Yuan, D. X., Zhang, M. L., Lin, Y. S., Qin, J. M., and Ran, J. C., 2005, Oxygen isotope records of stalagmites from southern China: Quaternary Science, v. 25, no. 2, p. 157–163 (in Chinese with English abstract).

Cheng, H., Zhang, P. Z., Spötl, C., Edwards, R. L., Cai, Y. J., Zhang, D. Z., Sang, W.C., Tan, M., and An, Z. S., 2012, The climatic cyclicity in semiarid-arid central Asia over the past 500,000 years: Geophysical Research Letters, v. 39, no. 1. https://doi.org/10.1029/2011GL050202.

Clemens, S. C., Prell, W. L., and Sun, Y., 2010, Orbital-scale timing and mechanisms driving Late Pleistocene Indo-Asian summer monsoons: Reinterpreting cave speleothem $\delta^{18}O$: Paleoceanography, v. 25, no. 4. https://doi.org/10.1029/2010PA001926.

Cosford, J., Qing, H., Mattey, D., Eglington, B., and Zhang, M., 2009, Climatic and local effects on stalagmite $\delta^{13}C$ values at Lianhua Cave, China: Palaeogeography, Palaeoclimatology, Palaeoecology, v. 280, no. 1-2, p. 235–244.

Craig, H., 1961, Isotopic variations in meteoric waters: Science, v. 133, no. 3465, p. 1702−1703. https://doi.org/10.1126/science.133.3465.1702.

Dansgaard, W., 1964, Stable isotopes in precipitation: Tellus, v. 16, no. 4, p. 436−468. https://doi.org/10.3402/tellusa.v16i4.8993.

Dayem, K. E., Molnar, P., Battisti, D. S., and Roe, G. H., 2010, Lessons learned from oxygen isotopes in modern precipitation applied to interpretation of speleothem records of paleoclimate from eastern Asia: Earth and Planetary Science Letters, v. 295, no. 1-2, p. 219−230. https://doi.org/10.1016/j.epsl.2010.04.003.

Ding, Y. H., and Chan, J. C. L., 2005, The East Asian summer monsoon: an overview: Meteorology and Atmospheric Physics, v. 89, no. 1-4, p. 117−142. https://doi.org/10.1007/s00703-005-0125-z.

Duan, W., Ruan, J., Luo, W., Li, T., Tian, L., Zeng, G., Zhang, D., Bai, Y., Li, J., Tao, T., Zhang, P., Baker, A., Tan, M., 2016, The transfer of seasonal isotopic variability between precipitation and drip water at eight caves in the monsoon regions of China: Geochimica et Cosmochimica Acta, v. 183, no. 15, p. 250−266. https://doi.org/10.1016/j.gca.2016.03.037.

Eagle, S., W. Orndorff, Schwartz, B., Doctor, D., Gerst, J. and Schreiber, M., 2015, Analysis of hydrologic and geochemical time-series data at James Cave, Virginia: Implications for epikarst influence on recharge in Appalachian karst aquifers: Geological Society of America Special Papers, v. 516, p. SPE516-15.

Fairchild, I. J., and Baker, A., 2012, Speleothem science: from process to past environments: v. 3, John Wiley & Sons. https://doi.org/10.1002/9781444361094.

Fairchild, I. J., and Treble, P. C., 2009, Trace elements in speleothems as recorders of environmental change: Quaternary Science Reviews, v. 28, no. 5-6, p. 449−468. https://doi.org/10.1016/j.quascirev.2008.11.007.

Fairchild, I. J., Smith, C. L., Baker, A., Fuller, L., Spötl, C., Mattey, D., and McDermott, F., 2006, Modification and preservation of environmental signals in speleothems: Earth-Science Reviews, v. 75, no. 1-4, p. 105−153. https://doi.org/10.1016/j.earscirev.2005.08.003.

Fernandez-Cortes, A., Sanchez-Moral, S., Cuezva, S., Cañaveras, J. C., and Abella, R., 2009, Annual and transient signatures of gas exchange and transport in the Castañar de Ibor cave (Spain): International Journal of Speleology, v. 38, no. 2, p. 6. https://doi.org/10.5038/1827-806X.38.2.6.

Feng, W., Banner, J. L., Guilfoyle, A. L., Musgrove, M., and James, E. W., 2012, Oxygen isotopic fractionation between drip water and speleothem calcite: A 10-year monitoring study, central Texas, USA: Chemical Geology, v. 304, p. 53−67. https://doi.org/10.5038/1827-806X.38.2.6.

Feng, W., Casteel, R. C., Banner, J. L., and Heinze-Fry, A., 2014, Oxygen isotope variations in rainfall, drip-water and speleothem calcite from a well-ventilated cave in Texas, USA: Assessing a new speleothem temperature proxy: Geochimica et Cosmochimica Acta, v. 127, p. 233−250. https://doi.org/10.1016/j.gca.2013.11.039.

Genty, D., Labuhn, I., Hoffmann, G., Danis, P. A., Mestre, O., Bourges, F., Wainer, K., Massault, M., Van Exter, S., Regnier, E., Orengo, P., Falourd, S., and Minster, B., 2014, Rainfall and cave water isotopic relationships in two south France sites: Geochimica et Cosmochimica Acta, v. 131, p. 323−343. https://doi.org/10.1016/j.gca.2014.01.043.

Hu, C., Henderson, G., Huang, J., Chen, Z., and Johnson, K., 2008, Report of a three-year monitoring programme at Heshang Cave, central China: International Journal of Speleology, v. 37, p. 143–151. https://doi.org/10.5038/1827-806X.37.3.1.

Johnsen, S. J., Dansgaard, W., and White, J. W. C., 1989, The origin of Arctic precipitation under present and glacial conditions: Tellus B, v. 41, p. 452−468. https://doi.org/10.3402/tellusb.v41i4.15100.

Lambert, W. J., and Aharon, P., 2011, Controls on dissolved inorganic carbon and $\delta^{13}C$ in cave waters from DeSoto Caverns: implications for speleothem $\delta^{13}C$ assessments: Geochimica et Cosmochimica Acta, v. 75, no. 3, p. 753–768. https://doi.org/10.1016/j.gca.2010.11.006.

Li, T., Li, H., Xiang, X., Kuo, T. S., Li, J., Zhou, F., Chen, H., and Peng, L., 2012, Transportation characteristics of $\delta^{13}C$ in the plants-soil-bedrock-cave system in Chongqing karst area: Science China Earth Sciences, v. 55, no. 4, p. 685−694. https://doi.org/10.1007/s11430-011-4294-y

Li, T. Y., Shen, C. C., Li, H. C., Li, J. Y., Chiang, H. W., Song, S. R., Yuan, D. X., Lin, C. D.-J., Gao, P., Zhou, L. P., Wang, J. L., Ye, M. Y., Tang, L. L., Xie, S. Y., 2011, Oxygen and carbon isotopic systematics of aragonite speleothems and water in Furong Cave, Chongqing, China: Geochimica et Cosmochimica Acta, v. 75, no. 15, p. 4140−4156. https://doi.org/10.1016/j.gca.2011.04.003.

Li, Y. X., Rao Z. G., Liu, X. K., Jin, M., and Chen, F. H., 2015, Interannual correlations between modern precipitation $\delta^{18}O$ and precipitation amount recorded by GNIP stations in China and India: Chinese Science Bulletin, v. 60, no. 80, p. 741–743 (in Chinese with English abstract). https://doi.org/10.1360/N.972014-00838.

Liñán, C., Vadillo, I., and Carrasco, F., 2008, Carbon dioxide concentration in air within the Nerja Cave (Malaga, Andalusia, Spain): International Journal of Speleology, v. 37, p. 99–106. https://doi.org/10.5038/1827-806X.37.2.2.

Liu, J. B., Chen, J. H., Zhang, X. J., Li, Y., Rao, Z. G., and Chen, F. H., Holocene East Asian summer monsoon records in northern China and their inconsistency with Chinese stalagmite $\delta^{18}O$ records: Earth-Science Reviews, v. 148, p. 194−208. https://doi.org/10.1016/j.earscirev.2015.06.004.

Liu, J., Song, X., Yuan, G., Sun, X., Liu, X., Wang, Z., and Wang, S., 2008, Stable isotopes of summer monsoonal precipitation in southern China and the moisture sources evidence from $\delta^{18}O$ signature: Journal of Geographical Sciences, v. 18, no. 2, p. 155−165. https://doi.org/10.1007/s11442-008-0155-9.

Liu, J., Song, X., Yuan, G., Sun, X., Liu, X., and Wang, S., 2009, Characteristics of $\delta^{18}O$ in precipitation over Eastern Monsoon China and the water vapor sources: Chinese Science Bulletin, v. 54, no. 2, p. 3521−3531.

Liu, J., Song, X., Yuan, G., Sun, X., and Yang, L., 2014, Stable isotopic compositions of precipitation in China: Tellus B: Chemical and Physical Meteorology, v. 66, no. 1, 22567.

Luo, W. J., and Wang, S. J., 2008, Transmission of oxygen isotope signals of precipitation-soil water-drip water and its implications in Liangfeng Cave of Guizhou, China: Chinese Science Bulletin, v. 53, no. 21, p. 3364−3370.

Merlivat, L., and Jouzel, J., 1979, Global climatic interpretation of the deuterium-oxygen 18 relationship for precipitation, Journal of Geophysical Research, v. 84, no. C8, p. 5029−5033. https://doi.org/10.1029/JC084iC08p05029.

Pape, J. R., Banner, J. L., Mack, L. E., Musgrove, M., and Guilfoyle, A., 2010, Controls on oxygen isotope variability in precipitation and cave drip waters, central Texas: USA, Journal of Hydrology, v. 385. no. 1-4, p. 203−215. https://doi.org/10.1016/j.jhydrol.2010.02.021.

Paulsen, D. E., Li, H. C., and Ku, T. L., 2003, Climate variability in central China over the last 1270 years revealed by high-resolution stalagmite records: Quaternary Science Review, v. 22, no. 5-7, p. 691−701. https://doi.org/10.1016/S0277-3791(02)00240-8.

Pausata, F. S., Battisti, D. S., Nisancioglu, K. H., and Bitz, C. M., 2011, Chinese stalagmite $\delta^{18}O$ controlled by changes in the Indian monsoon during a simulated Heinrich event: Nature Geoscience, v. 4, no. 7, p. 474−480. https://doi.org/10.1038/ngeo1169.

Pfahl, S., and Sodemann, H., 2014, What controls deuterium excess in global precipitation?: Climate of the Past, v. 10, no. 2, p. 771−781. https://doi.org/10.5194/cp-10-771-2014.

Pfahl, S., and Wernli, H. 2008, Air parcel trajectory analysis of stable isotopes in water vapor in the eastern Mediterranean: Journal of Geophysical Research, v. 113, no. D20104. https://doi.org/10.1029/2008JD009839.

Pu, J., Wang, A., Yin, J., Shen, L., Sun, Y., Yuan, D., and Zhao, H., 2015, Processes controlling dripwater hydrochemistry variations in Xueyu Cave, SW China: implications for speleothem palaeoclimate signal interpretations: Boreas, v. 44, no. 3, p. 603−617. https://doi.org/10.1111/bor.12117.

Rao, Z. G., Li, Y. X., Zhang, J. W., Jia, G. D., and Chen, F. H., 2016, Investigating the long-term palaeoclimatic controls on the δD and $\delta^{18}O$ of precipitation during the Holocene in the Indian and East Asian monsoonal regions: Earth-Science Reviews, v. 159, p. 292−305. https://doi.org/10.1016/j.earscirev.2016.06.007.

Rao, Z. G., Liu, X. K., Hua, H., Gao, Y. L., and Chen, F. H., 2015, Evolving history of the East Asian summer monsoon intensity during the MIS5: inconsistent records from Chinese stalagmites and loess deposits: Environmental Earth Sciences, v. 73, no. 7, p. 3937−3950. https://doi.org/10.1007/s12665-014-3681-z.

Rozanski, K., Sonntag, C., and Münnich, K. O., 1982, Factors controlling stable isotope composition of European precipitation: Tellus, v. 34, no. 2, p. 142–150. https://doi.org/10.3402/tellusa.v34i2.10796.

Ruan, J. Y. and Hu, C. Y., 2010, Seasonal variations and environmental controls on stalagmite calcite crystal growth in Heshang Cave, central China: Chinese Science Bulletin, v. 55, no. 34, p. 3929−3935. https://doi.org/10.1007/s11434-010-4193-1.

Spötl, C., Fairchild, I. J., and Tooth, A. F., 2005, Cave air control on dripwater geochemistry, Obir Caves (Austria): implications for speleothem deposition in dynamically ventilated caves: Geochimica et Cosmochimica Acta, v. 69, no. 10, p. 2451–2468. https://doi.org/10.1016/j.gca.2004.12.009.

Tan, M., 2009, Circulation effect: climatic significance of the short term variability of the oxygen isotopes in stalagmites from monsoonal China—dialogue between paleoclimate records and modern climate research: Quaternary Science, v. 29, no. 5, p. 851−862. (in Chinese with English abstract)

Tan, M., 2014, Circulation effect: response of precipitation $\delta^{18}O$ to the ENSO cycle in monsoon regions of China: Climate Dynamic, v. 42, no. 3-4, p. 1067−1077. https://doi.org/10.1007/s00382-013-1732-x.

Wang, B., Clemens, S. C., and Liu, P., 2003, Contrasting the Indian and East Asian monsoons: implications on geologic timescales: Marine Geology, v. 201, no. 1-3, p. 5−21. https://doi.org/10.1016/S0025-3227(03)00196-8.

Wang, J., Chen, Z., Zhang, M. P., and Huang, H. F., 2011, The genetic sorts of the typical karst caves in Tianguishan, Hebei province: Journal of Mountain Science, v. 29, no. 2, p. 188−194 (in Chinese with English abstract).

Wang, Y. J., Cheng, H., Edwards, R. L., An, Z. S., Wu, J. Y., Shen, C. C., and Dorale, J. A., 2001. A high-resolution absolute dated late Pleistocene monsoon record from Hulu Cave, China: Science, v. 294, no. 5550, p. 2345−2348. https://doi.org/10.1126/science.1064618.

Wang, Y. J., Cheng, H., Edwards, R. L., Kong, X. G., Shao, X. M., Chen, S. T., Wu, J. Y., Jiang, X. Y., Wang, X. F., and An, Z. S., 2008, Millennial- and orbital-scale changes in the East Asian monsoon over the past 224,000 years: Nature, v. 451, p. 1090−1093. https://doi.org/10.1038/nature06692.

Welker, J.M., 2000, Isotopic ($\delta^{18}O$) characteristics of weekly precipitation collected across the USA: An initial analysis with application to water source studies: Hydrological Processes, v. 14, no. 8, p. 1449−1464. https://doi.org/10.1002/1099-1085(20000615)14:8<1449::AID-HYP993>3.0.CO;2-7.

Williams, P. W., and Fowler, A., 2002, Relationship between oxygen isotopes in rainfall, cave percolation waters and speleothem calcite at Waitomo, New Zealand: Journal of Hydrology (New Zealand), v. 41, p. 53−70.

Yin, J. J., Li, H. C., Rao, Z. G., Shen, C. C., Mii, H. S., Pillutla, R. K., Hu, . M., Li, Y. X., Feng, X. H., 2017, Variations of monsoonal rain and vegetation during the past millennium in Tiangui Mountain, north China reflected by stalagmite $\delta^{18}O$ and $\delta^{13}C$ records from Zhenzhu Cave: Quaternary International, v. 447, p. 89−101. https://doi.org/10.1016/j.quaint.2017.06.039.

Zhang, M. L., Zhu, X. Y., Wu, X., Yin, J. J., and Pan, M. C., 2015, $\delta^{18}O$ characteristics of meteoric precipitation and its water vapor sources in the Guilin area of China: Environmental Earth Sciences, v.74, no. 2, p. 953−976. https://doi.org/10.1007/s12665-014-3827-z.

Zheng, S. H., Hou, F. G., and Ni, B. L., 1983, Study on the hydrogen and oxygen stable isotopes in meteoric precipitation of China: Chinese Science Bulletin, v. 13, p. 801−806 (in Chinese).

Zhou, T. J., and Yu, R. C., 2005, Atmospheric water vapor transport associated with typical anomalous summer rainfall patterns in China: Journal of Geophysical Research, v. 110, no. D08104. https://doi.org/10.1029/2004JD005413.

Okan Külköylüoğlu, Mehmet Yavuzatmaca, Derya Akdemir, Benjamin F. Schwartz, Benjamin T. Hutchins. Description of a new tribe *Cabralcandonini* (Candonidae, Ostracoda) from karst aquifers in central Texas, U.S.A. *Journal of Cave and Karst Studies*, v. 81, no. 2, p. 136-151. DOI:10.4311/2018ES0128

DESCRIPTION OF A NEW TRIBE *CABRALCANDONINI* (CANDONIDAE, OSTRACODA) FROM KARST AQUIFERS IN CENTRAL TEXAS, U.S.A.

Okan Külköylüoğlu[1, C], Mehmet Yavuzatmaca[1], Derya Akdemir[2], Benjamin F. Schwartz[3,4], Benjamin T. Hutchins[4,5]

ABSTRACT

Cabralcandonini tribe n., with the type genus *Cabralcandona* gen. n. from an artesian well in the San Marcos, Texas (U.S.A.) and six other genera from karst aquifers in Texas, is proposed as a new tribe of the subfamily Candoninae (Candonidae) (Crustacea, Ostracoda). The new tribe and genus have morphological features that distinguish them from other members of the subfamily. The most diagnostic characteristics of the type genus are (1) two horn-like structures developed on the antero- and postero-dorsal margins of the left valve, (2) numbers of central muscle scars, (3) hexagonal or pentagonal (honeycomb-like) ornamentation on the subrectangular shaped carapace, (4) four segmented second antenna in both sexes, (5) absence of an exopod on A2, (6) shape and size of Y aesthetasc, (7) absence of e, f and g setae on cleaning leg, (8) flagellum (whip-like) uropod morphology, (9) shape of hemipenis, and (10) reduction in number of segments and setae on other limbs. Taxonomic keys for the tribes of the subfamily Candoninae including Cabralcandonini tribe n. are presented.

Introduction

Artesian wells are windows into otherwise inaccessible deep aquifer systems, and flowing artesian wells bring groundwater directly from the aquifer to the land surface. The name “artesian” traces its origins to the Province of Artois, France (Carpenter, 1891), where artesian groundwaters have been tapped for centuries. Natural and man-made artesian systems can support human usage, hypogean organisms, and many ecosystems including lentic and lotic aquatic habitats (Danielopol, 1978; Holsinger and Longley, 1980; Ponder, 2004; Külköylüoğlu, 2009; Culver and Pipan, 2009; Garza et al., 2015).

Artesian wells often discharge hypogean organisms, and some wells have a long history of intensive biological monitoring and sampling. Because of these efforts, and the fact that they allow access into an otherwise-inaccessible ecosystem, some artesian wells are associated with unique and high species diversity. Increasing our knowledge of groundwater species abundance and diversity, along with the biogeographic and ecologic processes that have contributed to observed diversity patterns, can support sound conservation activities and policies (Lopez et al., 2017).

Ostracods are small (adult freshwater forms range from 0.3 to 5.4 mm in length) aquatic invertebrates and are one of the most abundant and diverse groups of Crustacea. They can be found in almost all marine to freshwater habitats in natural (springs, creeks, rivers, pools, lakes, ditches etc.) and artificial settings (e.g., troughs, wells, canals, dams, ponds, etc.). Ostracods have a pair of valves (a carapace) composed of low magnesium / calcium ratio calcite (Chivas et al., 1986). Because of this calcified carapace, ostracods can be fossilized in sediments and are known from at least the Silurian period, about 425 Ma (Siveter, 2008; Williams et al., 2008). Individual species prefer certain environmental conditions (Külköylüoğlu, 1998), therefore, ostracods are excellent model organisms for evolutionary (Cohen and Johnston, 1987; Chaplin and Ayre, 1997), ecological (De Deckker, 1981; Külköylüoğlu, 2009), biological (Kesling and Crafts, 1962; Lopez et al., 2002) and paleontological studies (Tunoğlu, 2002; Tuncer and Tunoğlu, 2015). In addition, they are useful as indicators of water quality (Hoff, 1942; Wise, 1961; Bromley and Por, 1975; Benson, 1990; Mezquita et al., 1999; Külköylüoğlu and Vinyard, 2000).

The family, Candonidae, known for its worldwide distribution (Danielopol, 1978; Danielopol et al., 2011; Smith, 2011), contains at least 515 species (Martens and Savatenalinton, 2011; Külköylüoğlu et al., 2017a-e). Karanovic (2018) stated that no species of Candonopsini have ever been recorded from North America due to a lack of freshwater ostracod studies on the continent, failing to recognize the several genera and species (e.g., *Comalcandona, Lacrimacandona, Ufocandona, Rugosuscandona*) reported from Texas groundwaters (Külköylüoğlu et al., 2011; 2017a-d; 2018). Although there is debate about the taxonomic position of some species (see. e.g., Higuti and Martens, 2012; 2014), there are more than 46 genera described in the subfamily Candoninae (Karanovic, 2001; Külköylüoğlu et al., 2011; Külköylüoğlu et al., 2017a-e; Külköylüoğlu and Gibson, 2018). Most recently, descriptions of 5 new species from Texas (Külköylüoğlu

[1]Department of Biology, Faculty of Arts and Science, Bolu Abant İzzet Baysal University, 14280, Bolu, Turkey.
[2]Institute of Geology and Mineralogy, University of Cologne, Zülpicher Straße 49A, 50674 Cologne, Germany.
[3]Edwards Aquifer Research and Data Center, Texas State University, San Marcos, TX 78666, USA
[4]Department of Biology, Texas State University, San Marcos, TX 78666, USA
[5]Texas Parks and Wildlife Department, 4200 Smith School Road, Austin TX 78744, USA
[C]Corresponding Author: kulkoyluoglu_o@ibu.edu.tr

et al., 2017a-e) increased the number of known species in the subfamily to 47 with 10 genera in North America. Of these, there are now more than 33 species endemic to North America (Karanovic, 2006; Külköylüoğlu et al., 2017a-e). Because of known undescribed taxa and a lack of studies in the area, these numbers are believed to be underestimated for the subfamily.

Here, we propose *Cabralcandonini* tribe n. and *Cabralcandona* gen. n. with the type species (*Cabralcandona mixoni* sp. n.) from the San Marcos Artesian Well, San Marcos, Texas, U.S.A.: the sixth genus found and described from this well. Six genera (*Ufocandona*, *Rugosuscandona, Lacrimacandona, Schornikovdona, Comalcandona, Bicornucandona*) previously included in other tribes are also transferred into the new tribe due to shared characteristics in carapace and soft body parts (see Külköylüoğlu et al., 2017a,b).

Methods

Site Description

The San Marcos Artesian Well (SMAW) (Fig. 1) is known for its exceptional biodiversity (Longley, 1981; Culver and Sket, 2000; Hutchins et al., 2014, 2016; Külköylüoğlu et al., 2017a-e; Külköylüoğlu and Gibson, 2018). It was completed in a relatively shallow portion of the confined zone of the San Antonio Pool in the Edwards Aquifer of Texas in 1895 (Stejneger, 1896). At 59.5 m deep, the well intersects a 1.5 m tall conduit (Holsinger and Longley, 1980) from which the water and biological materials are presumed to discharge. Excluding the new species proposed herein, 36 stygobiont species are known from the well (Hutchins 2018), and the number is rapidly increasing as renewed efforts describe undocumented diversity. Ten of these species (an undescribed erpobdellid leech, the cyclopoid copepod *Cyclops cavernarum* Ulrich, 1902, the asellid isopod *Lirceolus smithii* (Ulrich 1902), the helminth parasites *Amphibiocapillaria texensis* Moravec & Huffman 2000 and *Dendronucleata americana* Moravec & Huffman 2000, and five ostracods (Külköylüoğlu et al., 2017a-e)) are only known from the single site or the nearby San Marcos Spring (Chippindale, 2000; Hutchins et al., 2014, 2016; Külköylüoğlu et al., 2017a-e). More than 50 % of the 51 described stygobiont species known from this central Texas region are endemic to the Edwards Aquifer (Hutchins, 2018). However, considering the number of documented undescribed taxa and lack of in-depth studies in the region, the actual diversity of the well and aquifers are unknown, and higher species richness certainly exists (Schwartz et al., 2018).

Water quality is generally high at the site, which has been dye traced to San Marcos Springs, less than 1 km to the northeast (see details in Ogden et al., 1986). In November 2013, water temperature at the well averaged 22.3 °C (SD $\pm$ 0.01), dissolved oxygen averaged 5.3 mg/l (SD $\pm$ 0.01) and electrical conductivity averaged 608 µS/cm (SD $\pm$ 0.50).

Sample Collection and Description

All materials were collected from the type locality (Fig. 1) with a drift-net (100 µm mesh size) placed on the outflow pipe. Sample collection intervals ranged from 24 to 72 hours, and each sample was sorted under a dissecting microscope to count and identify all invertebrates to lowest taxonomic level (species, for most organisms). All organisms were stored in 95 % ethanol in glass vials with poly-seal caps.

Ostracods were dissected in lactophenol solution using fine needles under a stereomicroscope, and soft body parts were mounted on glass slides, covered with coverslips, and sealed with clear fingernail polish. Each slide was labeled with a unique catalog number. Valves were kept in micropaleontological slides whenever possible. External views of carapace and valves were acquired by Scanning Electron Microscope (JEOL 6335 F SEM) after ostracods were prepared with hexamethyldisilazane (HMDS) as a drying agent at the TÜBİTAK-MAM Institute (Gebze, Turkey). SEM images of the internal views of the valves were also taken with Scanning Electron Microscope at the Research Service Center, Texas State University (U.S.A.). Line drawings of the soft body parts of holotype and allotype specimens were made with a camera lucida (Olympus U-DA) attached to an Olympus BX-51 microscope before the drawings were digitized in Adobe Illustrator CS5 (ADOBE). The following literature was used during species description: Broodbakker and Danielopol, 1982; Martens, 1987; Meisch, 2000, and Karanovic, 2004, 2005a-c, 2006, 2007, 2011, 2012, 2013, 2018. Methodological details can be found in Külköylüoğlu et al. (2017a-e). Materials and slides prepared for identification (catalog numbers OK-TX-AW036-055: 07-12) are stored at the Limnology Laboratory of the Biology Department, Abant İzzet Baysal University (Bolu, Turkey), and are available upon request.

Clustering Analyses

WinClada, version 1.00.08 (Nixon, 2002) along with the NONA program was used to elucidate best clustering relationships among 49 genera of the subfamily Candoninae. Two outgroup genera, *Cypria* and *Cyclocypris*, were chosen due to their distinct morphological characteristics compared to genera of the subfamily (for details see Karanovic, 2007). All of the 31 morphological characters (Table 1) and taxa used in the reduced model of Karanovic (2007) were included. We added 5 more characters and 10 genera published since 2007 to this data matrix (Table 1). Additional characters were chosen based on their importance for identification and prevalence in current taxonomic keys (e.g., see Meisch, 2000; Karanovic, 2007, 2012; Higuti and Martens, 2012, 2014). For example, there were no character states of Mxl in the origi-

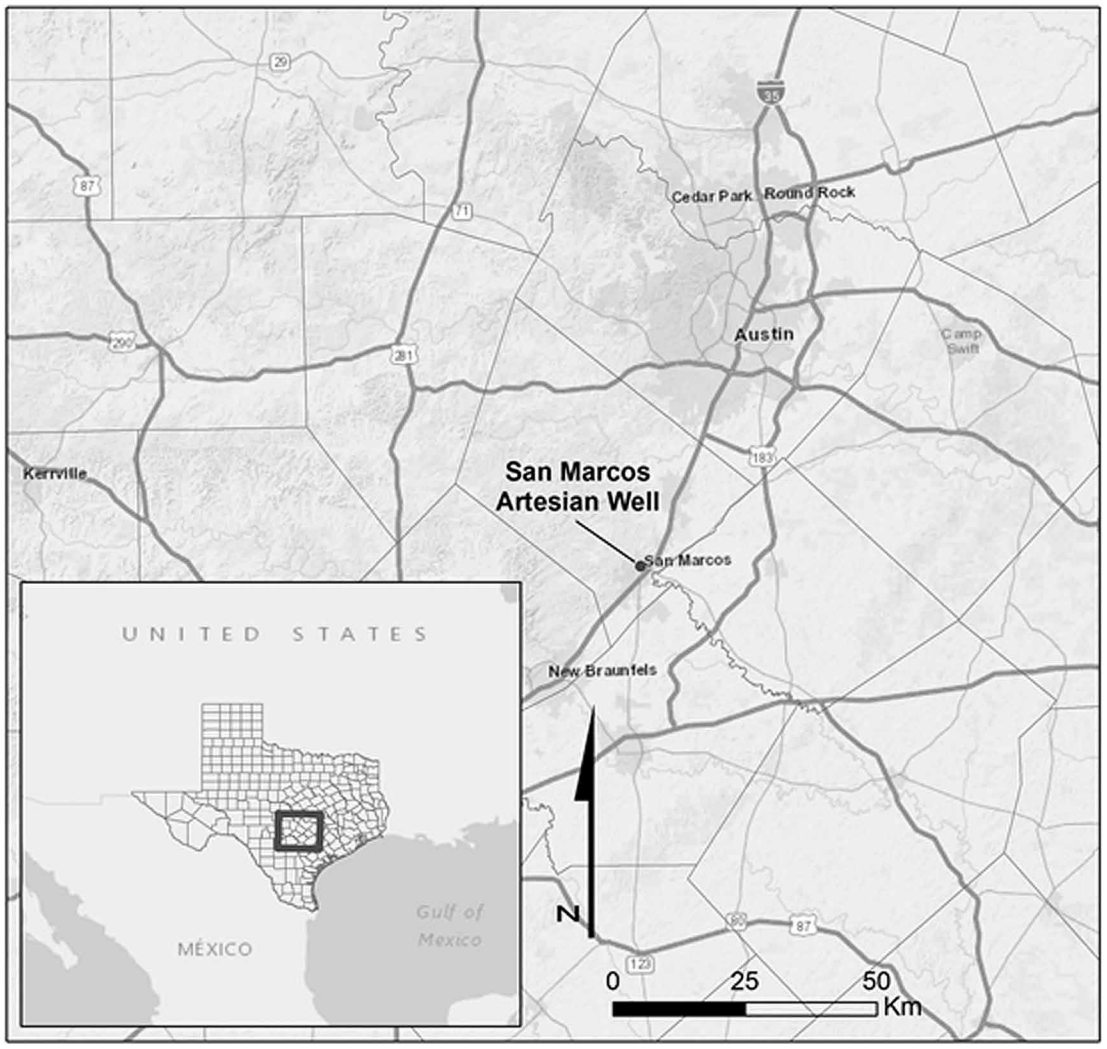

Figure 1. Type locality of *Cabralcandona mixoni* gen. et sp. nov. from Texas, U.S.A.

nal data matrix of Karanovic (2007). However, Mxl appears around the 7th larval (A7) stage (Meisch, 2000; Smith and Martens, 2000; Díaz and Lopretto, 2017) and is therefore an important character used in taxonomic keys. All characters in the data matrix were coded and weighted during computation of consistency (Ci) and retention (Ri) indices. As described in Karanovic (2007), except for the characters 23−30 and 33, which were weighted by 2, all characters were weighted by 1. Phylogenetic analysis was conducted via a heuristic search in WinClada-Nona along with the following default parameters of the Rachet Island Hopper application whenever possible: 200 replications; 1 tree to hold/iteration; 3 characters to sample; 10 random constraint levels and amb-poly= (amb: collapsing a branch if the ancestor and descendant have different states under the same resolutions of multi state characters or character states are unknown; poly: treating trees as collapsed). During which, tree bisection and reconnection (TBR+TBR) method of branch-swapping was repeated to search for the trees where the tree is cut about half and reconnected the remaining branches.

Abbreviations

A1, first antenna; A2, second antenna; G1−G3 and GM, Gm, claws on A2; H, height; L, length; LV, left valve; Md, mandibula; Mxl, maxillula; RV, right valve; T1, first thoracopod; T2, second thoracopod; T3, third thoracopod; UR, uropod; W, width.

Results

Systematic Description
Class: Ostracoda Latreille, 1802
Subclass: Podocopa Sars 1866
Order: Podocopida Sars, 1866
Suborder: Cypridocopina Baird, 1845
Superfamily: Cypridoidea Baird, 1845
Family: Candonidae Kaufmann, 1900
Subfamily: Candoninae Kaufmann, 1900
Tribe: Cabralcandonini tribe n.

Table 1. Total of 36 (0−35) morphological characters used in the cladistic analysis of the 49 genera belonging to nine tribes of the subfamily Candoninae (changed from Karanovic 2007).

Genus	Morphological Characteristic																																			
	0	1	2	3	4	5	6	7	8	9	10	11	12	13	14	15	16	17	18	19	20	21	22	23	24	25	26	27	28	29	30	31	32	33	34	35
Cypria	0	0	0	0	0	0	0	1	1	0	0	0	1	0	0	0	0	1	0	0	0	0	1	0	0	0	0	0	0	0	0	0	0	1	0	0
Cyclocypris	0	0	0	0	0	0	0	0	1	0	0	0	0	0	0	0	0	0	0	0	0	0	0	0	0	0	0	0	0	0	0	0	0	0	0	0
Acandona	0	0	0	0	0	1	1	1	1	0	0	0	0	1	0	1	1	0	1	0	0	0	0	0	0	0	0	0	1	1	0	0	0	1	0	0
Amphitritecandona	1	0	1	0	0	1	1	1	1	1	0	0	0	1	0	1	1	1	0	1	1	0	0	0	1	0	0	0	0	0	0	1	0	0	0	0
Areacandona	0	0	1	1	0	1	1	1	1	1	1	0	0	0	0	1	1	1	0	*	0	1	0	0	1	0	0	0	0	0	0	1	0	0	0	0
Baicalocandona	1	0	0	0	0	1	1	0	1	0	0	1	0	1	0	1	1	0	?	1	0	0	1	0	0	0	0	0	1	1	0	0	0	*	0	?
Caaporacandona	0	0	1	1	0	1	1	?	?	0	0	0	0	1	0	?	?	1	1	1	0	0	0	?	?	?	?	?	1	0	1	0	0	0	0	1
Candona	0	0	0	0	0	1	1	1	1	0	0	1	0	1	0	1	1	0	1	1	0	0	1	1	0	0	0	0	1	1	0	0	0	1	0	0
Neglectocandona	0	0	0	0	0	1	1	1	1	0	0	1	0	1	0	1	1	0	1	1	0	0	1	1	0	0	0	0	1	1	0	0	0	0	0	0
Candonopsis	0	0	0	0	0	1	1	0	1	1	0	0	1	0	0	1	1	0	0	0	1	*	0	0	0	0	0	1	1	1	0	0	0	1	0	0
Abcandonopsis	0	0	0	0	0	1	1	0	1	1	0	0	1	0	0	1	1	1	1	*	1	*	0	0	0	0	0	1	1	1	0	0	0	1	0	0
Caribecandona	0	0	1	0	0	1	1	0	1	1	0	0	0	0	0	1	1	0	0	0	1	1	0	0	0	0	1	1	1	1	0	0	0	1	0	0
Cryptocandona	0	0	0	0	0	1	1	1	1	0	0	0	0	1	0	1	1	0	0	0	0	0	0	0	0	0	0	0	0	0	0	0	0	1	0	?
Cubacandona	0	0	0	0	0	1	1	0	1	?	0	0	0	0	0	1	1	0	1	0	1	0	0	0	0	0	1	1	1	1	0	0	0	0	0	0
Danielocandona	0	0	1	1	0	1	1	1	0	0	0	0	0	1	0	1	1	1	1	1	1	1	0	0	0	0	0	0	0	0	0	1	0	1	0	0
Deminutiocandona	0	0	1	1	0	1	1	1	*	1	0	0	0	1	0	1	1	1	*	1	0	*	0	0	0	0	0	0	0	0	0	1	0	1	0	1
Eucandona	0	0	0	0	0	1	1	0	1	0	0	1	0	1	0	1	1	0	1	1	0	0	1	1	0	0	0	0	1	1	0	1	0	1	0	0
Fabaeformiscandona	0	0	0	0	0	1	1	1	1	0	0	0	0	1	0	1	1	0	1	1	0	0	1	1	0	0	0	0	1	1	0	0	0	1	0	0
Kencandona	0	0	1	1	0	1	1	1	0	1	0	0	0	1	0	1	1	0	0	1	0	1	0	0	0	0	0	0	0	0	0	1	0	1	0	0
Humphreyscandona	1	0	1	0	0	1	1	1	1	1	0	0	0	0	0	1	1	1	0	*	0	1	0	0	1	0	0	0	0	0	0	0	0	0	0	0
Indocandona	0	0	0	0	0	1	1	1	0	0	0	0	0	1	0	1	1	?	0	1	0	1	0	0	0	1	0	0	0	0	0	1	0	1	0	0
Leicacandona	0	0	1	1	0	1	1	1	1	1	0	0	0	1	0	1	1	1	*	1	0	*	1	0	0	0	0	0	0	0	0	1	0	0	0	0
Marococandona	0	0	*	*	0	1	1	0	1	0	0	0	1	0	0	1	1	1	1	1	1	*	0	0	0	0	0	1	1	1	0	0	0	0	0	0
Meischcandona	0	0	1	1	0	1	1	?	?	1	0	0	0	1	?	?	?	1	1	1	0	1	0	?	?	?	?	?	0	0	0	0	0	0	0	0
Meridiescandona	0	0	1	0	0	1	1	1	*	1	0	0	0	0	0	1	1	1	0	0	0	0	0	0	1	0	0	0	0	0	0	0	0	0	0	0
Namibcypris	1	1	1	0	0	1	1	?	?	?	1	0	0	1	1	1	1	1	1	1	1	1	?	0	0	0	0	0	1	1	0	1	0	0	0	0
Nannocandona	0	0	1	1	0	1	1	?	?	1	0	0	0	1	0	?	?	1	1	1	0	0	0	?	?	?	?	?	1	1	1	1	0	0	0	0
Notacandona	1	0	1	1	0	1	1	1	*	1	0	0	0	1	0	1	1	1	0	0	0	0	0	0	0	1	0	0	0	0	0	0	0	0	0	0
Origocandona	0	0	1	1	0	1	1	1	1	1	0	0	0	0	0	1	1	1	0	0	0	0	0	0	0	1	0	0	0	0	0	0	0	0	0	0
Paracandona	0	0	0	0	0	1	1	?	?	?	0	0	0	1	0	1	1	0	0	0	0	0	0	0	0	0	0	0	1	1	0	?	0	0	0	0
Phreatocandona	0	0	0	0	0	1	1	?	?	0	0	0	0	1	0	?	?	1	1	1	0	1	0	?	?	?	?	?	1	1	0	1	0	0	0	?
Pierrecandona	1	0	1	1	0	1	1	1	1	1	0	0	0	0	0	1	1	1	0	0	0	0	0	0	1	0	0	0	0	0	0	1	0	0	0	0

Table 1. (*Continued*).

Genus	Morphological Characteristic																																		
	0	1	2	3	4	5	6	7	8	9	10	11	12	13	14	15	16	17	18	19	20	21	22	23	24	25	26	27	28	29	30	31	32	33	34	35
Pilbaracandona	1	0	1	1	0	1	1	1	1	1	0	0	0	0	0	1	1	1	0	0	0	1	0	0	1	0	0	0	0	0	0	1	0	0	0	0
Pioneercandonopsis	0	0	1	1	0	1	1	0	1	1	0	0	0	0	0	1	1	1	0	1	1	0	0	0	0	0	1	1	1	1	0	0	0	1	0	0
Schellencandona	0	0	0	0	0	1	1	1	0	0	0	0	0	1	0	1	1	0	1	1	0	0	1	0	0	0	0	0	1	1	0	0	0	1	0	0
Terrestricandona	0	0	1	0	1	1	1	?	?	1	0	0	0	1	0	?	?	0	1	1	0	0	0	?	?	?	?	?	1	0	1	0	0	0	0	?
Terrestricypris	0	0	1	1	1	1	1	?	?	1	0	0	0	1	0	?	?	0	1	1	0	0	0	?	?	?	?	?	1	0	1	0	0	0	0	1
Trajancandona	0	0	0	0	0	1	1	1	0	0	0	0	0	1	0	1	1	1	1	1	0	0	0	0	0	0	0	0	1	1	0	1	0	0	0	0
Trapezicandona	0	0	0	0	0	1	1	1	0	0	0	0	0	1	0	1	1	1	0	*	0	0	0	0	0	1	0	0	0	0	0	0	0	*	0	0
Typhlocypris	0	0	0	0	0	1	1	1	0	0	0	0	0	1	0	1	1	0	0	1	0	0	1	0	0	0	0	0	1	1	0	0	0	*	0	0
Pseudocandona	0	0	0	0	0	1	1	1	*	0	0	0	0	1	0	1	1	0	0	1	0	0	1	0	0	0	0	0	1	1	0	0	0	1	0	0
Latinopsis	0	0	0	0	1	1	1	0	1	1	?	0	0	0	0	1	1	0	0	0	1	0	1	0	1	0	1	0	1	1	0	0	0	1	0	0
Rugosuscandona	1	0	1	0	0	1	1	*	*	0	0	0	0	*	0	1	1	0	0	0	1	1	0	1	0	0	0	0	1	1	0	1	1	0	1	0
Ufocandona	0	0	*	*	1	1	1	0	1	0	0	1	0	*	0	1	1	0	1	1	1	1	0	1	0	0	0	0	1	1	0	1	1	0	1	1
Cabralcandona gen.n.	1	0	0	0	1	1	1	0	1	0	*	1	0	*	0	1	1	0	1	1	1	1	0	1	0	0	0	0	1	1	0	1	1	0	1	1
Lacrimacandona	0	0	0	0	0	1	1	0	0	0	0	1	0	*	0	1	1	0	0	1	1	0	0	1	0	0	1	0	1	1	0	0	0	1	1	0
Schornikovdona	0	0	1	1	0	1	1	1	*	0	0	0	0	*	0	1	1	0	0	0	0	1	0	1	0	0	1	0	1	1	0	1	0	1	1	1
Bicornucandona	1	0	0	0	1	1	1	0	0	0	0	0	0	*	0	1	1	0	0	1	0	0	0	1	0	0	1	0	1	1	0	0	1	0	1	0
Comalcandona	1	0	0	0	0	1	1	0	1	1	0	1	*	1	0	1	1	0	0	0	1	1	1	1	0	0	1	0	1	1	0	0	1	0	1	0
Hancockcandonopsis	0	0	0	0	0	1	1	0	1	1	*	0	0	0	0	1	1	0	0	1	1	0	0	1	0	0	0	0	1	1	0	0	0	1	0	0
Candobrasilopsis	0	0	0	0	0	1	1	0	1	1	0	0	1	1	0	1	1	0	0	0	1	0	?	1	1	0	0	?	0	0	0	0	0	1	0	1

Note that the two out group genera (*Cypria* and *Cyclocypris*) placed in the first two rows in the matrix. Character states: O.Surface of carapace: smooth / rarely ornamented (0), usually ornamented with hard ridges and/or holes (1); 1. Marginal pore canals: straight and equally long (0), branched and unequally long (1); 2. Number of AI segments: seven/eight (0), less (1); 3. Number of AI segments: 7/6 (0), 5 (1); 4. Exopod on AI: present (0), absent (1); 5. Rome's organ: present (0), absent (1); 6. Swimming setae on A2: present (0), absent (1); 7. Seta z1 on male A2: seta-like (0), claw-like (1); 8. Seta z2 on male A2: seta-like (0), claw-like (1); 9. G2 claw on female A2: shorter than GI and G3 (0), equally long as GI and G3 (1); 10. Number of rays on vibratory plate of Md: numerous (0), maximum of two (1); 11.Number of setae in bunch on Md palp: three (0), more (1); 12. Terminal segment on Md palp: square-shaped (0), several times longer than wide (1); 13. Setae in bunch on Md palp: wide and armed with only one row of setules (0), thin, and armed with many small setules all along and around (1); 14. Number of setae on protopod T1: numerous (0), only four (1); 15. Prehensile palps: segmented (0), unsegmented (1); 16. Prehensile palps: with additional subterminal bumps (0), without such bumps (1); 17. Basal seta on T2: present (0), absent (1); 18. Seta d2 on T3: present (0), absent (1); 19. Tf seta on T3: present (0), absent (1); 20. Posterior seta on CR: always present / very rarely absent (0), never present (1); 21. Posterior claw on CR: normal (0), reduced (1); 22. Appendage on genital field: never / extremely rarely present (0), always / most usually present (1); 23. Lobe g on hemipenis: very strongly sclerified (0), not strongly sclerified (1); 24. Lobe b on hemipenis: without chitinized dorsal part (0), with chitinized dorsal part (1); 25. Lobe a: normal (0), tiny and thin (1); 26. Lobe á: present (0), absent (1); 27. Lobe a: different (0), centrally positioned with lower and usually flat b and h lobes, or b lobe with a ventral projection (1); 28. Terminal segment of T3: with two short and one long setae (0), different (1); 29. Terminal segment of T3: different (0), with two long and one short setae (1); 30. Terminal segment of T3: different (0), Th2 seta transformed into long claw (1). 31. Exopod on A2: present (0), absent/reduced (1); 32. t setae on A2: present (0), absent (1); 33. Male sexual bristles on A2: absent (0); present (1). 34: Setae in bunch on Md palp: with row of setules (0), without setules (1). 35. Terminal segment of MxI palp: normal (0); minute (1). Note that multiple and missing character states correspond to *, ?, respectively (adapted from Karanovic 2007, 2018) and characters (31−35) are newly used in this study.

Type genus: *Cabralcandona* gen. n.

Other genera: *Bicornucandona* Külköylüoğlu et al., 2011, *Rugosuscandona* Külköylüoğlu et al., 2017, *Ufocandona* Külköylüoğlu et al., 2017, *Lacrimacandona* Külköylüoğlu et al., 2017, *Schornikovdona* Külköylüoğlu et al., 2017, *Comalcandona* Külköylüoğlu and Gibson 2017.

Etymology. The name is a combination of the last name of Dr. Maria Cristina Cabral with the genus *Candona* of the subfamily Candoninae. Gender feminine.

Diagnosis: A small candonine (< 0.5 mm in average). Carapace subrectangular (or at most one valve oval). Carapace partially or fully ornamented with hexagonal and/or pentagonal cells. Pore canals short to long with sensory setae. Four to five central muscle scars (also see discussion). Dorsally, carapace wide or narrow. Inner lamella broader on at least one marginal side than the other. Inner lamella with or without node-like structure (tubercules). A1 six- to eight-segmented. A2 four-segmented without exopod. t1-4-setae absent or not transformed to bristles in male. Aesthetasc Y very long with at least two segments. Md palp with a squarish terminal segment fused with medial claw. Third endite of Mxl with one or two smooth bristles. Prehensile palps of T1 not segmented and symmetric to slightly asymmetric. T2 five-segmented with one basal (d1) seta. T3 four segmented without dp seta and *e* seta. Terminal segment of T3 with two long and one short setae. UR with one anterior claw and rami or flagellum (whip) type (cf. Cypridopsinae type), without setae. Hemipenis moderate in size and with rounded *h* lobe. Zenker's Organ small, with six or seven whorls of spines. Female genital field without processes.

Genus *Cabralcandona* gen. n.

Type species: *Cabralcandona mixoni* sp. n.

Other species: The genus is presently monospecific.

Etymology. The generic name is dedicated to the genus *Candona* after Dr. Maria Cristina Cabral for her continuous contribution to the knowledge and work on Ostracoda. Gender feminine.

Diagnosis.

In lateral view, carapace subrectangular, LV overlaps RV. LV with two horns; one dorso-anteriorly and one dorso-posteriorly. In dorsal view, carapace is very narrow with greatest width near mid-line. Hinge adont. Valve surface ornamented with hexagonal cells with normal pores bearing sensory setae. Internal view, LV with 8−10 well-developed tubercules ventrally on the posterior end. Four to five muscle scars visible in about the center of the valves. RV without such tubercules. A1 seven-segmented. A2 four-segmented with a well-developed claw-like seta on protopodite in both sexes. Exopodial plate and setae absent. t setae absent. Aesthetasc Y very long. G1-3 claws dimorphic in sexes, G2 claw in females long, about the same length as all segments. Md palp with a wide terminal segment and with three claws, claw in the middle fused with terminal segment. Gamma seta absent. Mxl-palp with a very short terminal segment. Third endite with one short, smooth bristle. Prehensile palps slightly asymmetric in the males. No vibratory plate and no *a* seta present in T1. T2 five-segmented with one long basal seta (d1). T3 four-segmented with one basal seta (d1), "*e*-*f*-*g*" setae absent. Terminal segment of T3 with two long and one slightly shorter claw-like setae. UR with flagellum type (rod-like) anterior claw, without setae and posterior claw. Hemipenis with rounded *h* lobe. Zenker's organ with seven (5+2) whorls of spines. Female genital field small, without appendages.

Type species: *Cabralcandona mixoni* sp. n. (Figs 2–5)

Etymology. The species is named after Bill Mixon for his contributions to the Texas Speleological Survey, Texas Cave Management Association, and Association for Mexican Cave Studies.

Type locality. San Marcos Artesian Well (SMAW), Hays County, Texas, U.S.A.:
29°53'22.5" N, −97°56'11.3" W, ~177 m ASL.

Material Examined.

Holotype: One male dissected, with soft body parts in lactophenol solution and sealed with translucent nail polish on one slide (no: OK-TX-AW036:01). Valves kept in micropaleontological slides (no: OK-TX-AW036:02). Collected on April 15, 2013 by Benjamin F. Schwartz and Benjamin T. Hutchins from the type locality.

Allotype: One female dissected, with soft body parts in lactophenol solution and sealed with translucent nail polish on one slide (no: OK-TX-AW36:03-04). Collected on April 15, 2013 by Benjamin F. Schwartz and Benjamin T. Hutchins from the type locality.

Dissected paratypes: One male (no: OK-TX-AW052:05-06) and one female (no: OK-TX-AW052:07-08) from the type locality. Collected November 29, 2013 by Benjamin F. Schwartz and Benjamin T. Hutchins from type locality.

Non-dissected paratypes: three males and four females, and six juveniles kept in 70 % ethanol. Collected on May 21, 22, and 23, 2013; November 6, 16, and 29, 2013; December 5, 9, 13, and16, 2013; June 23 and 26, 2015; July 30, 2015; December 7, 2015 and November 2, 2016 by Benjamin F. Schwartz and Benjamin T. Hutchins from the type locality.

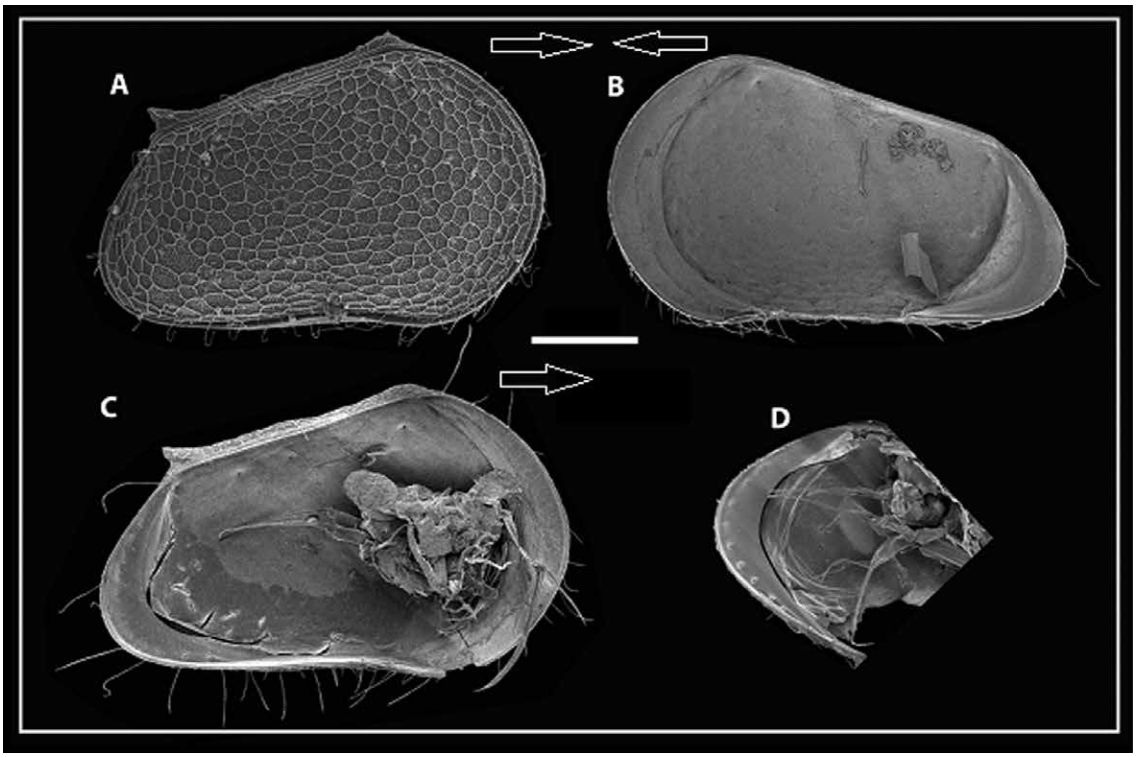

Figure 2. *Cabralcandona mixoni* gen. et sp. nov. male (A-C), female (D). A) Right side external view of whole carapace; B) RV internal view; C) LV internal view; D) LV internal view with node-like tubercles on posterior end. Arrows point anteriorly. Scale bar: 100 µm.

Description

Diagnosis: The diagnosis of the new species is similar to that of the genus.

Male: Measurements: L= 0.44–0.52 mm (average 0.48 mm) (n = 3), H = 0.27–0.30 mm (average 0.28 mm) (n = 3), W = 0.13–0.14 mm (average 0.14 mm) (n = 2). LV overlapping RV from all sides (Fig. 2A). Carapace subrectangular in lateral view. Anterior margin rounded and broader than posterior margin, dorsal margin tapering posteriorly. Greatest height located in front of mid-length closer to anterior margin (Fig. 2A−C). Carapace surface ornamented with wrinkled hexagonal cells, with small angular crenulated ridges inside these cells (Figs. 3D−F). Dorsal margin straight (not rounded). LV with two well-developed horn-like structures dorsally, anterior one slightly bent over RV (Fig. 2C). Normal pore canals with long sensory setae (Fig. 3F). Marginal pore canals reduced or short and not branched. Hinge adont. Carapace thick and opaque white in color. Four to five central muscle scars located near center (Fig. 3E. In dorsal view, carapace is fusiform-shaped, anterior margin more pointed and compressed than posterior end. Calcified inner lamella in RV smooth, slightly broader on posterior margin than on anterior margin (Fig. 2B). LV with 8−10 node-like tubercules posteriorly (Fig. 2C). Fused zone wide in both ends. Selvage thin in LV, not seen in RV.

A1 (Fig. 4A): seven-segmented. First segment articulated, with two anterior setae, one long claw-like stiff seta reaching about to the end of the third segment, and another medium-sized seta extending to midpoint of second segment. Rome and Wouters organs not seen. Second to fifth segments without setae. Penultimate segment with three equally long distal setae. Terminal segment with two equally long setae and one slightly short aesthetasc ya. All setae of A1 smooth. Length ratio of seven segments measured on centerline: 1.00 : 1.20 : 0.50 : 0.33 : 0.33 : 0.33 : 0.25.

A2 (Fig. 4B): four-segmented. First segment (protopodite) with a long claw-like postero-distal seta. Exopod absent on the second segment. Aesthetasc Y three segmented, very long and whip-like. Antero-distal setae is long and about the size of the GM claw. Setae t1-4 absent. Natatory (swimming) setae and aesthetascs y1-3 not seen (cf. female). z1 and z3 setae short and about the size of terminal segment, z2 seta is claw-like and about the same size as the G2 claw. G1 claw absent, G3 seta-like about one half of the GM claw. Gm claw less than half the length of G3. Claws and setae almost smooth.

Md (Fig. 4C): Md-coxa small compared to the palp, with six to seven smooth teeth and a small seta about one half the length of the longest tooth. Dorsal seta is almost the same size as the teeth. Md-palp four-segmented. First segment with two almost equally long smooth setae (S1, S2) posteriorly, and one shorter alpha (α) seta about one third the length of the S2-seta. Vibratory plate not seen. Second segment with four (3+1) sub-equally long claw-like setae. Beta seta absent. Third segment with one well-developed claw-like slightly plumose seta posteriorly and one small seta. Gamma seta absent. Terminal segment wide, with three claws, the middle one fused with the terminal segment. The middle and posterior claws plumose, anterior claw smooth and longer than the former two claws. No setae seen on anterior edge of the segments. Length ratios of four segments measured along centerline: 1.10 : 1.00 : 1.00 : 0.50.

Mxl (Fig. 4D): with three endites and a palp. Vibratory plate with seven to eight long plumose setae. Base of the first endite bearing one long seta slightly plumose about the length of the palp. First and second endites bearing four

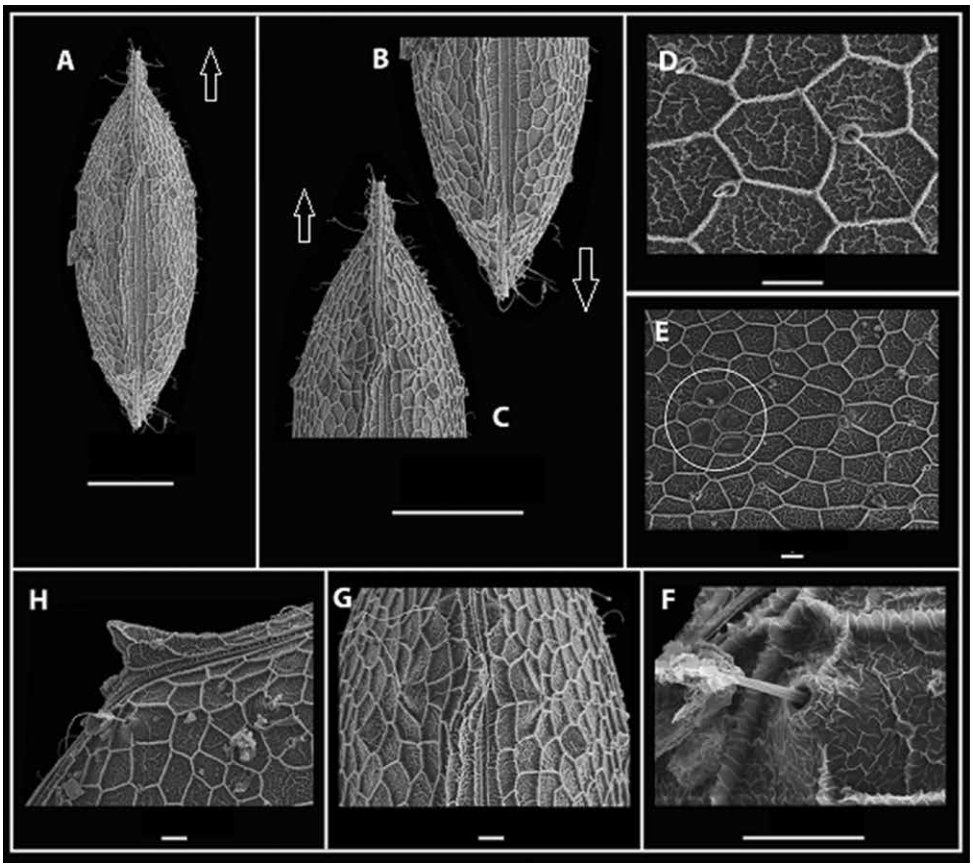

Figure 3. *Cabralcandona mixoni* gen. et sp. nov. female (A−C, H−G), male (D−F). A) Dorsal view of carapace; B) Dorsal view of posterior horn C) Dorsal view of anterior horn ; D) Close view of hexagonal ornamentations; E) Muscle scars; F) Close view of pore opening with sensory seta (note wrinkled cells on surface); G) Close dorsal view of anterior horn; H) Lateral view of posterior horn. Scale: 10 µm for D−E. Arrows point anteriorly.

and six short apical setae, respectively. Third endite with one smooth bristle-like seta about one half the length of the longest seta, and two long and one short slightly plumose setae. Mxl palp with elongated penultimate segment and two smooth setae, terminal segment about one quarter length of first segment, quadrate, and with three setae about the same length of two segments. Rake-like organ (Fig. 4E): comb-like with small teeth. Hypostome (Fig. 4F) simple rounded.

T1 (Fig. 4G-H): with well-developed and slightly asymmetric prehensile palps. Palps not divided, distal end hook-shaped. End of apical margin of the palps with three spine-like structures and one smooth seta above these spines. Left palp slightly longer and thinner than right palp. Vibratory plate not visible. *a* seta absent. Setae *b*, *c*, and *d* smooth and almost equally long. Masticatory process with 5 medium-sized apical setae.

T2 (Fig. 5B): five segmented with a long (d1) slightly serrated basal seta on the first segment, about the same size as the second segment. Setae dp and d2 absent. *e*, *f*, and *g* setae ($e > f > g$) present on second, third and penultimate segments, respectively. Terminal segment with one well-developed long and smooth claw (h2), reaching about half the length of the second segment. Setae h1 and h3 not seen.

T3 (Fig. 5A) four-segmented. First segment with a medium sized smooth d1 seta. d2 and dp setae absent; *e*, *f*, and *g* setae absent. Terminal segment quadrate to trapezoidal, with three smooth claw-like setae (length: h3 = h1 > h2). Setae h1 and h3 long about the length of last two segments. Hemipenis (Fig. 5C) with a rounded lobe *h*. Lobe *b* subtriangular. Lobe *a* with a pointing end dorsally. M process not visible. UR flagellum like with elongated ramus. Anterior and posterior setae absent. UR attachment simple. Zenker's organ (Fig. 5D) with seven (5+2) whorls of spines, ending with a wide sperm canal.

Female: L = 0.37–0.44 mm (average 0.41 mm) (n = 2), H = 0.23–0.24 mm (average 0.23 mm) (n = 2), W = 0.14–0.14 mm (average 0.14 mm) (n = 2). Carapace similar to that of male in shape (Figs. 2D, 3A-C, G-H), except for slight differences in size. All G-claws on A2 smooth (Fig. 5E). A short subapical seta present on the anterior end of the penultimate segment. Aesthetascs y1 and y2 absent, aesthetasc y3 small and about the size of terminal segment. Lengths: G3 > G1 > GM > G2 > Gm. G2 claw about half length of G1 and G3 claws. Gm seta-like and about 4x the length of the terminal segment. Genital field small without appendages (Fig. 5G). All other soft parts are similar to those of the male. T1 normally developed with three subequally long h1, h2, and h3 setae on distal end of endopod (Fig. 5F). Masticatory process with 5 plumose and 1 smooth setae. One medium-sized smooth "d" seta present.

Sympatric Ostracods

In addition to *Cabralcandona mixoni* sp. n. et gen. n., five other hypogean ostracod species (*Ufocandona hannaleeae*, *Rugosuscandona scharfi*, *Lacrimacandona wisei*, *Cypria lacrima*, *Namiotkocypria haysensis*, (Külköylüoğlu et al., 2017a-d, Külköylüoğlu 2018) have also been documented at the San Marcos Artesian Well.

Phylogeny

Cluster analysis produced a majority consensus tree with 117 steps (Ci = 27, Ri = 72) for the 49 genera, using the 36 morphological characters in more than 100 equally parsimonious trees (Fig. 6). *Cabralcandona* gen. n. is clearly

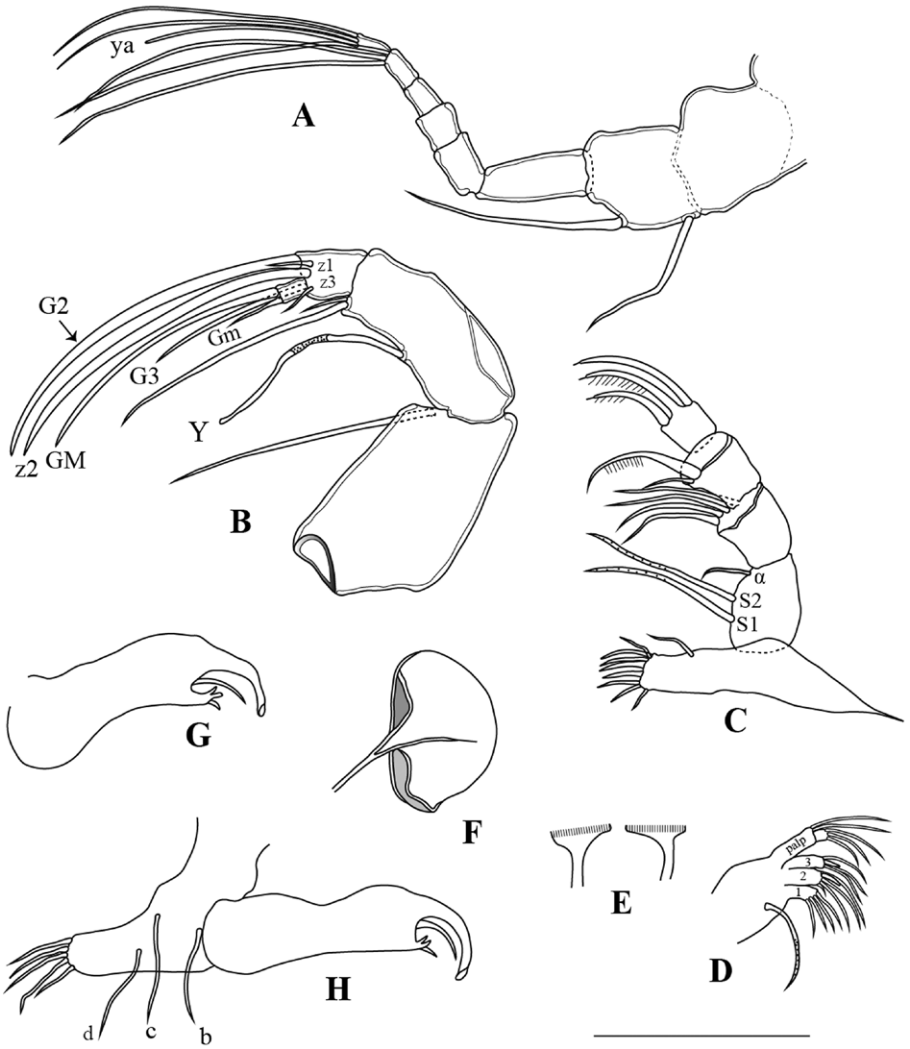

Figure 4. *Cabralcandona mixoni* gen. et sp. nov. Male: A) Antennule (A1); B) Antenna (A2); C) Mandible (Md); D) Maxillule (Mx1); E) Rake-like organ; F) Hypostome; G) Right clasping organ; H) Left clasping organ. Scale: 50 µm for A−C, E; 40 µm for D; 60 µm for F; 25 µm for G−H.

separated from other genera but clustered together with six other genera (*Rugosuscandona*, *Ufocandona, Bicornucandona Lacrimacandona*, *Schornikovdona*, *Comalcandona*) in the new tribe. However, cluster tree results suggest uncertainty in the taxonomic placement of several other genera. Indeed, relatively high Ci and Ri values suggest the prevalence of homoplastic change and/or convergence among the genera of the subfamily. However, following the current taxonomic keys (see discussion), the scenario may be seen differently where placement of some genera among the tribes differs.

Discussion

Cabralcandona gen. n. is assigned as the type genus of the new tribe Cabralcandonini tribe n., which shares some common characteristics with genera of the tribe Candonopsini, including a trapezoidal carapace, short marginal pore canals, A1 six or seven segmented, absence of bristles on A2 in males, terminal claw of Md palp fused with the apical segment, presence of two long and one short setae on the terminal segment of T3, female genital field without appendages, numbers of rows of spines on Zenker's organ, and absence of posterior seta on UR. Also see discussion about the taxonomic placements of *Candonopsis* in Higuti and Martens (2012) and *Abcandonopsis* in Karanovic (2004).

Several characteristics distinguish *Cabralcandona* from other genera, notably the two horn-like structures positioned dorsally on the LV, on nearly opposite ends of the hinge. *Bicornucandona* bears two horns on the LV but they are located in about the center of dorsal margin. We consider these structures diagnostic for the new genus, since they are also present in juveniles. Three of the genera placed closely to each other in the new tribe (*Cabralcandona* gen. n., *Rugosuscandona* and *Ufocandona*) seem to exhibit more similarities with one another than with other genera. For example, all three bear hexagonal and/or pentagonal cell-type ornamentations on the carapace surface although these structures are scarce and mostly restricted to marginal zones in *Ufocandona*.

Külköylüoğlu et al. (2017 a-c) stressed the importance of carapace ornamentation for species identification and as indication of microhabitat characteristics. The authors point out that carapace ornamentation may be more prominent in fossil (i.e., Paleogene-Neogene) forms (Krstić, 1972; Krstić and Guan, 2000) relative to recent forms. The ornamentations unique to Cabralcandonini may imply that the tribe shares a close relationship to ancestral forms. However, without fossil representatives of the Cabralcandonini genera, this hypothesis remains unsupported. Below, we discuss some body parts, and compare each with other taxonomic groups.

Several body parts are informative about the relationship between Cabralcandonini and other taxonomic groups:

1. Muscle scars: The subfamily Candoninae and tribe Candonopsini are characterized by six (one elongated + 3 anterior + 2 posterior) central muscle scars (Karanovic, 2004), previously characteristic for the Candonidae family (Meisch, 2000). In Cabralcandonini, there are only five internal scars, one of which is faint or invisible in external view. Muscle scars are invisible (or not very obvious) in external view in three genera (*Ufocandona*,

Rugosuscandona, Lacrimacandona) although they can be seen more clearly in *Cabralcandona mixoni* sp. n. et gen. n., and others (*Schornikovdona*, *Comalcandona*, *Bicornucandona*).

2. A1: The numbers of segments and chaetotaxy of A1 differ among genera (Karanovic, 2005a, b, c). Five genera (*Ufocandona, Lacrimacandona*, *Comalcandona*, *Bicornucandona*, *Cabralcandona* gen. n.) possess about seven segments while *Schornikovdona* bears five segments in A1. However, *Pioneercandonopsis*, and both *Rugosuscandona* and *Caribecandona* possess four and six A1 segments, respectively. As suggested previously (Karanovic and Marmonier (2003), Higuti and Martens (2014), Smith and Kamiya (2015), and Külköylüoğlu et al. (2017a-c, e)), a reduction in the numbers of segments of any organ or appendage (i.e., A1) likely represents a derived character state, possibly arising via paedomorphosis (Danielopol, 1978, 1980).
3. A2: Both females and males of the new genus have four segments in A2 without an exopodial plate. Although four or five A2 segments are found in different candonid genera (Karanovic, 2001, 2003a,b, 2012), absence of the exopod (or exopodial plate) is only known from *Rugosuscandona* and *Ufocandona* (but see exception in the males of *Ufocandona*) (Külköylüoğlu et al., 2017a,b). There are no sensory bristles on the A2 of males of the new genus, which is similar to five other genera (*Rugosuscandona*, *Ufocandona*, *Comalcandona*, *Cubacandona* and *Marococandona*). The new genus exhibits a sexually dimorphic character in the length of G-claws (G1−G3, GM, Gm), similar to those seen in several other genera in the tribe Candonopsini (Karanovic, 2006; Külköylüoğlu et al., 2017c). For example, G1–G3 claws on A2 are unequally long in three genera (*Lacrimacandona*, *Pioneercandonopsis* and *Meridiescandona*), but several North American species (e.g., *Candona peircei* Turner, 1895; *C. sigmoides* Sharpe, 1897; *C. suburbana* Hoff, 1942; *C. acuta* Hoff, 1942; *C. crogmaniana* Turner, 1894; *C. inopinata* Furtos, 1933; *C. intermedia* Furtos, 1933; *Eucandona rectangulata* (Alm, 1914); *Typhlocypris elliptica* (Furtos, 1933)) bear subequally sized claws (Karanovic, 2006; Külköylüoğlu et al., 2017a-d).
4. Md-palp: This is also one of the important diagnostic characteristic that separates the new tribe Cabralcandonini from other tribes of the subfamily (Table 1). While setae in bunch on the Md palp have no setules in the new tribe, these setae bear setules in other tribes. Besides, there are important differences in the numbers and shape of setal structures of the palp between *Cabralcandona* gen. n. and other members of the subfamily. For example, only the alpha (α) seta is present (beta and gamma setae absent on the other segments) on the first segment of the palp in the new genus. While alpha seta absent in *Rugosuscandona*, none of these setae (alpha, beta, and gamma) are present in the genus *Ufocandona*. Furthermore, *Cabralcandona* gen. n. has a group of 4 claw-like setae on the second segment (diagnostic character) while some other genera have 3 (e.g., *Rugosuscandona*) (Külköylüoğlu et al., 2017b), four (e.g., *Candonopsis*, *Ufocandona, Comalcandona*) or five (3+2) setae (e.g., *Maroco-*

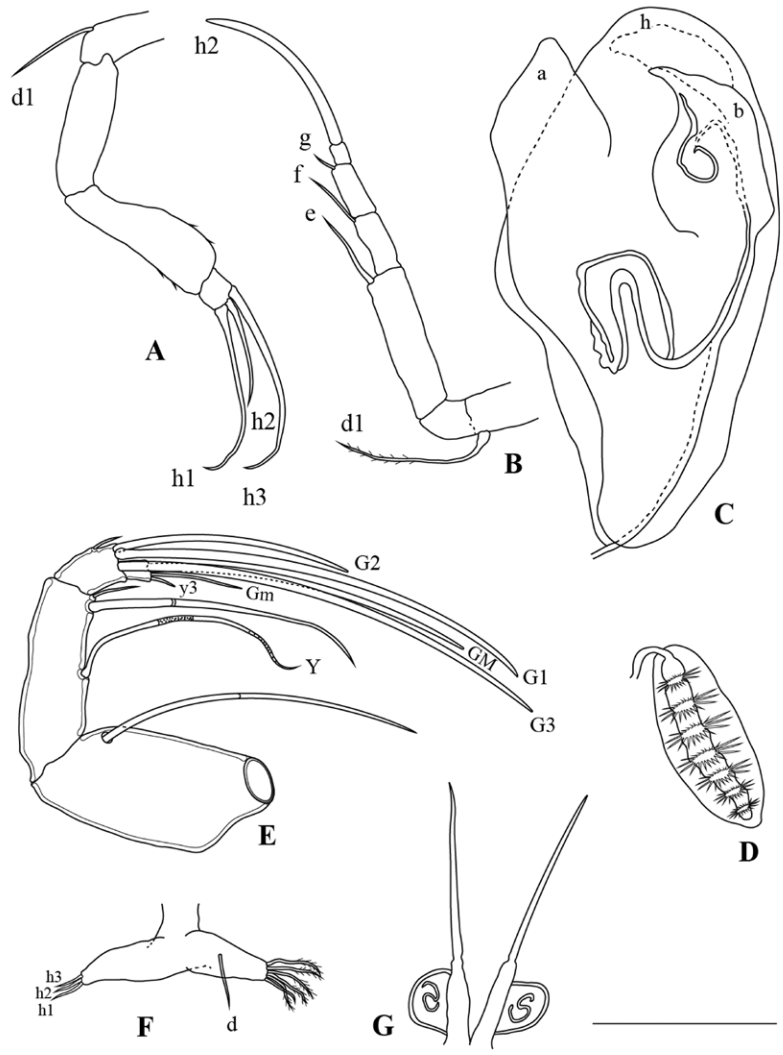

Figure 5. *Cabralcandona mixoni* gen. et sp. nov. A) T3; B) T2; C) Hemipenis; D) Zenker's organ; E) Female Antenna (A2); F) T1; G) Uropod of female with genital organ. Scale: 50 µm for A−C, E; 60 µm for D; 55 µm for F-G.

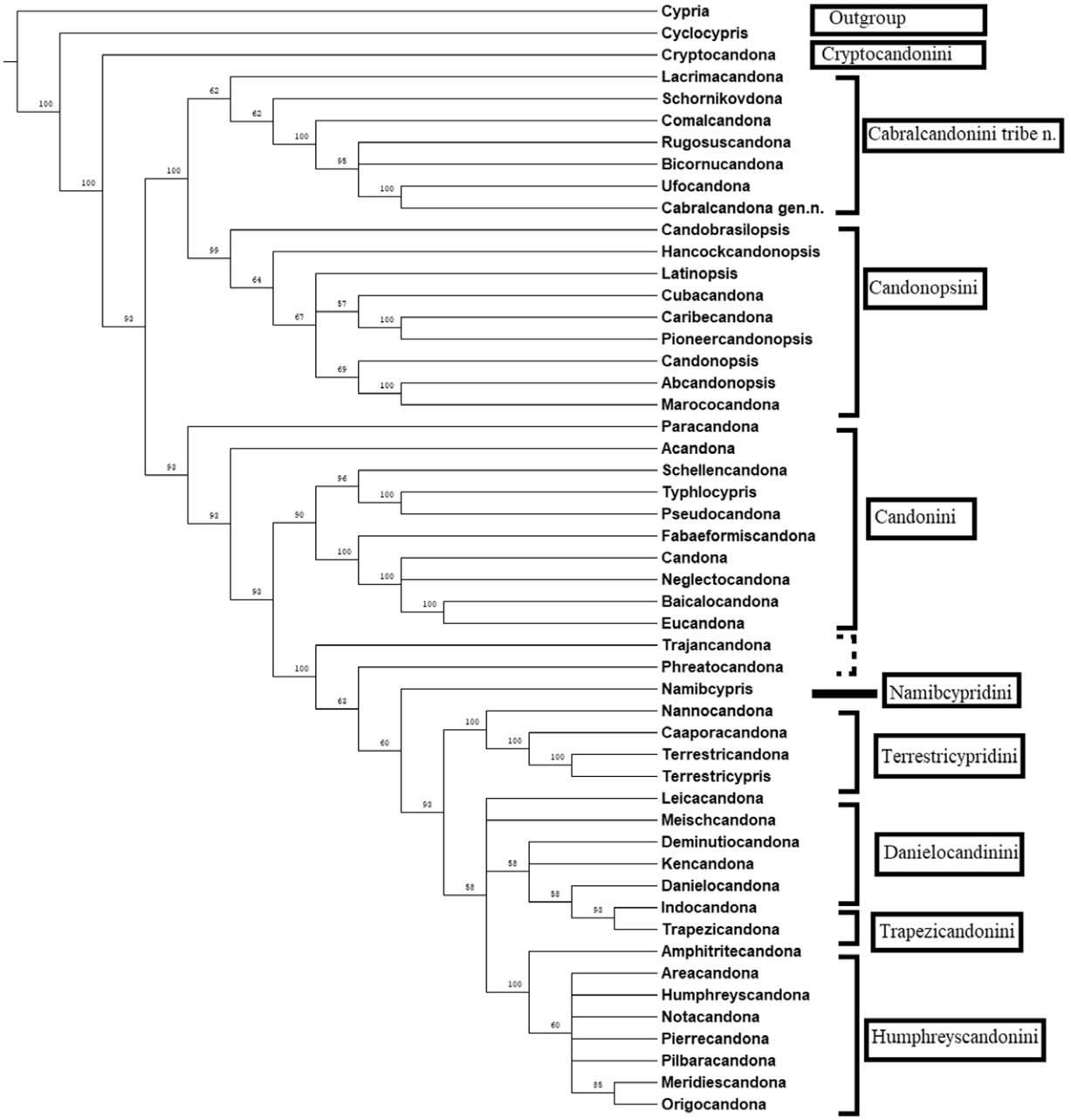

Figure 6. Clustering relationships of nine tribes of the subfamily Candoninae with Cabralcandonini tribe. n. and its new genera *Cabralcandona* gen. n.

candona) (Marmonier et al., 2005). The size of the terminal segment is variable among genera of both tribes Candonopsini and Cabralcandonini tribe n. According to the taxonomic key of Karanovic (2012), one of the main differences between the Md-palp of *Candonopsis* and *Latinopsis* is the size of the Md palp. While the former has a long palp (length of terminal segment more than 3× longer than width), the latter genus has a nearly square terminal segment (Karanovic and Datry, 2009). *Cabralcandona* gen. n. has a relatively large terminal segment fused with the center claw. The segment is relatively large with an almost square shape. Such differences are common not only in the new tribe but also among other tribes within Candonidae (e.g., see Broodbakker, 1983; Karanovic, 2001, 2008, 2012; Karanovic and Datry, 2009; Higuti and Martens, 2012, 2014; Külköylüoğlu et al., 2017a-d).

5. Mxl: *Cabralcandona* gen. n. is the only genus within the tribe that bears a short and smooth seta on the third endite of Mxl. The number of setae on the palp varies from 5 to 10 among the genera of the tribe Candonopsini but in *Cabralcandona* gen. n., there are two and three smooth setae on the penultimate and terminal segments of the palp, respectively. *Ufocandona* is the only genus with 5 setae, whereas the other genera have 8, 9, or 10 setae and claws (e.g., *Candonopsis linnaei* Karanovic, 2008). Herein, we only consider the differences in the number of setae. However, there are additional differences in the type of seta (e.g., plumose, setose or smooth: Smith and Kamiya, 2015; Karanovic, 2011; Külköylüoğlu and Gibson, 2018).

6. T1: *Cabralcandona* gen. n. has nearly symmetrical male prehensile palps, like three other genera of the subfamily **Candoninae** (cf. *Latinopsis*, *Pioneercandona*, *Rugosuscandona*). The absence of a vibratory plate in T1 in *Cabralcandona* gen. n. is also unusual, first reported for *Rugosuscandona*, and not common in members of the tribe Candonopsini. Additionally, *Rugosuscandona* and *Cabralcandona* gen. n. are the only genera in the new tribe that do not have *a* seta. This warrants further investigation since description of this seta along with others (*b*, *c*, *d* setae) can be difficult due to their small size.
7. T2−T3: The numbers of setae (*e*, *f*, *g* and basal (d1) setae) on T2 in the new genus is similar to related genera (but compare the type and size of setae in Külköylüoğlu et al., 2017a-d; Külköylüoğlu and Gibson, 2018) except for *Cubacandona*, *Candonopsis* and *Lacrimacandona*. In contrast, T3 of *Cabralcandona* gen. n. has only one basal (d1) seta and no *e*, *f*, *g* setae, similar to *Rugosuscandona*. Considering that all other genera of the new tribe bear at least two basal and one of the three other setae, the reduced setation on thoracic legs may be an additional adaptation to underground environments.
8. UR: *Cabralcandona* gen. n. has a flagellum type UR (diagnostic character of the genus) that is very similar to members of the subfamily Cypridopsinae. This character is also present in *Ufocandona* and *Rugosuscandona*. Two claws and two setae on UR is a common character state in cypridoid ostracods (Meisch, 2000) although the appendage is variable among members of Candoninae. *Caribecandona* (Broodbakker, 1983), *Indocandona* (Gupta, 1984), *Candonopsis* (e.g., see *Candonopsis* (*Abcandonopsis) aula*) (Karanovic, 2004), and *Bicornucandona* (Külköylüoğlu et al., 2011) have a single claw on the UR while *Lacrimacandona* has two small claws. A flagellum (or whip-like) type UR is very rare among the species of Candoninae (but see e.g., *Danielocandona lieshoutae* (Broodbakker, 1983)). Once again, the new genus exhibits a reduction in soft body parts. Indeed, McKenzie (1982) and Higuti and Martens (2012) pointed out that such reduction in size and chaetotaxy in the uropodal ramus of cypridoid species has occurred many times in different lineages, as an example of parallel evolution (homeomorphy) in non-marine ostracods. Knowledge about increased appendage length or reduction may provide additional understanding about habitat type. For example, in amphipods and isopods, increased setation and increased appendage length is often associated with open water type subterranean habitats (i.e. phreatic zones, vadose zones) while reduced setation and reduced appendage length is often associated with closed water type habitats (i.e. hyporheic zones) (Marmonier et al., 2005; Culver and Pipan, 2009).
9. Zenker's Organ: The new genus has 5+2 whorls of spines on the Zenker's organ. A similar pattern can be found in the members of the tribe Candonopsini (see discussion in Külköylüoğlu et al., 2017b, c).
10. Hemipenis: *Cabralcandona* gen. n. has a relatively small hemipenis (and Zenker's Organ) compared to other genera (e.g., cf. *Lacrimacandona*, *Rugosuscandona*). We were not able to observe an M-process in the hemipenis, but other parts (lobes) are unique to the genus. For example, lobe *a* with a sharp pointing end is clearly visible.

Cabralcandona gen. n. and two other congenera (*Rugosuscandona* and *Ufocandona*) are closely separated from others and clustered in the new tribe (Fig. 6). Although these three genera show clear morphological differences at the genetic level, they also share the following characters (Table 1) in common: 1) carapace ornamented with hexagonal or pentagonal cells, 2) numbers of segments in A2, 3) absence of t seta on A2, 4) absence of gamma seta on Md, 5) absence of seta a on T1, 6) presence of basal seta on T2 and T3, 7) absence of seta e on T3, 8) two long and one short setae on T3, 9) presence of rod-like (flagellum) claw on UR, 10) square or medial lobe in hemipenis. The tribe Candonopsini (Candoninae, Candonidae) previously included 13 subgenera (*Abcandonopsis*, *Candobrasilopsis*, *Candonopsis, Caribecandona, Comalcandona, Cubacandona*, *Hancockcandonopsis*, *Lacrimacandona, Latinopsis, Marococandona, Pioneercandonopsis, Rugosuscandona, Ufocandona*) but four genera (*Comalcandona, Lacrimacandona, Rugosuscandona, Ufocandona)* are now transferred to the new tribe Cabralcandonini tribe n.

Relationships among genera depicted in Figure 6 differ from the consensus tree of Karanovic (2007), because of potential factors including 1) the use of additional characters (e.g., absence of exopod in A2, flagellum-like UR), and 2) the number of genera included (49 versus 39 (sub)genera). Presence of polytomies among some genera also suggests that the number of characters may not be enough to discriminate clustering groups. Based on the cluster tree (Fig. 6), four other genera (*Bicornucandona*, *Comalcandona*, *Lacrimacandona*, *Schornikovdona*) can be tentatively placed with three closely related genera (*Cabralcandona* gen. n., *Rugosuscandona*, *Ufocandona*) of the new tribe. Considering that all these seven genera are found from the same geographic location and similar habitats (artesian well and/or spring waters), placement of these genera into the new tribe may be supported by the cluster tree. However, this placement does not correspond to the most current taxonomic keys (e.g., see Karanovic, 2007, 2012, 2018), in which some of these genera have already been described in other tribes. For example, presence or absence of posterior seta on the uropod is one of the main taxonomic character states separating the two close tribes Candonini (seta present) and Candonopsini (seta absent) (Karanovic, 2012). Following the key, for example, two genera (*Bicornucandona* and

Schornikovdona) belong to the tribe Candonini while two others (*Comalcandona*, *Lacrimacandona*) are placed in the tribe Candonopsini. Similarly, *Trajancandona* and *Phreatocandona* are supposed to be found in the tribe Candonini but the tree (Fig. 6) apparently separates these two from others. Although Karanovic (2007) reached a similar result, she included these two genera into the tribe Candonini following the taxonomic key. Relatively high Ci and Ri values suggest considerable uncertainty in the placement of genera within tribes because of a high degree of homoplasy. Karanovic (2007, 2018) emphasized that the phylogeny and evolution of Candonopsini needs to be investigated with molecular data (also see Hiruta et al., 2016). Although we agree that molecular data is valuable for phylogenetic analysis, obtaining adequate sample size across all or most taxa can present a challenge for construction of comprehensive molecular-based phylogenies.

Adaptations and Ecology

According to Marmonier et al. (2005, and references therein), and Külköylüoğlu et al. (2017b,c), hypogean (groundwater) ostracods may exhibit at least seven different morphological and reproductive specializations to groundwater conditions: 1) smaller body size, 2) anopthalmy or reduction in eye pigmentation, 3) reduction or loss of appendage length and setation, 4) changes in carapace shape, 5) elongation in appendages (e.g. legs and/or claws) or sensory setae (e.g., Y aesthetasc), 6) reduction of some extremities in males, 8) increase in egg size. Almost all genera in Cabralcandonini tribe n. exhibit these adaptations, although we currently do not have information on reproductive characteristics, including clutch and egg size. Overall, these adaptations clearly suggest that members of *Cabralcandona* gen. n. are restricted to hypogean habitats. Additionally, we can make some hypotheses about microhabitats in which these species may occur. For example, *Ufocandona hannaleeae* possesses asymmetric valves (oval LV and more subrectangular RV) while *Rugosuscandona wisei* and *Cabralcandona mixoni* sp. n. are rectangular and subrectangular in shape, respectively. According to Pipík and Bodergat (2005, 2007), some Candonine species with triangular and rectangular carapaces and a pointed posteroventral margin inhabit relatively stable habitats with minimal environmental fluctuations and species with a subcircular outline (e.g., *Cypria*) inhabit unstable environments.

Conclusions

Based on the characteristics discussed above, we propose Cabralcandonini tribe n. as a new tribe of the subfamily Candoninae. Hence, there are now nine tribes (Candonini Kaufmann, 1900; Candonopsini Karanovic, 2004; Cryptocandonini Karanovic, 2007; Danielocandonini Karanovic, 2007; Humphreyscandonini Karanovic, 2005, Namibcypridini Martens, 1992; Terrestricypridini Pinto et al., 2005; Trapezicandonini Karanovic, 2007, Cabralcandonini tribe n. Külköylüoğlu et al., in here) in the subfamily. However, ongoing studies strongly suggest that ostracod species diversity in at least some underground waters is unique and higher than currently acknowledged.

Key to the Tribes of Subfamily Candoninae: (Modified from Karanovic 2012)

1. Setae in bunch on Md palp without row of setules.....Cabralcandonini tribe n.
   – Setae in bunch on Md palp with row of setules.....2
2. Terminal segment of T3 with one long claw.……...Terrestricypridini
   – Terminal segment of T3 without long claw.……...3
3. Terminal segment of T3 with two long and one short setae……..4
   – Terminal segment of T3 with two short and one long setae……..6
4. T3 without basal seta……...…Namibcypridini
   –T3 with seta……..5
5. Posterior seta on the UR present……. Candonini
   – Posterior seta on the UR absent…… Candonopsini
6. Chitinized projection on the inner lobe of hemipenis present……Humphreyscandonini
   – Chitinized projection on the inner lobe of hemipenis absent……...7
7. A1 5-segmented……...……Danielocandonini
   – A1 7-segmented……...……...8
8. Basal seta on T2 present, outer lobe on hemipenis robust…….Cryptocandonini
   – Basal seta on T2 absent, outer lobe on the hemipenis thin…...Trapezicandonini

Acknowledgements

We thank Kristen Porter-Utley (Bartlett College of Science and Mathematics, Bridgewater State University) and Serdar Dinç (Bolu Abant İzzet Baysal University) for their help obtaining information about the WinClada program. Weston Nowlin, Zachary Schwartz, Jonny Scalise, and Aaron P. Swink are acknowledged for providing facilities and assisting with sorting raw samples and counting ostracods at the Freeman Aquatic Center, Texas State University. Cem Berk (The Scientific and Technological Research Council of Turkey − Marmara Research Center, Kocaeli, Turkey) and Dr. Michael K. Opoku (Research Service Center, Texas State University, Texas, U.S.A.) are thanked for their help

on SEM photography. We also thank the Department of Biology (Texas State University) and the Fulbright Research Scholarship program for their support.

References

Benson, R.H., 1990, Ostracoda and the discovery of global Cainozoic palaeoceanographical events, *in* Whatley, R., and Maybury, C., eds., Ostracoda and Global Events: Chapman and Hall, Cambridge, p. 41–59.

Bromley, H.J., and Por, F.D., 1975, The metazoan fauna of a sewage-carrying wadi, Nahal Soreq (Judean Hills, Israel): Freshwater Biology, v. 5, p. 121–133. https://doi.org/10.1111/j.1365-2427.1975.tb00126.x.

Broodbakker, N.W., 1983, The subfamily Candoninae (Crustacea, Ostracoda) in the West Indies: Bijdragen tot de Dierkunde, v. 53, p. 287–326.

Broodbakker, N.W., and Danielopol, D.L., 1982, The chaetotaxy of Cypridacea (Crustacea, Ostracoda) limbs: proposals for a descriptive model: Bijdragen tot de Dierkunde, v. 52, p. 103–120.

Carpenter, L.G., 1891, The artesian wells of Colorado and their relation to irrigation, *in* The State Agricultural College, The Agricultural Experiment Station, Bulletin No.16: Fort Collins, Colorado, p. 1–28.

Chaplin, J.A., and Ayre, D.J., 1997, Genetic evidence of widespread dispersal in a parthenogenetic freshwater ostracod: Heredity, v. 78, p. 57–67. https://doi.org/10.1038/hdy.1997.7.

Chippindale, P.T., 2000, Species boundaries and species diversity in the Central Texas Hemidactyliine Plethodontid salamanders, genus *Eurycea, in* Bruce, R.C., Jaeger, R.G., and Houck, L.D., eds., The Biology of Plethodontid Salamanders: Boston, Springer, 149–165. https://doi.org/10.1007/978-1-4615-4255-1_6.

Chivas, A.R., De Deckker, P., and Shelley, J.M.G., 1986, Magnesium and strontium in non-marine ostracod shells as indicators of palaeosalinity and palaeotemperature: Hydrobiologia, v. 143, p. 135–142. https://doi.org/10.1007/BF00026656.

Cohen, A.S., and Johnston, M.R., 1987, Speciation in brooding and poorly dispersing lacustrine organisms: Palaios, v. 5, p. 426–435. https://doi.org/10.2307/3514614.

Culver, D.C., and Pipan. T., 2009, Biology of caves and other subterranean habitats: Oxford, Oxford University Press, 272 p.

Culver, D.C., and Sket, B., 2000, Hotspots of subterranean biodiversity in caves and wells: Journal of Cave and Karst Studies, v. 62, p. 11–17.

Danielopol, D.L., 1978, Über Herkunft und Morphologie der Süsswasser–hypogäischen Candoninae (Crustacea, Ostracoda): Sitzungsberichte Österreichische Akademie der Wissenschaften Mathematisch-Naturwissenschaftliche, Kl. (I) 187, p. 1–162.

Danielopol, D.L., 1980, An essay to assess the age of the freshwater interstitial ostracods of Europe: Bijdragen tot de Dierkunde, v. 50, p. 243–291.

Danielopol, D.L., Baltanás, A., Morocutti, U., and Österreicher, F., 2011, On the need to renew the taxonomic system of the Candoninae (Non-Marine Ostracoda, Crustacea). Reflexions from an analysis of data using the Yule Process: Geo-Eco-Marina 17: 195–210.

De Deckker, P., 1981, Taxonomy and ecological notes of some ostracods from Australian inland waters: Transactions of the Royal Society of South Australia, v. 105, p. 91–138.

Díaz, A.R., and Lopretto, E.C., 2017, Postembryonic development of nonmarine ostracod *Chlamydotheca arcuata* (Sars, 1901) (Crustacea: Ostracoda), reared in the laboratory: Turkish Journal of Zoology, v. 41, p. 209–226. https://doi.org/10.3906/zoo-1512-13.

Garza, S.J., Wilson, K.R., and Bowser, G., 2015, Removal of artesian wells in Great Sand Dunes National Park and its aftermath on small mammals, plant cover, and area disturbance by ungulates: Park Science, v. 32, p. 57–64.

Higuti, J., and Martens, K., 2012, Description of a new genus and species of Candonopsini (Crustacea, Ostracoda, Candoninae) from the alluvial valley of the Upper Paraná River (Brazil, South America): European Journal of Taxonomy, v. 33 p. 1–31. https://doi.org/10.5852/ejt.2012.33.

Higuti, J., and Martens, K., 2014, Five new species of Candoninae (Crustacea, Ostracoda) from the alluvial valley of the Upper Paraná River (Brazil, South America): European Journal of Taxonomy, v. 106, p. 1–36. https://doi.org/10.5852/ejt.2014.106.

Hiruta, S.F., Kobayashi, N., Katoh, T., and Kajihara, H., 2016, Molecular phylogeny of cypridoid freshwater Ostracods (Crustacea: Ostracoda), inferred from 18S and 28S rDNA sequences: Zoological Science, v. 33, p. 179–185. https://doi.org/10.2108/zs150103.

Hoff, C.C., 1942, The Ostracods of Illinois: Illinois Biological Monographs, v. 19, p. 1–196.

Holsinger, J.R., and Longley, G., 1980, The subterranean amphipod crustacean fauna of an artesian well in Texas: Smithsonian Contributions to Zoology, v. 308, p. 1–62. https://doi.org/10.5479/si.00810282.308.

Hutchins, B.T., 2018, The conservation status of Texas groundwater invertebrates: Biodiversity and Conservation, v. 27, p. 475–501. https://doi.org/10.1007/s10531-017-1447-0.

Hutchins, B.T., Engel, A.S., Nowlin, W.H., and Schwartz, B.F., 2016, Chemolithoautotrophy supports macroinvertebrate food webs and affects diversity and stability in groundwater communities: Ecology, v. 97, p. 1530–1542. https://doi.org/10.1890/15-1129.1.

Hutchins, B.T., Schwartz, B.F., and Nowlin, W.H., 2014, Morphological and trophic specialization in a subterranean amphipod assemblage: Freshwater Biology, v. 59, p. 2447–2461. https://doi.org/10.1111/fwb.12440.

Karanovic, I., 2001, *Meischcandona* gen. nov. from Africa, with a key to the genera of the subfamily Candoninae (Crustacea, Ostracoda): Bulletin de l'Institut Royal des Sciences Naturelles de Belgique Biologie, v. 71, p. 93–99.

Karanovic, I., 2003a, Towards a revision of Candoninae (Crustacea: Ostracoda): description of two new genera from Australian groundwaters: Species Diversity, v. 8, p. 353–383. https://doi.org/10.12782/specdiv.8.353.

Karanovic, I., 2003b, A new genus of Candoninae (Crustacea, Ostracoda, Candonidae) from the subterranean waters of southwestern Western Australia: Records of the Western Australian Museum, v. 21, p. 315–332. https://doi.org/10.18195/issn.0312-3162.21(4).2003.315-332.

Karanovic, I., 2004, Towards a revision of Candoninae (Crustacea, Ostracoda): on the genus *Candonopsis* Vávra, with descriptions of new taxa: Subterranean Biology, v. 2, p. 91–108.

Karanovic, I., 2005a, Towards a revision of Candoninae (Crustacea: Ostracoda): Australian representatives of the subfamily, with descriptions of three new genera and seven new species: New Zealand Journal of Marine and Freshwater Research, v. 39, p. 29–75. https://doi.org/10.1080/00288330.2005.9517292.

Karanovic, I., 2005b, Comparative morphology of the Candoninae antennula, with remarks on the ancestral state in ostracods (Crustacea, Ostracoda) and proposed new terminology: Spixiana, v. 28, p. 141–160.

Karanovic, I., 2005c, A new Candoninae genus (Crustacea: Ostracoda) from subterranean waters of Queensland, with a cladistic analysis of the tribe Candonopsini: Memoires of the Queensland Museum, v. 50, p. 303–319.

Karanovic, I., 2006, Recent Candoninae (Crustacea, Ostracoda, Candonidae) of North America: Records of the Western Australian Museum, v. 71, p. 1–75. https://doi.org/10.18195/issn.0313-122x.71.2006.001-075.

Karanovic, I., 2007, Candoninae ostracodes from the Pilbara region in Western Australia: Crustaceana Monographs (Brill, Leiden), v. 7, p. 1–432. https://doi.org/10.1163/ej.9789004156937.i-434.

Karanovic, I., *2008,* A new species of the genus *Candonopsis* (Crustacea, Ostracoda) from Western Australia: Records of the Western Australian Museum, v. 24, p. 411–419. https://doi.org/10.18195/issn.0312-3162.24(4).2008.411-419.

Karanovic, I., 2011, On the recent Cyclocypridinae (Podocopida, Candonidae) with description of two new genera and one new species: Zootaxa 2820: 1-61. https://doi.org/10.11646/zootaxa.2820.1.1.

Karanovic, I., 2012, Recent freshwater Ostracods of the world: Crustacea, Ostracoda, Podocopida: Heidelberg, Springer Publishing, 608 p. https://doi.org/10.1007/978-3-642-21810-1

Karanovic, I., 2013, *Earicandona*, new genus and the first record of *Typhlocypris pratensis* (Crustacea, Ostracoda) from South Korea: Journal of Species Research, v. 2, p. 145–158. https://doi.org/10.12651/JSR.2013.2.2.145

Karanovic, I., 2018, A new Candonopsini (Ostracoda) genus from subterranean waters of New South Wales (Australia): Zootaxa, v. 4379, p. 247–267. https://doi.org/10.11646/zootaxa.4379.2.6.

Karanovic, I., and Datry, T, 2009, Overview of Candoninae (Crustacea, Ostracoda) of South America and the West Indies, with the description of two new species and one new genus: Zootaxa, v. 2267, p. 1–25. https://doi.org/10.11646/zootaxa.2267.1.1.

Karanovic, I., and Marmonier, P., 2003, Three new genera and nine new species of the subfamily Candoninae (Crustacea, Ostracoda, Podocopida) from the Pilbara region (Western Australia): Beaufortia, v. 53, p. 1–51.

Kesling, R.V., and Crafts, F.C., 1962, Ontogenetic increase in Archimedean weight of the ostracod *Chlamydotheca unispinosa* (Baird): American Midland Naturalist, v. 68, p. 149–153. https://doi.org/10.2307/2422641.

Krstić, N., 1972, Rod *Candona* (Ostracoda) iz kongerijskikh slojeva juzhnog dela Panonskog basena (Genus *Candona* (Ostracoda) from *Congeria* beds of Southern Pannonian Basin): The Serbian Academy of Sciences and Arts, Section of Natural and Mathematical Sciences, Monographs v. 9, p. 1–145.

Krstić, N., and Guan, S., 2000, A proposal for the systematics of the subfamily Candoninae ostracodes with the description of the *Macedocandona*, new genus: Geologica Macedonica, v. 14, p. 25–48.

Külköylüoğlu, O., 1998, Freshwater Ostracoda (Crustacea) and their quarterly occurrence in Şamlar Lake (İstanbul, Turkey): Limnologica, v. 28, p. 229–235.

Külköylüoğlu, O., 2009, Ecological succession of freshwater Ostracoda (Crustacea) in a newly developed rheocrene spring (Bolu, Turkey): Turkish Journal of Zoology, v. 33, p. 115–123.

Külköylüoğlu, O., 2018, A new genus and species in the ostracod family Candonidae (Crustacea: Ostracoda) from Texas, USA: Journal of Natural History, v. 52, p. 1295–1310. https://doi.org/10.1080/00222933.2018.1456574.

Külköylüoğlu, O., and Gibson, R., 2018, A new Ostracoda (Crustacea) genus, *Comalcandona* gen. nov., from Texas, U.S.A.: Turkish Journal of Zoology, v. 42, p. 18–28. https://doi.org/10.3906/zoo-1611-52.

Külköylüoğlu, O., Gibson, R., Diaz, P.H., and Colin, J.P., 2011, *Bicornucandona* gen. nov., sp. nov. (Crustacea, Ostracoda) from Finegan Springs (Texas, U.S.A.): Zootaxa, v. 3059, p. 47–58. https://doi.org/10.11646/zootaxa.3059.1.3.

Külköylüoğlu, O., Yavuzatmaca, M., Akdemir, D., Schwartz, B., and Hutchins, B., 2017a, A new genus (*Ufocandona* n. gen.) of Ostracoda (Crustacea) from an artesian well, Texas, North America: European Journal of Taxonomy, v. 372, p. 1–18.

Külköylüoğlu, O., Akdemir, D., Yavuzatmaca, M., Schwartz, B., and Hutchins, B., 2017b, *Rugosuscandona*, a new genus of Candonidae (Crustacea, Ostracoda) from Texas, North America: Species Diversity, v. 22, p. 175–185.

Külköylüoğlu, O., Akdemir, D., Yavuzatmaca, M., Schwartz, B., and Hutchins, B., 2017c, *Lacrimacandona* n. gen. (Crustacea: Ostracoda: Candonidae) from the Edwards Aquifer, Texas (U.S.A.): Zootaxa, v. 4277, p. 261–273. https://doi.org/10.11646/zootaxa.4277.2.6.

Külköylüoğlu, O., Akdemir, D., Yavuzatmaca, M., Schwartz, B., and Hutchins, B., 2017d, *Cypria lacrima* sp. nov. a new Ostracoda (Candonidae, Crustacea) species from Texas, U.S.A.: Zoological Studies, v. 56, p. 15. doi:10.6620/ZS.2017.56-15.

Külköylüoğlu, O., Yavuzatmaca, M., Akdemir, D., Diaz, P.H., and Gibson, R., 2017e, On *Schornikovdona* gen. nov. (Ostracoda, Candonidae) from rheocrene springs in Texas (U.S.A.): Crustaceana, v. 90, p. 1443–1461. https://doi.org/10.1163/15685403-00003707.

Külköylüoğlu, O., and Vinyard, G.L., 2000, The distribution and the ecology of the freshwater Ostracoda (Crustacea) collected from springs of Nevada, Idaho, and Oregon: A preliminary study: Western North American Naturalist, v. 60, p. 291–303.

Longley, G., 1981, The Edwards Aquifer: Earth's most diverse groundwater ecosystem?: International Journal of Speleology, v. 11, p. 123–128. https://doi.org/10.5038/1827-806X.11.1.12.

Lopez, L.C.S., Gonçalves, D.A., Mantovani, A., and Rios, R.I., 2002, Bromeliad ostracods pass through amphibian (*Scinaxax perpusillus*) and mammalian guts alive: Hydrobiologia, v. 485, p. 209–211. https://doi.org/10.1023/A:1021315223774.

Lopez, M.L.D., Magbanua, F.S., Mamaril, A.C., and Papa, R.D.S., 2017, Variations in microcrustacean (Crustacea: Cladocera, Copepoda) assemblages from selected groundwater-dependent ecosystems in the greater Luzon and Mindoro Island faunal regions (Philippines): insights to tropical groundwater ecology: Inland Waters, v. 7, p. 428–439. https://doi.org/10.1080/20442041.2017.1368597.

Marmonier, P., Boulal, M., and Idbennacer, B., 2005, *Marococandona*, a new genus of Candonidae (Crustacea, Ostracoda) from southern Morocco: morphological characteristics and ecological requirements: International Journal of Limnology, v. 41, p. 57–71. https://doi.org/10.1051/limn/2005006.

Martens, K., 1987, Homology and functional morphology of the sexual dimorphism in the antenna of *Sclerocypris* Sars, 1924 (Crustacea, Ostracoda, Megalocypridinae): Bijdragen tot de Dierkunde, v. 57, p. 183–190.

Martens, K., and Savatenalinton, S., 2011, A subjective checklist of the Recent, free-living, non-marine Ostracoda (Crustacea): Zootaxa, v. 2855, p. 1–79. https://doi.org/10.11646/zootaxa.2855.1.1.

McKenzie, K.G., 1982, Homeomorphy: Persistant joker in the taxonomic pack, with the description of *Bradleycypris* gen. nov. *in* Bate RH, Robinson E, Sheppard LM (Eds.), Fossil and Recent Ostracods: Chichester, Ellis Horwood Ltd., p. 407–438.

Meisch, C., 2000, Freshwater Ostracoda of Western and Central Europe (Süsswasserfauna von Mitteleuropa): Heidelberg, Spektrum Akad, Verlag / Gustav Fischer, 522 p.

Mezquita, F., Tapia, G., and Roca, R.C., 1999, Ostracoda from springs on the eastern Iberian Peninsula: Ecology, biogeography and paleolimnological implications: Palaeogeography, Palaeoclimatology, Paleoecology, v. 148, p. 65–85. https://doi.org/10.1016/S0031-0182(98)00176-X.

Nixon, K.C., 2002, WinClada version 1.00.08: Ithaca, N.Y., Published by the author.

Ogden, A.E., Quick, R.A., and Rothermel, S.R., 1986, Hydrochemistry of the Comal, Hueco, and San Marcos Springs, Edwards Aquifer, Texas, *in* Abbott, P.L., Jr., and Woodruff, C.M., eds., The Balcones Escarpment: Geology, Hydrology, Ecology and Social Development in Central Texas: San Antonio, Tex., Geological Society of America, p. 115−131.

Pipík, R., and Bodergat, A.M., 2005, Espèces du groupe de *Candona candida, Candona neglecta* et quelques Candona à l'aspect morphologique problématique (Candonidae, Ostracoda) du Bassin de Turiec (Miocène supérieur, Slovaquie): *Annales de Paléontologie, v. 91, p. 279–309*. https://doi.org/10.1016/j.annpal.2005.05.003.

Pipik, R., and Bodergat, A.M., 2007, Candoninae trapézoïdales (Crustacea, Ostracoda) du Bassin de Turiec (Slovaquie) du Miocène supérieur: systématique, écologie et évolution. Upper Miocene trapezoidal Candoninae (Crustacea, Ostracoda) of the Turiec Basin (Slovakia): Systematics, ecology and evolution: Geobios, v. 40, p. 645–676. https://doi.org/10.1016/j.geobios.2006.02.003.

Ponder, W.F., 2004, Endemic aquatic macroinvertebrates of artesian springs of the Great Artesian Basin – progress and future directions: Records of the South Australian Museum Monograph Series, v. 7, p. 101–110.

Schwartz, B.F., Hutchins, B.T., Schwartz, Z.G., Hess, A.J., and Bonett, R.M., 2018,

Cirolanides wassenichae sp. nov., a freshwater, subterranean Cirolanidae (Isopoda, Cymothoida) with additional records of other species from Texas, United States: Zootaxa, v. 37, p. 7-61. doi: 10.1016/j.anndiagpath.2018.08.004.

Siveter, D.J., 2008, Ostracods in the Palaeozoic?, Senckenbergiana lethaea, v. 88, p. 1–9. https://doi.org/10.1007/BF03043973.

Smith, R.J., 2011, Groundwater, spring and interstitial Ostracoda (Crustacea) from Shiga Prefecture, Japan, including descriptions of three new species and one new genus: Zootaxa, v. 3140, p. 15–37. https://doi.org/10.11646/zootaxa.3140.1.2.

Smith, R.J., and Kamiya, T., 2015, Four new species of the subfamily Candoninae (Crustacea, Ostracoda) from freshwater habitats in Japan: European Journal of Taxonomy, v. 136, p. 1–34. https://doi.org/10.5852/ejt.2015.136.

Smith, R.J., and Martens, K., 2000, The ontogeny of the cypridid ostracod *Eucypris virens* (Jurine, 1820) (Crustacea, Ostracoda): Hydrobiologia, v. 419, p. 31–63. https://doi.org/10.1007/978-94-017-1508-9_3.

Stejneger, L., 1896, Description of a new genus and species of blind tailed batrachian from the subterranean waters of Texas: Proceedings of the United States National Museum, v. 18, p. 619–621. https://doi.org/10.5479/si.00963801.1088.619.

Tuncer, A., and Tunoğlu, C., 2015, Early Pleistocene (Calabrian) Ostracoda assemblage and paleoenvironmental characteristics of the Fevzipaşa Formation, Western Anatolia: Micropaleontology, v. 61, p. 69–83.

Tunoğlu, C., 2002, Pontian Leptocytheridae and Cytheridae (Ostracoda) species from the eastern Black Sea Region of Turkey: Geologica Carpathica, v. 53, p. 333–346.

Ulrich, C.J. 1902, A contribution to the subterranean fauna of Texas: Transactions of the American Microscopical Society, v. 23, p. 83–102.

Williams, M., Siveter, D.J., Salas, M.J., Vannier, J., Popov, L.E., and Pour, M.G., 2008, The earliest ostracods: the geological evidence: Senckenbergiana lethaea, v. 88, p. 11. https://doi.org/10.1007/BF03043974.

Wise, C.D., 1961, Taxonomy and Ecology of freshwater ostracods of south-central Texas [Ph.D. thesis]: New Mexico, University of New Mexico. p.334.

GUIDE TO AUTHORS

The *Journal of Cave and Karst Studies* is a multidisciplinary journal devoted to cave and karst research. The *Journal* is seeking original, unpublished manuscripts concerning the scientific study of caves or other karst features. Authors do not need to be members of the National Speleological Society, but preference is given to manuscripts of importance to North American speleology.

LANGUAGES: The *Journal of Cave and Karst Studies* uses American-style English as its standard language and spelling style, with the exception of allowing a second abstract in another language when room allows. In the case of proper names, the *Journal* tries to accommodate other spellings and punctuation styles. In cases where the Editor-in-Chief finds it appropriate to use non-English words outside of proper names (generally where no equivalent English word exist), the *Journal* italicizes them. However, the common abbreviations i.e., e.g., et al., and etc. should appear in roman text. Authors are encouraged to write for our combined professional and amateur readerships

CONTENT: Each paper will contain a title with the authors' names and addresses, an abstract, and the text of the paper, including a summary or conclusions section. Acknowledgments and references follow the text. Manuscripts should be limited to 6,000 words and no more than 10 figures and 5 tables. Larger manuscripts may be considered, but the *Journal* reserves the right to charge processing fees for larger submissions.

ABSTRACTS: An abstract stating the essential points and results must accompany all articles. An abstract is a summary, not a promise of what topics are covered in the paper.

STYLE: The *Journal* consults The Chicago Manual of Style on most general style issues.

REFERENCES: In the text, references to previously published work should be followed by the relevant author's name and date (and page number, when appropriate) in brackets. All cited references are alphabetical at the end of the manuscript with senior author's last name first, followed by date of publication, title, publisher, volume, and page numbers. Geological Society of America format should be used (see http://www.geosociety.org/documents/gsa/pubs/GSA_RefGuide_Examples.pdf). Please do not abbreviate periodical titles. Web references are acceptable when deemed appropriate. The references should follow the style of: Author (or publisher), year, Webpage title: Publisher (if a specific author is available), full URL (e.g., http://www.usgs.gov/citguide.html), and the date the website was accessed in brackets. If there are specific authors given, use their name and list the responsible organization as publisher. Because of the ephemeral nature of websites, please provide the specific date. Citations within the text should read: (Author, Year).

SUBMISSION: Manuscripts are to be submitted via the PeerTrack submission system at http://www.edmgr.com/jcks/. Instructions are provided at that address. At your first visit, you will be prompted to establish a login and password, after which you will enter information about your manuscript and upload your manuscript, tables, and figure files. Manuscript files can be uploaded as DOC, WPD, RTF, TXT, or LaTeX. Note: LaTeX files should not use any unusual style files; a LaTeX template and BiBTeX file may be obtained from the Editor-in-Chief. Table files can be uploaded as DOC, WPD, RTF, TXT, or LaTeX files and figure files can be uploaded as TIFF, AI, EPS, or CDR files. Extensive supporting data may be placed on the Journal's website as supplemental material at the discretion of the Editor-in-Chief. The data that are used within a paper must be made available upon request. Authors may be required to provide supporting data in a fundamental format, such as ASCII for text data or comma-delimited ASCII for tabular data.

DISCUSSIONS: Critical discussions of papers previously published in the *Journal* are welcome. Authors will be given an opportunity to reply. Discussions and replies must be limited to a maximum of 1000 words and discussions will be subject to review before publication. Discussions must be within 6 months after the original article appears.

MEASUREMENTS: All measurements will be in Systeme Internationale (metric) except when quoting historical references. Other units will be allowed where necessary if placed in parentheses and following the SI units.

FIGURES: Figures and lettering must be neat and legible. Figure captions should be on a separate sheet of paper and not within the figure. Figures should be numbered in sequence and referred to in the text by inserting (Fig. x). Most figures will be reduced, hence the lettering should be large. Photographs must be sharp and high contrast. Figures must have a minimum resolution of 300 dpi for acceptance. Please do not submit JPEG images.

TABLES: See http://caves.org/pub/journal/PDF/Tables.pdf to get guidelines for table layout.

COPYRIGHT AND AUTHOR'S RESPONSIBILITIES: It is the author's responsibility to clear any copyright or acknowledgement matters concerning text, tables, or figures used. Authors should also ensure adequate attention to sensitive or legal issues such as land owner and land manager concerns or policies and cave location disclosures.

PROCESS: All submitted manuscripts are sent out to at least two experts in the field. Reviewed manuscripts are then returned to the author for consideration of the referees' remarks and revision, where appropriate. Revised manuscripts are returned to the appropriate Associate Editor who then recommends acceptance or rejection. The Editor-in-Chief makes final decisions regarding publication. Upon acceptance, the senior author will be sent one set of PDF proofs for review. Examine the current issue for more information about the format used.

Journal of Cave and Karst Studies

Volume 81 Number 2 June 2019

CONTENTS